Macauley, Gavin Martin (2020) *Skating on spin ice: On the application of Lorentz microscopy and numerical techniques to characterise phase transitions and non-equilibrium phenomena in artificial spin ices.* PhD thesis.

https://theses.gla.ac.uk/81979/

Skating on Spin Ice

On the application of Lorentz microscopy and numerical techniques to characterise

phase transitions and non-equilibrium phenomena in artificial spin ices

Gavin Martin Macauley

Materials and Condensed Matter Physics Group

School of Physics and Astronomy

University *of* Glasgow

Submitted in partial fufilment of the requirements for the Degree of *Doctor of Philosophy*

July 2020

«Considerate la vostra semenza:
fatti non foste viver come bruti,
ma per seguir virtute e canoscenza. »

"Consider where you come from:
you were not made to live as brutes,
but to pursue virtue and knowledge."

—Inferno, Canto XXVI, v.118-120, Dante

'Tell me one last thing,' said Harry. 'Is this real? Or has it all been happening inside my head?'

Dumbledore beamed at him, and his voice sounded loud and strong in Harry's ears even though the bright mist was descending again, obscuring his figure.

'Of course it is happening inside your head, Harry, but why on earth should that mean that it is not real?'

—Harry Potter and the Deathly Hallows, J.K. Rowling

Abstract

Artificial spin ices are arrays of nano-scale magnetic islands correlated by the interactions of their associated macrospins. They have proven an excellent playground in which to study phase transitions and non-equilibrium phenomena. Originally envisaged as a two-dimensional analogue to the frustrated rare-earth pyrochlores, they are now seen in their own right as promising candidates for a wide range of applications, including nanomagnetic computation and magnonics. At the same time, the capability of tuning their behaviour—whether by means of the constituent material, the fabrication pattern, or the application of external stimuli—enables the realisation of unusual aspects of statistical physics.

This thesis comprises a combined numerical and experimental study of artificial spin ice. The aims are twofold. First, it seeks to address how magnetic order and defect textures are influenced by the choice of lattice geometry. Second, it considers one route towards making artificial spin ice configurable via a coupling to a site-specific exchange bias.

In the initial segment of this thesis, the recently studied pinwheel form of artificial spin ice is described. This is created by rotating each island in the square lattice about $45°$ through its centre. The rotation angle of the islands acts as a proxy for a mechanism to vary the interactions between spins. A transition between antiferromagnetism in the square lattice and ferromagnetism in the pinwheel lattice is predicted. The phase diagram and critical exponents of the transition are obtained numerically.

The nature of this transition is confirmed experimentally using *in-situ* Lorentz transmission electron microscopy on thermally annealed cobalt arrays. Varying degrees of thermalisation are observed across the samples, as well as an apparent change in the nature of the defects: from one-dimensional strings in square ice to two-dimensional vortex-like structures for geometries similar to pinwheel. The numerical scaling of these quantities is consistent with that predicted by the Kibble-Zurek mechanism.

Finally, a two-dimensional hybrid artificial spin ice is outlined. In this, exchange bias is inserted at specific sites to constrain the magnetisation dynamics of individual islands. By examining correlations, a model for the influence of this pinning is constructed. As the density of constrained spins is varied, different magnetic textures are observed following a simulated field demagnetisation. These simulations show good agreement with results obtained experimentally. In this manner, local control over individual islands provides a route to tuning the global response of the array, thus making the system configurable. This is an essential step towards device-based applications.

Taken together, these results illustrate the interplay between topology and magnetic order in artificial spin structures, and enable the exploration of critical phenomena in frozen and glassy systems. The findings presented here demonstrate conclusively that artificial spin ice is an excellent test bed with which to probe out-of-equilibrium dynamics. They will also underpin its potential use in fields which are reliant on adressing specific microstates, such as neuromorphic computing.

Declaration

This thesis is a record of my work as part of the Materials and Condensed Matter Physics group in the School of Physics and Astronomy at the University of Glasgow during the period 2016-2020. Some of the work described in this thesis can be found in the following publications:

1. R. Macêdo, G. M. Macauley, F. S. Nascimento, and R. L. Stamps. "Apparent ferromagnetism in the pinwheel artificial spin ice". In: *Phys. Rev. B* 98 (1 July 2018), p. 014437. DOI: 10.1103/PhysRevB.98.014437

2. G. M. Macauley et al. "Tuning magnetic order with geometry: Thermalization and defects in two-dimensional artificial spin ices". In: *Phys. Rev. B* 101 (14 Apr. 2020), p. 144403. DOI: 10.1103/PhysRevB.101.144403

3. Y. Li et al. "Superferromagnetism and Domain-Wall Topologies in Artificial "Pinwheel" Spin Ice". In: *ACS Nano* 13.2 (Feb. 2019), pp. 2213–2222. DOI: 10.1021/acsnano.8b08884

4. G. W. Paterson et al. "Heisenberg pseudo-exchange and emergent anisotropies in field-driven pinwheel artificial spin ice". In: *Phys. Rev. B* 100 (17 Nov. 2019), p. 174410. DOI: 10.1103/PhysRevB.100.174410

The following publication is currently in review:

5. V. M. Parakkat, G. M. Macauley, R. L. Stamps, and K. M. Krishnan. "Configurable artificial spin ice with site-specific local magnetic fields". In: (*review,2020*)

In order, these appear as Refs. [1, 2, 3, 4, 5] in the Bibliography. Chapters 5 and 6 summarise Refs. [1] and [2], respectively. Chapter 7 is mainly an account of the work listed as Ref. [5], although it incorporates aspects of the remaining two publications. Each chapter contains a statement of attribution, making clear my contribution to the work. In addition, two Julia software packages, JASI and JIsing, were developed. These allow for Monte Carlo simulations of artificial spin ice and Ising systems. Documentation and installation instructions for these packages are available in an online repository [6, 7].

This thesis has not been submitted elsewhere for any other degree or qualification.

Acknowledgements

boss. Finally, to Becky, all my love. Thank you for being there for me. I dedicate this thesis to my family, to Becky and to all of my friends for—simply everything. I couldn't have done it without you.

Contents

List of Figures

List of Tables

1

Introduction

Artificial spin ices (ASIs) are arrays of strongly correlated sub-micron magnetic islands in which the individual elements are coupled through their magnetostatic interactions [8]. These arrays were originally envisaged as a two-dimensional (2D) analogue of the magnetic frustration present in bulk rare-earth pyrochlores [8]. The aspect ratio of these elements is usually chosen so that they behave as single magnetic domains, which can be described by means of an Ising-like variable. The long-range dipolar field between islands mixes spin and spatial degrees of freedom. As a result, the ordering within arrays is strongly dependent on the exact arrangement and orientation of the islands [9, 10]. By tailoring interactions locally, it is possible to obtain experimentally tractable mesoscopic counterparts to atomistic systems [11].

While ASI systems were first conceived in 2006, Ising-like systems made of magnetic islands have been studied extensively over the course of several decades [12], and continue to merit attention for the unusual ordering they manifest [13, 14, 15]. In recent years, advances in precision lithography have enabled the field of artificial spin ice to encompass a wider family of Hamiltonians, including Potts-like [16, 17] and dipolar XY [18, 19, 20] models. The individual microstates of these systems can be interrogated using magnetic microscopy (e.g. magnetic

force microscopy [21], photo-emission electron microscopy [22, 23] or Lorentz transmission electron microscopy [24, 25, 26, 2]). These methods allow us to examine the response to external stimuli such as applied field [27, 28], electrical current [29, 30] or temperature [23, 2]. ASIs thus provide us with new platforms in which to examine aspects of physics otherwise not directly observable. These include glassiness [31]; charge fragmentation [32]; and topologically-induced textures such as magnetic 'monopoles' [33, 22, 34], Dirac strings [35], and mesocopic domain walls [28].

Broadly speaking, this thesis sets out to address two questions:

1. How does the topology of the lattice influence both the magnetic ordering and the defect structures that form during a thermal annealing?

2. Can we use local magnetic fields to make artificial spin ice configurable?

In tackling these topics, our discussion will draw on aspects of critical phenomena and non-equilibrium physics to classify phase transitions in these systems. The findings, which we report here, are an essential prerequisite to understanding fully the collective behaviour of artificial spin ice lattices. This will help to lay the groundwork for uses in novel computer hardware, including in logic devices [36, 37] and in neuromorphic computing [38], for which an understanding of the inter-element interactions is crucial to tuning the response of the system. In this context, ensuring that the individual microstates in artificial spin ice can be addressed in a reproducible fashion is currently the matter of active research [39, 40, 41].

1.1 | Thesis overview

The thesis is structured as follows.

Chapter 2 serves as a primer for the topics in magnetism and artificial spin ice that we subsequently explore in this thesis. We give a heuristic account of the origin of atomic magnetism from which we develop the energy terms relevant to a study of ferromagnetic materials. Finite difference micromagnetic simulations are described. These are used throughout this thesis to extract physically reasonable values for parameters. A brief literature review of artificial spin ice is provided.

Chapter 3 discusses phase transitions in magnetic systems and the use of Monte Carlo techniques as a way to simulate them. We illustrate our points by applying them to the 2D Ising model, which is often taken as a limiting case to describe short-range interactions within artificial spin ices. We outline the finite-size scaling ansatz, which is useful in obtaining the critical exponents of second-order phase transitions, and describe replica exchange Monte Carlo.

Chapter 4 describes the experimental techniques used in this study to fabricate and, subsequently, to capture images of the magnetic configuration of artificial spin ice arrays. The fundamentals of focused electron beam induced deposition are explained. This method allows for the rapid prototyping of 2D structures, such as those as we investigate. Transmission electron microscopy, with a particular focus on the Fresnel mode of Lorentz microscopy, is introduced.

Chapter 5 is the first results chapter. In this chapter, we outline a recently studied form of artificial spin ice, the pinwheel lattice. This geometry is formed by rotating every island in the classic square artificial spin ice through 45° about its centre. This island rotation angle defines a continuum of geometries. We discuss the effect of this rotation on the dipolar interaction between islands, and show that it leads to a weakening of the stronger first-nearest-neighbour couplings which dominate the square lattice. Using equilibrium Monte Carlo simulations, we predict a transition in ground state spin ordering between antiferromagnetism in the square lattice to ferromagnetism in the pinwheel lattice. Finally, we consider low-energy configurations of the pinwheel ice, and draw an analogy with the structures that form in continuous magnetic media.

Chapter 6 confirms this transition in ordering experimentally by using *in-situ* Lorentz transmission electron microscopy on thermally annealed cobalt samples. We discuss how to interpret experimental Fresnel images of ASI arrays and how to extract from them a measurement of the correlations. In probing this transition, we examine how different tiling patterns approach equilibrium. We find that relaxation timescales are set indirectly through island rotation angle. As a result, we observe varying amounts of ground state magnetic texture, reflecting the extent to which arrays have been thermalised. This acts as a springboard to a discussion of non-equilibrium phenomena and, in particular, the Kibble Zurek mechanism of defect formation. We characterise defect textures in the two phases and show numerically that they scale with the exponent appropriate to the 2D Ising universality class.

Chapter 7 takes a different approach. Rather than considering a change to the geometry of the lattice, we couple islands in the classic square ice to site-specific external fields. These are supplied via an exchange bias layer applied to certain islands. By varying the density of spins pinned in this way, we gain a degree of control over local correlations. We estimate relaxation timescales in the presence of this pinning, and show that these influence ordering processes. We simulate a field-driven demagnetisation and compare the results with those obtained experimentally by our collaborators. Finally, we show that the pinning effectively tunes critical phenomena in these systems.

Chapter 8 summarises the conclusions of this thesis and advances a plan for future research.

2

Magnetism

2.1 | Introduction

This chapter is divided into two parts. The first outlines aspects of fundamental magnetism necessary for the analysis of artificial spin ice (ASI). The second presents a summary of key results in ASI that we will use frequently in later chapters.

The chapter is structured as follows. Sec. 2.2 defines the magnetic moment and describes the origin of atomic magnetism. We highlight the link between magnetism and angular momentum, and use this to justify the differential equations which govern magnetic materials in Sec. 2.3. The continuum approximation—central to micromagnetism—is outlined in Sec. 2.4 along with a discussion of the relevant energy terms. In Sec. 2.5, a brief literature review of ASI . This focuses on placing the field of study in context, and on those systems which show unusual phase transitions. The chapter concludes in Sec. 2.6 by describing how micromagnetic simulations provide a route to model accurately the behaviour of ASIs. This chapter is entirely review material.
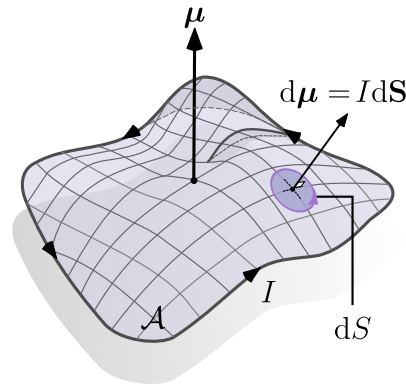
Figure 2.1: Definition of the magnetic moment in terms of elementary current loops. The circulating current, I, encloses a surface, $\mathcal{A}$, and gives rise to a moment, $\boldsymbol{\mu}$. The direction of the unit normal, $\hat{\mathbf{n}}$, and, hence, the net moment is determined by the 'right-hand-rule' for conventional current.

2.2 | Magnetic moments

The central quantity of magnetism is the magnetic moment, $\boldsymbol{\mu}$ [42]. In classical electromagnetism, this is conventionally defined with respect to a loop of wire. Given a current, I, circulating around an infinitesimal loop of area, $\mathrm{d}S$, the infinitesimal magnetic moment, $\mathrm{d}\boldsymbol{\mu}$, is given by

$$\mathrm{d}\boldsymbol{\mu} = I\,\mathrm{d}\mathbf{S}. \tag{2.1}$$

The differential vector, $\mathrm{d}\mathbf{S} = \mathrm{d}S\,\hat{\mathbf{n}}$, is defined such that $\hat{\mathbf{n}}$ is a unit vector perpendicular to the plane of the loop, and with a sense uniquely determined by the direction of conventional current. For an extended current distribution, i.e. a loop of finite size, we calculate the magnetic moment by summing the infinitesimal moments so that

$$\boldsymbol{\mu} = \int_{\mathcal{A}} \mathrm{d}\boldsymbol{\mu} = \int I(\mathbf{r})\,\mathrm{d}\mathbf{S}, \tag{2.2}$$

where $\mathcal{A}$ is the surface enclosed by I as in Fig. 2.1.

2.2.1 Origin of atomic magnetism

Equation (2.2) provides a heuristic explanation for the origin of atomic magnetic moments. The orbital motion of an electron of charge $-e$ and mass m_e around the nucleus gives rise to
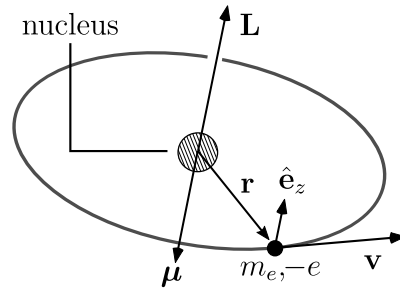
Figure 2.2: Origin of *classical* atomic magnetism. An electron (filled circle) orbiting an atomic nucleus (hashed circle) possesses an angular momentum, **L**. The orbit defines a circle of radius, r, and gives rise to a magnetic moment, $\boldsymbol{\mu}$. The negative charge of the electron ensures that **L** and $\boldsymbol{\mu}$ are antiparallel.

an *orbital angular momentum*, **L**. By definition, this angular momentum is

$$
\begin{aligned}
\mathbf{L} &\equiv \mathbf{r} \times \mathbf{p} \\
&= m_e v r\, \hat{\mathbf{e}}_z,
\end{aligned}
\tag{2.3}
$$

where v is the velocity of the orbiting electron; **r** its position vector with respect to the atomic nucleus; and $\hat{\mathbf{e}}_z$ a unit vector perpendicular to the plane of motion as shown in Fig. 2.2. The orbiting electron gives rise to a current $I = -e/T$ where $T = 2\pi r/v$ is the period. The electron sweeps out a circle of radius $r = |\mathbf{r}|$. The magnetic moment of the electron is then

$$
\begin{aligned}
\boldsymbol{\mu} &= I\,\mathbf{A} \\
&= \frac{-e}{2m_e}\,\mathbf{L} \\
&= -\frac{\mu_B}{\hbar}\,\mathbf{L},
\end{aligned}
\tag{2.4}
$$

where in the last line we have used the definition of the magneton, $\mu_B \equiv e\hbar/(2m_e)$.[1] By eq. (2.4), the magnetic moment of a *classical* electron is proportional in magnitude—but orientated antiparallel—to its orbital angular momentum.

In reality, the total angular momentum of an electron, **J**, also contains a contribution from its intrinsic angular momentum: the spin, **S**. Namely we have the vector sum,

$$
\mathbf{J} = \mathbf{L} + \mathbf{S}.
\tag{2.5}
$$

---

[1] The Bohr magneton, $1\,\mu_B = 9.274009994(57) \times 10^{-24}\,\mathrm{J\,T^{-1}}$ with dimensions $[L][A]^2$, corresponds to the magnetic moment of a 1s electron in hydrogen [43].

We define the gyromagnetic ratio, γ, as the constant of proportionality between the magnetic moment of the electron and its total angular momentum so that

$$\boldsymbol{\mu} = -\gamma \mathbf{J}. \tag{2.6}$$

In many transition metals, the orbital angular momentum is *quenched*, i.e. $\mathbf{L} = \mathbf{0}$, and the magnetic moment is determined principally by the intrinsic angular momentum (in effect, orbital effects can be neglected). [2] In terms of magnetic moments and spins then, "to speak of one is to speak of the other" [45] and the notation $\boldsymbol{\mu}$ for $\mathbf{S}$ (or even $\mathbf{m}$) is interchangeable. The converse example, *orbital* magnets (materials which are magnetic by dint of non-zero $\mathbf{L}$), have been recently demonstrated in bilayer graphene whereby one layer is twisted with respect to the other [46].

In passing, we note that the gyromagnetic ratio of an isolated electron is given by

$$\gamma_e = 1.76 \times 10^{11} \text{ rad s}^{-1} \text{ T}^{-1}, \tag{2.7}$$

based on the value given in Ref. [43]. Relation (2.6) is a general result: magnetic moments are associated with angular momenta. This has been experimentally demonstrated by both the Einstein–de Haas effect [47] (in which introducing a net magnetic moment causes rotation) and the Barnett effect (in which rotation induces a magnetic moment) [48].

2.2.2 Bohr-van Leeuwen theorem

Equation (2.6) was based on purely classical arguments. That it holds true quantum mechanically is just serendipity [49]. In any case, such reasoning will only take us so far: the Bohr-van Leeuwen theorem [50, 51] demonstrates that magnetic moments cannot exist in thermal equilibrium at least with respect to the distributions of classical statistical mechanics. Any true treatment of magnetism must therefore be explicitly *quantum*.

---

[2]In an isolated atom, the projection of $\mathbf{L}$ onto an arbitrary axis results in an eigenvalue m_ℓ which is a good quantum number. In a crystal however, this is no longer the case as the potential is not necessarily rotationally invariant. This can couple states which have different m_ℓ [44]. The resulting crystal wavefunctions are linear superpositions of the eigenfunctions for the isolated atom, ψ_ℓ. These are generally of the form $\psi_{m_\ell} \pm \psi_{-m_\ell}$ which have overall $m_\ell = 0$.
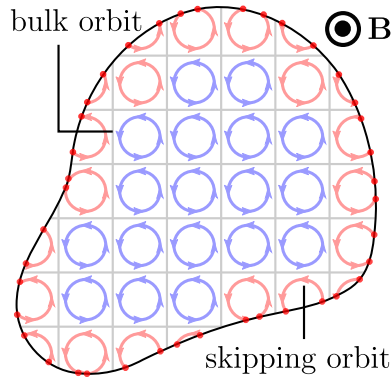
Figure 2.3: Bohr-van Leeuwen theorem and skipping orbits. A magnetic field, **B**, is applied to a material. Electrons move in cyclotron orbits. The net clockwise circulation of the bulk orbits (blue) is cancelled by the net anticlockwise circulation of the incomplete skipping orbits at the sample boundary (red).

This seems counter-intuitive. When a magnetic field is applied to a material, electrons perform cyclotron orbits with a radius,

$$r = \frac{m_e v}{eB},\tag{2.8}$$

as in Fig. 2.3. As these orbits are all in the same sense, we would naively expect the material to acquire a net moment. Indeed, electrons in the bulk do possess an overall circulation (shown anticlockwise in Fig. 2.3). However, electron near the boundary of the material cannot perform complete loops; instead, they are scattered elastically from the sample surface in *skipping orbits*. These skipping orbits have a net clockwise circulation which exactly cancels the opposite circulation from the bulk. As a result, the material has no moment.

2.3 | Torque

In this section, we discuss the form of the differential equation governing the motion of magnetic moments. In the Heisenberg picture of Quantum Mechanics, the time dependence of a physical system is folded into the operators while the state vectors—the kets—remain constant in time [52]. A general operator, $\hat{A}(t)$, in the Heisenberg picture evolves according to

$$\frac{\mathrm{d}}{\mathrm{d}t}\hat{A}(t) = \frac{1}{i\hbar}\left[\hat{A}(t), \mathcal{H}\right] + \left(\frac{\partial \hat{A}}{\partial t}\right)_{\mathcal{H}},\tag{2.9}$$

where $\mathcal{H}$ is the Hamiltonian of the system. The components of the angular momentum operator, $\hat{\mathbf{J}}$, satisfy the canonical commutation relations,

$$[\hat{J}_i, \hat{J}_j] = i\epsilon_{ijk}\hat{J}_k, \tag{2.10}$$

where ϵ_{ijk} is the Levi-Civita symbol. [3]

In applying these relations to eq. (2.9), it can be shown that the components of $\hat{\mathbf{J}}$ satisfy the cross product

$$\frac{\mathrm{d}}{\mathrm{d}t}\hat{\mathbf{J}} = \hat{\mathbf{J}} \times \frac{\partial\mathcal{H}}{\partial\hat{\mathbf{J}}}. \tag{2.11}$$

Dropping the 'hat' notation, and making a change of variables through $\boldsymbol{\mu} = -\gamma\mathbf{J}$ allow us to rewrite this in terms of the magnetic moment,

$$\frac{\mathrm{d}}{\mathrm{d}t}\boldsymbol{\mu} = \gamma\boldsymbol{\mu} \times \frac{\partial\mathcal{H}}{\partial\boldsymbol{\mu}}, \tag{2.12}$$

where the partial derivative of the Hamiltonian with respect to $\boldsymbol{\mu}$ is itself a vector with components $\partial\mathcal{H}/\partial\mu_\alpha$ for $\alpha \in \{x, y, z\}$. We define this quantity as the effective field, $\mathbf{H}_{\mathrm{eff}}$, through

$$\mathbf{H}_{\mathrm{eff}} = -\frac{1}{\mu_0}\frac{\partial\mathcal{H}}{\partial\boldsymbol{\mu}}, \tag{2.13}$$

where μ_0 is the permeability of free space. This allows us to rewrite eq. (2.12) as

$$\frac{\mathrm{d}}{\mathrm{d}t}\boldsymbol{\mu} = -\mu_0\gamma\,\boldsymbol{\mu} \times \mathbf{H}_{\mathrm{eff}}. \tag{2.14}$$

By analogy with classical physics, we recognise eq. (2.14) as a torque equation for the magnetic moment. Indeed, in some instances, it suffices to treat the magnetic moment as a purely classical vector which precesses around the direction of the effective field as in Fig. 2.4. It also follows that

$$\boldsymbol{\mu} \cdot \frac{\mathrm{d}\boldsymbol{\mu}}{\mathrm{d}t} = \frac{1}{2}\frac{\mathrm{d}}{\mathrm{d}t}|\boldsymbol{\mu}^2| = 0, \tag{2.15}$$

and so the torque equation preserves the length of the magnetic moment.

---

[3]The Levi-Civita tensor is the fully antisymmetric tensor, defined in three dimensions according to

$$\epsilon_{ijk} = \begin{cases} +1 & \text{if } (i, j, k) \text{ is an even permutation of } (1, 2, 3) \\ -1 & \text{if } (i, j, k) \text{ is an odd permutation of } (1, 2, 3) \\ 0 & \text{otherwise} \end{cases}.$$
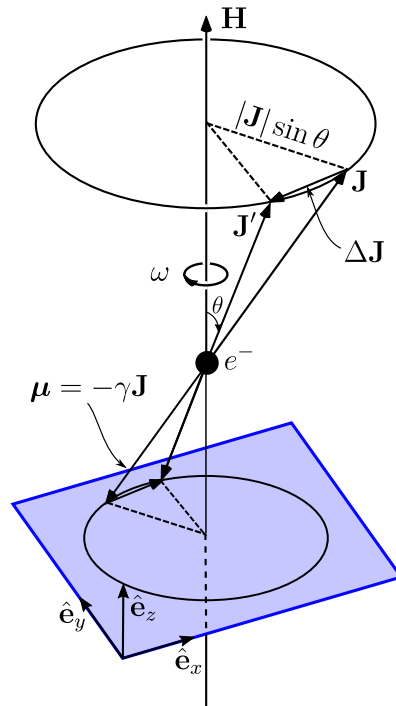
Figure 2.4: Precession of magnetic moments in a magnetic field. An electron with total angular momentum, **J**, and magnetic moment, $\boldsymbol{\mu} = -\gamma\mathbf{J}$, precesses around the direction of an applied field, **H**, with angular frequency, ω. The magnetic field is aligned along the $z-$axis and the magnetic moment traces out a cone of semi-angle θ.

Equation (2.14) represents the dynamics of a single magnetic moment. In general, we are interested in the behaviour of materials containing many magnetic moments, say, 10^{23} or more. To this end, we define an ensemble quantity, the magnetisation, which is the density of magnetic moments in some volume element, $d\mathcal{V}$, of a magnetic body:

$$\mathbf{M}(\mathbf{r}) = \frac{\sum_i \boldsymbol{\mu}_i}{d\mathcal{V}}, \tag{2.16}$$

where the sums runs over all the moments in the volume element.

In the (unphysical) limit of an infinitesimal volume containing a still substantial number of magnetic moments, we may replace the discrete sum in eq. (2.16) by a smooth function of position and time: $\mathbf{M} = \mathbf{M}(\mathbf{r}, t)$. This is the essence of micromagnetism: the true coarse-grained nature of atomistic magnetic moments is replaced by a continuum approximation. In this sense, the prefix *micro-* is a misnomer. Rather, the usefulness in taking $\mathbf{M}(\mathbf{r}, t)$ depends on assuming a macroscopic model of slowly varying atomistic moments.

Table 2.1: Example saturation quantities, M_S and B_S for materials considered in this thesis. The saturation field is related to the saturation magnetisation through $B_S = \mu_0 M_S$. Values taken from [55]

	M_S [kAm^{-1}]	B_S [T]
Fe	1714	2.15
Co	1422	1.78
Ni	484	0.61
Ni$_{80}$Fe$_{20}$	860	1.08

Given that the torque equation, eq. (2.14), preserves norms, we immediately conclude that the magnitude of the magnetisation field is everywhere constant and does not change in time. We call this magnitude the nn magnetisation of a material: $M_S = M_s \equiv |\mathbf{M}|$. For arrays of artificial spin ice, M_S is most often measured by saturating the sample in an external magnetic field using vibrating sample magnetometry [53, 54]. Table 2.1 lists typical values for the saturation magnetisation for materials considered in this thesis; an equivalent quantity, the saturation field, $B_s = \mu_0 M_S$, is also given. It is often convenient to rescale any dynamical equation for $\mathbf{M}$ in terms of a unit-length vector field $\mathbf{m}(\mathbf{r}, t)$ by $\mathbf{M} = M_S\,\mathbf{m}$.

Further, suppose that the effective field is rigorously re-defined as the functional derivative of the Hamiltonian with respect to the magnetisation,

$$\mathbf{H}_{\text{eff}} = -\frac{1}{\mu_0}\left(\frac{\delta \mathcal{H}[\mathbf{m}]}{\delta t}\right). \tag{2.17}$$

Then, the precession equation becomes simply

$$\frac{\mathrm{d}}{\mathrm{d}t}\mathbf{m} = -\gamma\,\mathbf{m} \times \mathbf{H}_{\text{eff}}, \tag{2.18}$$

provided the gyromagnetic ratio is also rescaled through $\mu_0\gamma \to \gamma$. We describe the terms of the energy functional, $\mathcal{H}[\mathbf{m}]$, more fully in Sec. 2.4 onwards.

2.3.1   Landau-Lifshitz-Gilbert equation

Equation (2.18) is pathological for a true physical system as it neglects damping. In particular, it suggests that the magnetisation precesses around the direction of the applied field but never
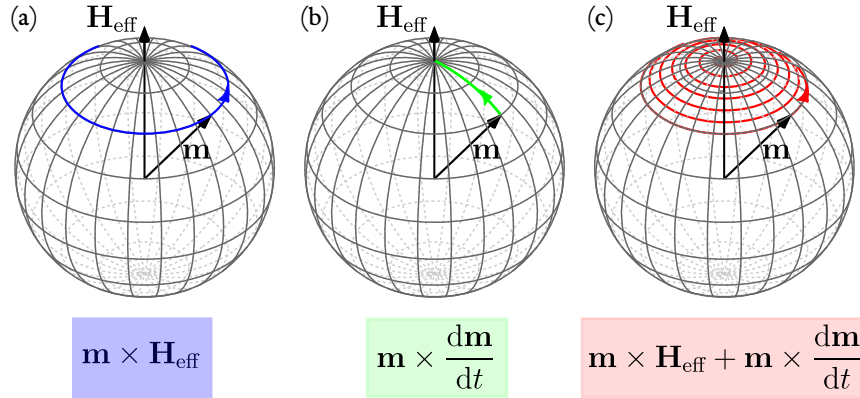
Figure 2.5: Decomposing the magnetisation dynamics of the LLG equation. (a) Undamped precessional motion of **m** around the effective magnetic field, $\mathbf{H}_{\text{eff}}$ (c.f. Fig. 2.4). (b) A frictional force related to the velocity of the magnetisation promotes alignment with $\mathbf{H}_{\text{eff}}$. (c) The full LLG equation combines motion from both (a) and (b): **m** continues to precess but eventually aligns with effective field.

aligns with it. In reality, the kinetic energy of **m** and its associated angular momentum are dissipated into the crystal lattice through both direct (e.g. phonons) and indirect (spin waves) means [56].

To model this, Landau and Lifshitz introduced a phenomenological term to remove energy from the system. Their differential equation—the *Landau-Lifshitz* (LL) equation [57]—is written

$$\frac{\mathrm{d}\,\mathbf{m}}{\mathrm{d}t} = -\gamma\,\mathbf{m} \times \mathbf{H}_{\text{eff}} - \lambda\,\mathbf{m} \times \left(\mathbf{m} \times \mathbf{H}_{\text{eff}}\right), \qquad (2.19)$$

such that λ is a damping parameter with dimensions of frequency. Gilbert proposed a further modification [58] to the right-hand side; namely that

$$\frac{\mathrm{d}\,\mathbf{m}}{\mathrm{d}t} = -\gamma\,\mathbf{m} \times \mathbf{H}_{\text{eff}} + \alpha\,\mathbf{m} \times \frac{\mathrm{d}\,\mathbf{m}}{\mathrm{d}t}. \qquad (2.20)$$

In this form, the dissipation arises from a frictional force related to the 'velocity' of the magnetisation, $\mathrm{d}\,\mathbf{m}/\,\mathrm{d}t$. This friction is weighted by the Gilbert damping constant, α. Equation (2.20) is called the *Landau-Lifshitz-Gilbert* (LLG) equation and is the standard equation used in numerical packages to model the dynamics of magnetisation [Sec. 2.6]. For a single moment it describes damped precession in which the moment spirals and eventually aligns with the

direction of the effective field, as shown in Fig. 2.5. The LL and LLG equations are not in fact independent; it is simple to show that the rescaling,

$$\gamma \longmapsto \frac{\gamma}{1+\alpha^2}\,, \qquad \lambda \longmapsto \frac{\gamma\alpha}{(1+\alpha^2)}\,, \tag{2.21}$$

transforms (2.19) into (2.20) precisely.

2.3.2 Types of magnetic order

Materials can be classified according to their magnetic ordering and, by extension, according to their response to an applied field. The susceptibility, χ, relates the magnetisation of a magnetic material to the applied field through

$$\mathbf{M} = \chi\,\mathbf{H}. \tag{2.22}$$

In a somewhat simplified picture, a ferromagnet is a material in which the spins spontaneously align along a preferred direction in the absence of an applied field, while an antiferromagnet is a material in which neighbouring spins anti-align under the same conditions [left and middle panels of Fig. 2.6(a), respectively]. Materials in which the spins are randomly orientated [right panel, Fig. 2.6(a)] can be grouped by the sign of their susceptibility as either paramagnetic ($\chi > 0$) or diamagnetic ($\chi < 0$).

The Curie-Weiss law governs the temperature dependence of the susceptibility above the ordering temperature of a material. This critical, ordering temperature for a ferromagnet is called the Curie temperature, T_C; while its counterpart for an antiferromagnet is called the Néel temperature, T_N. The behaviour of the inverse susceptibility, $1/\chi$, is shown for a ferromagnet, antiferromagnet, and paramagnet in Fig. 2.6(b).

A typical phase diagram for a ferromagnet is given in Fig. 2.6(c). Below the Curie temperature, the material exhibits a spontaneous magnetisation. The low temperature behaviour of $\mathbf{M}$ is governed by the Bloch law, which predicts a power-law dependence of $T^{3/2}$ [44]. Near to T_C, the magnetisation vanishes according to $(1 - T/T_C)^{1/2}$. We discuss this effect in more detail in Chapter 3.

There are other types of spontaneous magnetic ordering, including ferrimagnets, and variants of the above, including canted antiferromagnets, but this thesis will mainly consider the transition between antiferromagnetism and ferromagnetism.
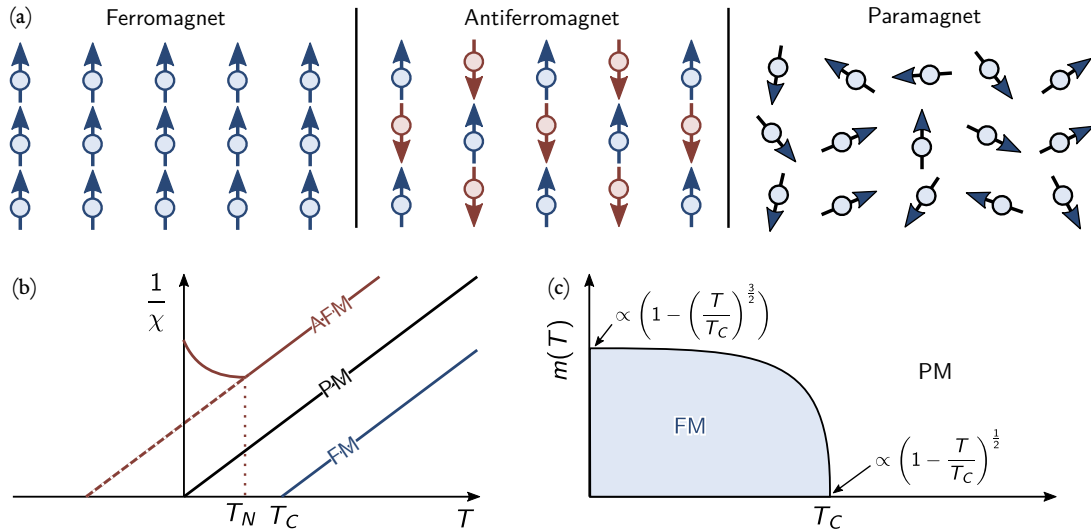
Figure 2.6: Classes of magnetic order. (a) L-R: a ferromagnet (in which neighbouring spins are aligned); an antiferromagnetic (in which neighbouring spins are antiparallel); and a paramagnet (in which no spontaneous magnetic order exists). (b) Schematic of inverse susceptibility, $1/\chi$, against temperature, T, for the materials in (a). The critical temperatures for a ferromagnet and antiferromagnet are called the Curie temperature, T_C, and the Néel temperature, T_N, respectively. (c) Phase diagram of a ferromagnet. Above T_C, thermal fluctuations are sufficient to destroy magnetic order and the system is paramagnetic. Low and near-T_C expansions of $m(T)$ are indicated.

2.4 | Energy functional

The Hamiltonian of a generic magnetic material can be written as the volume integral of the magnetic (free) energy density, $w(\mathbf{r})$, such that

$$\mathcal{H}[\mathbf{m}] = \int_{\mathcal{V}} \mathrm{d}^3\,\mathbf{r}\,w(\mathbf{r}). \tag{2.23}$$

Finding the ground state—or, equilibrium—configuration for a magnetic system thus reduces to solving a variational problem:

$$\delta\left(\int_{\mathcal{V}} \mathrm{d}^3\,\mathbf{r}\,w(\mathbf{r})\right) = 0.^4 \tag{2.24}$$

---

[4]C.f. Feynman in [49]: "Let us show you something interesting that we have recently discovered: *All of the laws of physics can be contained in one equation.* That equation is $U = 0$. What a simple equation! Of course, it is necessary to know what the symbol means. U is a physical quantity which we will call the 'unworldliness' of the situation."

We can write the total energy as the sum of several terms,

$$\mathcal{H} = \mathcal{E}_{\text{exch.}} + \mathcal{E}_{\text{Zeeman}} + \mathcal{E}_{\text{dip.}} + \mathcal{E}_{\text{anis.}}..., \tag{2.25}$$

where the individual contributions arise from the exchange, Zeeman, demagnetising and aniso-tropic interactions, respectively. This is not an exhaustive list, but these are the most important contributions to encapsulate the essential physics of most artificial spin ices. We now examine these terms in turn.

2.4.1 Exchange Energy

The exchange energy has its origins in the antisymmetry of electron wavefunctions under par-ticle interchange. Dirac [59] and Heisenberg [60] independently showed that an appropriate exchange Hamiltonian for two spins is

$$- \mathcal{J} \, \mathbf{s}_i \cdot \mathbf{s}_j, \tag{2.26}$$

where the sign of the exchange constant, $\mathcal{J}$, promotes either ferromagnetic ($\mathcal{J} > 0$, all spins aligned) or antiferromagnetic ($\mathcal{J} < 0$, neighbouring spins anti-aligned) order. Van Vleck subsequently generalised this result to more complicated atomic orbitals [61].

The Pauli exclusion principle requires that the overall wavefunction of fermions must be antisymmetric. It follows then that the symmetry of the spin configuration necessarily restricts the allowed spatial configurations for such a system (and vice versa). [5] Since different spatial configurations have different Coulomb energies (as they depend on the distribution of charged particles), this implies that spin configurations can be linked with electrostatic energy terms. As the magnitude of the exchange energy is set by Coulombic repulsion, we typically have

$$\mathcal{J} \sim \frac{e^2}{4\pi\epsilon_0 a} \sim 0.1 \text{ eV}, \tag{2.27}$$

---

[5]Of course, this assumes that the total wavefunction of the system, Ψ, can be written as the product of orbital and spin wavefunctions. For example, for a two-electron system, we would have

$$\Psi = \phi(\mathbf{r}_1, \mathbf{r}_2) \otimes \chi(\mathbf{s}_1, \mathbf{s}_2),$$

provided the spin-orbit coupling is small. Antisymmetry of one part under exchange then implies symmetry of the other.

assuming a realistic value, $a = 5\,\text{Å}$, for the lattice constant. This is equivalent to a temperature of approximately 1150 K.

For an extended lattice of spins, we can rewrite the exchange Hamiltonian in terms of the angle between neighbouring spins, $\mathbf{s}_i$ and $\mathbf{s}_j$. Writing ϕ_{ij} for this angle, we obtain

$$\mathcal{E}_{\text{exch}} = |\,\mathbf{s}\,|^2 \sum_{\langle i,j \rangle} \mathcal{J}_{ij} \phi_{ij}^2. \tag{2.28}$$

Here, the energy is measured with respect to a reference state in which all spins are aligned. For small angles, this expression can be expanded as a Taylor series about a given lattice point [62]. Then, in the limit of a continuous material (as in micromagnetism), we can re-express this exchange contribution as

$$\mathcal{E}_{\text{exch}} = \mathcal{A} \int_{\mathcal{V}} \mathrm{d}^3\,\mathbf{r} \big(\nabla\,\mathbf{m}\big)^2, \tag{2.29}$$

such that the exchange stiffness, $\mathcal{A}$, is the bulk analogue of the exchange constant, $\mathcal{J}$. This approximation is valid so long as the magnetisation is slowly changing in space or, equivalently, so long as the angle between neighbouring spins changes gradually.

2.4.2   Zeeman energy

A magnetic moment, $\boldsymbol{\mu}$, placed in a magnetic induction, $\mathbf{B}$, acquires a potential energy,

$$- \boldsymbol{\mu} \cdot \mathbf{B}. \tag{2.30}$$

This energy is minimised when the moment aligns parallel with the direction of the field. For a continuum description in terms of the unit-magnetisation, $\mathbf{m}$, we integrate over the volume of the sample so that

$$\mathcal{E}_{\text{Zeeman}} = -\mu_0 M_S \int_{\mathcal{V}} \mathrm{d}^3\,\mathbf{r}\,\mathbf{m} \cdot \mathbf{B}. \tag{2.31}$$

This represents the Zeeman coupling between the magnetisation vector field and the applied field. Clearly, in a multi-domain material, the application of $\mathbf{B}$ favours the growth of those domains aligned with the external field and the shrinkage of those opposed to the direction of the field.

2.4.3 Dipolar energy

Each magnetic moment is a source of dipolar fields and couples to every other moment in a material through magnetostatic interactions. For the specific case of two point magnetic dipoles, $\mathbf{s}_i$ and $\mathbf{s}_j$, at positions $\mathbf{r}_i$ and $\mathbf{r}_j$, the coupling is

$$\mathcal{E}_{i,j}^{\mathrm{dip}} = \frac{\mu_0}{4\pi} \left[\frac{\mathbf{s}_i \cdot \mathbf{s}_j}{r_{ij}^3} - \frac{3(\mathbf{s}_i \cdot \mathbf{r}_{ij})(\mathbf{s}_j \cdot \mathbf{r}_{ij})}{r_{ij}^5} \right], \tag{2.32}$$

where $\mathbf{r}_{ij} = \mathbf{r}_j - \mathbf{r}_i$ is the relative separation. For a discrete system of N spins, the dipolar field acting on spin i as a result of the other $(N-1)$ spins is

$$\begin{aligned}
\mathbf{H}_i^{\mathrm{dip}} &= -\frac{1}{\mu_0} \frac{\partial}{\partial \mathbf{s}_i} \mathcal{E}^{\mathrm{dip}} \\
&= \frac{1}{4\pi} \sum_{j \neq i}^{N} \left[\frac{\mathbf{s}_j}{r_{ij}^3} - \frac{3(\mathbf{s}_j \cdot \mathbf{r}_{ij}) \mathbf{r}_{ij}}{r_{ij}^5} \right].
\end{aligned} \tag{2.33}$$

Assuming two spins of moment $s \sim \mu_B$, separated by 1 Å, the typical order of magnitude for this interaction is $\mu_B^2/(4\pi r^3) \sim 60$ μeV or, equivalently, 1 K. In general, most magnetic materials order at higher temperatures (1043 K for iron, 1100 for cobalt [44]) and so the dipolar interaction alone is insufficient to explain their behaviour. As we shall discuss, some rare-earth materials, such as the pyrochlore holmium titanate, are *dipolar-ordered* and so their magnetism emerges at millikelvin temperatures [63]. Similarly, artificial spin ices are magnetostatically-coupled and so the dipolar interaction is the dominant one between islands.

The effect of the dipolar interaction is noticeable on macroscopic length scales. Here, the competition between exchange and magnetostatic interactions is responsible for magnetic domain formation. In the absence of an applied field, bulk samples of a magnetic material tend to be demagnetised, i.e. they exhibit no net magnetisation. This occurs because their internal structure admits, on average, a collection of randomly oriented magnetic domains. To see this, we translate eq. (2.32) into the continuum approximation. Ampére's Law in differential form states that for a magnetic field, $\mathbf{H}$, a current density, $\mathbf{J}$, and an electric field, $\mathbf{E}$,

$$\nabla \times \mathbf{H} = \mu_0 \left(\mathbf{J} + \epsilon_0 \frac{\partial \mathbf{E}}{\partial t} \right). \tag{2.34}$$

In the absence of free and displacement currents, eq. (2.34) simplifies to $\nabla \times \mathbf{H} = 0$. The magnetic field is thus conservative and can be written as the gradient of some scalar potential, ϕ_M, so that

$$\mathbf{H} = -\nabla \phi_M. \tag{2.35}$$

In this scenario, the magnetic field is often referred to as the *demagnetising* field, $\mathbf{H}_{\mathrm{d}}$[6]. The constitutive relation for magnetic materials, $\mathbf{B} = \mu_0 (\mathbf{H} + \mathbf{M})$, together with Gauss's Law for the magnetic induction, $\nabla \cdot \mathbf{B} = 0$, allow us to write

$$\nabla \cdot \mathbf{H}_{\mathrm{d}} = -\nabla \cdot \mathbf{M} = \nabla^2 \phi_M. \tag{2.36}$$

By analogy with electrostatics, sources and sinks of the magnetisation act as pseudo charges for the demagnetising field. Equation (2.36) is valid inside the magnetic material. In vacuum, $\mathbf{M} = \mathbf{0}$, and there is no distinction between the magnetic field and the magnetic induction. There, the differential equation becomes simply

$$\nabla^2 \phi_M = \mathbf{0}, \tag{2.37}$$

which is Laplace's equation. Maxwell's equations require that the components of $\mathbf{H}$ parallel and $\mathbf{B}$ perpendicular to an interface are continuous. These enforce matching conditions for the scalar potential and its first derivative. Without loss of generality, we can state these for the potential inside and outside the sample as

$$\phi_M^{\mathrm{in}} = \phi_M^{\mathrm{out}} \text{ and } (\nabla \phi_M^{\mathrm{out}} - \nabla \phi_M^{\mathrm{in}}) \cdot \hat{\mathbf{n}} = \mathbf{M} \cdot \hat{\mathbf{n}}, \tag{2.38}$$

where $\hat{\mathbf{n}}$ is the local unit normal to the surface [62].

Using the method of Green's functions and requiring that ϕ_M is "well behaved" for $r \rightarrow \infty$, the general solution to eq. (2.36), subject to the boundary conditions, is

$$\phi_M(\mathbf{r}) = \frac{1}{4\pi} \left(-\int_{\mathcal{V}} \frac{\nabla' \cdot \mathbf{M}}{|\mathbf{r} - \mathbf{r}'|} \, \mathrm{d}V' + \int_{\mathcal{S}} \frac{\mathbf{M} \cdot \mathrm{d}\mathbf{S}'}{|\mathbf{r} - \mathbf{r}'|} \right), \tag{2.39}$$

where the integrations are carried out over the volume of the ferromagnetic body, $\mathcal{V}$, and its surface, $\mathcal{S}$, defined through the outward normal $\hat{\mathbf{n}}$, respectively. The demagnetising field is

---

[6]'De-' because its effect is to *oppose* the magnetisation that gives rise to it. As magnetostatic fields are long-range, it exists also outside a magnetic material where it is often referred to as the *stray* field.

found through application of eq. (2.35). Evaluating this solution for ϕ_M is not trivial, except in highly symmetric situations. We can give a physical interpretation to its form, however. The first term is analogous to the integral of a volume charge density, $\rho_M = -\nabla \cdot \mathbf{M}$, while the second term is similar to the integral of a surface charge density, $\boldsymbol{\sigma}_M = \mathbf{M} \cdot \hat{\mathbf{n}}$. For a continuous body, the magnetostatic energy is then

$$\mathcal{E}_{\text{dip.}} = -\frac{\mu_0}{2} \int_{\text{all space}} \mathbf{H}_{\text{d}}^2 \, dV \qquad (2.40)$$

$$= -\frac{\mu_0}{2} \int_{\mathcal{V}} \mathbf{H}_{\text{d}} \cdot \mathbf{M} \, dV, \qquad (2.41)$$

from which it is clear that the energy is minimised by reducing the distribution of pseudo-magnetic charges. This explains the propensity for magnetic materials to form domains.

2.4.4   Anisotropy Energy

The exchange Hamiltonian, as expressed in eq. (2.26), is completely isotropic, which is to say the energy is independent of the direction of spontaneous magnetisation. In reality, there may exist certain preferred directions for $\mathbf{m}$ which are energetically more favourable. We refer to this as the anisotropy energy. We will distinguish between two cases: magnetocrystalline and shape anisotropy.

2.4.4.1 Magnetocrystalline anisotropy. Magnetocrystalline anisotropy arises from the spin-orbit coupling of electrons in the lattice and acts to lower the energy of certain crystallographic directions.[7] In such a case, it is energetically more favourable for $\mathbf{m}$ to lie along these *easy* axes. This contribution is (non-trivially) dependent on the symmetry group of the crystal lattice, and the shapes of the allowed atomic orbitals. The simplest case—observed in e.g. hexagonal and cubic structures—is that of uniaxial anisotropy. We define a certain unit direction, $\hat{\mathbf{n}}$, to develop an energy term of the form

$$\mathcal{E}_{\text{a}} = \int_{\mathcal{V}} -K \left(\mathbf{m} \cdot \hat{\mathbf{n}} \right)^2 d^3 \, \mathbf{r}, \qquad (2.42)$$

where $K > 0$, an energy-density, is the anisotropy constant. It is clear that increasing the component of $\mathbf{m}$ along $\hat{\mathbf{n}}$ lowers the energy of the state.

---

[7] The spin-orbit coupling appears as a term proportional to $\mathbf{L} \cdot \mathbf{S}$ in the crystal Hamiltonian.

(a) Spherical nano-particle   (b) Hard axis orientation   Easy axis orientation

Sphere radius, r Stadium-shaped isand
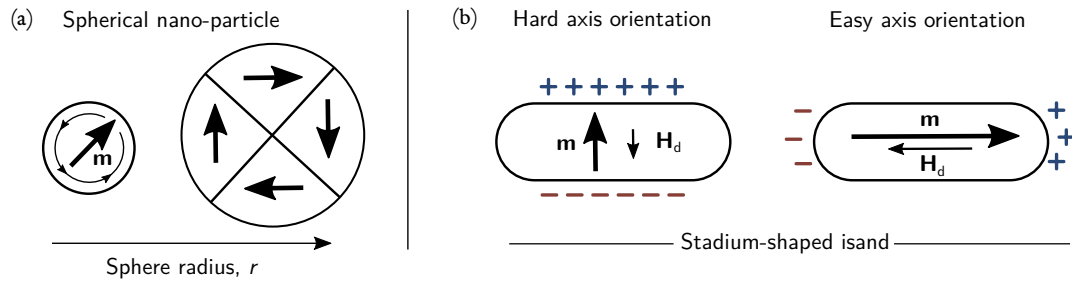
Figure 2.7: Shape anisotropy for spherical nano-particles and stadium-shaped single domain islands. (a) For sufficiently small radii, the symmetry of a sphere implies there is no preferred direction for magnetisation. As the radius is increased, the magnetostatic charge can be minimised by forming a flux closure state. (b) For stadium-shaped islands, like in ASI, the in-plane short axis is an effective hard axis. This reflects the build-up of magnetic charge, indicated by the blue and red symbols.

2.4.4.2 Shape anisotropy. By contrast to magnetocrystalline anisotropy, shape anisotropy is a consequence of magnetostatic interactions. It is determined by the physical, macro-scale dimensions of a sample rather than its crystal structure. For example, the rotational symmetry of a perfect sphere implies there is no *a priori* direction along which all moments would spontaneously align as shown in Fig. 2.7(a).[8] Were the sphere elongated along a certain direction, this long axis would become an effective easy axis as in Fig. 2.7(b). This reflects the build-up of magnetic charges—north and south *pseudo*-poles—which appear on the surface of the sample. The charge density, which acts as the sources and sinks of the demagnetising field, is minimised when the magnetisation lies along the 'long' axis. This energy term is particularly important for small elongated magnetic elements such as those used in artificial spin ice arrays. In fact, as we discuss later, it sets the largest energy scale of the problem—far greater than even the dipolar interactions between islands.

2.5 | Artificial spin ice

In this section, we present a brief review of some relevant topics from the field of artificial spin ice. This section is not intended to be exhaustive, and there exist many comprehensive

---

[8]That moments do align in such a circumstance is an example of spontaneous *symmetry-breaking*.
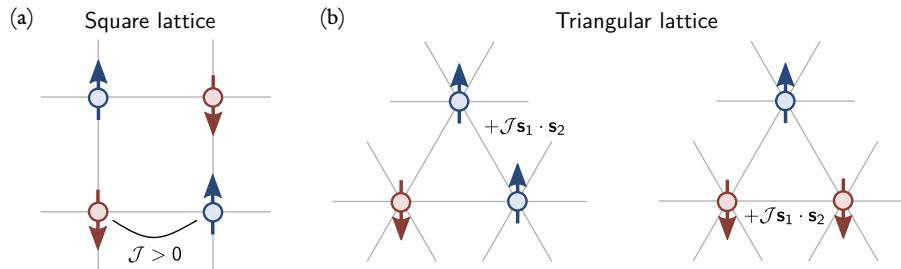
Figure 2.8: Frustration in lattice spin systems. An antiferromagnetic exchange, $\mathcal{J}\,\mathbf{s}_1 \cdot \mathbf{s}_2$, with $\mathcal{J} > 0$ on (a) square and (b) triangular lattices. Each lattice point is associated with a single magnetic moment. (a) The antiferromagnetic interaction can be completely satisfied on the square lattice to give the Néel ground state. (b) In contrast, the triangular plaquette is frustrated: one pair of neighbours remain aligned even in the ground state.

reviews of the field, including those by Nisoli *et al.* [64], by Heyderman and Stamps [65], and, most recently, by Skjærvø *et al.* [66].

2.5.1 Frustration

Artificial spin ices are examples of geometrically frustrated systems. Considered the "unifying theme" of complexity in the physical sciences [67], frustration refers to the inability of a system to satisfy competing interactions. In general, it leads to a large degeneracy in ground states. In a magnetic context, the prototypical example of a frustrated system is a two-dimensional antiferromagnet on a triangular lattice. This has a Hamiltonian of the form,

$$\mathcal{H} = \mathcal{J} \sum_{\langle i,j \rangle} \mathbf{s}_i \cdot \mathbf{s}_j, \tag{2.43}$$

where $\mathbf{s}_i = \pm 1$ is the spin at site i, and $\mathcal{J} > 0$ is a coupling constant which promotes antiparallel alignment between immediate neighbours. Arranging spins on a square lattice can be done by inspection, such that the Néel ground state is realised [Fig. 2.8(a)]. As Wannier demonstrated however, this is not the case on a triangular plaquette for which one bond is always left unsatisfied [Fig. 2.8(b)] [68]. Since the system can, in principle, select any of the degenerate ground states, it retains a residual entropy down to absolute zero.

A similar effect was noted originally in water-ice. There, the tetrahedral arrangement of ice molecules promotes the formation of a ground state in which two hydrogen ions sit close

and two hydrogen ions sit far from each oxygen centre. There are six possible permutations of their locations, which results in six degenerate ground states. This two-in-two-out *ice-rule* was first postulated by Bernal and Fowler [69], and then applied by Pauling [70] to calculate a value for the residual entropy which gave good agreement with experiment [71].

Following on from work of Anderson in spinels [72], it was noted that the frustration in water ice could be mapped onto a ferromagnnetic class of rare earth pyrochlores. These are tetrahedral lattices populated by magnetic ions (such as Ho^{3+} in the case of holmium titanate, $Ho_2Ti_2O_7$) in which a strong crystal field ensures that the moments from the ions act like Ising variables. This mimics the effect of the incommensurate bonding distances in water ice. Ramirez *et al.* first measured the residual entropy of these materials [73], while Castelnovo *et al.* predicted that excitations should behave similarly to emergent magnetic monopoles [74]. In this scheme, a monopole and anti-monopole pair are connected by a chain of reversed spins, akin to the flux tube predicted by Dirac [75].

2.5.2   Projecting frustration into the plane

Observing the exact microstate of water-ice or bulk spin ice materials is not possible within the current limitations of experimentation. To circumvent this, Wang *et al.* [8] created a planar analogue, composed of a regular arrangement of single domain magnetic islands which are coupled through their magnetostatic interactions. This artificial square spin ice is formed by two interleaved sublattices of stadium-shaped islands, and can be obtained by projecting the pyrochlore lattice along the (001) direction. Those points where four islands abut are termed vertices. As each island can point in one of two bi-stable orientations, there are 2^4 distinct vertices. In an approach now standard in the field, these are sorted into four types, T_1-T_4, of increasing dipolar energy, as in Fig. 2.9. Types, T_1 and T_2, are 'two-in-two-out' ice-rule vertices and are the lowest in energy. For these states, two moments in each vertex point in towards the centre, and two moments point out from the centre. By flipping a single spin, a T_3 vertex is obtained, with charge $\pm 2\mathcal{Q}$. The highest energy vertices, T_4, are 'four-in/four-out' states, with charge $\pm 4\mathcal{Q}$. Types T_2 and T_3 are considered ferromagnetic vertices as they carry a net moment.

These islands, first fabricated by Wang et al., were too thick to be thermally active at least within the limits of experimentally accessible temperatures. That is, the energy barrier separating the two, stable orientations of a single island was many orders of magnitude greater than thermal energy at room temperature. In such a situation, the observed array configurations do not accord with the Boltzmann distribution, though an effective temperature can still be developed [76].

To probe the low energy states of their arrays, Wang et al. subjected them to a rotating field demagnetisation protocol. This involves applying a rotating in-plane magnetic field with a magnitude which is stepped down over time. Such protocols have been extensively applied to the study of continuous magnetic media (for example, in the analysis of rock samples [77]) for which the aim is to flush remanent magnetisation from the sample. Initially, when the field magnitude is large, the magnetisation simply tracks the applied field. As the field magnitude is decreased however, domains with a coercivity higher than the current field value freeze out. In granular materials, vibro-fluidisation is used to drive the system to a low-energy state such as in the case of assemblies of closed packed dice [78].

Wang *et al.* found a preference for ice-rule vertices in strongly coupled systems following the demagnetisation protocol. Correlations were only short-ranged, however. The ground state order in the square lattice was shown to be composed of a chequerboard pattern of alternating T_1 vertices (first discussed in Ref. [8] and subsequently observed by Morgan *et al.* in Ref. [79]). Around the same time, Tanaka *et al.* published work on a honeycomb network which also obeyed a form of ice-rule [21].

Since then, the field of artificial spin ice has grown to include other lattice geometries, which give rise to aspects of statistical physics beyond the ice rule. By projecting the pyrochlore lattice along the (111) direction, the kagome lattice is obtained. This offers a rich phase diagram, whereby the system transitions from the high temperature paramagnetic phase to a disordered ice phase, then to a charge-ordered phase, before finally settling in a long-range ordered chiral state as the temperature is lowered [80, 81]. These results were indirectly confirmed by observing a critical slowing down in relaxation timescales using low energy muon spectroscopy [82], although the low temperature phases have yet to be directly observed [66].
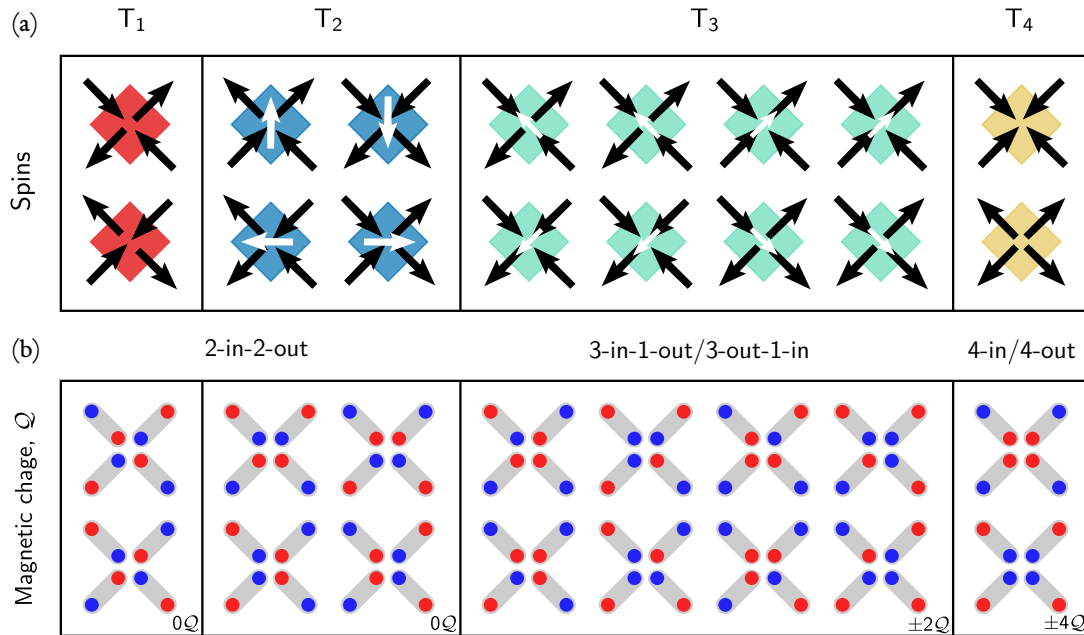
Figure 2.9: The sixteen vertices in square ice in terms of their (a) spin configuration, represented by the black arrows; and (b) magnetic charge, $\mathcal{Q}$, in terms of North and South poles (red and blue dots, respectively). Vertices are represented by coloured squares. A consistent colour coding is used throughout this work. This allows for discrimination when arrays are displayed as vertex maps. All vertices within a given type are degenerate. For T_2 and T_3, the net moment and magnitude are indicated by the white arrow. Types are sorted L-R in terms of increasing dipolar energy—see Chapter 5 Sec. 5.4.

Morrison *et al.* outlined a scheme for designing new, extensively degenerate artificial spin ice lattices based on site-specific decimation of the classic square geometry [83]. Some of these ideas were realised in the form of the shakti and Santa Fe lattices, both of which exhibit non-trivial kinetics [84]. Similarly, quasicrystal-like patterns made of both isolated islands [85] and connected nanowires [86, 87, 88] have been fabricated. These host spatially varying magnetic frustration.

2.5.3 Applications of artificial spin ice

Beyond affording us this opportunity to study fundamental aspects of condensed matter physics, there have been some recent proposals to explore the potential uses of artificial spin ice in in computer systems. Somewhat arbitrarily, these can be split into magnonic applications (where spin waves are manipulated by the magnetic state of the system [89]) or device-based

applications (where the ASI itself acts as the hardware with which to perform computational operations [90]).

In conventional computing, the central processing unit (CPU)—ordinarily, a metal-oxide-semiconductor integrated circuit—executes instructions, A physically-separate memory unit stores both those instructions and any data, input or output, required for the program. Since CPU and memory are not collocated, they are normally connected via a data bus. This is an elegant and efficient design solution but the finite bandwidth for data transfer between CPU and memory necessarily limits the speed with which instructions can be executed on large amounts of data. This is referred to as the von Neumann bottleneck.

Bio-inspired neuromorphic computation offers a possible solution to this problem by creating artificial analogues of neurons and synapses [38, 91]. Just as in the brain, these components would both compute and store information. Initial examples have been demonstrated using spintronic nano-oscillators, which have been trained to recognise vowel sounds [92].

Previous research has shown that artificial spin arrays exhibit memory effects when cycled through minor field loops [93] while Jensen *et al.* have noted the similarity of the network structure of artificial spin ice to that envisaged by neuromorphic computing [94]. In fact, this analogy can be made exact: Hopfield showed that neural networks can be mapped onto spin glass models [95] (a relevant example for artificial spin ice, the Ising model, is introduced in Chapter 3). Artificial spin ice would appear therefore to offer one possible route to realising this form of computation.

Two stumbling blocks remain, however. The first refers to our current inability to set the exact configuration of the system, though recent work using stray fields and magnetic force microscopy may provide a solution [41]. Meanwhile, a solution to the second problem would require a reliable mechanism to adjust the interactions between nanomagnets on-the-fly. That is, once an artificial spin ice array has been fabricated, the magnitude of the interactions between elements is defined completely. Neuromorphic computing requires some way of adjusting the *weights* between artificial neurons so as to carry out operations.

2.6 | Micromagnetic simulations of artificial spin ice

The most accurate way of modelling artificial spin ice would be to solve the LLG equation, eq. (2.20), directly with the appropriate boundary conditions. However, this is a non-linear partial differential equation for which analytical solutions cannot be found except in simple cases. Those situations which are exactly soluble often depend on linearising **m** around some preferred direction, or on assuming a spatially-uniform effective field. This necessarily restricts the geometries that can be tackled and, consequently, the LLG equation is solved numerically.

Wysin *et al.* attempt this for artificial spin ice by approximating the islands as point dipoles and introducing a stochastic field [96] through an approach called Langevin dynamics. A more accurate method—one in which the true physical extent of the islands is captured—is to use micromagnetic simulations. These solve the LLG equation approximately through either a finite difference, or a finite element scheme, although these approaches are limited to a small systems and short timescales [4].

This thesis makes use of two open-source finite difference software packages: OOMMF [97] and Mumax3 [98]. In the finite difference approach, the simulation universe is divided into equally-sized cuboidal cells. A piece of material (an island within an array, for example) can then be described as an aggregate of some number of cells. A single magnetic moment is assigned to the centre of each cell. It is assumed that the magnetisation takes this value everywhere inside the boundary of the cell. The LLG equation is solved numerically by re-expressing derivatives as quotients through a suitable numerical approximation. For example, Mumax3 uses the Runge-Kutta-Fehlberg method (RK4/5) for calculating the dynamical evolution of **m**, while energy minima are located using the RK2/3 method [99].

Assuming a uniform magnetisation within each cuboid, the exchange length sets an upper bound on the cell size through

$$l_{\text{ex}} = \sqrt{\frac{2\mathcal{A}}{\mu_0 M_S^2}}, \qquad (2.44)$$
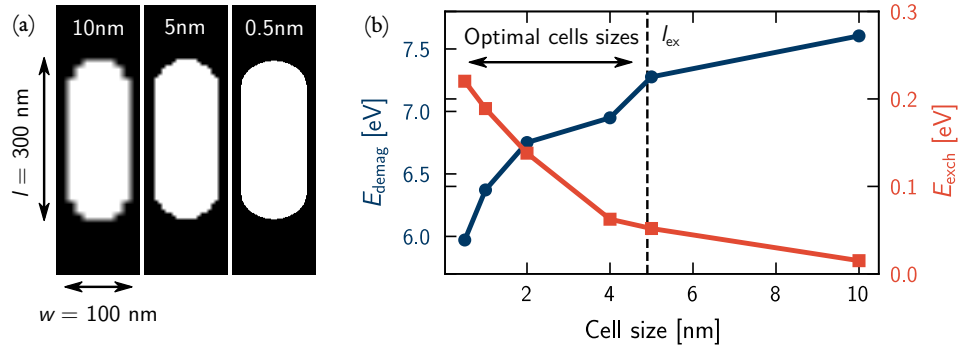
Figure 2.10: Effect of decreasing cell size in micromagnetic simulations of a single domain magnetic island. (a) A single domain magnetic island of length 300 nm, width 100 nm, and thickness 3 nm, is simulated in one of its bi-stable configurations. The parameters used are those appropriate to cobalt [Chapter 6]. The islands approximate better the shapes commonly used in experiment as the cell size is decreased. The cell size is indicated in white. (b) Below the exchange length, marked by the dashed vertical line, the magnetostatic and exchange energies continue to change with cell size [blue and red, respectively].

which gives the approximate distance for which short-range exchange phenomena dominate over magnetostatic interactions. Using the material parameters we report for cobalt in Chapter 6, we obtain $l_{\text{ex}} \approx 4.46$ nm.

The downside to using finite difference schemes is that they struggle to approximate curved interfaces [Fig. 2.10(a)]. This introduces local change to the anisotropy direction at edges, reflecting an accumulation of magnetic charge. For the simulations we report in this thesis, the structures were smoothed by sub-sampling (`EdgeSmooth = 8` in MUMAX3) and offset by half a cell to give a gradated edge. Further, the long axis of islands was aligned with the simulation grid to ensure that the staircase effect was only present on the semi-circular ends. The change in energy of a typical single domain magnetic island as a function of cell size is shown in Fig. 2.10(b).

Micromagnetic simulations offer the most complete way of capturing the behaviour of artificial spin ices as they are capable of modelling the extended nature of individual islands and their field distribution. Realistic values of quantities, such as the energy barrier to reversal, can thus be estimated. Furthermore, they also provide dynamical information with a direct

correspondence to real timescales. By way of contrast, we will introduce the concept of a dipolar-coupled Ising model in Chapter 3. However, this model has no in-built dynamics and so we must justify how our choice of time evolution is appropriate for a given system (see, for example, the discussion in Chapter 7).

2.7 | Summary

This chapter has provided a brief introduction to nanomagnetism and the field of artificial spin ice. We outlined the relevant energy terms, and discussed how the islands in artificial spin ice are coupled through long-range magnetostatic interactions. By arranging the nanomagnets in various patterns, different magnetic textures can be engineered—this forms the central idea of this thesis. As we justify in Chapter 5, the inter-island dipolar interactions drive the phase behaviour of the system as a whole. In contrast, the shape anisotropy of a single presents the largest energy scale and thus control the approach to equilibrium. This affects the results we present in Chapters 6 and 7 (on annealing with temperature and field, respectively).

3

Numerical methods to capture phase transitions in artificial spin ices

3.1 | Introduction

Many physical systems lack exact solutions. Sometimes, the equations governing them can be written down. Often, they cannot. Even when they can be described mathematically, a solution may prove intractable when dealing with just a few particles never mind a realistic number. One reason for this is the exponential increase in the number of microstates as more degrees of freedom are added to a system. For example, an artificial spin array with *just* 256 islands possesses $2^{256} \approx 10^{78}$ configurations—almost exactly the Eddington number, N_{Edd}, an early estimate for the number of protons in the universe [100].

To surmount these difficulties, we turn to numerical methods. This chapter will explain the rationale behind applying Monte Carlo techniques to artificial spin ices. These allow relatively large systems to be simulated and, hence, they bridge the gap between what is possible in micromagnetism and what is measurable in experiment. In the remainder of this thesis,

Monte Carlo methods will be combined with finite difference simulations of the Landau-Lifshitz-Gilbert equation, as discussed in Chapter 2. This will allow us to predict the response of artificial spin ices to both temperature and external magnetic fields.

This chapter is structured as follows: Sec. 3.2 reviews topics from statistical mechanics, including partition functions, ensembles averages, and thermodynamic variables. Sec. 3.3 briefly treats the concept of phase transitions, and critical exponents. Sec. 3.4 discusses the Ising model, perhaps the simplest lattice model in physics and a limiting case for artificial spin ices. Sec. 3.5 introduces Markov Chain Monte Carlo methods and the Metropolis Hastings-algorithm, before applying them to the two-dimensional (2D) Ising model in Sec. 3.6. Finally, in Sec. 3.7, replica exchange Monte Carlo, also known as parallel tempering, is introduced. This technique is useful for studying disordered and highly frustrated systems such as those we consider in Chapters 5 and 7.

In essence, this chapter is review material. However, the illustrative examples were generated in `JIsing`, a Julia simulation package developed as part of this thesis. Documentation and installation instructions for this package are available in an online repository [7].

3.2 | Statistical Mechanics

In this section, we present a brief review of Statistical Mechanics. This section draws heavily on the presentations found in [101, 102, 103, 104]. We have noted the impossibility of solving Hamiltonians for a realistic number of particles. Instead, we obtain quantitative information about a system by considering macroscopic properties which emerge from the underlying microstates. The relationship between these two viewpoints is governed by the *ergodic hypothesis*[1], which states that all accessible microstates are equally likely given sufficient time. For our purposes, this means that ensemble averages and time averages are identical, with their results being what we perceive as thermodynamic properties.

---

[1] Also referred to as the averaging postulate [102].

3.2.1 Statistical ensembles and partition functions

Throughout this thesis, we will often refer to *ensembles*. First introduced by Gibbs [105], these are collections of identical systems which operate under the same Hamiltonian (as opposed to, say, an ensemble of constituent particles *within* a given system). By the ergodicity postulate, averages over these ensembles are exactly equivalent to the averages when a single system is allowed to evolve in time. Partition functions provide a route to connect the microscopic description of physical systems with their bulk thermodynamics through means of *ensemble averages*. We distinguish between three types of statistical ensemble and their associated partition functions:

3.2.1.1 The micro-canonical ensemble. The *micro-canonical ensemble* is the set of microstates with fixed particle number, N, volume, V, and energy, E. The probability that a state, $|n\rangle$, with energy, E_n belongs to the micro-canonical ensemble is

$$\mathcal{P}(n) = \delta(E - E_n), \tag{3.1}$$

where δ is the Dirac delta function[2]. The micro-canonical partition function, z, is simply the number of microstates, degenerate by definition, in the set:

$$z(N, V, E) = \int \prod_i d\mathbf{p}_i \, d\mathbf{q}_i \, \delta(E - \mathcal{H}(\{\mathbf{p}_i, \mathbf{q}_i\})), \tag{3.2}$$

where the integration is performed over phase space. The micro-canonical ensemble describes systems which have reached equilibrium.

3.2.1.2 The canonical ensemble. The *canonical ensemble* is the set of microstates of a system in contact with a heat bath at a constant temperature, T. Microstates in this ensemble no longer all have the same energy, but do have the same particle number, volume and temperature. The thermal reservoir is to be considered both large enough that its supply of heat is inexhaustible, and small enough so as not to perturb directly the energy levels of the system.

---

[2]The Dirac delta function, $\delta(x)$, is defined through the sifting property,

$$\int_{-\infty}^{\infty} dx \, f(x)\delta(x - a) = f(a),$$

for a function, f.

Its sole function is maintaining the system in thermal equilibrium; otherwise we can ignore it. It can be shown that the relevant probability distribution is the Boltzmann-Gibbs distribution [101] so that the probability that the system is in state $|n\rangle$ with energy E_n is

$$\mathcal{P}(n) \propto \mathrm{e}^{-\beta E_n}, \tag{3.3}$$

where $\beta \equiv 1/(k_B T)$ is the inverse thermodynamic temperature. [3] The canonical partition function, Z, acts as the normalisation constraint for these probabilities, namely,

$$
\begin{aligned}
Z(N, V, T) &= \int \prod_i \mathrm{d}\mathbf{p}_i \, \mathrm{d}\mathbf{q}_i \, \exp\left(- \frac{\mathcal{H}(\{\mathbf{p}_i, \mathbf{q}_i\})}{k_b T} \right) \\
&= \sum_n \mathrm{e}^{-E_n/k_B T},
\end{aligned}
\tag{3.4}
$$

where in the second line we have re-expressed the integral in an alternative form as a sum over discrete states. The appropriate thermodynamic potential for the canonical ensemble is the free energy,

$$F = -k_B T \log(Z). \tag{3.5}$$

In fact, it can be shown that thermal equilibrium demands that F is at a minimum, which is simply a restatement of the Second Law of Thermodynamics [102]. For the majority of this thesis, we will work in the canonical ensemble and look at ways of sampling the free energy.

3.2.1.3 The grand canonical ensemble. For completeness, the *grand canonical ensemble* is the generalisation of the canonical ensemble where systems are free to exchange conserved quantities beyond simply heat. Often this discussion is framed in terms of exchanging particles, N, but equally well applies to any conserved quantity e.g. electric charge. Conservation of a given quantity necessitates the introduction of an associated chemical potential, μ. A system in the grand canonical ensemble then sits at a fixed μ and T i.e. in chemical and thermal equilibrium. The probability that a system is in state $|n\rangle$ is

$$\mathcal{P}(n) \propto \mathrm{e}^{-\beta(E_n - \mu N_n)}, \tag{3.6}$$

---

[3]After the 2019 redefinition of the SI base units [106], the Boltzmann constant is defined exactly as $k_B = 1.38064852 \times 10^{-23}$ m^2 kg s^{-2} K^{-1}, with dimensions $[M][L]^2[T]^{-2}[K]^{-1}$. Throughout this thesis, we will use *natural units* in which $k_B = 1$ or, equivalently, in which k_B is folded into the dimensions of derived quantities. In this scheme, temperature, energy, and even magnetic fields can have the same units.

with the grand canonical partition function being

$$
\begin{aligned}
\mathcal{Z}(T, \mu, V) &= \int \prod_i \mathrm{d}\mathbf{p}_i \, \mathrm{d}\mathbf{q}_i \, \exp\left[-\frac{\mathcal{H}(\{\mathbf{p}_i, \mathbf{q}_i\})}{k_b T} \right] \\
&= \sum_n \mathrm{e}^{-(E_n - \mu N_n)/k_B T}.
\end{aligned}
\tag{3.7}
$$

The generalisation of eq. (3.5) is the grand canonical *Landau* potential:

$$
\begin{aligned}
\Phi &= -k_B T \log(\mathcal{Z}) \\
&= F - \mu N,
\end{aligned}
\tag{3.8}
$$

which is the Legendre transform of F. We will return obliquely to the grand canonical ensemble in Chapter 7, where we couple ASI lattices to external disorder (which, in effect, acts as sources of chemical potential).

Knowledge of the appropriate partition function is sufficient to describe a system completely. Indeed, all thermodynamic quantities can be obtained from it by differentiation with respect to a suitable parameter. For this reason, it is sometimes called the *generating functional* of statistical mechanics [52]. We illustrate this point with some examples.

3.2.2 Thermal averages

Working in the canonical ensemble, the expectation value of an observable, $\mathcal{O}$, is

$$
\langle \mathcal{O} \rangle = \sum_n \mathcal{O}_n \mathrm{e}^{-\beta E_n},
\tag{3.9}
$$

where $\mathcal{O}_n$ is the value of that the observable takes in the state $|n\rangle$. In a notation more directly applicable to the energy spectrum of artificial spin ices, we write expectation values as discrete 'sums-over-states'. We apply eq. (3.9) to derive three key quantities.

3.2.2.1 Internal energy. The internal energy of the system, $U \equiv \langle E \rangle$. is the sum of the energies of each state weighted according to their Boltzmann probabilities, namely

$$
\begin{aligned}
U &= \frac{1}{Z} \sum_n E_n \mathrm{e}^{-\beta E_n} \\
&= -\frac{\partial}{\partial \beta} \log(Z).
\end{aligned}
\tag{3.10}
$$

3.2.2.2 Heat Capacity. The heat capacity at constant volume, C_V, is the derivative of eq. (3.10) with respect to T:

$$
\begin{aligned}
C_V &= \left(\frac{\partial U}{\partial T}\right)_V \\
&= \frac{1}{k_B T^2} \frac{\partial^2}{\partial \beta^2} \log(Z).
\end{aligned}
\tag{3.11}
$$

Alternatively, we can re-express C_V in terms of fluctuations. The mean-square fluctuation about $\langle E \rangle$ is defined through

$$
(\Delta E)^2 = \langle (E - \langle E \rangle)^2 \rangle = \langle E^2 \rangle - \langle E \rangle^2.
\tag{3.12}
$$

The second moment of the energy, $\langle E^2 \rangle$, can be calculated from the partition function via

$$
\langle E^2 \rangle = \frac{1}{Z} \sum_n E_n^2 \, \mathrm{e}^{-\beta E_n} = \frac{1}{Z} \frac{\partial^2}{\partial \beta^2} Z.
\tag{3.13}
$$

Combining eqs. (3.12) and (3.13) gives

$$
C_V = \frac{\langle E^2 \rangle - \langle E \rangle^2}{k_B T^2},
\tag{3.14}
$$

which is a remarkable result. Fluctuations are outwith the purview of classical thermodynamics and yet eq. (3.14) connects them directly to the macroscopic response of the system to temperature.

3.2.2.3 Susceptibilities. Eq. (3.14) is a particular case of a more general result: response functions can be expressed in terms of fluctuations. The susceptibility of $\mathcal{O}$ with respect to a field h, written $\chi_{\mathcal{O}}$, is defined via

$$
\begin{aligned}
\chi_{\mathcal{O}} &= \lim_{h \to 0} \frac{\partial}{\partial h} \langle \mathcal{O} \rangle \\
&= \beta \big(\langle \mathcal{O}^2 \rangle - \langle \mathcal{O} \rangle^2 \big),
\end{aligned}
\tag{3.15}
$$

which is called the linear response theorem [107]. The most useful application for our purposes is the magnetic susceptibility, χ, which depends on fluctuations in the magnetisation, $M = \sum_i s_i$, through

$$
\chi = \frac{\langle M^2 \rangle - \langle M \rangle^2}{k_B T}.
\tag{3.16}
$$

However, we will also consider susceptibilities relating number densities to temperature [Chapter 5] and to field [Chapter 7].

As a final comment, we have defined U, C_V, and χ in an extensive manner, i.e. they grow with system size. Where appropriate however, we will tend to display results intensively, i.e. scaled per island.

3.3 | Phase transitions and critical exponents

Much of this thesis will be devoted to probing phase transitions in artificial spin ices. Generally, systems are said to exist in phases, which are characterised by uniformities in their behaviour. Phase transitions demarcate the boundary between phases; sharp discontinuities in observables can occur as they are crossed. Crossing the critical line is usually achieved by varying the temperature, though there also exist phase transitions which are caused by changes in field [108], pressure [109], or disorder [110]. In fact, there is even a class of quantum phase transitions, which persist at 0 K provided a suitable detuning parameter is altered [111].

Conventionally, phase transitions are associated with spontaneously broken symmetries. In this framework, a high symmetry, disordered phase gives way to a low symmetry, ordered one as the phase transition is traversed. A famous example is the Higgs mechanism in which the broken symmetry of the vacuum potential gives rise to mass [112, 113, 114]. The idea of symmetry breaking suggests it would be useful to define an order parameter. This is some function of variables that appear in the Hamiltonian, and is zero in the disordered phase and non-zero elsewhere. In Chapter 2, we described the order parameter for a ferromagnet, which is the magnetisation, $\langle \mathbf{M} \rangle$. This is non-zero below the Curie temperature as the spins are aligned, but vanishes as the spins become randomly orientated at high temperatures. As a ferromagnet becomes ordered, the ensemble of spins spontaneously breaks rotational symmetry and chooses a preferred direction along which to point.

In an attempt to classify phase transitions, Ehrenfest considered discontinuities in derivatives of the Gibbs free energy, G [115]. According to this scheme, a phase transition is of order n if n is the smallest differential of G which exhibits a discontinuity. First order transitions, such as that between liquid-water and ice [116], are associated with a latent heat. For the most part,
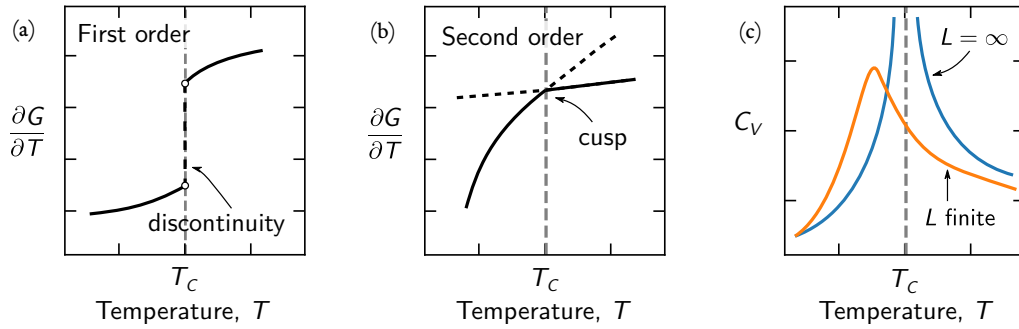
Figure 3.1: Ehrenfest classification of phase transitions. (a) First order phase transition, in which the first derivative of G exhibits a discontinuity. (b) Second order phase transition, in which a kink in the first derivative of G corresponds to a discontinuity in its second derivative. (c) Phase transitions are only defined in the thermodynamic limit ($L = \infty$); otherwise the sharp nature of the transition is smeared out by finite-size-effects.

we will study second order, magnetic transitions (compare Figs. 3.1(a) and (b)). Goldenfeld refers to these as continuous phase transitions [117], because the Ehrenfest classification fails to capture the fact that thermodynamic variables diverge at a second order transition rather than exhibit a simple discontinuity. To some extent, this nomenclature has been partially adopted in artificial spin ice [118].

Finally, we note that phase transitions are properly defined only in the thermodynamic limit of infinite systems [119]. This follows from the requirement that the free energy density remain finite [117]. In the thermodynamic limit, systems self-average and the effect of fluctuations decreases under all conditions except at the critical temperature. For our purposes, this means we must consider artificial spin ice arrays with a large number of islands. In a finite system, phase transitions are smeared out and discontinuities are not observed, as in Fig. 3.1(c). This also shifts slightly the position of the critical temperature with respect to that of the infinite lattice.

3.3.1   Universality

It turns out that disparate physical systems can exhibit the same form of behaviour near to their respective phase transition. As an example, Ref. [120] notes the similarity among avalanches in plate tectonics, in the unfurling of crumpled paper [121, 122], and in magnetic systems [123],

where it is known as Barkhausen noise [124]. This phenomenon is referred to as universality, and is captured by defining a set of *critical exponents*. These exponents describe how thermodynamic observables scale in the vicinity of a phase transition. For example, the Bloch law, which describes how the spontaneous magnetisation of a ferromagnetic changes with temperature, has a functional form,

$$M(T) \propto \left(1 - \frac{T}{T_C}\right)^{\beta},$$ (3.17)

near to the Curie temperature, T_C. In this context, β is called the critical exponent of the magnetisation. Critical exponents are experimentally accessible quantities; for example, neutron scattering experiments performed on the antiferromagnet MnF_2 measure its associated exponent $\beta = 0.335 \pm 0.001$ [125]. This is precisely the same exponent that governs the transition in density between a liquid and a gas [117], even though there is little similarity between these two systems at first sight. A set of critical exponents defines a universality class; systems with the same critical exponents are said to belong to the same universality class.

Typically, critical exponents are determined by the dimensions of the space in which the system resides, and the symmetry and range of its interactions [103]. This is not quite the complete picture, as there can exist a continuum of varying exponents in situations where the interaction is long-ranged [126], or in spin glasses which possess so-called fractal dimensions [127].

For a given system, it is convenient to define a reduced temperature, $\tilde{t} = (T - T_C)/T_C$, in terms of the critical temperature, T_C. This quantity represents how far the system is from the phase transition. Around T_C, it is assumed that a generic observable, $\mathcal{O}$, can be expanded in powers of $\tilde{t}$ according to

$$\mathcal{O}(\tilde{t}) = A_\lambda \tilde{t}^\lambda \sum_{i=0}^{\infty} a_i \tilde{t}^i,$$ (3.18)

where $\tilde{t}^\lambda$ is known as the leading order contribution, and A_λ and $\{a_i\}$ are constants. Then, the critical exponent, λ, is defined by the limit

$$\lambda \equiv \lim_{\tilde{t} \to 0} \frac{\ln \mathcal{O}(\tilde{t})}{\ln \tilde{t}},$$ (3.19)

as in Ref. [128]. A positive (negative) critical exponent corresponds to the observable tending to zero (diverging). For the most part, we will not obsess over the rigorous definition of

Table 3.1: Summary of common critical exponents for magnetic systems. The spatial dimension is denoted d. The correlation function, correlation length and correlation time will be described in Sec. 3.6. After Binney [129].

Exponent	Related quantity	Definition	Restrictions
α	Heat capacity	$C_V \sim t^{-\alpha}$	$T \to T_c, B = 0$
β	Magnetisation	$m \sim t^{\beta}$	$T \to T_c^-, B = 0$
γ	Susceptibility	$\chi \sim t^{-\gamma}$	$T \to T_c, B = 0$
δ	Critical isotherm	$m \sim B^{1/\delta}$	$T = T_c, B \to 0$
η	Correlation function	$\mathcal{G} \sim 1/r^{d-2+\eta}$	$T = T_c, B = 0$
ν	Correlation length	$\xi \sim t^{-\nu}$	$T = T_C, B = 0$
z	Correlation time	$\tau \sim \xi^{-\nu z}$	—

critical exponents, suffice that they exist; that they can be measured both experimentally and numerically; and that estimating them tells us something fundamental about the nature of our artificial spin ice. Some of the critical exponents that we will calculate for our arrays are given in Table 3.1, along with conditions for measuring them.

3.4 | The Ising Model

The Ising model is perhaps the simplest lattice model in Statistical Mechanics. Originally proposed by Lenz to his doctoral student, Ising, it involves a lattice of N sites, indexed by i. Associated with each site, there is a single two-state degree of freedom, s_i, which conventionally takes values in $\{-1, +1\}$. In analogy with magnetic moments, these values represent spin up ($s_i = +1, \uparrow$) and spin down states ($s_i = -1, \downarrow$). The restriction to two states mimics strong uniaxial anisotropy, which is a good approximation for many materials. A given configuration is specified uniquely by the set of numbers, $\{s_i\}$.

The Ising Hamiltonian is written

$$\mathcal{H} = \mathcal{J} \sum_{\langle ij \rangle} s_i s_j - \sum_i B_i s_i. \tag{3.20}$$

The first term represents a coupling, of strength $\mathcal{J}$, between spins in the lattice, where the notation, $\langle ij \rangle$, indicates that only nearest neighbour pairs are counted. This is a very simple form of exchange interaction (c.f. with the exchange integral of Chapter 2, Sec. 2.4.1) but differs from the Heisenberg model in being purely classical. The Ising interaction can be generalised to include different coupling constants and classes of neighbouring spins.

The second term is the Zeeman coupling to external fields; in the most general case, these fields may be site-specific so that B_i is the external field at site i. We will explore site-specific local fields in the context of artificial spin ice in Chapter 7 but this term is omitted in what follows.

The one-dimensional case was solved by Ising [130]. It exhibits a second order phase transition at $T = 0$. The two-dimensional case was solved first by Onsager [131][4], who found that it exhibited an order-disorder transition at a critical temperature, T_C, defined through

$$k_B T_C = \frac{2\mathcal{J}}{\ln(1 + \sqrt{2})} \approx 2.269\mathcal{J}, \tag{3.21}$$

and that the specific heat diverges logarithmically. The exact solution for the magnetisation and specific heat are shown in Fig. 3.2 for the case $\mathcal{J} = 1$. In both panels, the critical temperature is indicated by the dashed vertical line. The three-dimensional Ising model remains unsolved.

The Ising model is ubiquitous across physics as it either directly describes many systems or acts as a limiting case. For example, square artificial spin ice has been approximated as an effective Ising model with nearest-neighbour interactions [134, 96, 13]. In solving any Ising-like model, computational techniques such as Monte Carlo methods are almost invariably necessary.

---

[4]Sethna describes the solution as a tour-de-force but "bewilderingly complicated" [132]. In a letter to Casimir, Pauli stated that nothing much of interest had happened in physics during World War II save for Onsager's solution of the 2D Ising model [133].
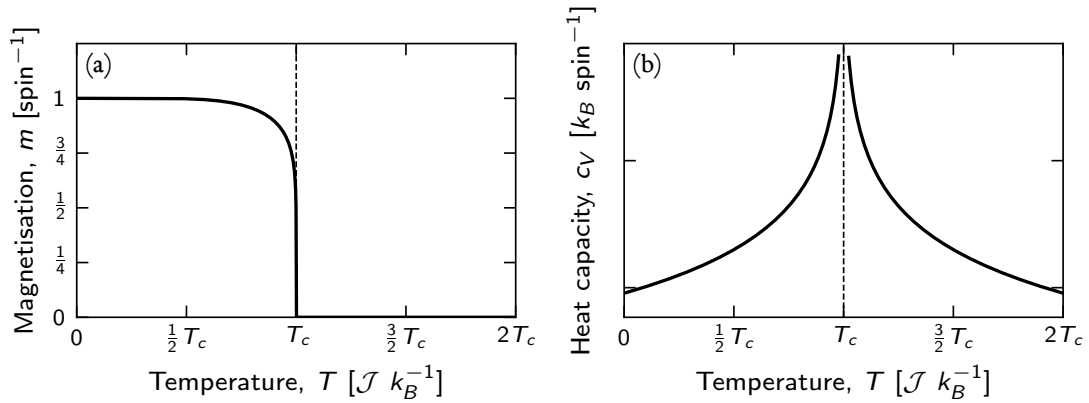
Figure 3.2: Onsager (exact) solution for (a) magnetisation, m, and (b) heat capacity, c_V, as a function of temperature, T, in the 2D Ising model. The heat capacity exhibits a logarithmic singularity at T_c (dashed line).

3.5 | Monte Carlo methods

Monte Carlo methods provide ways of approximating integrals by drawing random samples from carefully chosen probability distributions. In this respect, they are examples of stochastic processes. Rather than the partition function itself, we are usually interested in calculating the expectation value of an observable as in eq. (3.9). However, approximating $\langle \mathcal{O} \rangle$ by sampling just some subset of the microstates without *a priori* knowledge of the probability distribution can easily lead to incorrect results. For example, suppose that probability distribution is peaked around a particular state, say, the ground state of the system. Only the value of the observable in that state will contribute to the expectation value of eq. (3.9); other states will not. In systems with a large number of microstates, randomly choosing a representative sample of states—so-called *simple sampling*—is unlikely to yield physically meaningful results.

The essence of the Monte Carlo approach is to choose a subset of states which do contribute strongly to this average; that is, to estimate $\langle \mathcal{O} \rangle$ from a small number of important terms rather than from every microstate. For obvious reasons, this is referred to as *importance sampling*. To achieve this, we introduce the concept of a *Markov Chain*.

3.5.1 Markov Chain

Let us write $s(t)$ to specify the configuration of our system at time, t. For our purposes, a configuration bookkeeps the orientation of every spin (whether in a 2D Ising lattice or ASI array). A Monte Carlo simulation proposes a small random change to $s(t)$ in order to generate a trial configuration, s_{trial}. This trial configuration is then accepted or rejected according to some rule—the *cost function*. If the trial configuration is accepted, then $s(t+1) = s_{\text{trial}}$. If the trial configuration is rejected, then $s(t+1) = s(t)$. This process is repeated to generate a chain of states which span a passage of Monte Carlo time. We emphasise that Monte Carlo time does not represent the true passage of time, though the two can be related in certain situations—an idea to which we will return in Chapter 7. The directed set[5] of configurations,

$$\ldots s(t-2) \to s(t-1) \to s(t) \to s(t+1) \to s(t+2) \ldots, \qquad (3.22)$$

is known as a Markov chain provided that the probability of accepting the trial state depends only on the current state. Processes which forget their initial conditions are called *Markovian*. The probability that a state appears is always non-zero in the Boltzmann distribution. Markov chains approximating the Boltzmann distribution are thus capable of visiting any point in the phase space of a Hamiltonian provided they are run for long enough, i.e. they are ergodic. By finding a rule that generates successive configurations in accordance with the Boltzmann distribution, good estimates for expectation values can be obtained. The most widely-used example is the Metropolis-Hastings algorithm.

3.5.2 Metropolis-Hastings Algorithm

> "The purpose of this paper is to describe a general method, suitable for fast electronic computing machines, of calculating the properties of any substance which may be considered as composed of interacting individual molecules." [135]

The Metropolis Algorithm was developed at Los Alamos National Laboratory as a collaboration between Nicholas Metropolis, and the Rosenbluth and Teller families [136, 135, 137]. In

---

[5]Actually, a directed *graph*.

1970, it was extended by Hastings to cover more general cases [138]. The resulting algorithm—the *Metropolis-Hastings* (MH) algorithm—generates a Markov chain based on the energy difference between the current and trial states. The algorithm is non-deterministic; that is, multiple runs will generate different Markov chains. The time evolution is described by a master equation,

$$\frac{\partial}{\partial t}\mathcal{P}_s(t) = \sum_{s' \neq s} \left[\mathcal{T}_{s' \to s}\mathcal{P}_{s'}(t) - \mathcal{T}_{s \to s'}\mathcal{P}_s(t) \right], \tag{3.23}$$

where $\mathcal{P}_s(t)$ is the probability that the system is in configuration s at time t, and $\mathcal{T}_{s' \to s}$ is the transition rate from s' to s. The first term within the sum describes all processes which reach s and the second term all processes which leave s. As $t \to \infty$, we want the probabilities to approach the Boltzmann distribution. In equilibrium, $\partial \mathcal{P}_i / \partial t$ vanishes and we obtain the principle of detailed balance,

$$\mathcal{T}_{s' \to s}\mathcal{P}_{s'}^{\text{eq}} = \mathcal{T}_{s \to s'}\mathcal{P}_s^{\text{eq}}, \tag{3.24}$$

which states that the flow into and out of s exactly balance. In equilibrium, it follows that the ratio of the transition probabilities must be a function of the change in energy between the configurations, $\Delta E = E_s - E_{s'}$, i.e.,

$$\frac{\mathcal{T}_{s \to s'}}{\mathcal{T}_{s' \to s}} = \exp\left(-\frac{E_s - E_{s'}}{k_b T} \right) = \exp\left(-\frac{\Delta E}{k_b T} \right). \tag{3.25}$$

In principle, any choice of transition rate which satisfies eq. (3.25) is acceptable. The MH choice takes the form

$$\mathcal{T}_{s \to s'} = \begin{cases} \frac{1}{\tau_0} \exp(-\Delta E / k_B T) & \text{if } \Delta E > 0 \\ \frac{1}{\tau_0} & \text{if } \Delta E < 0, \end{cases} \tag{3.26}$$

where τ_0 is the time required to move between configurations (in effect, the time to flip a spin). Without loss of generality, we can set $\tau_0 = 1$ and rescale as appropriate.

In this thesis, the MH algorithm has been implemented in the context of single-spin-flip dynamics. We summarise this as follows for the Ising model though our comments apply equally well to artificial spin ice. The system is initialised in a random configuration at temperature, T, and with energy, E. A single spin flip is suggested. The energy difference, ΔE, is calculated. A random number, **x**, is drawn from the interval $[0, 1)$. The trial move is accepted if **x** $<$

$\exp(-\beta \Delta E)$, else it is rejected and the configuration is not updated. The process is repeated. We define a Monte Carlo step[6] (MCS) as N single spin updates for a lattice of N spins. As a consequence, this ensures that a Monte Carlo step scales with system size. The chain is run for an initial burn-in period; this ensures that it reaches equilibrium and that states appear in accordance with the Boltzmann distribution. Then, observables are sampled after a chosen number of Monte Carlo steps. The pseudocode for this process is contained in Algorithm 1.

---

[6]Variously, also, a Monte Carlo sweep.

Algorithm 1 Implementation of the Metropolis-Hastings algorithm for a system at temperature, T. The Markov Chain is equilibrated for `burnSteps` MCS. The value of the observable, `O`, is then computed by averaging over `thermSteps` MCS.

```
 1: function METROPOLIS(T, burnSteps, thermSteps)
 2:
 3:     initialise S                          # Starting configuration
 4:     initialise currentE = E(S)                # Starting energy
 5:     initialise O = 0
 6:
 7:     for i=1:burnSteps do                      # Begin burn-in
 8:         propose S'
 9:         compute trialE = E(S')
10:         compute cost = currentE - trialE
11:         if rand(0,1) < exp(-cost/T) then
12:             S = S'
13:             currentE = trialE
14:         end if
15:     end for
16:
17:     for i=1:thermSteps do                     # Begin averaging
18:         propose S'
19:         compute trialE = E(S')
20:         compute cost = currentE - trialE
21:         if rand(0,1) < exp(-cost/T) then
22:             S = S'
23:             currentE = trialE
24:         end if
25:         compute O = O(S)            # Compute O in current config.
26:     end for
27:
28:     return O/thermSteps
29:
30: end function
31:
32: function E(S)          # Subroutine:  return energy of config S
33: end function
34:
35: function O(S)        # Subroutine:  return observable in config S
36: end function
37:
```

3.6 | Metropolis Hastings algorithm applied to the 2D Ising Model

In this section, we apply the Metropolis Hastings algorithm to the 2D Ising model on a square lattice. We introduce the concept of spatial and temporal correlations functions, and describe the finite-size-scaling technique, which can be used to extract critical exponents. These concepts feature heavily in the results portion of this thesis. More prosaically, this section stands as a proof-of-concept by reproducing accepted analytic results. The software package used to generate results in this section, `JIsing` [7], shares crucial portions of its underlying structure with the other package used to generate results for ASI systems, `JASI` [6], which is described in Chapter 5.

3.6.1 Thermal averages

In Fig. 3.3, we display thermal averages from Monte Carlo simulations for the internal energy, heat capacity, magnetisation and magnetic susceptibility as a function of temperature in the 2D Ising model. In general, 10^4 MCS were sufficient to ensure thermalisation, and observables were calculated using both 10^4 and 10^5 MCS to ensure convergence. Results are averaged over at least 10 independent runs. Six systems sizes are considered, ranging from $L = 8$ to $L = 256$. For comparison, the Onsager solution for m is shown in Fig. 3.3(c). Agreement between the numerical results and the exact solution for an infinite lattice becomes better as the thermodynamic limit is approached. Similarly, the peaks in c_V and χ become sharper and their locations move towards $2.269 \, \mathcal{J} k_B^{-1}$ for larger system sizes though, of course, there is no divergence in the simulations.

Typical snapshots of the spin-states of an $L = 256$ lattice are shown in Fig. 3.4 for temperatures below, on, and above the critical temperature. In these panels, the spin-up and spin-down states are represented by white and black squares, respectively. Below T_C [Fig. 3.4(a)], the system is in a majority spin-up state (a large domain of white squares). Thermal fluctuations ensure that there exist some spin-down regions though these tend to be small and, as the system is cooled further, they evaporate. In this example, the system has spontaneously ordered into
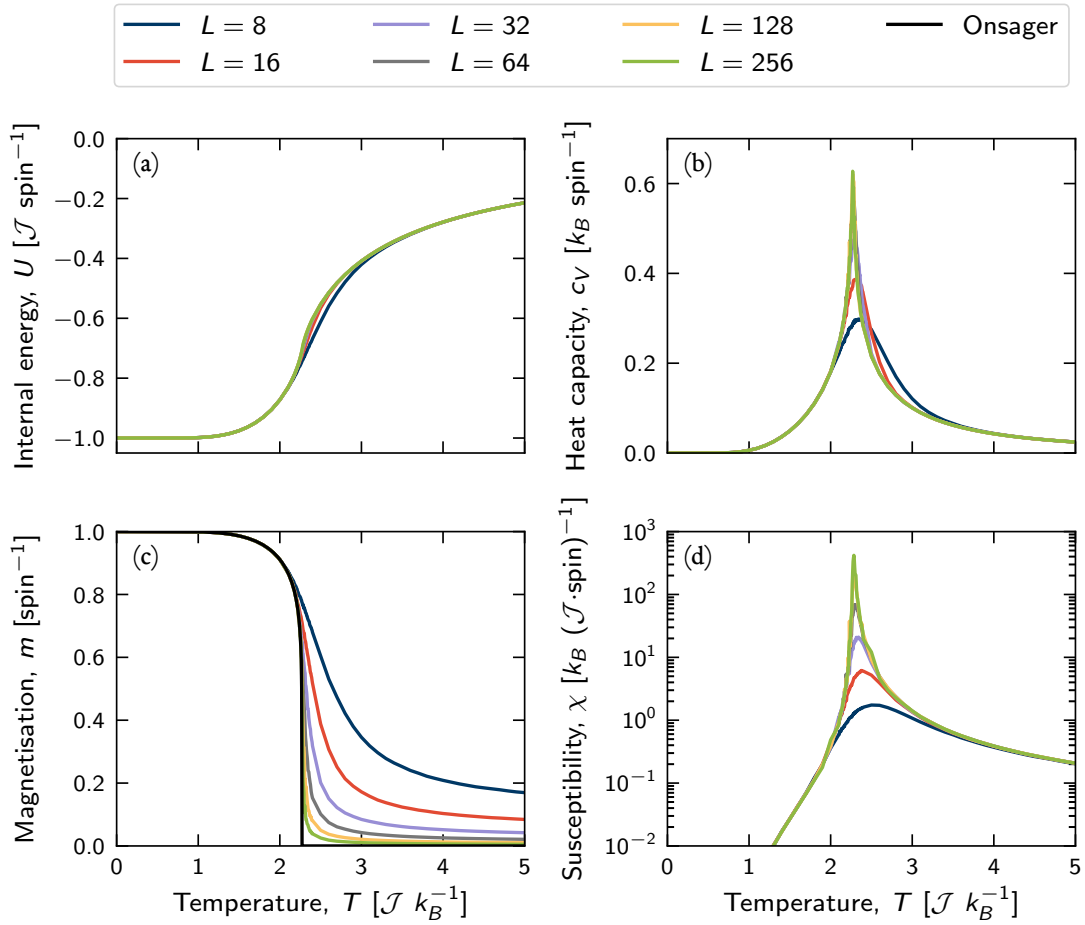
Figure 3.3: Thermal behaviour of (a) the internal energy, U, (b) the specific heat per spin, c_V, (c) the magnetisation, m, and (d) the magnetic susceptibility, χ, in the 2D Ising model. Data obtained from ten independent MC simulations using the MH algorithm. Error bars have been omitted for clarity. Six system sizes are considered; colours as in the superscribed legend. The Onsager solution for m appears in black in (c). Quantities are scaled per spin.

the $s_i = +1$ state. At $T = T_C$ [Fig. 3.4(b)], fluctuations are present across all length scales. The system cannot yet choose a preferred ground state and domains of both orientations are present. Above T_c [Fig. 3.4(c)], entropy wins out as $k_B T \gg \mathcal{J}$, so the spins are effectively uncoupled. The panel appears randomised.

Before closing this section, we discuss assigning errors to Monte Carlo observables. There are many different schemes used to quantify statistical errors taken from a single MC run. These include the bootstrap and jacknife methods, both of which rely on sampling subsets of the measurements [139]. In general, the standard deviation is not an appropriate measure of the
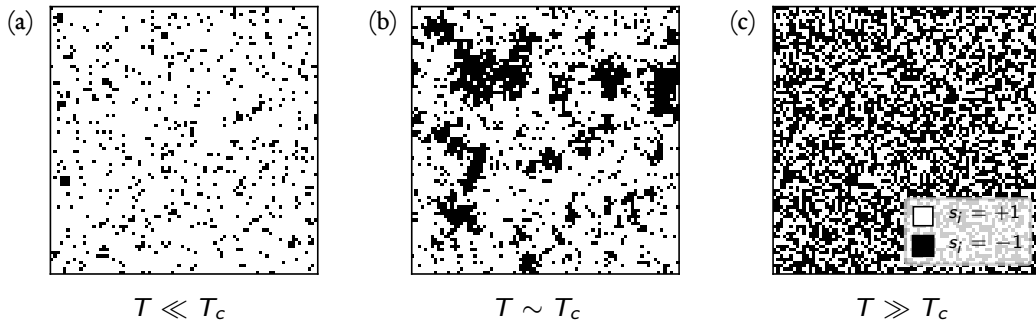
Figure 3.4: Example configurations of an $L = 256$ Ising model at temperatures: (a) $T \ll T_C$ where the system is more-or-less in the ordered phase; (b) $T \sim T_C$ where clusters are visible across all length scales; and (c) $T \gg T_C$ in the paramagnetic phase. White (black) squares indicate up (down) spins, as indicated in the legend to (c).

error in a single run, as successive steps in the Markov chain are not statistically independent. To circumvent this, throughout this thesis, we perform multiple parallel simulations, each sampled under a different random seed. This generates independent estimates for an observable, for which the standard deviation is a valid measure of the error. By way of example, we show the relative error in c_V for the $L = 256$ lattice as averaged over ten independent runs in Fig. 3.5. At both high and low temperatures, the standard deviation is small and the errors are less than 1%. In the critical region around the phase transition, the relative error increases substantially and is maximal at T_C (denoted by the dashed vertical line). This is not an artefact of the MC algorithm. Near to the critical point, regions of spins are able to fluctuate over all length scales. Commensurate with this, there exists large fluctuations in quantities such as the magnetisation and energy. These critical fluctuations are an innate feature of any system undergoing a phase transition. There is a related effect, critical slowing down, in which the relaxation timescales become longer near to the phase transition. We explore these phenomena in our discussion of correlations in the next section.

3.6.2 Spatial and temporal correlations

We can connect the thermal observables of the previous section to experimentally accessible quantities through the use of correlation functions. These capture the extent to which a spin
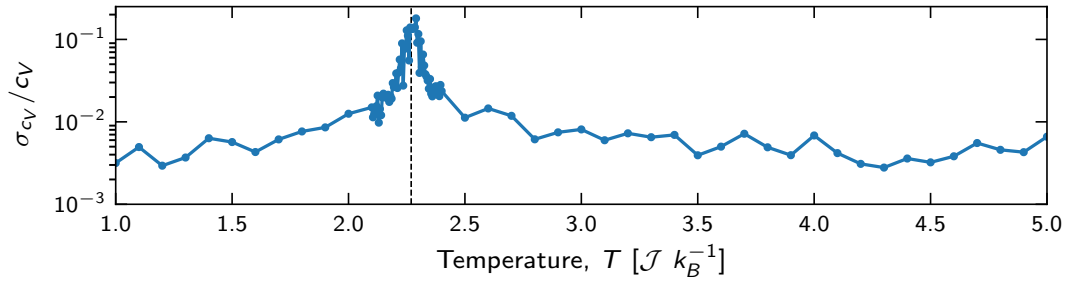
Figure 3.5: Relative error in the heat capacity of the $L = 256$ Ising model as a function of temperature. The critical temperature is indicated by the dashed, vertical line. The error, σ_{c_V}, is taken as the standard deviation of ten independent measurements of the heat capacity. Far from the critical point, the relative error is negligible ($< 1\%$). Near to the critical point however, critical fluctuations innate to any second order phase transition dominate. The effect of this is to increase the size of the error by several orders of magnitude.

affects its neighbours. Given two spins, s_1 and s_2, at positions $\mathbf{x}$ and $\mathbf{x} + \mathbf{r}$, between times t and $t + \tau$, a general form for the connected two-point correlation function is

$$\mathcal{G}(\mathbf{r}, \tau) = \langle s_1(\mathbf{x}, t) \cdot s_2(\mathbf{x} + \mathbf{r}, t + \tau) \rangle - \langle s_1(\mathbf{x}, t) \rangle s_2(\mathbf{x} + \mathbf{r}, t + \tau) \rangle, \qquad (3.27)$$

which is evaluated at a specific temperature, T. Correlation functions defined in this way offer an alternative method to obtaining thermodynamic quantities [139, 140]. For example, it can be shown that the magnetic susceptibility, $\chi(T)$, is related to $\mathcal{G}(r)$ through $\chi = \langle \mathcal{G}(r, 0) \rangle / (k_B T)$.

3.6.2.1 Spatial correlations. The equal-time two-point correlation function is

$$\mathcal{G}(r) = \langle s_1(\mathbf{x}) \cdot s_2(\mathbf{x} + \mathbf{r}) \rangle - \langle s_1(\mathbf{x}) \rangle s_2(\mathbf{x} + \mathbf{r}) \rangle. \qquad (3.28)$$

This drops off in distance with a form $\mathcal{G} \sim \exp(-r/\xi)$, where ξ is the correlation length [141]. This length can be related to the average size of domains in a magnetic system. Exactly on the critical temperature, eq. (3.28) breaks down to be replaced by

$$\mathcal{G}(r)|_{T_C} \sim \frac{1}{r^{d-2+\eta}}, \qquad (3.29)$$

where d is the dimensionality of the system and η is a critical exponent (c.f. Table 3.1).
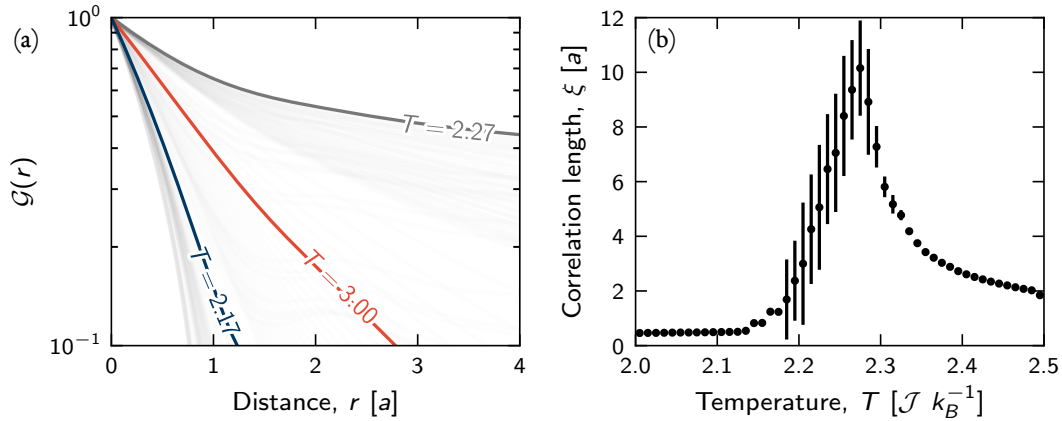
Figure 3.6: Spatial correlations in the 2D Ising model for a square lattice of size $L = 32$. (a) The correlation function, $\mathcal{G}(r, T)$, is plotted on semilogarithmic axes. Faded lines are samples of $\mathcal{G}(r)$ drawn approximately uniformly from the interval $T \in [0, 5] \mathcal{J}k_B^{-1}$. Three temperatures are highlighted explicitly: above (red), below (blue), and near to (grey) the critical temperature at which correlations persist. (b) The correlation length, ξ, is extracted from the data in (a) by finding the point at which $\mathcal{G}$ drops to $1/e$ as discussed in the text. Error bars represent 1σ when the data is averaged over 10 independent realisations. Note that ξ does not diverge at the phase transition; rather, the finite size of the system ensures there is a cut-off.

As a concrete example, Fig. 3.6(a) displays samples of $\mathcal{G}(r)$ for the 2D Ising model drawn approximately uniformly from the interval $T \in [0, 5] \mathcal{J}k_B^{-1}$. Three temperatures are highlighted explicitly: below (blue), at (grey) and above (red) T_C. Only near to the critical temperature do correlations persist to large r. An estimate for ξ can be made by locating the point at which $\mathcal{G}(r)$ falls to $1/e$ of its original value. This is shown in Fig. 3.6(b) for the case of an $L = 32$ system. As with the thermodynamic observables presented in Sec. 3.6.1, the correlation length does not diverge but, rather, approaches an upper limit of $L/2$.

The correlation length is a common figure-of-merit in analysing the establishment of long-range ordering in artificial spin ices, where it is usually extracted from the magnetic structure factor [142, 34, 143]. This is the reciprocal space representation of eq. (3.28), and is the form most readily obtained by scattering processes. We will return to measuring the correlation length in experimental samples in Chapter 6.

3.6.2.2 Autocorrelation. Rather than considering spins separated in space, the autocorrelation function measures the probability that a quantity remains correlated in time [144]. For example, the time-displaced autocorrelation of the magnetisation is given by

$$\mathcal{C}^M(t) = \langle m(t) \cdot m(t') \rangle - \langle m(t) \rangle^2, \tag{3.30}$$

for times t and t'. As with spatial correlations, this decays away from the critical temperature according to $\exp(-t/\tau)$, where the correlation time τ is the temporal analogue of ξ. Among others, Newman and Barkema [139] define an integrated autocorrelation time, τ_{int}, through

$$\tau_{\text{int}} = \int_0^\infty \mathrm{d}t \, \mathcal{C}^M(t) \,, \tag{3.31}$$

which is a measure of the extent to which successive steps in the Markov chain are decorrelated, and is additionally useful in assigning uncertainties to observables. Again, we stress that time in Monte Carlo simulations does not necessarily correspond to real time in the dynamical evolution of a system. In Chapter 7, we will consider further the autocorrelation time, and use it to justify why introducing local disorder in an array can affect physical relaxation times in real system.

We depict in Fig. 3.7(a) the autocorrelation of the magnetisation, $\mathcal{C}^M(T)$, and the energy, $\mathcal{C}^E(T)$, in the 2D Ising model. The integrated autocorrelation times of both quantities show a pronounced peak near to the phase transition [Fig. 3.7(b)]. This effect is referred to as critical slowing down, and is a consequence of the fact that the dynamics of a system become viscous around the critical region [145]. In this instance, the choice of Monte Carlo algorithm determines the exact nature of this slowing, although physical systems also exhibit arrested dynamics near to a phase transition [146]. The correlation time scales according to $\tau \sim \xi^{-\nu z}$, where z is the dynamic critical exponent. For the Metropolis-Hastings algorithm, the dynamic critical exponent is approximately 2 [139].

3.6.3 Finite-size scaling

The most common approach to extracting critical exponents from Monte Carlo simulation is via a finite-size scaling analysis. In the thermodynamic limit, the correlation length is unbounded through $\xi \sim \tilde{t}^{-\nu}$, where $\tilde{t}$ is the reduced temperature. In a finite lattice however,
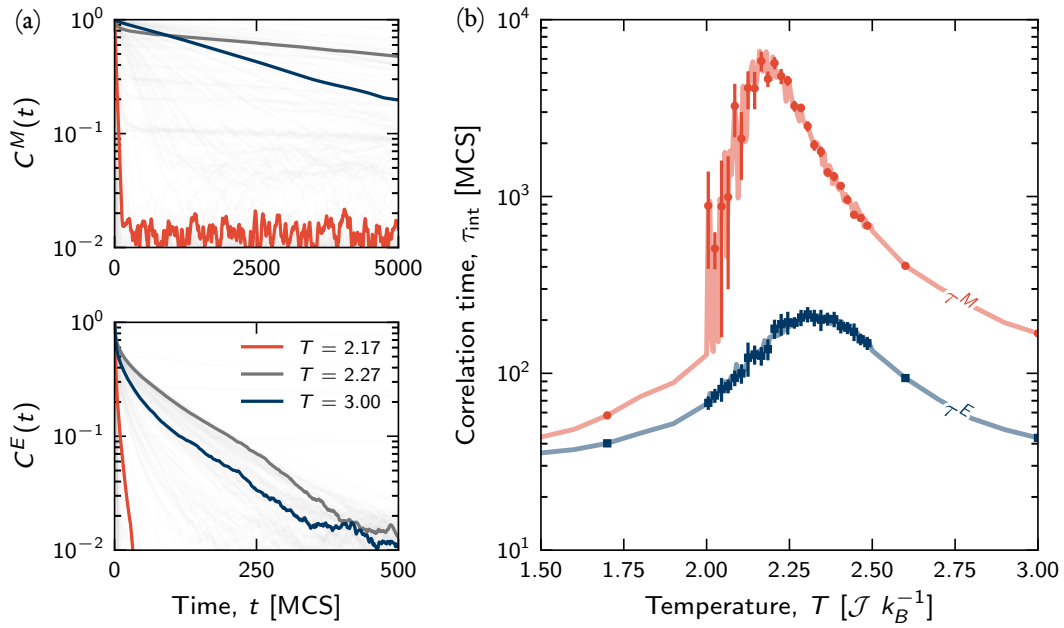
Figure 3.7: Autocorrelation functions in the 2D Ising model for a square lattice of size $L = 32$, simulated using the Metropolis-Hastings algorithm. (a) The autocorrelation function for the magnetisation [upper panel] and energy [lower panel] with three temperatures highlighted explicitly: above (red), below (blue), and near to (grey) the critical temperature at which correlations persist. Faded lines are samples of $\mathcal{C}(t)$ drawn approximately uniformly from the interval $T \in [0, 5] \mathcal{J} k_b^{-1}$. (b), The corresponding integrated autocorrelation times for m [red, upper curve] and E [blue, lower curve] as a function of temperature. Both exhibit a peak near to T_C, consistent with the effects of critical slowing down. Time is measured in terms of Monte Carlo steps (MCS). Error bars represent 1σ when the data is averaged over 10 independent realisation

the system size caps ξ. Finite-size scaling interpolates between these two regimes by means of a scaling ansatz [147, 148]. According to this hypothesis, at T_C, variables should behave as

$$C_V \propto L^{\alpha/\nu} \tag{3.32a}$$

$$M \propto L^{-\beta/\nu} \tag{3.32b}$$

$$\chi \propto L^{\gamma/\nu}, \tag{3.32c}$$

where α, β, and γ are the critical exponents associated with the specific heat, magnetisation, and magnetic susceptibility, respectively. Logarithmic plots of, say, $M(T_C)$ against L should appear linear. Ratios of critical exponents can then be extracted from the gradient of the

best-fit line. We demonstrate conclusively the validity of this approach in Fig. 3.8, for the magnetisation, susceptibility and heat capacity.

Extracting critical exponents from a finite-size scaling suffers from several inherent difficulties, however. First, the relations in eq. (3.32) only hold for sufficiently large system sizes; for small L, so-called corrections to scaling introduce non-linearities. This is most obvious in Fig. 3.8(c) where the data for C_V are significantly non-linear below $L = 16$. This can be mitigated by fitting only to large L, though there is no hard-and-fast rule as to what constitutes 'large' in this context. Second, it requires good estimates of quantities exactly at the critical temperature. However, this is precisely the point at which critical fluctuations and critical slowing down make it hard to obtain reliable averages. Third, it requires the critical temperature be known to a high degree of accuracy. For the systems we consider in this thesis, T_C is not known *a priori*. Binder showed that a cumulant quantity,

$$g_m = 1 - \frac{1}{3}\frac{\langle m^4 \rangle}{\langle m^2 \rangle}, \tag{3.33}$$

provided one such route to determining it accurately [149]. For large enough system sizes, curves of $g_m(L, T)$ against T cross at a fixed-point, which is exactly the critical temperature. We illustrate this effect in Fig. 3.9(a) for various system sizes of the 2D Ising model. The common, mutual intersection points are located close to the exact critical temperature as indicated by the dashed, vertical line in the inset. A widely used method is to find the intersection point using the intersection of ascending pairs of system sizes, i.e. L_1/L_2, L_2/L_3 for $L_1 < L_2 < L_3$. This is shown in Fig. 3.9(b), from which an average value of the critical temperature can be obtained: $T_C = 2.265 \pm 0.013$. This is less than 2% away from the accepted value [eq. (3.21)].

We compare the exponents extracted from the finite-size scaling approach with those of the exact solution and those obtained from a mean field treatment in Table 3.2. The MC estimates show good agreement with the exact values. We will use the finite-size scaling technique to obtain the critical exponents for a class of artificial spin systems in Chapter 5.
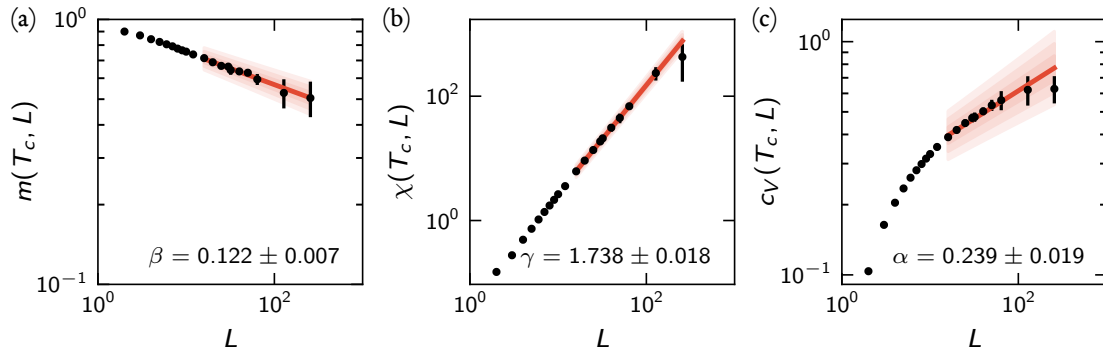
Figure 3.8: Finite-size scaling at the critical temperature of the 2D Ising model for (a) the magnetisation, m, (b) the susceptibility, χ, and (c) the heat capacity, c_V. To mitigate corrections to scaling, only system sizes above $L = 16$ are used for fitting [approximately, data in the right half of each plot]. The 1-, 2-, and 3-σ confidence intervals are shaded around the best-fit. Critical exponents (here, the gradients of the best-fit lines) are indicated in each case. See Table 3.2 for a summary.
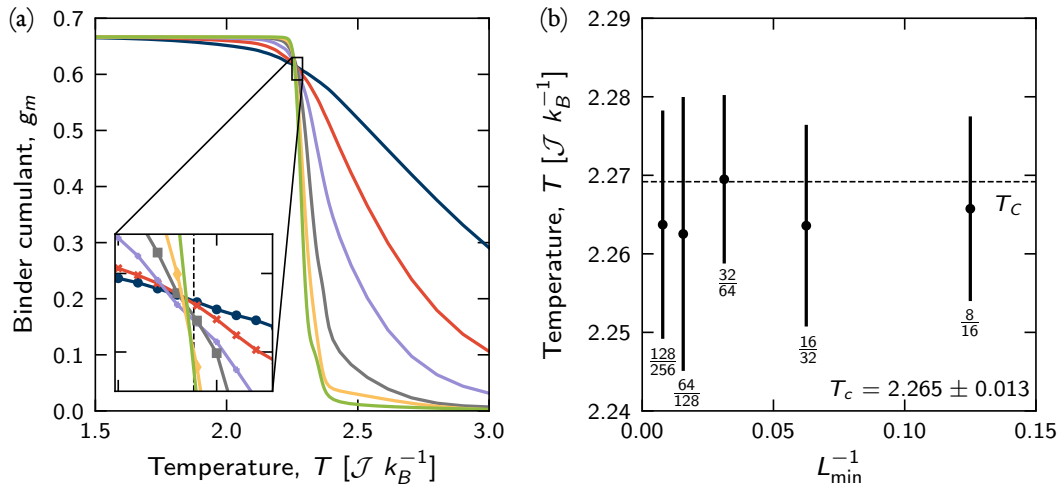
Figure 3.9: Binder cumulant and estimating the critical temperature from Monte Carlo simulations of the 2D Ising model. (a) Binder cumulant of the magnetisation, $g_m = 1 - \langle m^4 \rangle / (3 \langle m^2 \rangle^2)$, as a function of temperature for the 2D Ising model. Inset: the curves mutually intersect in a region about the critical temperature [dashed, vertical line]. (b) Estimating the critical temperature by finding the intersection between ascending pairs of system sizes. As expected, the intersection does not appear to scale with system size.

Table 3.2: Summary of critical exponents for the 2D Ising model. From L-R: the exact values given by the Onsager solution; the exponents predicted by mean field theory; and the estimates based on the Monte Carlo results presented in this chapter. Excellent agreement is noted between the MC results and those predicted by theory for all variables except α. Significantly, finite-size scaling is more accurate than mean field theory in this case. In general, mean field theory proves more reliable in higher dimensions or, at least, once above the upper critical dimension of the system. In two dimensions, it tends to overestimate results as it discounts fluctuations.

	2D Ising Model		
	Exact	Mean field theory	Monte Carlo
$T_C \, [\mathcal{J} k_B^{-1}]$	≈ 2.269	4	2.265 ± 0.013
α	0	0	0.239 ± 0.019
β	$^{1}/_{8}$	$^{1}/_{2}$	0.122 ± 0.007
γ	$^{7}/_{4}$	1	1.738 ± 0.018

3.7 | Replica exchange—parallel tempering—Monte Carlo

Many of the ASI lattices we consider in this thesis possess either highly degenerate configurations [Chapters 5 and 6] or quenched disorder [Chapter 7]. In such instances, we commonly encounter metastability, whereby the system becomes trapped in a local potential well that is not the ground state. These systems possess long relaxation timescales, which make it difficult to access their low-energy states both experimentally and numerically. From a Monte Carlo standpoint, it becomes difficult both to equilibrate such systems and then to obtain reliable averages when using the Metropolis-Hastings algorithm.

To circumvent this, we introduce the idea of replica exchange Monte Carlo, which is also called parallel tempering (PT) [150] . In PT Monte Carlo, M independent replicas of the system are simulated at different temperatures in the set $\{T_1, T_2...T_M\}$. After performing a fixed number of MC moves within each replica, swaps between replicas at adjacent temperatures,

T_i and T_{i+1}, are proposed. These are accepted with probability,

$$\mathcal{P}(E_i, T_i \leftrightarrow E_{i+1}, T_{i+1}) = \min(1, e^{\Delta\beta_i \Delta E_i}), \qquad (3.34)$$

where $\Delta\beta_i = \beta_{i+1} - \beta_i$ and $\Delta E_i = E_{i+1} - E_i$. For a real system, this is equivalent to repeatedly heating and cooling as a way of using thermal agitation to overcome the energy barriers associated with metastability.

Fig. 3.10(a) offers a cartoon representation of the rationale behind this method. Suppose that the system becomes trapped in a potential well at a low temperature, indicated by the blue ball. Thermal fluctuations, $k_B T$, are insufficient to move the ball into the other low-energy state. By heating the system however, the free energy landscape becomes smoothed out. This allows the ball to roll into another minimum at a high temperature, before the system is cooled back down. In this way, replicas that become jammed in metastable states at low temperatures (where the autocorrelation time is large), are able to diffuse to higher temperatures (where the autocorrelation time is short) before subsequently finding their way to the ground state. These swap moves are equivalent to a guided walk in temperature space [Fig. 3.10(b)], such that a given replica moves between the temperature extremes according to the MH criterion. Clearly, the effectiveness of this method hinges on the exact choice of temperatures. We discuss the method of assigning temperatures more fully while considering the results in Chapter 5.
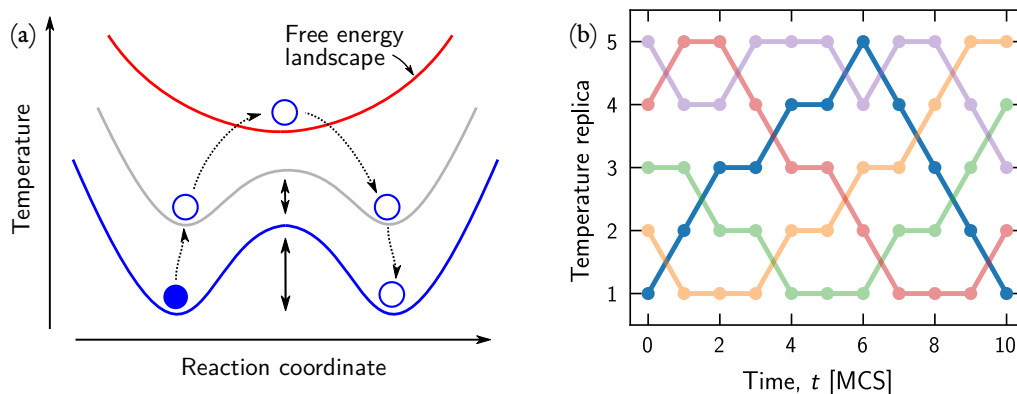
Figure 3.10: Illustration of replica exchange Monte Carlo. (a) Systems which become trapped in a potential well at low temperatures [blue line] are able to escape by diffusing to higher temperatures [red line] before eventual cooling. By heating the system, dips in the free energy landscape are smoothed out. (b) Replicas perform a random walk in temperature space as a function of Monte Carlo time. This allows them to wander up and down between the extremes of the temperature range.

3.8 | Summary

This chapter has provided an account of the numerical techniques which will be used to probe artificial spin ices throughout the remainder of this thesis. Monte Carlo methods were introduced; these prove indispensable in calculating observables for situations in which no exact description of the system can be found. By way of example, we applied them to the 2D Ising model on the square lattice and recovered the accepted results. We followed this by discussing correlations and the finite-size scaling approach. In turn, this led us to consider the role of critical exponents in characterising phase transitions. Finally we outlined the use of parallel tempering Monte Carlo to tackle problems associated with the occurence of metastable states during calculations. This allowed us to discuss the role of correlations, and finite-size scaling. In what follows, we return to these topics frequently.

4

Experimental methods

4.1 | Introduction

This chapter presents an outline of the techniques which have been used during the experimental part of this project to fabricate artificial spin ice arrays and to acquire images elucidating their magnetic configurations. In Sec. 4.2, we start by describing briefly the fundamentals of electron microscopy and follow this, in Sec. 4.3, with a discussion of Lorentz microscopy. We concentrate on the Fresnel mode of Lorentz microscopy because it is the principal imaging method used throughout this work. We then proceed to derive an expression for the contrast in these Fresnel images. From them we can extract the magnetic configurations of artificial spin ice arrays to compare with our theoretical predictions. In Sec. 4.4, focused electron beam induced deposition (FEBID) is introduced. This technique allows for the rapid prototyping of two- and three-dimensional magnetic structures, such as those which we will probe in Chapter 6.

4.2 | Electron microscopy

Electron microscopy (EM) has become an indispensable tool in materials science and condensed matter physics for dimensions too small to be resolved by conventional optical microscopy. Excellent spatial discrimination can be combined with, among other things, *in-situ* chemical and magnetic studies. One instrument can thus provide access to both real and reciprocal space, as well as spectroscopic and compositional information. Its versatility forms the basis of the multi-dimensional electron microscopy paradigm, in which a complete picture of a material is obtained by combining signals from multiple techniques [151, 152].

The advent of electron microscopy can be traced to the concept of wave-particle duality. In 1924, de Broglie advanced the revolutionary hypothesis that all massive particles had a complementary wavelike nature [153].[1] For a particle of momentum, p, the associated de Broglie wavelength is

$$\lambda = \frac{h}{p},\tag{4.1}$$

where h is the quantum of action.[2] Shortly thereafter, the demonstration of electron diffraction by G. P. Thomson [155] and, separately, by Davisson and Germer [156, 157] confirmed this relationship. The first electron microscope was constructed in 1932 by Knoll and Ruska [158], with commercial models available from 1939 [159]. The underlying principles of electron microscopes remain the same to this day. They comprise a source of electrons which provide the illumination; an optical system which focuses the illumination onto the sample, collects the transmitted signal and magnifies it; and a series of detectors which record the output. In this chapter, we will focus on transmission electron microscopy (TEM), i.e. the situation in which the electron beam acquires information as it passes through the sample.

---

[1] J. J. Thomson compares this duality to "the struggle between a tiger and a shark, each is supreme in his own element but helpless in that of the other." [154]

[2] In the SI system [106], the Planck constant is defined as $h = 6.62607015 \times 10^{-34}$ Js, with dimensions $[M][L]^2[T]^{-1}$.

4.2.1 In pursuit of smaller wavelengths

In the framework of Fourier optics, a converging lens is an entity which takes the field distribution impinging on its front focal plane and returns the Fourier transform in the back focal plane [160]. This action can be justified by invoking Huygens' principle, which states that every point on a wavefront acts the source of a new set of spherical wavelets. The dynamical evolution of the wave is defined by the mutual interference pattern, which is to say the sum, of these wavelets. A lens transforms the wavefront incident on the front focal plane into its Fourier components in the back focal plane. Any imaging system, including an electron microscope, can be described in terms of at least two lenses.

The Fourier transform of the intensity emitted by a distant point source and collected over a finite solid angle is the point spread function; in reality, this manifests itself as a smearing in which the point is transformed into a disc, called the Airy disc. The radius of the central disc is given by the Abbe limit,

$$d = \frac{\lambda}{2n\sin\theta},\tag{4.2}$$

where n is the refractive index of the medium and θ is the collection angle. The factor $n\sin\theta$ is called the numerical aperture, NA, of the device. Abbe postulated that any image is composed of an overlapping array of such spots. Resolving an image thus necessitates discriminating between adjacent Airy discs and so eq. (4.2) sets a fundamental diffraction limit on the performance of any imaging system.[3] Assuming a typical wavelength for light in the visible spectrum of 500 nm and NA = 1[4], the diffraction limit is 250 nm, which is well above the length scale of many features considered in this thesis.

The use of electrons, as opposed to visible light, allows resolution at smaller length scales. Electrons, accelerated through a voltage V, have a wavelength,

$$\lambda = \frac{h}{\sqrt{2m_e eV\left(1 + \frac{eV}{2m_e c^2}\right)}},\tag{4.3}$$

---

[3]Equivalently, for image formation, an optical system must collect more than just the central spot in a diffraction pattern. The diffraction limit is the distance between the undeflected, zero-order spot, and the first interference maximum—the Rayleigh criterion.

[4]In modern light-based optics, values between 1 [161] and 1.5 [162] for the NA are common.

where c is the speed of light, and m_e and $-e$ are the mass and charge of the electron, respectively. The accelerating voltage used in this thesis is 200 kV, for which the wavelength of the electrons is 2.51 pm. At this voltage, electrons move with relativistic speeds ($>$ 0.1c), and so eq. (4.3) incorporates a correction to their rest mass. In the absence of this correction, the wavelength is 2.73 pm; we show a comparison between the semi-classical and relativistic regimes in Fig. 4.1 for accelerating voltages up to 1 MeV.
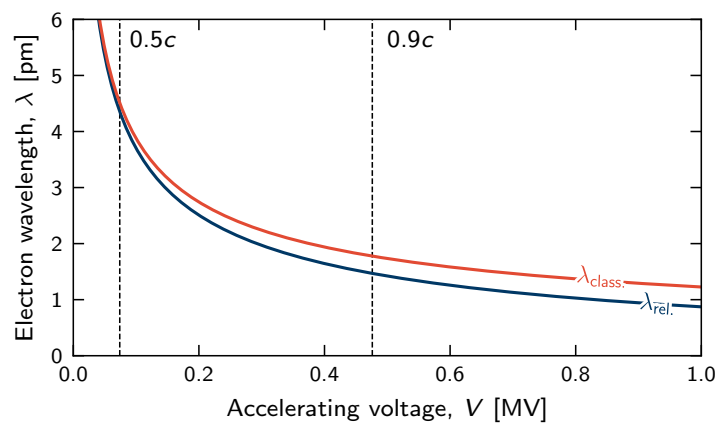
Figure 4.1: Comparison between the non-relativistic (red) and relativistic (blue) wavelengths, λ, of electrons accelerated through a potential difference, V. Accelerating voltages which give electrons speeds of 0.5c and 0.9c are marked explicitly. For the accelerating voltage used in this thesis, 200 kV, the electrons are travelling at 0.7c.

4.2.2 Electron-sample interactions

An increase in resolution over light-based techniques is not the only advantage conferred by electron microscopy. At the same time, we can also extract information from the various ways in which the electrons interact with the sample. For example, electron energy loss spectroscopy relies on inelastically scattered electrons to provide information about sample composition [163] while this thesis uses the deflection of electrons by magnetic fields to map spin configurations in artificial spin ice arrays. Electrons incident on a sample can be transmitted or reflected [Fig. 4.2(a)], undergoing scattering processes that are either elastic (conserves energy) or inelastic (does not conserve energy).

The reflected signal is the domain of scanning electron microscopy (SEM), which allows surface imaging and elemental analysis. The most common imaging mode in SEM operates by collecting secondary electrons. These are electrons which are ejected from conduction or valence bands in a material through inelastic interactions with the beam electrons. Backscattered electrons are electrons from the incident beam which are reflected through large angles as a result of Coulombic repulsion from atomic nuclei. This is referred to as Rutherford scattering [164]. We will discuss the role of secondary and back-scattered electrons in FEBID as part of Sec. 4.4.

In TEM, transmitted electrons can be elastically or inelastically scattered. In a quantum-mechanical description, transmission leads to a modulation of the amplitude and phase of the incident wavefront as it passes through the sample [Fig. 4.2(b)].

By-products of inelastic processes include x-rays, which may be emitted in either the forward or backward directions. Along with Auger electrons, these can be used for elemental characterisation [165, 166, 167]. A selection of other processes is included in Fig. 4.2.

4.2.3 Electron source

An electron gun acts as the source of illumination in a TEM. There are two main types of sources: thermionic emission, and cold field emission. In thermionic emission, a sample of material (e.g. LaB_6 or tungsten) is resistively heated to lower the work function such that electrons are boiled off. In cold field emission guns, a large bias voltage is applied to a tungsten tip, which has a typical radius of 100 nm. The positive bias creates a strong electric field gradient, which lowers the energy barrier to tunnelling for the electrons. In both cases, emitted electrons are accelerated to the desired voltage, and brought to an initial focus at the gun crossover. The size of the spot at crossover determines the spatial coherence of the beam. In general, cold field emission guns can be focused to a smaller crossover than can thermionic emitters. This makes their use preferred for high resolution, analytical or magnetic imaging in EM as these depend on coherent illumination [169]. The microscope used in this thesis, the JEOL ARM200cF TEM, is equipped with a cold field emission gun.
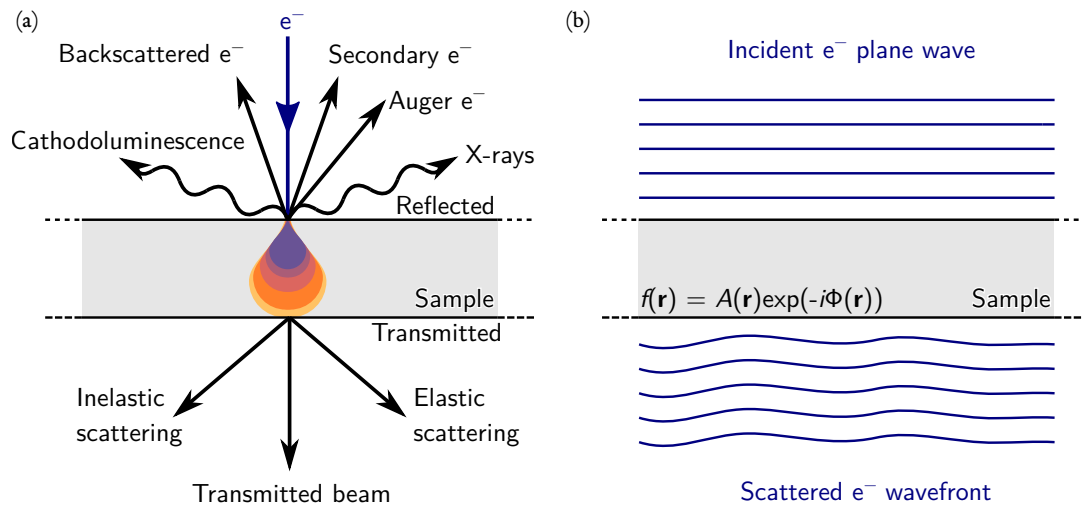
Figure 4.2: Interactions incident between electrons and a material. (a) A distinction is made between signals which are reflected and transmitted through the sample [upper and lower halves of the plot, respectively]. Electronic (electromagnetic) signals are indicated by the straight (curly) arrows. As discussed later in Sec. 4.4, FEBID relies on secondary and back-scattered electrons. The list of named processes is by no means comprehensive. (b) In transmission electron microscopy, the amplitude and phase of the incident electron wave front is modulated through sample interactions. This can be represented by a sample scattering function, $f(\mathbf{r})$. Panel (b) has been redrawn from [168].

4.2.4 Aberrations

The focusing system in a TEM is composed of electromagnetic lenses. These use magnetic fields to alter the trajectory of the electrons, akin to the way in which regions of different refractive indices bend light in an optical system. Unlike conventional lenses however, their strength can be adjusted on-the-fly by varying their supply current. Magnetic lenses suffer from imperfections that degrade their performance and, hence, the resolution of the instrument. At best, most electron microscopes are aberration-limited to about 50λ [170]. In order of decreasing severity, the three principal sources of error are spherical aberration, chromatic aberration, and astigmatism. In analogy with optical systems, we can denote electron trajectories by rays though, as we discussed in Chapter 2, electrons trace helical paths in a magnetic field. A perfect imaging system [Fig. 4.3(a)] maps all rays emanating from a point in the object plane to a single point in the image plane.

In the case of spherical aberrations, off-axis electrons are focused more strongly than are

those travelling close to the optic axis. This is shown in Fig. 4.3(b). This is the electromagnetic equivalent of the breakdown in the paraxial approximation observed in conventional optical lenses. Spherical aberrations smear out point-like structures into discs in the image plane, such that radius of these discs is given by $C_s\beta^3$, where β is the maximum collection angle of the lens or aperture, and C_s is the coefficient of spherical aberration. The coefficient of spherical aberration in the JEOL ARM200cF is $C_s = 0.5$ mm. Scherzer proposed a method of correcting for spherical aberration, which relies on using multipolar lenses to diverge off-axis rays back to a single focus [171, 172]. These aberration correctors in the JEOL ARM200cF reduce the radius of this disc of confusion down to 78 pm.

Chromatic aberration arises from the fact that the illumination electrons are not all of the same energy. Rather, there is an intrinsic spread in energies, ΔE, and, hence, in wavelength by application of eq. (4.3). This is shown in Fig. 4.3(c) for 'fast' and 'slow' electrons [solid and dashed lines, respectively]. The spread in the beam energy of the JEOL ARM200cF is 0.27 eV. A similar phenomenon is also observed in conventional optical microscopy, in which the refractive index varies with wavelength. The effects of this aberration can be reduced by using sources which produce monochromatic electrons, or by using a monochromator to select the energy window.

Finally, astigmatism refers to inhomogeneities in the electromagnetic lenses arising from, say, microstructural defects in the material of the pole pieces, or imperfections introduced in fabrication. This can be mitigated by using octupolar magnets, called stigmators, to apply an opposing field. For completenes, we note that this discussion of aberration has been limited to conventional, objective-on TEM. In Lorentz microscopy, defocusing the set-up to image a plane above or below that in which the sample sits, is an additional—often desired—source of aberration.

4.2.5 Operating principles of TEM

Transmission electron microscopes can be operated in two modes: conventional, in which plane wave illumination is used, or scanning, in which a focussed probe is rastered over the sample. In this thesis, we use conventional TEM (CTEM). In what follows, we will use the acronyms TEM and CTEM interchangeably. This method of image formation is illustrated in
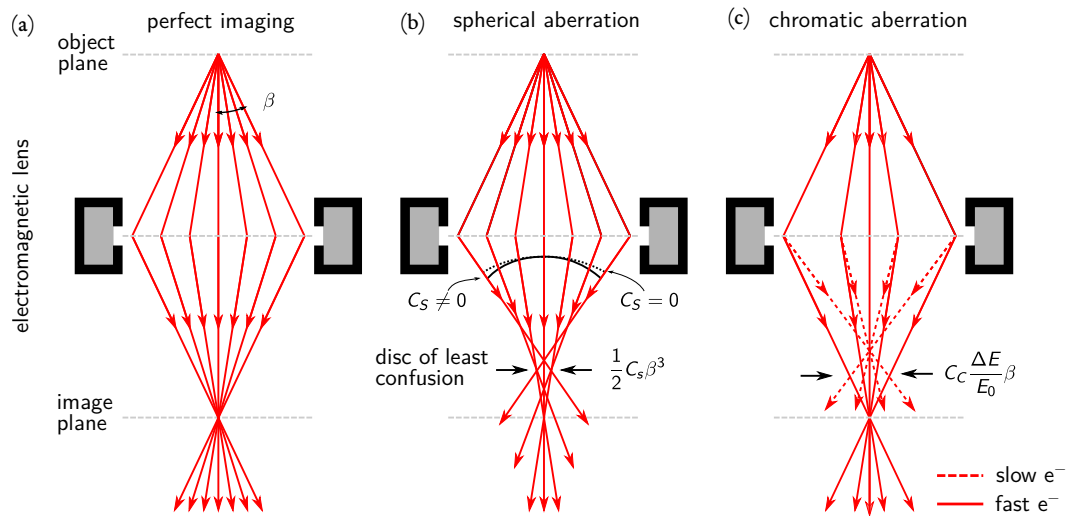
Figure 4.3: Aberrations in electron microscopy. (a) A perfect imaging system. A point in the object plane is mapped to a point in the image plane by the action of the lens. The collection angle, β, is marked. (b) A system with spherical aberration. Rays further from the optic axis are bent more, causing a deviation [solid black] from the ideal spherical wavefront [dashed black]. The radius of the disc of least confusion is given by $\frac{1}{2}C_s\beta^3$, where C_s is the coefficient of spherical aberration. (c) A system with chromatic aberration. Slow electrons are deflected more than fast electrons by the electromagnetic lenses. This reflects a spread, ΔE, about the mean energy, E_0, of the beam. In this case, the radius of the disc of least confusion is given by $C_C \Delta E / E_0 \beta$.

Fig. 4.4, which mimics approximately the setup of the JEOL ARM200cF TEM. Irrespective of the mode, a spherical wave is emitted by the electron source and focused to a point at the gun crossover.

In TEM, the condenser system is composed of the lenses, C1 and C2, which act in concert with the upper objective lens, O1 [marked explicitly, upper half of Fig. 4.4]. These produce a collimated beam that is incident on the sample. The C1 lens adjusts the spot size of the beam, while the C2 lens controls illumination. In the JEOL ARM200cF, the sample is placed between the upper and lower objective lenses (unlike some other instruments, in which it sits above the objective). The lower objective lens, O2, collects the Fourier transform of the transmitted beam in its back focal plane. An objective aperture is inserted here; this determines the collection angle and serves to improve contrast in the final image as it removes scattered electrons. If the aim is to record the diffraction pattern rather than a real space image, the

objective aperture is removed and a selected area aperture is inserted into the image plane. In Lorentz TEM, O1 and O2 are nulled and an objective Lorentz minilens takes their place; this is shown between the image and back focal planes in Fig. 4.4. This Lorentz lens is situated further from the sample, and is weaker than either of the main objective lenses. In effect, for Lorentz TEM, the objective is switched off. The normal field in the sample plane, ~ 2 T, is reduced to a remanent value < 0.015 T. This field can be almost completely nulled yet further by applying current to the objective lenses. This is discussed more in Sec. 4.3.

This Lorentz lens is situated further from the sample, and is weaker than either of the main objective lenses. The projector system magnifies the signal on to the detector screen. CTEM can be used to collect real space images or diffraction patterns. These are selected by setting the object plane of the intermediate lens to the back focal plane or image plane of the lower objective, respectively.

4.2.5.1 Principle of image formation. We have previously mentioned that optical systems are devices which effectively carry out Fourier transforms. In this section, we will introduce the transfer function formalism to make this more concrete; this will aid our discussion of Fresnel contrast in Sec. 4.3.2.

In CTEM, suppose that the incident electron wavefunction is a plane wave, with uniform amplitude and phase. Without loss of subsequent generality, we take

$$\psi_{\text{incident}} = 1, \tag{4.4}$$

to represent the incident beam. On transmission through a sample of thickness, t, the amplitude and phase of the electrons are modulated by their interactions with the sample. This can be captured by a multiplicative sample function such that, after transmission, the electron wavefunction is

$$\psi_t(\mathbf{r}) = a(\mathbf{r})e^{-i\phi(\mathbf{r})}, \tag{4.5}$$

where $a(\mathbf{r})$ and $\phi(\mathbf{r})$ are the amplitude and phase shift introduced by the sample. We can simplify things considerably by setting the amplitude of the transmitted wave to unity. Further, if the sample is very thin, it can be treated as a weak-phase object, i.e. $\phi \ll 1$, and the
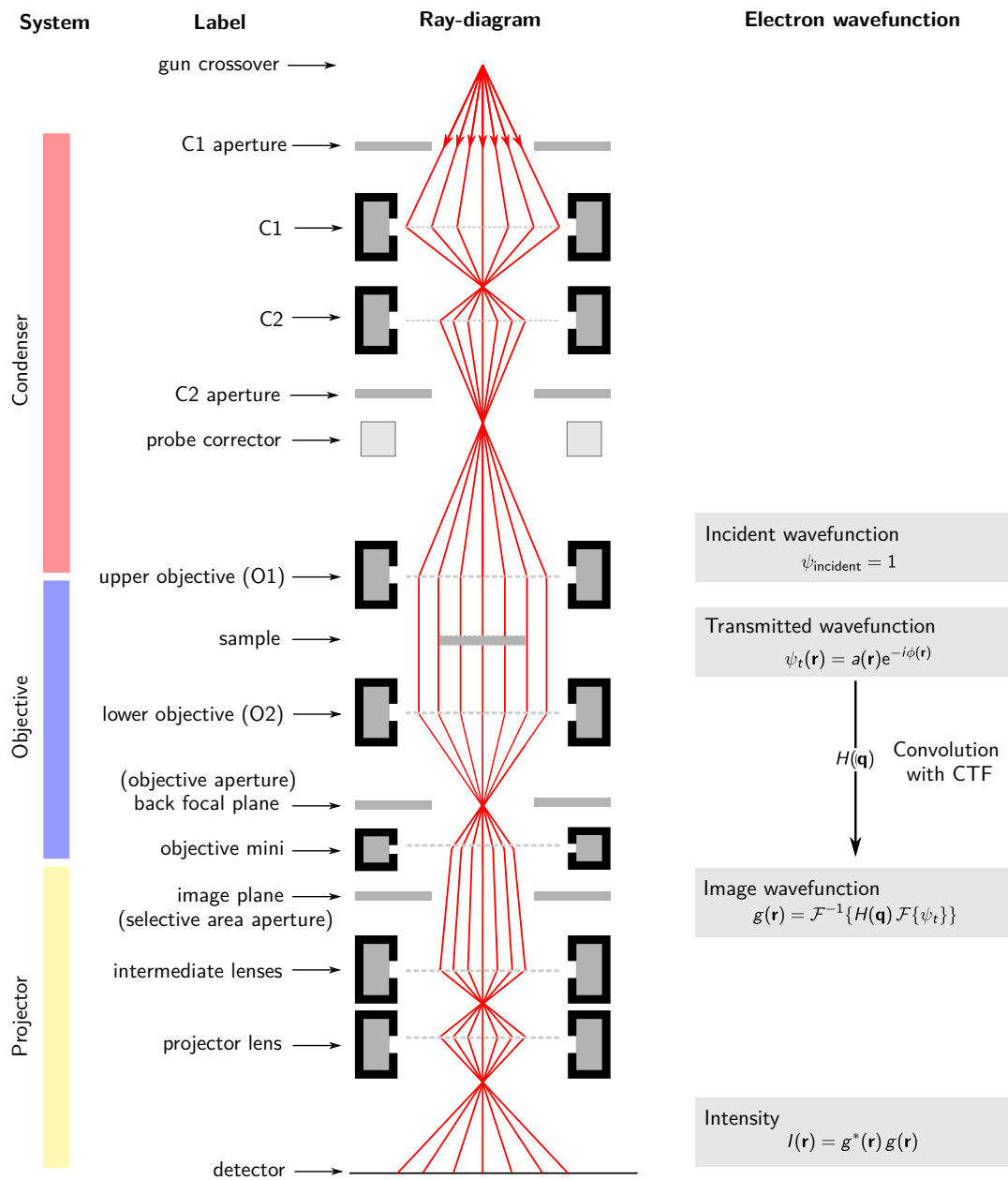
Figure 4.4: Ray diagram for CTEM configured in imaging mode. The condenser, objective and projector systems are marked. The setup approximately mimics that of the JEOL ARM200cF. Right panel: transfer function formalism. The incident wavefunction is modified by interactions with the sample to produce the transmitted wavefunction, $\psi_t(\mathbf{r})$. The image wavefunction, $g(\mathbf{r})$, is the convolution of ψ_t with the contrast transfer function of the microscope. The detector records the intensity, $I = g^*(\mathbf{r})g(\mathbf{r})$, of the image wavefunction.

exponential in eq. (4.5) expanded about zero to give

$$\psi_t(\mathbf{r}) \approx 1 - i\phi(\mathbf{r}). \tag{4.6}$$

As we shall discuss, magnetic thin films behave as strong phase objects. The objective transforms the sample function in its object plane into its Fourier representation in the back focal plane, $\Psi(\mathbf{q})$.[5] In imaging mode, the projector system magnifies the field present in the back focal plane of the objective. In doing so, it applies an inverse Fourier transform. The image function, $g(\mathbf{r})$, is the convolution of the transmitted wavefunction with the point spread function of the microscope, $h(\mathbf{r})$, that is,

$$
\begin{aligned}
g(\mathbf{r}) &= \psi(\mathbf{r}) \otimes h(\mathbf{r} - \mathbf{r}') \\
&= \int d\mathbf{r}' \, \psi(\mathbf{r}) \, h(\mathbf{r} - \mathbf{r}'),
\end{aligned}
\tag{4.7}
$$

where the notation $\otimes$ represents the convolution operator. The detector records the intensity of this image function i.e., $I = g^*(\mathbf{r})g(\mathbf{r})$. Equivalently, we can work in terms of reciprocal space, $\mathbf{q}$, to recast eq. (4.7) as

$$G(\mathbf{q}) = \Psi(\mathbf{q})H(\mathbf{q}).\text{[6]} \tag{4.8}$$

The quantity, $H(\mathbf{q})$, is called the contrast-transfer-function of the microscope, and describes how spatial frequencies in the sample are transferred to the image. In doing so, the effects of apertures, illumination conditions, and aberrations are subsumed into $H(\mathbf{q})$ by writing

$$H(\mathbf{q}) = A(\mathbf{q})E(\mathbf{q})e^{-i\chi(\mathbf{r})}. \tag{4.9}$$

Since apertures block spatial frequencies higher than some cut-off, the aperture function, $A(\mathbf{q})$, is a low-pass filter. The envelope function, $E(\mathbf{r})$, describes the spatial and temporal coherence of the beam. These are controlled by the angular and energetic spread of the electrons, respectively. Coherent aberrations are described by the phasor, $e^{-\chi(\mathbf{q})}$, for which an approximate expression,

$$\chi(\mathbf{q}) = \frac{2\pi}{\lambda}\left(C_s\frac{\lambda^4\mathbf{q}^4}{4} - \Delta f\frac{\lambda^2\mathbf{q}^2}{2}\right), \tag{4.10}$$

---

[5]We will use uppercase letters to indicate the Fourier transform of a function

[6]We have used the convolution theorem to rewrite the Fourier transform of a convolution in terms of a product of the individual Fourier representations.

is given in [169], in terms of the defocus, Δf. By way of comparison, a perfect microscope in which no apertures are inserted would possess a contrast transfer function, $H(\mathbf{q}) = 1$, since it admits all spatial frequencies equally.

4.3 | **Lorentz microscopy**

Lorentz microscopy is an umbrella term that encompasses several magnetic imaging techniques within electron microscopy. Since its first demonstration in 1959 [173], it has proved a versatile tool for both static and dynamic measurements of magnetic materials, including artificial spin ice [174, 26, 175, 3, 2]. Several distinct modes are possible; these include Fresnel, Foucault, electron holography, and differential phase contrast. Since this thesis uses the Fresnel mode of Lorentz microscopy, our discussion naturally centres on it though we briefly describe some other techniques in Sec. 4.3.3.

Lorentz microscopy can be explained using both a semi-classical argument and a full quantum mechanical framework. In the classical picture, an electron of charge $-e$ with velocity $\mathbf{v}$ moving in a region of magnetic induction $\mathbf{B}$ is subject to a *Lorentz* force via

$$\mathbf{F} = -e\,\mathbf{v} \times \mathbf{B}, \tag{4.11}$$

which give rises to circular motion. In passing through a thin, magnetic sample therefore, an electron will be deflected by this force. Two further points are worth noting. First, the force on the electron arises from the magnetic induction rather than the magnetisation, $\mathbf{M}$. As discussed in Chapter 2, the constitutive equation relates these quantities through the stray field, $\mathbf{H}$, according to

$$\mathbf{B} = \mu_0(\mathbf{H} + \mathbf{M}). \tag{4.12}$$

As a result, only in certain, simple situations can the magnetisation be unambiguously inferred from the deflection. Second, only those components of $\mathbf{B}$ in a plane perpendicular to the instantaneous direction of motion contribute to the Lorentz force. To illustrate how this deflection arises, Fig. 4.5(a) depicts a thin film of saturation magnetisation, M_S, which is uniformly magnetised in the y-direction so that $\mathbf{M} = M_S\hat{\mathbf{e}}_y$ using the inscribed coordinate system. This film has thickness, t, as marked. Since $\nabla \cdot \mathbf{M} = 0$ for this system, the magnetic

induction and the magnetisation are effectively the same and we can write $\mathbf{B} = B_S\hat{\mathbf{e}}_y$ in terms of the saturation field, $B_S = \mu_0 M_S$. An electron is incident along the sample normal and deflected through an angle, β. The momentum transferred to the incident electron by the Lorentz force is directed along $-\hat{\mathbf{e}}_x$ and has magnitude,

$$\begin{aligned} p_x &= \int_0^t \mathbf{F} \cdot \mathrm{d}\,\mathbf{s} \\ &= eB_St, \end{aligned}$$ (4.13)

where $\mathrm{d}\,\mathbf{s}$ is an infinitesimal path element along the electron trajectory. Assuming that the electron stays mainly along the optic axis, the deflection angle is given by the ratio of the momenta in the x- and z-directions; that is

$$\beta = \frac{p_x}{p_z} = \frac{eB_St}{mv} = \frac{e\lambda}{h}B_St,$$ (4.14)

where in the final step we have used the de Broglie relation, eq. (4.1).[7] For 200 keV electrons, the prefactor has a value

$$\frac{e\lambda}{h} \approx 606 \;\mu\mathrm{rad}\;\mathrm{T}^{-1}\mathrm{nm}^{-1}.$$ (4.15)

A 3 nm film of cobalt with saturation magnetisation, $M_S = 1.4\,\mathrm{MAm}^{-1}$, gives rises to a deflection of 3.2 μrad. For comparison, the fcc form of cobalt has a lattice constant, $a = 3.54\,\text{Å}$. The first allowed Bragg reflection is from the (111) plane for which the scattering angle is 6 mrad—more than three orders of magnitude greater than the Lorentz deflection. Our assumption that the electron stays mainly along the optic axis is thus valid.

In a quantum mechanical approach to this scenario, the phase of the electron wavefunction is modified by a coupling to the electric potential, V, and the magnetic vector potential, $\mathbf{A}$.[8] This Aharonov-Bohm phase shift [176] is given by

$$\phi(\mathbf{r}) \equiv \phi_e(r) + \phi_m(r)$$ (4.16)

$$= \frac{e}{\hbar}\left(\frac{1}{v}\int_{\mathcal{P}} V(\mathbf{r})\,\mathrm{d}s - \int_{\mathcal{P}} \mathbf{A}(\mathbf{r})\cdot\mathrm{d}\,\mathbf{s}\right),$$ (4.17)

where we have split the electrostatic, ϕ_e, and magnetic, ϕ_m, phase contributions explicitly. The integrations are carried out over the electron path, $\mathcal{P}$; several such paths are shown in

[7]The inclusion of the Planck constant, h, makes clear that is only a *semi*-classical picture.
[8]The magnetic vector potential satisfies $\mathbf{B} = \nabla \times \mathbf{A}$, though this does not uniquely define it.
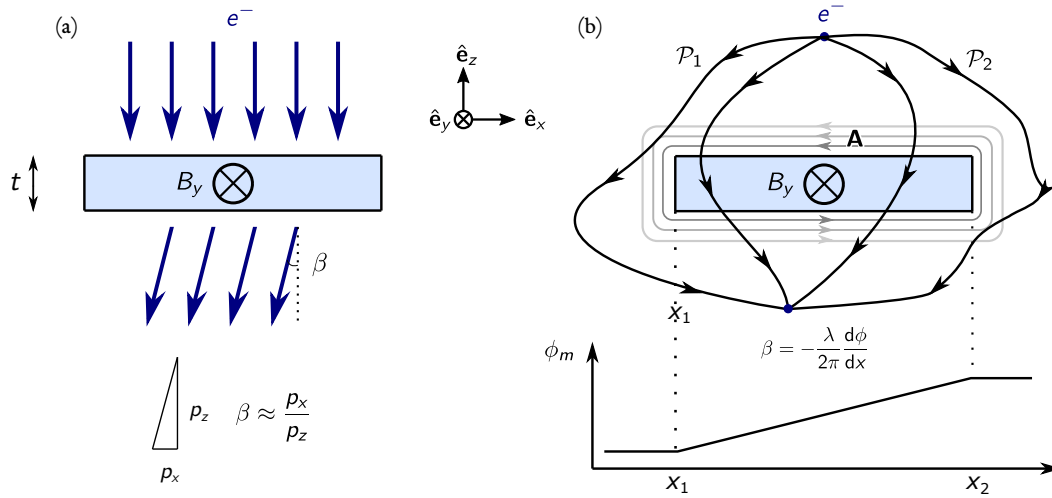
Figure 4.5: Deflection of an electron travelling through a region of magnetic induction, **B**, according to a semi-classical and quantum-mechanical framework. (a) In the classical picture, the deflection arises from the Lorentz force. A value for the deflection angle, β, can be calculated by considering the momentum imparted to the electron by the field. (b) The Aharaonov-Bohm effect explains this deflection through a coupling the complex phase of the electron wavefunction to the magnetic vector potential, **A**.

Fig. 4.5(b). Considering first the magnetic phase contribution, the phase difference between $\mathcal{P}_1$ and $\mathcal{P}_2$ is

$$
\begin{aligned}
\Delta\phi_m &= \phi_1 - \phi_2 \\
&= \frac{e}{\hbar} \oint \mathbf{A}(\mathbf{r}) \cdot \mathrm{d}\,\mathbf{s},
\end{aligned}
\tag{4.18}
$$

where the integral is carried out over the closed loop, $\mathcal{P}_1 - \mathcal{P}_2$. Note that we have chosen to illustrate this effect for a path which does not enter the material—though our comments apply equally well to any arbitrary closed loop. Applying Stokes' theorem, this can be rewritten as a surface integral of the magnetic flux,

$$
\begin{aligned}
\Delta\phi_m &= \frac{e}{\hbar} \int \nabla \times \mathbf{A}\, \mathrm{d}\,\mathbf{S} \\
&= \frac{e}{\hbar} \int \mathbf{B} \times \hat{\mathbf{e}}_y\, \mathrm{d}S,
\end{aligned}
\tag{4.19}
$$

in the coordinate system defined in Fig. 4.5. The phase shift becomes

$$
\Delta\phi_m = \frac{eB_s t}{\hbar}\Delta x,
\tag{4.20}
$$

where $\Delta x = x_2 - x_1$. By taking the gradient of the phase in the plane perpendicular to motion, the Lorentz deflection angle is recovered:

$$\beta = -\frac{\lambda}{2\pi}\nabla\phi_m, \tag{4.21}$$

which connects the classical and quantum-mechanical pictures. Remarkably, even paths that do not enter the region of magnetic induction acquire a phase shift. Ref. [52] presents an elegant explanation for this based on topology. The wave function for the closed loop $\mathcal{P}_1 - \mathcal{P}_2$ is defined everywhere in $\mathbb{R}^2$ except in the region of magnetic induction. The symmetry group of electrodynamics is $U(1)$, which is equivalent to the unit circle. Assigning a phase in this scenario amounts to drawing a circle around a hole; this can be done in two disjoint ways which cannot be transformed into each other. Akin to skyrmionic systems [177], this defines a topologically protected winding number and, as a result, the phase shift cannot be absorbed by a change of gauge.

In the case of a constant electric field within the sample, the electrostatic phase contribution can be evaluated to give

$$\phi_e = \frac{e}{E}V_0 t, \tag{4.22}$$

where V_0 is the mean inner potential and E is the beam energy. The potential, V_0, describes the average effect of electrostatic fields from atoms in the sample. As a concrete example, recent measurements of FEBID deposited Co structures give $V_0 = 21.5$ V [178], which is somewhat lower than the value, 29.45 V, predicted by Stadelmann [179]. Nonetheless, assuming this value also holds in a 3 nm thin film of Co, we obtain a uniform phase shift of ~ 0.5 rad at 200 keV.

We emphasise at this point that all branches of Lorentz microscopy are phase imaging techniques; contrast thus arises through ϕ, or its derivatives.

4.3.1 The Fresnel mode

As drawn in Fig. 4.4, the sample sits in a plane between the upper and lower objective lenses. Uncompensated, the field in this region is on the order of 1 T—large enough to saturate most magnetic materials into single domains. While the islands in artificial spin ice have strong

shape anisotropy, previous work on kagome and pinwheel lattices have shown that external out-of-plane fields can affect in-plane switching characteristics [180, 4]. In Lorentz microscopy, the objective lens is nulled to ensure a field-free environment. This is done by degaussing O1 and O2, and using an objective minilens as the principal focussing lens. Unfortunately, this has certain disadvantages. By necessity, the objective minilens is further from the sample and significantly weaker, which leads to a loss in resolution. Further, the coefficient of spherical aberration is larger for the minilens—often by several orders of magnitude [181]. Nevertheless, with suitable aberration correction, 1 nm resolution was proposed by Freitag *et al.* [181] and demonstrated conclusively in field-free STEM by McVitie *et al.* [182].

In the Fresnel mode of Lorentz microscopy, deflections are observed by defocusing the image plane to select a real object plane below the sample or a virtual object plane above the sample. These correspond to positive and negative defocus, Δf, respectively. Electrons deflected by neighbouring domains interfere at the positions of domain walls. This leads to alternating bright interference fringes and dark areas in the case of a multi-domain state [Fig. 4.6]. Since the Lorentz deflection angles are small, large values of defocus are required (> 1 mm is common). This consequently degrades the structural resolution present in the image. Further, the magnetic contrast becomes non-linear for large Δf.

4.3.2 Contrast in the Fresnel mode

In this section, we justify the way in which phase information from the transmitted wave appears in the intensity distribution of a Fresnel micrograph. In the absence of a coherence envelope and aperture cut-off, and assuming that the aberration function is slowly varying, we can expand the transfer function, χ, about $\mathbf{q} = 0$ to give

$$H(\mathbf{q}) = 1 - i\chi(\mathbf{q}), \text{ where } \chi(\mathbf{q}) = -\pi\Delta f \lambda \mathbf{q}^2. \tag{4.23}$$

The image wavefunction is then

$$\begin{aligned} g(\mathbf{r}) &= \mathcal{F}^{-1}\{H(\mathbf{q})\mathcal{F}\{\psi_t\}\} \\ &= \psi_t - i\mathcal{F}^{-1}\{\chi(\mathbf{q})\mathcal{F}\{\psi_t\}\}, \end{aligned} \tag{4.24}$$
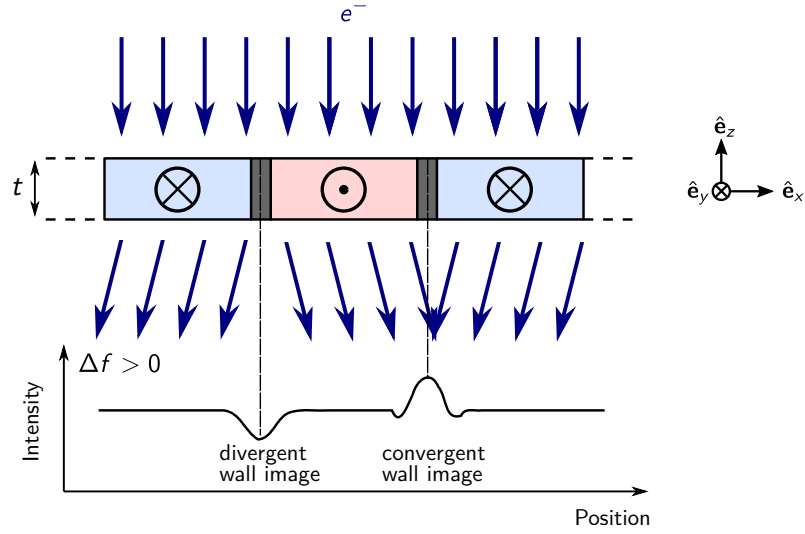
Figure 4.6: Schematic of imaging a multi-domain state using the Fresnel mode of Lorentz microscopy. Electrons are incident normal to the sample, here along the $-\hat{\mathbf{e}}_z$ direction. Three regions of uniform magnetisation are shown [alternating blue and red], separated by two 180° domain walls [grey]. The electrons are deflected by the integrated induction. We show here the case of positive defocus, in which a plane located Δf below the sample is imaged. This leads to interference patterns where the deflections converge and diverge. The contrast reverses for negative defocus, which images a virtual plane above the sample.

in terms of the transmitted wavefunction, $\psi_t(\mathbf{r})$. By expressing ψ_t as a Fourier decomposition, the image function can be simplified to

$$g(\mathbf{r}) = \psi_t(\mathbf{r}) - \frac{i}{4\pi}\lambda\Delta f\nabla^2\psi_t(\mathbf{r}).\tag{4.25}$$

The recorded signal is the intensity of g, namely,

$$I = |\psi_t|^2 + \frac{1}{16\pi^2}(\lambda\Delta f)^2(\nabla^2\psi_t)^2 - \frac{1}{4\pi}\lambda\Delta f\left[\psi_t^*(i\nabla^2\psi_t) + \psi_t(i\nabla^2\psi_t)^*\right].\tag{4.26}$$

Using eq. (4.5), we can write $\psi_t(\mathbf{r})$ as a phasor with amplitude, $a(\mathbf{r})$, and phase, $\phi(\mathbf{r})$. Neglecting terms in $(\Delta f\lambda)^2$, the intensity in a Fresnel image can be written as

$$I = a^2 - \frac{1}{2\pi}\lambda\Delta f\left[a^2\nabla^2\phi + 2a\nabla a\cdot\nabla\phi\right] + \mathcal{O}(\Delta f^2\lambda^2),\tag{4.27}$$

which agrees with the result derived in Ref. [183]. The quantity $|\psi_t|^2 = a^2$ is the intensity distribution of the in-focus image. When $\Delta f \neq 0$, extra contributions arise from those areas

where the Laplacian of the phase is non-zero, and in regions where there are simultaneous variations in both the amplitude and phase. Generally, variations in the amplitude, ∇a, can be associated with changes in the thickness of the material (which ultimately affects the transmission of the beam). For a uniform thin film, it is usually assumed that $\nabla a = 0$, and so the intensity becomes

$$ I \approx a^2 \left(1 - \frac{\lambda}{2\pi} \Delta f \nabla^2 \phi \right). \tag{4.28} $$

Finally, we note that the intensity is linear in Δf so that the contrast reverses going from under- to over-focus.

We illustrate this in the context of a single domain magnetic island. Here, variations in the amplitude are inevitable at the edges. A schematic is shown in Fig. 4.7(a) in which the magnetisation is orientated as $\mathbf{M} = M_s \hat{\mathbf{e}}_y$. Given results we report in Chapter 6, a Gaussian thickness profile is used for the island shape, with a full-width-half-maximum of 100 nm and a height of 3 nm [Fig. 4.7(b)]. In this test, we assume that the amplitude of the incident wavefront is attenuated by 10% on transmission through the material [Fig. 4.7(c)]. Taking the material parameters for cobalt ($M_S = 1.4$ MAm^{-1}, $V_0 = 21.5$ V) and 200 keV beam electrons, the phase profiles and their derivatives are calculated in Fig. 4.7(d)-(f). The magnetic phase profile has been approximated as a sigmoid; the electrostatic phase profile has been calculated according to eq. (4.22). Three components are drawn: that arising from electrostatic effects (ϕ_e, blue); that arising from magnetic effects (ϕ_m, orange); and the total phase ($\phi_e + \phi_m$, green). Both the first and second derivatives exhibit a defined asymmetry, which allow for the magnetic state to be determined even though the system is single domain. Even considering different attentuation coefficients and the full expression involving ∇a [Fig. 4.7(g)-(i)], there still exists an asymmetry in the defocused image arising from the magnetic configuration. We will return to this idea in Chapter 6.

4.3.3 Other methods of magnetic imaging

We briefly summarise the other Lorentz TEM techniques so as to justify our choice of the Fresnel mode in imaging the magnetic configuration of artificial spin ice arrays.
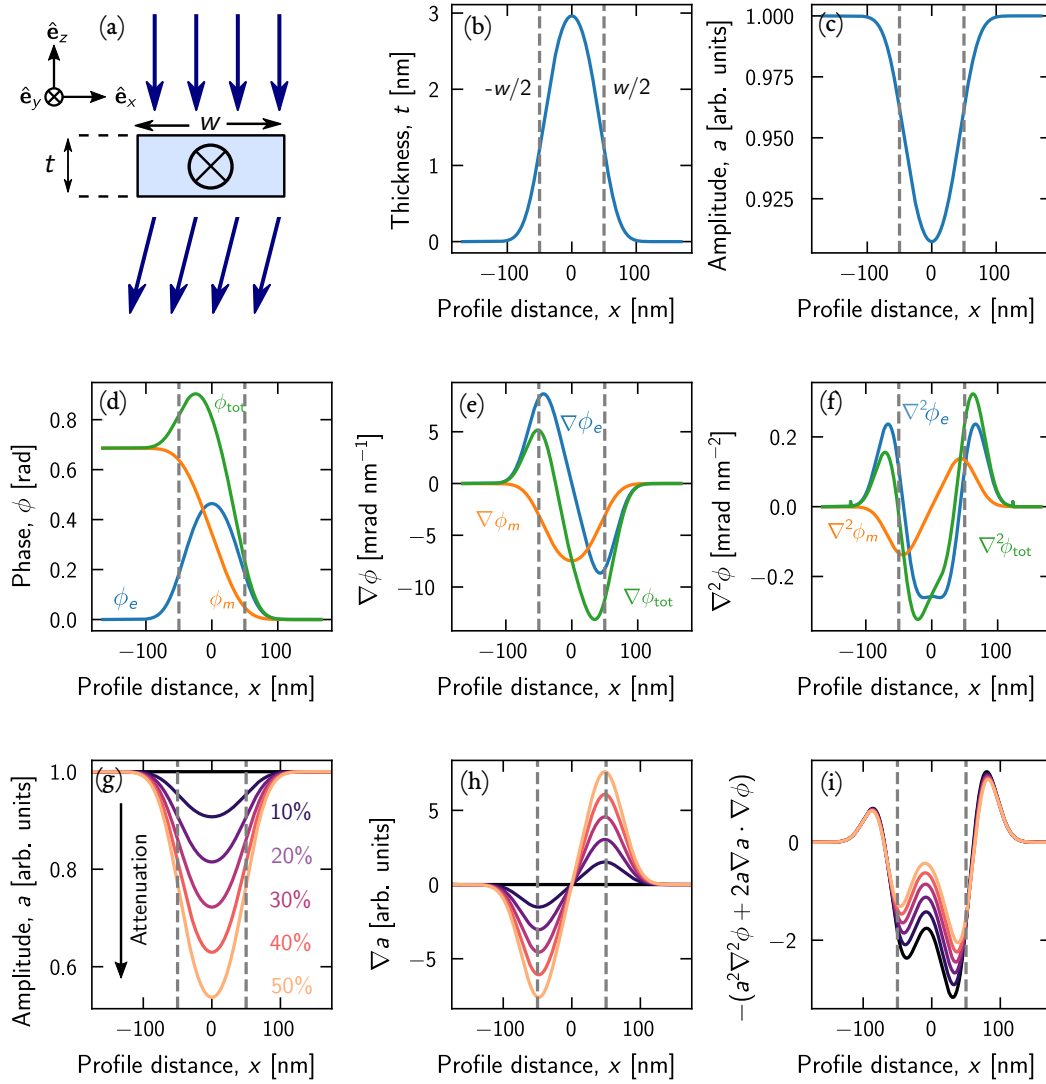
Figure 4.7: Simple model for the Fresnel contrast of a single domain magnetic island. (a) Single domain magnetic island of thickness, $t = 3$ nm, and width, $w = 100$ nm. The magnetic induction, **B**, is orientated along $\hat{\mathbf{e}}_y$. (b) A Gaussian thickness profile for the island, matching those deposited by FEBID. (c) The incident wave is attenuated on transmission through the islands. (d) Phase profiles. The electrostatic component (blue) is calculated as described in the text, based on a mean inner potential, $V_0 = 21.5$ eV. The magnetic phase (orange) is approximated as a hyperbolic tangent, with saturation magnetisation, $M_S = 1.4$ MAm^{-1}, The total phase profile, $\phi_m + \phi_e$, is shown in green. The first and second derivatives of these phase profiles are given in (e) and (f), respectively. In each case, the total phase component exhibits an asymmetry. (g) Different attenuation coefficients for the amplitude lead to different (h) ∇a profiles. (i) Nonetheless, there exists still an asymmetry when considering the full expression for the intensity in a Fresnel image. In all panels, the vertical lines delineate the extent of the island.

4.3.3.1 Foucault mode and low-angle diffraction. In Foucault mode, an aperture is placed in the back focal plane of the objective minilens. This is positioned with the intention of selecting a particular magnetic deflection. Only those domains which give rise to a deflection passed by the aperture appear bright in the final image. Magnetic domains with an opposite induction have their deflections blocked and appear dark. Like Fresnel, this is usually not a quantative technique (though certain modifications using a phase shifting aperture can render it so [184]). There is a related approach, low-angle diffraction, in which the back focal plane of the objective minilens is imaged directly [185]. Since the Lorentz deflection angles are small, this requires a very large camera length (> 100 m). In this technique, the diffraction pattern stems from scattering across the entirety of the illuminated area and so the information is quantitative but not spatially resolved.

Related to this, we note that neither a single Lorentz micrograph nor a standard Foucault image provides quantitative measurement of the magnetostatic phase (unless some simplifying assumptions are made). Teague [186] and, separately, van Dyck [187] outlined an approach based on the transport of intensity equation,

$$\nabla \cdot \left(a \nabla \phi \right) = \frac{2\pi}{\lambda} \frac{\partial I}{\partial z},$$

(4.29)

from which the total phase can be reconstructed using a series of images taken at different defoci. From this, the magnetic induction integrated over the thickness of the film can be obtained [188]. This has been applied to various magnetic systems including imaging reversal processes in square artificial spin ice [26].

4.3.3.2 Differential phase contrast. Differential phase contrast (DPC) is a STEM technique in which the individual deflection angles are mapped as a function of probe position (first discussed generally in [189] and subsequently in the context of magnetic specimens in [190]). From these angles, $\beta(\mathbf{r})$, the integrated induction is found by application of eq. (4.14). Since it is a STEM technique, this offers higher resolution than Fresnel imaging [191] at the expense of speed. Care must be taken when analysing DPC on polycrystalline magnetic samples as diffraction contrast may also arise from grains.

4.3.3.3 Electron holography. In electron holography, the beam transmitted through the sample is recombined with a reference beam, which has not interacted with the specimen, in order to generate an interference pattern. This is performed using a biprism to recombine the two displaced beams into a hologram. Electron holography was originally proposed by Gabor as a possible way to surmount lens aberrations [192, 193].

The work reported in this thesis uses the Fresnel mode exclusively. This can be justified on two counts. First, we do not need to map the integrated induction quantitatively; rather, we are interested in assigning a macrospin orientation to every island within an artificial spin ice array. Second, Fresnel imaging is a better option for dynamical measurements of transient processes, especially when combined with the high frame-rate of pixelated detectors such as the Medipix3 [194, 195].

4.4 | Focused electron beam induced deposition

This section discusses sample fabrication using focused electron beam induced deposition, with a particular application to writing artificial spin ice arrays. Many good review articles exist in this area, including those by van Dorp [196], by de Teresa *et al.* [197] and by Huth *et al.* [198].

4.4.1 Rationale

Broadly speaking, nano-deposition techniques can be separated into top-down and bottom-up approaches. In the top-down approach, structures are fabricated from a larger block of material through an etching or deposition process. Examples of this include electron beam [199], x-ray [200], or photo-lithography [201]. For the most part, these are confined to the plane, although recent advances in two-photon lithography have allowed nanowire lattices to be realised in three-dimensions through a scaffolding process [202, 203] or via chemical fluid deposition [204]. By contrast, a bottom-up approach refers to constructing aggregate structures from atomic or molecular components via, say, self-assembly.

In this vein, focused electron beam induced deposition (FEBID) can be considered a top-down approach which provides single-step, nano-scale printing—3D printers for the nano-world, as it were. In FEBID, a volatile precursor gas—composed of the target material bonded, usually, to some hydrocarbon ligands—is injected into an evacuated chamber. The precursor molecules are adsorbed onto the substrate surface[9]. There, the molecules diffuse and, after a characteristic residence time, escape. A focused electron beam is rastered across the surface. This cracks the precursor molecules into volatile and non-volatile components. Volatile components are pumped away, while the non-volatile part adheres to the surface. This is shown in Fig. 4.8.

Perhaps the first—inadvertent—description of FEBID was given in 1934 by Stewart [206], who observed the build-up of an insulating film on surfaces following prolonged electron or 'canal-ray'[10] bombardment. Even at the time, this was correctly attributed to polymerisation of residual organic vapours left in the reaction chamber. Ordinarily, this contamination can be a significant problem in both SEM and TEM imaging as it leads to the continuous growth of films or needles.

Unlike, say, electron beam lithography, FEBID does not require a physical mask or template for etching. As such, it is similar to chemical vapour deposition [207], except that dissociation is promoted directly by the action of the beam rather than through heat, and that the beam trajectory defines those areas where deposition is to occur. The dissociation occurs in the immediate vicinity of the beam and so high-resolution patterns can be fabricated. Previous work has achieved sub-10 nm structures in an SEM [208]. On smaller length scales, STEM techniques have been used to realise structures below 1 nm, though reproducibility of the volume and location of the deposit proves difficult [209, 210].

4.4.2 Interactions

In EBID, we distinguish between two classes of interaction: those between precursor molecules and the substrate; and those between precursor molecules and the electron beam.

---

[9] This is referred to in some texts as physisorption [205], which refers to weak surface binding through van der Waals interactions.

[10] That is, positive ions.

(a)

gas injection

focused e⁻ beam

Side-view

precursor

volatile by-product

adsorption →

impurities

diffusion

Substrate

deposition through dissociation (Co)

(b)

Top-down view

e.g. serpentine rastering

pitch
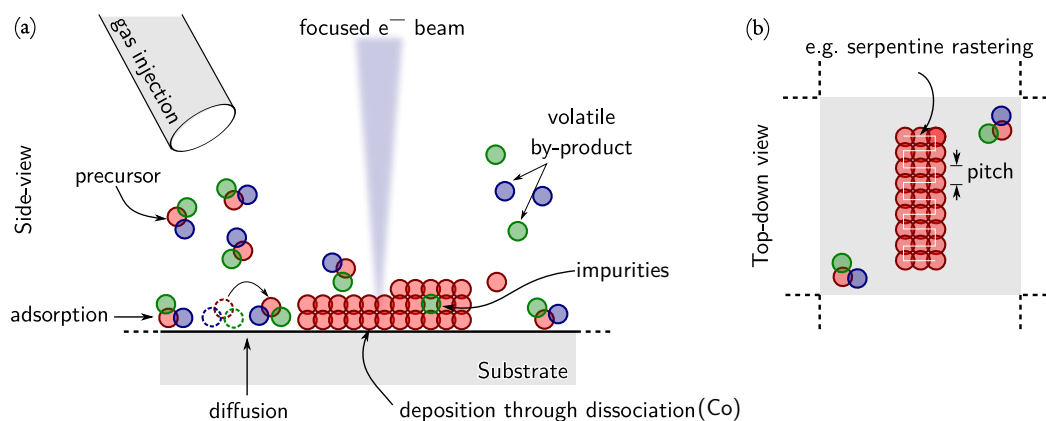
Figure 4.8: Schematic of the FEBID process. (a) An organo-metallic precursor gas is injected into the chamber. Precursor molecules bind lightly to the substrate surface. A targeted, high-energy electron beam is used to dissociate the precursor molecules. Deposition of the metal occurs in the area of the electron beam, while the volatile ligands are removed. (b) Example of serpentine rastering. After one pass is completed, the process is repeated to build up the deposition.

When the precursor is injected into the chamber, molecules are able to bind to the surface through weak van der Waals interactions. Diffusion across the surface occurs via thermal vibrations. After a characteristic residence time, τ, molecules desorb from the surface. Clearly, a longer residence time increases the probability that precursor molecules can be broken down by the electron beam and thus increases the yield [211, 212]. At the same time however, it leads to greater contamination within deposits as residual hydrocarbons also remain on the surface longer and are incorporated into the structures [212]. The residence time is not an intrinsic parameter but depends on environmental conditions during each deposition [212] and the nature of the precursor itself. Utke et al. discuss how the residence time often differs from predictions made by classical transition state theory, but can be estimated for a given set-up from steady-state deposition measurements [213].

As discussed in Sec. 4.2.2, secondary electrons are generated through inelastic processes when the incident beam interacts with the substrate. These secondary electrons can be re-emitted in the backwards direction, and have typical energies < 50 eV. Precursors tend to possess a peak in their dissociation cross-sections around this energy, though the exact reaction

mechanism can be quite complicated. Thorman *et al.* consider four related pathways[II] by which common precursors are broken down, and discuss the extent to which the different channels are enabled by electrons of different energies [214]. Irrespective of the pathway, however, the common factor is the capture of an electron, which then breaks bonds between the metal and its its ligands.

The set-up used in this thesis is a dual column Helios Plasma Focused Ion Beam instrument, with separate cobalt and iron gas injector systems (in the form of $Co_2(CO)_8$ and $Fe_2(CO)_9$ precursors). The cobalt precursor, $Co_2(CO)_8$, is perhaps the most commonly used magnetic precursor [197]. It possesses a relatively low spontaneous dissociation temperature, 100°C— equivalent to about 33 meV [215]. For comparison, secondary electrons typically have energies less than 50 eV.

4.4.3   Deposition purity and rate

The purity of FEBID-deposited structures varies. In general, incomplete dissociation of the precursor complex leaves hydrocarbon impurities in the deposition. There are several methods that attempt to mitigate this, such as increasing the temperature of the reaction vessel [216]. Co purity greater than 90% has been reported in structures deposited using $Co_2(CO)_8$ for both high [217] and low beam currents [218].

In terms of deposition rates, Fowlkes *et al.*, among others, discriminate between two deposition regimes: reaction-rate-limited, and mass-transport limited [219]. In the reaction-rate-limited regime, the deposition rate increases linearly with electron dose. This is the situation where the flux of gas molecules is greater than the flux of secondary electrons available to cause dissociation. In the mass-transport-limited regime by contrast, the deposition is limited by two factors: the rate at which precursor molecules are adsorbing onto the surface, and the rate at which they can diffuse to the deposition site. For high electron flux, the precursor can become depleted in the centre of patterns. This can lead to a hollowing effect [220]. In this thesis, we are interested in making very thin, planar samples, and so we will work mainly in the reaction-rate-limited regime. Fig. 4.9 shows the continuum between these two regimes. In the

---

[II]For completeness, these are dissociative electron attachment, neutral dissociation, dissociative ionisation, and dipolar dissociation.
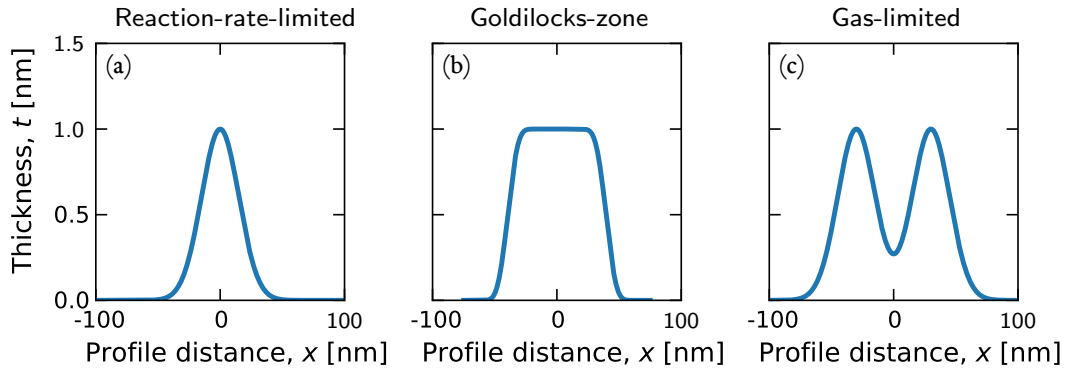
Figure 4.9: Growth regimes in FEBID. These vary between (a) reaction-rate-limited, where an increase in electrons brings about a linear increase in deposition volume and (c) gas limited, where the precursor can become depleted in the centre of the pattern. Panel (b) forms a sweet-spot between these two regimes. Curves loosely based on the model given in [219] for a target thickness of 1 nm.

reaction-rate-limited regime, approximately Gaussian profiles are formed [Fig. 4.9(a)], while in the mass-limited regime, the pattern becomes thinner towards its centre [Fig. 4.9(c)].

4.4.4 FEBID and artificial spin ice

In most studies, arrays of ASI are normally written using conventional electron beam lithography. Some recent work has investigated the use of FEBID as a fabrication mechanism, though it has been limited to individual islands or small clusters. For example, Keller *et al.* use a heteronuclear precursor to produce wire-frame cuboids of alloyed cobalt and iron [221]. Electron energy loss spectroscopy suggested purities in excess of 80%, and that the deposits consisted of a bcc Co/Fe phase intermixed with a spinel, with a grain size of about 5 nm [222]. In a series of studies [223, 224, 225], Pohlit *et al.* performed magnetometry measurement on single and multiple cobalt nanoelements, and observed a decrease in coercivity with temperature. Outwith artificial spin ice, FEBID has been used to fabricate various nanowire geometries in two and three dimensions [226, 227].

4.4.5 Summary

This chapter has focused on the particular aspects of TEM and FEBID which provide the indispensable experimental underpinning of this thesis. The operating principles of transmission electron microscopy were described. The Fresnel mode of Lorentz microscopy was outlined. A simple model for the Fresnel contrast expected for a single domain magnetic island was given. Applying a similar process to every island within arrays of artificial spin ice allows us to probe the exact microstate. Finally, focused electron beam induced deposition was introduced. We return to this technique in Chapter 6 in order to fabricate thermally active artificial spin ice.

5

Thermal processes in rotated artificial spin ice

5.1 | Introduction

In this chapter, we introduce a new form of artificial spin ice (ASI), which is created by rotating the islands in the canonical square ice through an angle, θ. For angles near to $45°$, a highly degenerate system is formed that exhibits ferromagnetism even though not all the spins are collinear. This stems from the mixing of the spin and spatial degrees of freedom in the dipolar interaction.

In Sec. 5.2, this new geometry is described; particular attention is paid to the $\theta = 45°$ case, which we refer to as *pinwheel* ice. In Sec. 5.3, we show that, irrespective of the underlying model, this rotation leads to a weakening of near-neighbour interactions, a coupling to further-out spins, and a bunching of energy levels. In Sec. 5.4, the equations underlying the behaviour of a small system are set out. Feedback-optimised [228, 229] parallel tempering [150] Monte Carlo is used to extract thermodynamic observables for large arrays. These show an intriguing

phase transition; one driven not by temperature but by the geometrical constraints of the tiling. These constraints force a ferromagnetic-ordered state for geometries close to the pinwheel lattice. In Sec. 5.5, the critical exponents are extracted as a function of angle. It is found that these systems belong to the 2D Ising universality class, up to corrections to scaling. Finally, in Sec. 5.6, we focus on the ground state configurations of pinwheel arrays, and discuss how array boundary and size provide an effective anisotropy by which the macro-domains in the ferromagnetic state can be tuned.

5.1.1 Attribution

The majority of the work in this chapter can be found in Ref. [1]. Alongside results discussed in Chapter 7, the finite-size scaling analysis and comments on the nature of the phase transition in this chapter form a separate paper, which is in preparation. The pinwheel geometry was originally conceived by RLS and FSN. RM investigated the behaviour of the critical temperature with rotation angle, connected it to the transitions envisaged by Landau and Binder [230], and drew the analogy of pinwheel arrays with naturally occurring ferromagnetic media. The manuscript was written by RM and me, with comments from the other authors. RLS and SMcV supervised the work. The remainder of the work reported here is my own.

The results presented in this chapter and, where specified above, in Ref. [1] were generated using JASI, a Julia simulation package I developed for Monte Carlo simulations of artificial spin ice systems. This package includes support for both Metropolis-Hastings and parallel tempering algorithms; is extensible to most common ASI lattices; and is well-optimised for the analysis of large ($> 10^4$ spins) systems in parallel on CPUs and, with some caveats, GPUs. Documentation and installation instructions for this package are available in an online repository [6].

5.2 | A class of geometries

Our base structure, the canonical square ice tiling [Fig. 5.1, left and right columns] is formed by two interleaved, orthogonal sublattices of uniformly aligned nanomagnets. From this tiling we obtain a continuum of geometries by rotating each nanomagnet about its centre through

an angle, θ. We choose the zero of this rotation, $\theta = 0°$, to be square ice, and term the $\theta = 45°$ geometry "pinwheel" ice (variously also "chiral" [180, 231] or "tilted square" [232] ice). The lattice constant, a, is taken as the distance between second-nearest neighbour islands as shown. For the case of finite arrays, different array edges are possible. For $\theta = 0°$ square ice, these are commonly termed 'open edge' (i.e. with dangling spins) and 'closed edge' (in which most edge spins have a partial complement of neighbours) [233]. These are shown in the left and right columns of Fig. 5.1, respectively. For $\theta = 45°$ pinwheel ice, we christen the corresponding terminations 'diamond edge' and 'lucky knot edge' [Fig. 5.1(a) and (b), middle column, respectively] [1].[1]

As with square ice, it is possible classify four island sub-units—*vertices*—into types such that configurations within a given type are degenerate. The structures of these vertices are emphasised in black for square and pinwheel ice in Fig. 5.1. In passing, we note that a pinwheel vertex does not involve four islands meeting head-on like in square ice and so "unit" would perhaps be a more appropriate description. As we want to compare types from square to pinwheel, we simply refer to them all as vertices.

Rotating each island in a vertex changes neither its type nor its ordering so that, say, a T_2 vertex carries a net moment irrespective of rotation angle. For any θ then, we are able to provide an equivalent description in terms of a lattice of interacting vertices [76], rather than the full ensemble of island spins. [2] As a reminder from Chapter 2, T_1 and T_4 vertices carry no net moment. In this regard, they are antiferromagnetic (AFM) vertices, as the island moments align antiparallel within each sublattice. Since T_2 and T_3 vertices carry a net moment, we consider them ferromagnetic (FM) vertices. For any given θ, the ordering within an array may be characterised in terms of its fractional population of vertex types, $n_i = n_i(\theta, T)$. The populations are not independent as they satisfy

$$\langle n_1 \rangle + \langle n_2 \rangle + \langle n_3 \rangle + \langle n_4 \rangle = 1. \tag{5.1}$$

---

[1]The latter appellation, the 'lucky knot edge', stems from its resemblance to a motif found in Chinese art and handicraft.

[2]Nothing is lost in this description. We do not coarse-grain [234] to translate the spin configuration into the vertex picture. In fact, a spin configuration is *over-determined* by specifying the location and type of each vertex, as a spin in the bulk of the array belongs to at least two vertices.

The number and locations of vertices change with rotation angle (compare the red boxes from L-R in Fig. 5.1), and so populations are always normalised with respect to the total number of vertices within an array. In Fig. 5.2, we depict the 16 possible pinwheel vertices in terms of their spin configuration, net moment, and magnetic charge; an analogous figure for square ice appears in Chapter 2, Fig. 2.9.
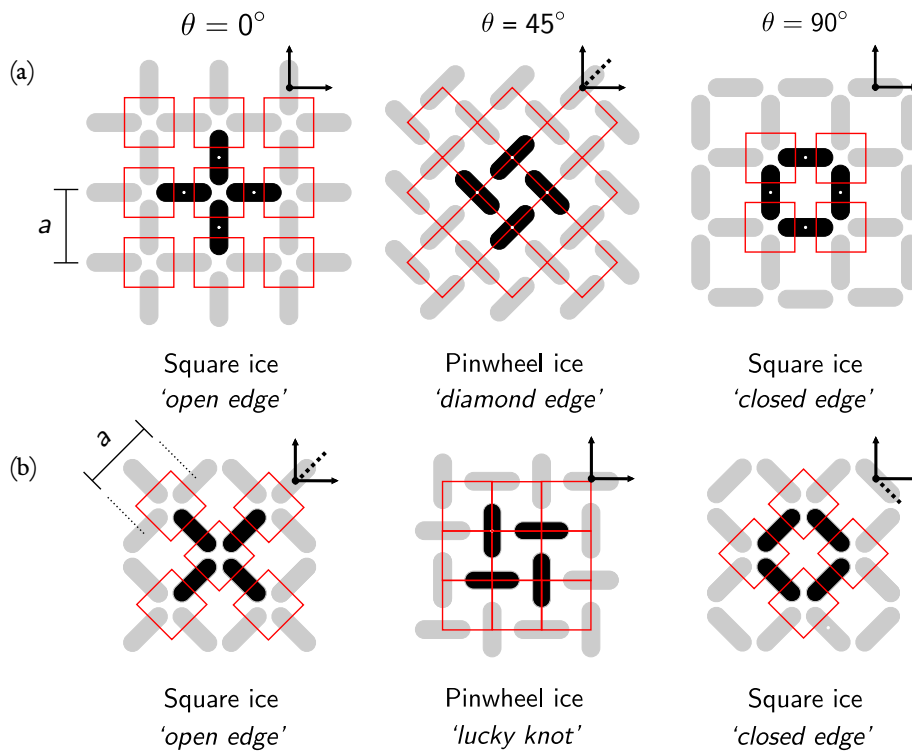
Figure 5.1: A continuum of geometries defined by rotation angle. The square ice tiling [left column] is deformed by rotating each angle about its centre through θ. The $\theta = 45°$ case is termed 'pinwheel' ice [middle column]. Rotating islands in pinwheel ice through 45° recovers square ice [right column]. Panels (a) and (b) depict two sequences of array rotations with different edge terminations (open and closed edged in square ice; diamond and lucky knot edge in pinwheel). The lattice constant, a, is taken as the distance between the centre of second-nearest neighbours. Common Cartesian axes are shown in each image. The location of vertices are marked in red. Comparing the two square ice patterns, vertex locations in the $\theta = 90°$ are offset by $a/2$ in the x- and y-directions to the $\theta = 0°$ case.
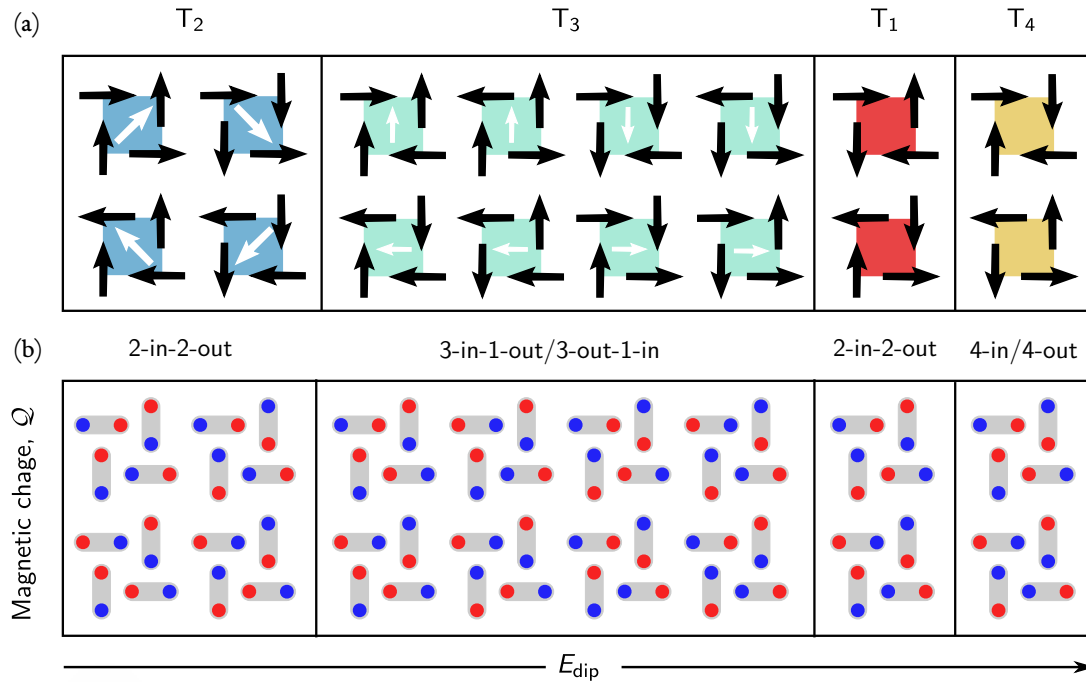
Figure 5.2: The sixteen vertices in pinwheel ice in terms of their (a) spin configuration, represented by the black arrows; and (b) magnetic charge, $\mathcal{Q}$, in terms of North and South poles (red and blue dots, respectively). Vertices are represented by coloured squares. A consistent colour coding is used throughout this work. This allows for discrimination when arrays are displayed as vertex maps. All vertices within a given type are degenerate. For T_2 and T_3, the net moment and magnitude are indicated by the white arrow. Types are sorted L-R in terms of increasing dipolar energy—see Sec. 5.4.

5.3 | Tuning interactions

5.3.1 Modelling spins

In this subsection, we justify the model used to uncover the effect of island rotation on ordering. In fact, we will return repeatedly to this model throughout the remainder of this thesis.

First, we assume that every island is a single domain, with an associated Ising-like spin. This reflects the strong shape anisotropy for the standard 'stadium-shaped' island, which constrains it to point approximately along the long axis. This has been confirmed experimentally for different island aspect ratios using a variety of techniques including magnetic force microscopy [8, 235, 236], Lorentz transmission electron microscopy [25], and x-ray photoemission electron

microscopy [237]. The collective behaviour of many such islands is determined by their mutual interactions, which can be represented in several ways.

5.3.1.1 Point dipole approximation. The simplest is to approximate each island by a point magnetic dipole located at its centre, such that the system is governed by the Hamiltonian,

$$\mathcal{H}_{\text{dip}} = \mathcal{D} \sum_{i \neq j} s_i s_j \left[\frac{\boldsymbol{\sigma}_i \cdot \boldsymbol{\sigma}_j}{r_{ij}^3} - \frac{3(\boldsymbol{\sigma}_i \cdot \mathbf{r}_{ij})(\boldsymbol{\sigma}_j \cdot \mathbf{r}_{ij})}{r_{ij}^5} \right], \tag{5.2}$$

where $\mathcal{D} = \mu_0 (M_s V)^2 / (4\pi a^3)$ provides a characteristic energy scale, and $\mathbf{r}_{ij} = \mathbf{r}_j - \mathbf{r}_i$ is a vector connecting the position of spin i to spin j. The spin at site i has a magnetic moment, $\mathbf{s}_i = s_i \boldsymbol{\sigma}_i$, with $s_i = \pm 1$ the polarity of the spin, and $\boldsymbol{\sigma}_i$ a unit vector parallel to the long axis of island i. The orientation of $\boldsymbol{\sigma}_i$ is dependent on the island rotation angle, θ, and the sublattice to which island i belongs. For example, using the coordinate system indicated in Fig. 5.1(a), the two sublattices are parallel to the unit directions

$$\frac{1}{\sqrt{2}} \begin{pmatrix} \cos\theta \\ \sin\theta \end{pmatrix} \text{ and } \frac{1}{\sqrt{2}} \begin{pmatrix} -\cos\theta \\ \sin\theta \end{pmatrix}. \tag{5.3}$$

Equation (5.2) is valid only in the far field, i.e. in situations where the separation of the islands is much greater than their physical extent. In general, this is not the case in ASI where islands are placed close together to promote strong coupling. For example, Rougemaille *et al.* show that it is necessary to include an extra nearest-neighbour exchange when seeking agreement between experiments on kagome lattices and models based on point magnetic dipoles [238]. This isotropic term reflects the effect of the physical extent of the nanomagnets on the strong coupling between first-nearest-neighbours in the kagome system. Nonetheless, this simple approach has been shown to accord well with physical results in square ASI, including those obtained under the application of field [8] and temperature [79].

5.3.1.2 Charged dumbbell model. An alternative approach—first applied by Castelnovo *et al.* in the context of bulk pyrochlores [74]—is to approximate each island of length L as a *charged dumbbell* in which monopoles of equal but opposite polarity sit at either end. This model introduces a free parameter, L/a, which plays the role of an inverse packing fraction: large L/a means that islands are spaced close together; small L/a means that the islands are

well separated. In analysis of square ASI, L/a has been shown to broaden the temperature range over which ice-rule-obeying T_1 and T_2 vertices form. [239] In the charged dumbbell picture, the energy of a configuration is simply the sum of pairwise Coulombic interactions of magnetic charges, namely

$$V(\mathbf{r}_{ij}) = \begin{cases} \mathcal{K} \dfrac{q_i q_j}{r_{ij}} & \text{if } i \neq j \\ \dfrac{\nu_0 q_i^2}{2} & \text{if } i = j, \end{cases} \tag{5.4}$$

where the indices now label charges, q_i, rather than islands, and $\mathcal{K} = \mu_0/4\pi$ is the analogue of the dipolar constant, $\mathcal{D}$. The finite self-energy, $\nu_0/2$, is required to reproduce the correct nearest-neighbour interaction. We would expect that for $L \ll a$, we recover the dipolar Hamiltonian and, indeed, Ref. [74] demonstrates that eq. (5.4) is functionally the same, up to small corrections which vanish with r^{-5}.

5.3.2 The effect of island rotation on interaction strengths

We show the energies of nearest-neighbour ($1nn$), second-nearest-neighbour ($2nn$) and third-nearest-neighbour ($3nn$) pairs as a function of θ for both the point dipole model [Fig. 5.3(a)] and the charged dumbbell model [Fig. 5.3(b)]. Broadly speaking, interaction energies above zero correspond to ferromagnetic alignment of pairs, while those below correspond to anti-ferromagnetic alignment. We take $L/a = 2/3$ for the charged dumbbell model, consistent with the experimental sizes used in Chapter 6. The following statements apply equally well to both approaches.

Square ASI is a system dominated principally by nearest-neighbour interactions: the $1nn$ interaction is maximal at $\theta = 0°$ and decreases to zero at $\theta = 45°$. A similar behaviour is observed for $2nn$ pairs, which reduce in magnitude around $\theta = 45°$. In contrast, the $3nn$ interaction increases with rotation angle and peaks at $\theta = 45°$. Indeed, for pinwheel ice, the strongest interaction is that between $3nn$ pairs although all couplings remain of comparable size within a radius of approximately $4a$.

We explain these two limiting cases heuristically in Fig. 5.3(c). Favourable, low-energy configurations are those in which pairs tend to align 'head-to-tail'. In doing so, their stray field reinforces the magnetic structure or, equivalently, closes flux loops. For square ice, assigning

favourable configurations within a vertex can be done by inspection. It is impossible, however, to define favourable and unfavourable alignments for adjacent islands in pinwheel spin ice. All four configurations for a two-island T-shape are degenerate.

Excellent agreement is observed between the dipolar and charged dumbbell models. This is expected: previous work has shown that these models agree on the qualitative ordering of energy levels in ASI [76]. In passing, we note that it is possible to estimate interaction energies within a full micromagnetic framework by, e.g., simulating isolated pairs of $1nn$ islands and accounting suitably for their self-energy. This produces behaviour similar to that described in Fig. 5.3(a,b) and is discussed in detail in the supplementary to [1]. As proof, Fig. 5.4 depicts the evolution of the nearest-neighbour couplings with angle for islands of dimension 300 nm $\times$ 100 nm $\times$ 3 nm, as calculated using MUMAX3 [98]. Typical material parameters for cobalt are assumed: $M_S = 1.4\,\mathrm{MAm^{-1}}$, with an exchange constant, $A_\mathrm{ex} = 21\,\mathrm{pJm^{-1}}$. The Gilbert damping constant, α, was set to 0.5 to hasten convergence.

Broadly speaking, the curves match those in Fig. 5.3, although the micromagnetic simulations predict that square ice is even more strongly coupled than either the point dipole or charged dumbbell models would suggest. The difference arises primarily from the fact that micromagnetism simulates the true physical extent of the islands. In this framework, the local magnetic moment within each island does not lie perfectly parallel everywhere to the long axis. As discussed in Chapter 2, there exists a competition between the exchange and magnetostatic energies. The magnetisation at either end of an island is able to cant so as to minimise the build-up of magnetic surface charge. In turn, this adjusts the stray field distribution, which couples neighbouring islands. We will return to these ideas in Chapters. 6 and 7.

Nonetheless, the key point is that the relative change in strength of various classes of coupling occurs irrespective of the model. All suggest that for angles around 45° further-out pairs of neighbours interact more strongly than nearby ones—a reflection of the relative separation of magnetic charges. It should be noted that while we treat θ as a continuous variable in this analysis, islands are not free to rotate. Once a geometry has been fabricated, the interactions are determined completely.

To summarise: in square ice, the interactions are 'front-loaded' with nearby pairs of islands interacting more strongly. In pinwheel ice, the nearest-neighbour interaction is completely

suppressed and there exists a gap in the interaction spectrum. The energetics for $\theta = 45°$ is determined by spins which are well-separated, peaking at $3nn$ though any non-zero interactions tend to be of a similar size. In this sense, each island in pinwheel ice 'sees' out to a more distant magnetic horizon compared with square ice. The angle, θ, acts as a proxy for controlling interactions between classes of neighbouring spins, and weakens the nearest-neighbour couplings which dominate the square lattice.

Both charged dumbbells and point dipole prove satisfactory at capturing the key behaviour of this island rotation. From now on, we will tend to model our islands as point dipoles and compare the results with those obtained from micromagnetic simulations of smaller, simpler lattices.
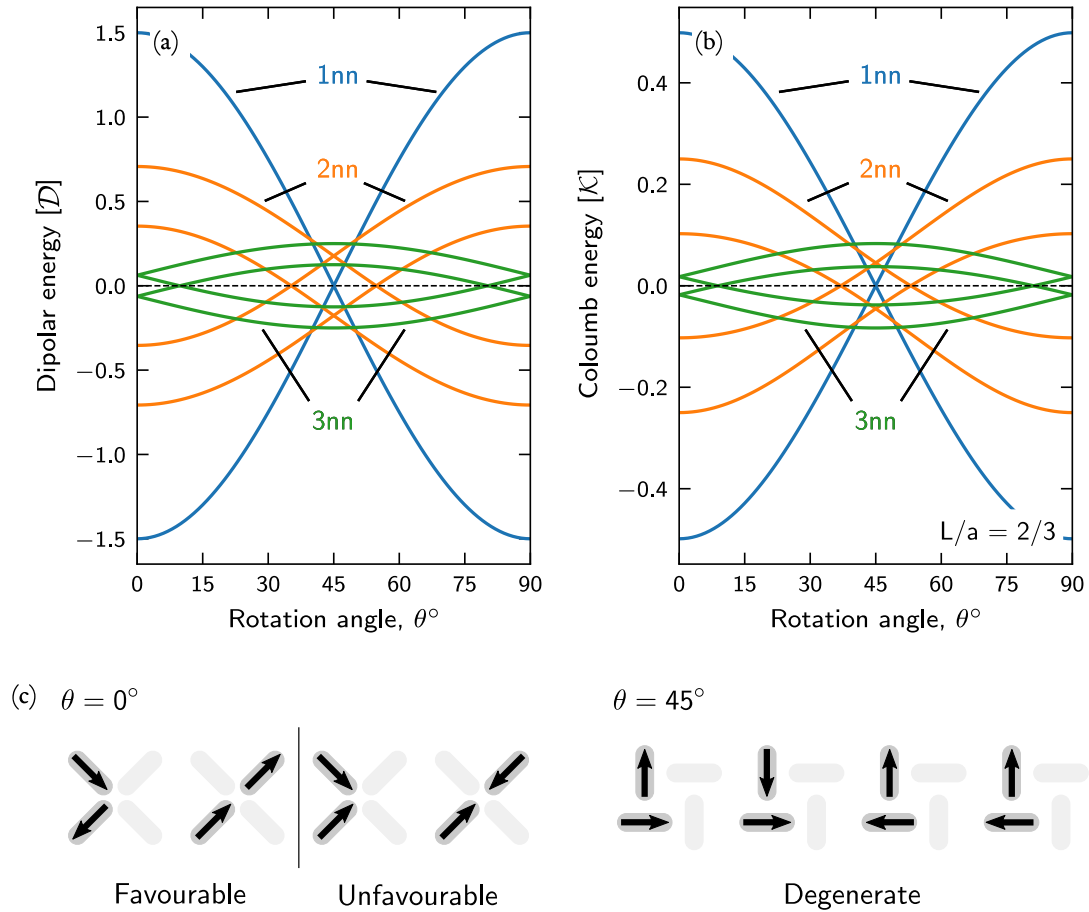
Figure 5.3: Interaction energy as a function of θ for $1nn$, $2nn$, and $3nn$ pairs in (a) the point dipole model, and (b) the charged dumbbell picture. Coupling energies above zero are indicative of ferromagnetic alignment of pairs; those below promote antiferromagnetic alignment of pairs. As the rotation angle is increased from $0°$, we see a weakening the of near-neighbour interactions and a strengthening of the coupling to further-out neighbours. This is observed under both approaches. (c) Defining favourable and unfavourable spin alignments within a vertex is simple in square ice [left panel], but the two island T-shape is four-fold degenerate in pinwheel spin ice [right panel].
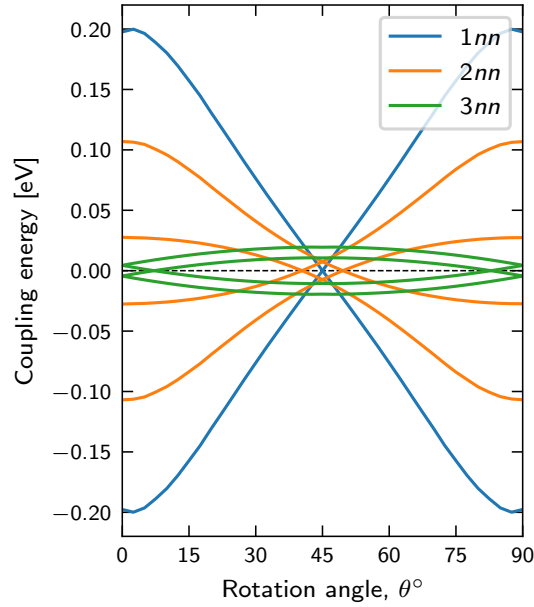
Figure 5.4: Interaction energy as a function of θ for $1nn$, $2nn$, and $3nn$ pairs calculated using MUMAX3. The simulated dimensions of the nanomagnets match those used in Chapter 6. Typical material parameters for cobalt are assumed.

5.4 | Thermal processes

5.4.1 A single vertex

First, let us consider the effect of rotating each island in a single vertex. As we shall see, this shows qualitatively the same behaviour as larger arrays and has the advantage that exact calculations are tractable. Working within the dipole approximation, it is easy enough to show that the energy, E_i, of a vertex of type, T_i, depends on θ through

$$E_1(\theta) = \frac{\mathcal{D}}{8\sqrt{2}}\left[\sqrt{2} + 3(\sqrt{2} - 8)\cos 2\theta\right];$$ (5.5a)

$$E_2(\theta) = \frac{\mathcal{D}}{8\sqrt{2}}\left[-\sqrt{2}(1 + 3\cos 2\theta)\right];$$ (5.5b)

$$E_3(\theta) = 0;$$ (5.5c)

$$E_4(\theta) = \frac{\mathcal{D}}{8\sqrt{2}}\left[\sqrt{2} + 3(\sqrt{2} + 8)\cos 2\theta\right].$$ (5.5d)

These are depicted in Fig. 5.5(a). For angles near to $0°$, the ground state is an antiferromagnetic T_1 vertex. In an asymmetric region about $45°$ however, the lowest energy state is a ferromag-

netic T_2 vertex. For a single vertex, this region of ferromagnetism corresponds approximately to $\theta \in [39.4°, 47.5°]$. [3] In square ice, the types possess four, well-separated energy levels whereas, for geometries similar to pinwheel, the energy levels are nearly degenerate—relatively speaking. This follows from the observation that at $\theta = 45°$, all interactions within a region of extent $4a$ are of a similar magnitude.

Given the limited number of configurations, it is possible to construct an analytic expression for the partition function and, hence, for every thermodynamic variable. In Fig. 5.5(b), we choose to show the residual entropy,

$$S_0 = \lim_{T \to 0} \frac{\partial F}{\partial T}, \tag{5.6}$$

where $F = -k_B T \log Z$ is the free energy. That this quantity is never zero is the hallmark of a frustrated system (which, by definition, has multiple ground states). Further, we note that the residual entropy is discontinuous: it jumps at those critical angles which mark the onset of ferromagnetic ordering. This suggests some form of phase—or, rather, vertex—coexistence through which the system supports both ferromagnetic and antiferromagnetic ordering.

5.4.2 Monte Carlo simulations

As discussed in Chapter 3, phase transitions are defined in the thermodynamic limit and so we now consider larger arrays to show that this preference for ferromagnetic T_2 ordering near to 45° is not a finite-size artefact. To do this, we implement parallel tempering (PT) Monte Carlo (MC) [150] to obtain expectation values for the Hamiltonian given in eq. (5.2).

5.4.2.1 Efficient selection of temperatures for parallel tempering Monte Carlo. As a reminder: in PT Monte Carlo, M independent replicas of the system are simulated at different temperatures in the set $\{T_1, T_2...T_M\}$. After performing a fixed number of MC moves

---

[3]Actually, we can show that the lower and upper critical angles are exactly

$$\frac{1}{2} \arccos \left[-\frac{\sqrt{2}}{3(\mp 4 + \sqrt{2})} \right].$$
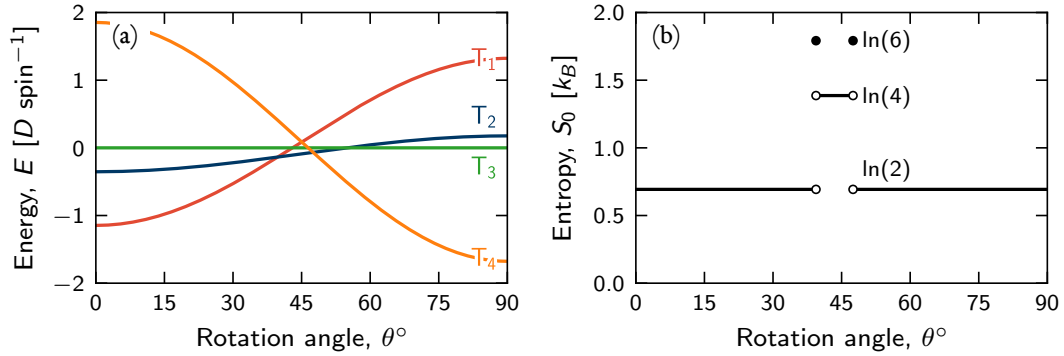
Figure 5.5: (a) Energy levels of a single vertex are plotted as a function of rotation angle, θ. Between 39.4° and 47.5°, the lowest energy state is T_2-ordered. (b) Discontinuities in the residual entropy, S_0, suggest there is AFM/FM phase coexistence at these critical angles. In general, the entropy is proportional to $\ln \Omega$, where Ω is the number of microstates. The number of ground states is indicated explicitly.

within each replica, swaps between replicas at adjacent temperatures, T_i and T_{i+1}, are proposed. These are accepted with probability,

$$\mathcal{P}(E_i, T_i \leftrightarrow E_{i+1}, T_{i+1}) = \min(1, e^{\Delta\beta_i \Delta E_i}), \tag{5.7}$$

where $\Delta\beta_i = \beta_{i+1} - \beta_i$ and $\Delta E_i = E_{i+1} - E_i$. In this way, replicas that become jammed in metastable states at low temperatures (where the autocorrelation time is large), are able to diffuse to higher temperatures (where the autocorrelation time is short) in order to surmount any barriers in the free energy. This has proved an effective method to thermalise highly frustrated systems including artificial spin ices [240, 241] and spin glasses [242].

Clearly, the effectiveness of PT hinges somewhat on the choice of temperature set. Choosing too large a range may require more CPU time than is available. Similarly, choosing too large a difference, $\Delta\beta_i$, may mean that replicas are seldom exchanged. Conventionally, a set is chosen such that the acceptance probability, eq. (5.7), is independent of the temperature and large enough that swaps are frequent (acceptance rates of 23% appear a common benchmark [243]). For our purposes, an acceptable temperature set for a PT simulation is one which samples a given temperature range finely enough so as to discriminate phase transitions while returning results in a computationally feasible time.

In this chapter (and subsequently), we implement the feedback-optimised method of Katz-graber *et al.* (discussed first in [228] and refined further in [229]). This is based on minimising the average Monte Carlo time that replicas take to complete a round trip in temperature space, i.e. the average number of steps required for a replica to return to its starting point, having visited both extremes in between. By performing initial trial runs, the fraction of replicas that diffuse from the minimum temperature, $T_{\min}$, to the maximum temperature, $T_{\max}$ is measured. This fraction defines a steady state current, J, created at $T_{\min}$ and destroyed at $T_{\max}$. The optimal temperature points are found by constructing a probability density about J subject to the constraint that the round-trip time is minimised. In reality, this is an iterative process whereby the optimised temperature set of the previous iteration acts as the starting set of the next. Usually, 10 or so iterations are sufficient to ensure convergence.

We make some adjustments to this procedure. These are explained in detail within JASI [6] but we summarise them as follows. Firstly, we sample relevant thermodynamic variables as well as J to construct the probability density for the optimal temperature set. Ensuring that replica swaps are accepted is equivalent to requiring sufficient overlap between the density of states at neighbouring temperatures. The difference in temperature between adjacent replicas should thus satisfy

$$T_{i+1} - T_i \sim \frac{T_i C_V}{\sqrt{N}}, \tag{5.8}$$

where C_V is the extensive heat capacity, and N is the number of spins in the system. Where the heat capacity diverges—near to a phase boundary for example—the acceptance probability, eq. (5.7), naturally goes to zero. By directly sampling thermodynamic variables as part of our optimisation procedure, we can concentrate temperature points close to bottlenecks such as phase transitions. This ensures good discrimination of observables in the vicinity of critical points. There are existing methods which compensate for the functional behaviour of the specific heat in this way, including those put forward by Kofke [244], by Rathore *et al.* [245], and by Predescu [246, 247]. We combine these approaches with that of [228] to generate our hybrid method.

5.4.2.2 Ewald summation. It is common to perform Monte Carlo simulation using *periodic boundary conditions* (PBC). This is of particular important for systems with long-range interactions. It is possible to introduce an arbitrary cut-off beyond which interactions are ignored [248]. These provide good estimates for situations in which the interactions die off quicker than r^{-3} as in the Lennard-Jones potential [249]. However, previous work has shown that this approach is more severe for the dipolar interaction as it amounts to introducing a shell of pseudo-charges at the cut-off [250] and leads to a greater truncation error for ferromagnetic systems compared with antiferromagnetic ones [251].

Using PBC, a given spin interacts not just with other spins in the array but with periodic images thereof [Fig. 5.6]. Unless otherwise stated, the full dipolar sum in eq. (5.2) is implemented. To accommodate the long-range nature of the dipolar interaction, we use *Ewald summation* [252].[4] This splits the slowly convergent dipolar term into two quickly convergent parts, evaluated separately in real and reciprocal space. A fuller account is given by Landau and Binder in [254].

5.4.2.3 Parameters. We consider system sizes ranging from 16 to 10000 islands (2×2 to 50×50 in terms of vertices, respectively). The upper limit is determined both by the necessity for speed, and by available computer memory. A lattice of N spins contains N^2 separate dipolar interactions. Supposing that each interaction is pre-calculated and stored in double-precision floating-point format [255], the 10000-spin lattice requires 1 Gb of memory per CPU.

A single Monte Carlo step (MCS) was taken to be N single spin flips *followed* by a sequence of PT replica swaps. That is, replicas are swapped according to the Metropolis-Hastings criterion after each conventional Monte Carlo sweep. For the finite-size scaling, the maximum system size considered is 3600 spins (a lattice of 30×30 vertices). In general, 10^4 MCS were sufficient to ensure thermalisation and observables were calculated using both 10^4 and 10^5 MCS to ensure convergence. Results are averaged over at least 10 independent runs; where error bars appear, they reflect one standard deviation in the data. For quantities obtained directly from the MC simulation, these errors are usually negligible ($\ll 1\%$). This reflects

---

[4]Unlike PT, this is not a new technique. One of its first uses was to calculate the mean inner potential in ionic crystals [253].
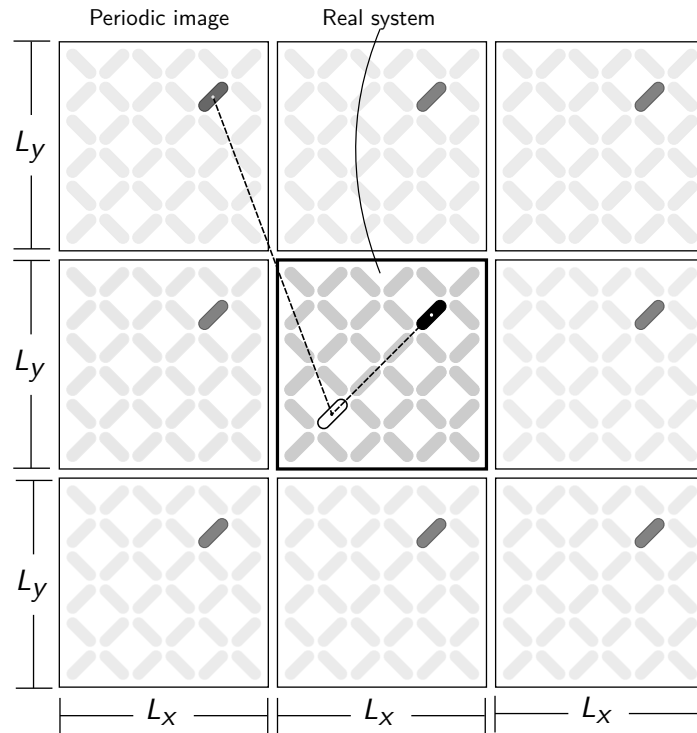
Figure 5.6: Lattice arrangement used to implement periodic boundary conditions in Monte Carlo. The real system is located in the centre, and identical images are tiled around. The interaction of a trial spin (white with black outline) with another (solid black) reflects both the real interaction in the physical system, and interactions with its images in the periodic copies.

the good statistical decorrelation in the Markov Chain that can be achieved with parallel tempering. As ever, larger systems can be treated and better statistics obtained given sufficient computational outlay.

5.4.3 Thermal processes

In Fig. 5.7(a), we depict the specific heat per spin, c_V, as a function of temperature for various angles, including $0°$ square and $45°$ pinwheel. The data is taken from simulations of a 50×50 vertex lattice (10000 spins). The specific heat capacity per spin,

$$c_V = \frac{1}{N} \frac{\langle E^2 \rangle - \langle E \rangle^2}{k_B T}, \tag{5.9}$$

exhibits a peak for all angles. As with the Ising model (compare to Chapter 3, Sec. 3.6), the temperature at which this peak occurs, T_C, marks the onset of ordering. Considering just the

square geometry, a peak is observed at approximately 7.2 $\mathcal{D}\,k_B^{-1}$[5], consistent with the results obtained by Silva *et al.* [256]. In this case, the twofold-degenerate ground state is antiferromagnetic as it is composed of a chequerboard pattern of T_1 vertices (not shown here, but discussed first in [8] and experimentally confirmed in [79]). By contrast, for angles close to the pinwheel geometry, a ferromagnetic ground state is attained. This FM ground state is fourfold degenerate, reflecting the four distinct T_2 vertices. That is, the system transitions from the two-in-two ice rule state at $\theta = 0°$ to a system in which the spins in both sublattices are aligned parallel to each other. We discuss further the predicted structure of this FM ground state in Sec. 5.6.

The specific heat is a useful measure as its definition, eq. (5.9), can be applied to all geometries. Another quantity of interest is the conventional order parameter for magnetic systems, the magnetisation m. Its response function, the susceptibility, χ, is defined through

$$\chi = \frac{1}{N}\frac{\langle m^2 \rangle - \langle m \rangle^2}{k_B T}. \tag{5.10}$$

There are several ways however in which to define m, based on counting particular subsets of spins. In Fig. 5.7(b,c), we show χ for two of these: the staggered magnetisation and the sublattice magnetisation. The definitions of these quantities are given in the respective insets for the case of an open edge 3×3 vertex square array. In the staggered picture, the array is modelled as a *quadrapartite* lattice (such that each island in a vertex belongs to a separate staggered sublattice). In the sublattice picture, the array is modelled as a *bipartite* lattice (such that two islands in each vertex belong to a sublattice). The staggered picture is the relevant one to describe the antiferromagnetic ordering within square ice. This is because the spins in each individual sublattice align antiparallel in square ice. The staggered susceptibility curves [Fig. 5.7(b)] exhibit peaks similarly to those for the specific heat. All arrays, irrespective of rotation angle, develop a net moment and a corresponding susceptibility within their staggered sublattices. However, only those arrays which possess ferromagnetic ground states show peaks in the sublattice susceptibility [Fig. 5.7(c)]. For angles outwith this ferromagnetic region, the net magnetisation is zero within a sublattice and so its susceptibility also vanishes. Arrays in the ferromagnetic region develop an overall magnetisation. This shows the same behaviour as the magnetisation within a sublattice, as expected.

---

[5]The dipolar constant, $\mathcal{D}$, has units of energy. In this reduced scheme then, temperature has units of $\mathcal{D}\,k_B^{-1}$.
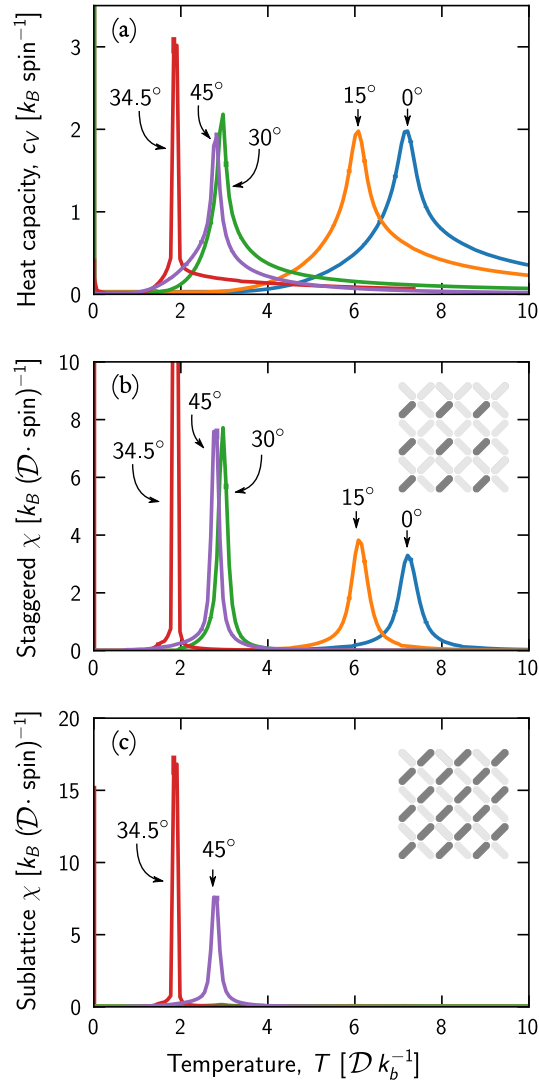
Figure 5.7: Thermal averages for (a) the specific heat capacity, (b) the susceptibility within a staggered sublattice and (c) the susceptibility within a sublattice. Data taken from 10 independent simulations of a 50×50 vertex array (10000 spins). The insets to (b) and (c) define a *staggered sublattice* and a *sublattice* for an open edge square array. For all angles, the specific heat and the staggered susceptibility are peaked at the critical temperature. This reflects the fact that all geometries develop a net moment at least within their staggered sublattices. Only those geometries that order ferromagnetically show a non-zero sublattice susceptibility.
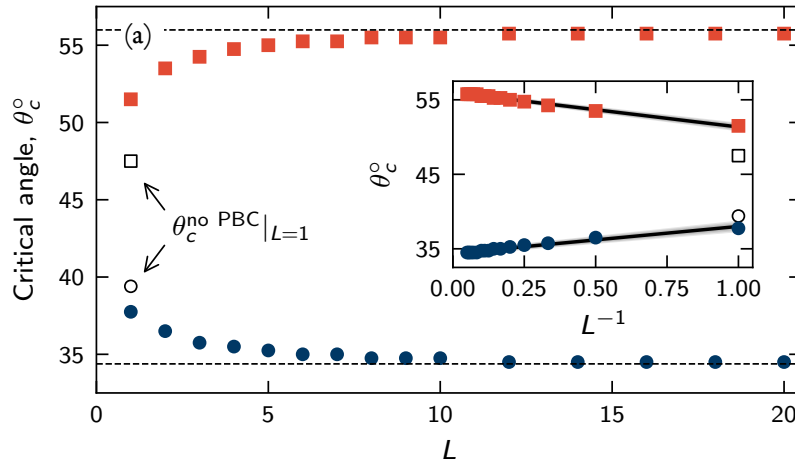
Figure 5.8: Upper (red squares) and lower (blue circles) critical angles, θ_c, are plotted as a function of system size, L. These angles demarcate the angular region for which FM ordering is preferred. Inset: same data but against L^{-1}. Fitting straight lines (shown in black with shaded 3-σ uncertainties) and extrapolating to find their y-intercept, we obtain an estimate for the critical angles for an infinite system: $(34.38 \pm 0.06)°$ and $(55.99 \pm 0.04)°$ for the upper and lower cases, respectively. For comparison, the exact values for a single isolated vertex are indicated by the unfilled markers (c.f. Section 5.4.1).

We make some further remarks. First, the transition to a dipolar-ordered ferromagnetic ground state is dependent on system size. This is quantified in Fig. 5.8, where we plot the upper and lower critical angles, θ_c, as a function of system size, L. These angles define the boundaries between which geometries adopt FM ordering (or, equivalently, for which geometries exhibit a peak in their sublattice susceptibility). The resolution in angle is $0.25°$. By plotting θ_c against L^{-1}, the data fall on two universal curves. Fitting straight lines to these and extrapolating to find the y-intercept, we obtain an estimate for the critical angles for an infinite system: $(34.38 \pm 0.06)°$ and $(55.99 \pm 0.04)°$ for the upper and lower cases, respectively. The critical angles are approximately symmetrical about the $\theta = 45°$ pinwheel geometry and correspond roughly to the region in which the $1nn$ interaction is no longer dominant (as shown in Fig. 5.3(a)). For system sizes above $L = 10$, the critical angle is within $0.5°$ of the thermodynamic limit.

Second, it is clear that the location and width of the peaks in c_V and χ depend on the rotation angle, θ. Thus we seek a method of accurately determining the critical temperature, T_C, for each geometry. This can be done quite effectively by considering the fourth-order
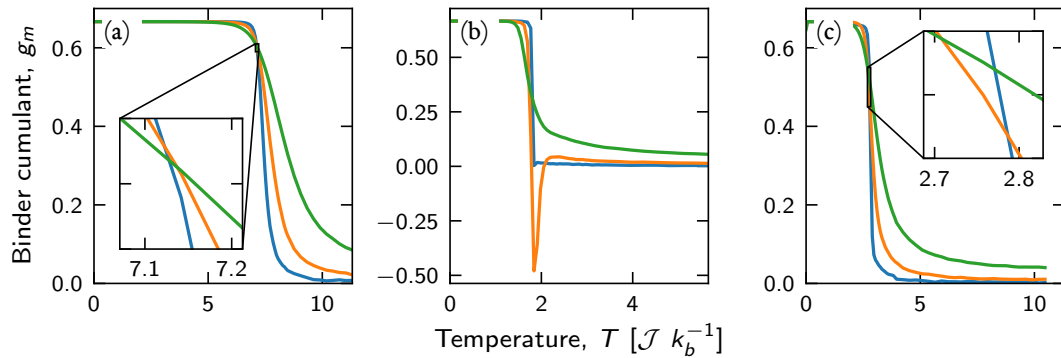
Figure 5.9: Binder cumulant for the magnetisation of a single staggered sublattice for (a) $\theta = 0°$, (b) $\theta = 34.5°$, and (c) $\theta = 45°$. In each case, three system sizes are shown: $L = 5, 10, 20$. The insets to (a) and (c) show that the curves pairwise intersect in a small region . The negative behaviour for the $L = 10$ system is the hallmark of a first order transition. Error bars are less than the linewidths.

Binder cumulant,

$$g_m = 1 - \frac{1}{3}\frac{\langle m^4 \rangle}{\langle m^2 \rangle^2}, \tag{5.11}$$

and determining the intersection point for different lattice sizes (c.f. Chapt. 3, Sec. 3.6). In Fig. 5.9, we show examples of g_m for three angles—$0°$, square ice; $45°$, pinwheel ice; and at the critical angle, $\theta_c = 34.5°$—as calculated using the staggered magnetisation. These show a monotonic drop-off from $1/3$ at $T = 0$, characteristic of a continuous (i.e. second-order) phase transition. The exception is the $\theta = 34.5°$, $L = 10$ case for which g_m is negative around the critical temperature. This suggests that the transition is first order on the critical angle [257, 258], though alighting exactly on $\theta_c(L)$ within the framework of a simulation is difficult.

As the spins are rotated from $0°$, the critical temperature moves towards lower values until $\theta_C = 34.38°$, at which point it begins to increase. The phase diagram summarising this behaviour is shown in Fig. 5.10 and comprises three distinct regions. First, for all rotation angles, the system is paramagnetic (PM) above the critical line. Second, below the critical line and for geometries with $\theta \in [0°, 34.38°] \cup [55.99°, 90°]$, the system has an antiferromagnetic ground state, composed of T_1 vertices. Third, below the critical line and in the narrow region centred on $45°$, the system is ferromagnetically ordered such that the ground state composed of T_2 vertices. In summary, as θ is increased from $0°$, the system transitions from a two-in-two-out
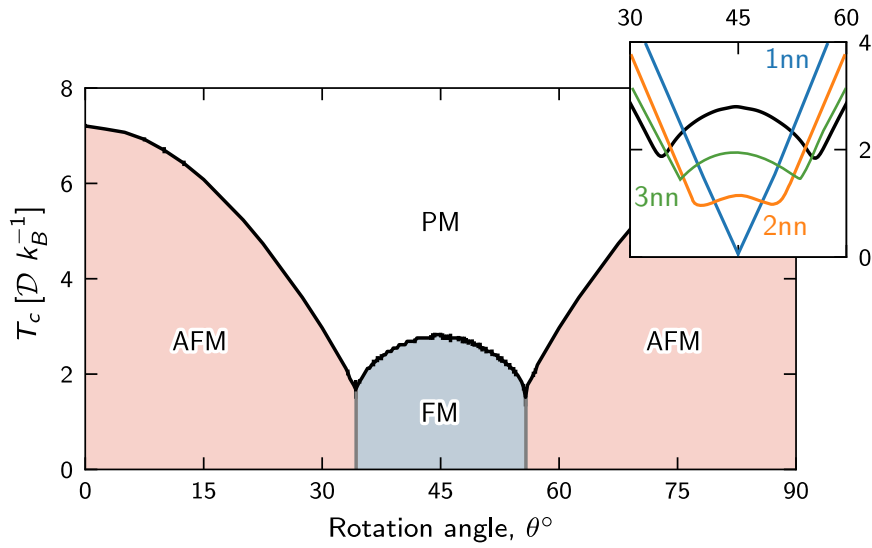
Figure 5.10: Phase diagram of $T_C(\theta)$, showing regions of paramagnetism (PM), antiferromagnetism (AFM), and ferromagnetism (FM). The critical temperatures were obtained using the intersection points of the Binder cumulant for different lattice sizes. Inset: a focus on the $[30°, 60°]$ region for which the analysis is repeated with a variable cut-off in the dipolar interaction.

T_1-vertex state to a two-in-two-out T_2-vertex state at $45°$—in effect, exchanging one ice-rule configuration for another. In doing so, the arrays develops an overall moment: a transition in magnetic ordering. This change in vertex populations suggests assigning a two-component order parameter, (n_1, n_2) to describe this transition.[6] We will return to this idea in Chapter 6.

The phase diagram resembles those envisaged by Landau and Binder for model Ising systems coupled out to $3nn$ neighbours [230] with some differences. In particular, the 'cusps' observed at $\theta = \theta_C$ do not occur at zero temperature unlike those in Ref. [230]. This arises from the contributions of neighbours beyond $1nn$ pairs. We justify this in the inset to Fig. 5.10, where we repeat the analysis for a range of different cut-offs in the dipolar interaction. For $1nn$ neighbours, the interaction at $\theta = 45°$ pinwheel vanishes by symmetry and the critical temperature is zero (consider the two island T-junction shown in Fig. 5.3). Otherwise, the effect of neighbours beyond $1nn$ is to move the critical line away from $T_c = 0$, and towards the result obtained when using the full dipolar sum.

---

[6]The choice of order parameter is not unique for a magnetic system. Previous work in ASI has defined a relevant order parameter by, for example, a phasor quantity [259], the extent of magnetic charge-crystallisation in the array [34], the magnetic structure factor [260], or through a scheme based on vertex moments [96].

5.5 | **Finite-size scaling**

To complete our discussion of the nature of this ordering transition with island rotation, we conduct a finite-size scaling analysis to identify the critical exponents. Coherent x-ray scattering provides quantitative evidence that square ASI belongs to the 2D Ising universality class [118]. It is not *a priori* obvious that this holds true for all angles. In general, critical exponents depend on the symmetry and dimension of the system, and the range of its interactions [103]. Here, the dimension and symmetry are unaffected: both square and pinwheel lattices exhibit C_4 symmetry, for example. However, the *effective* range of interactions—at least, in terms of which couplings are dominant—does shift markedly.

To assess this, we examine how the heat capacity, staggered magnetisation, and staggered susceptibility scale at the critical point, T_c. The associated exponents to these quantities are commonly denoted α, β, and γ, respectively. Example scaling curves are shown in Fig. 5.11 for four angles: square, pinwheel, and two near θ_C. In each case, the critical exponent (i.e., the gradient of the best-fit straight line) is marked. Linear behaviour is observed for both the square and pinwheel lattices, consistent with the scaling hypothesis. Those arrays near the critical angle exhibit anomalous behaviour, however. This is a consequence of the fact that not all system sizes share a common θ_C. For example, for $\theta = 34.5°$, the $L = 10$ and $L = 9$ systems order into ferromagnetic and antiferromagnetic ground states respectively. This leads to discontinuities in the scaling curves.

We show the evolution of these critical exponents over the range $[0°, 45°]$ in Fig. 5.12. The critical exponent, ν, associated with the scaling of the correlation length, ξ, is also given. The correlation length is extracted by fitting $\exp(-r/\xi)$ to measurements of the connected two-point correlation function,

$$\mathcal{G}(r) = \langle \mathbf{s}_i \cdot \mathbf{s}_j \rangle - \langle \mathbf{s}_i \rangle \cdot \langle \mathbf{s}_j \rangle .^7 \tag{5.12}$$

For the most part, these critical exponents show good agreement with those of the 2D Ising universality class for all angles except around θ_C [Fig. 5.12(b,c)]. The exponent associated with the

---

[7]Unlike the other critical exponents which can be extracted directly from the PT Monte Carlo, determining ξ requires a two-step process. As a result, its error has likely been underestimated in Fig. 5.12.

specific heat, α, is consistently higher than the predicted value, namely $\alpha^{\text{Ising}} = 0$. This arises because finite-size corrections to the heat capacity remain significant for larger lattices than they do for m or for χ; a similar effect was noted for the 2D Ising model in Chapt. 3, Sec. 3.6.

We will use this result—that all geometries belong to the 2D Ising universality class—when discussing non-equilibrium phenomena in Chapter 6.
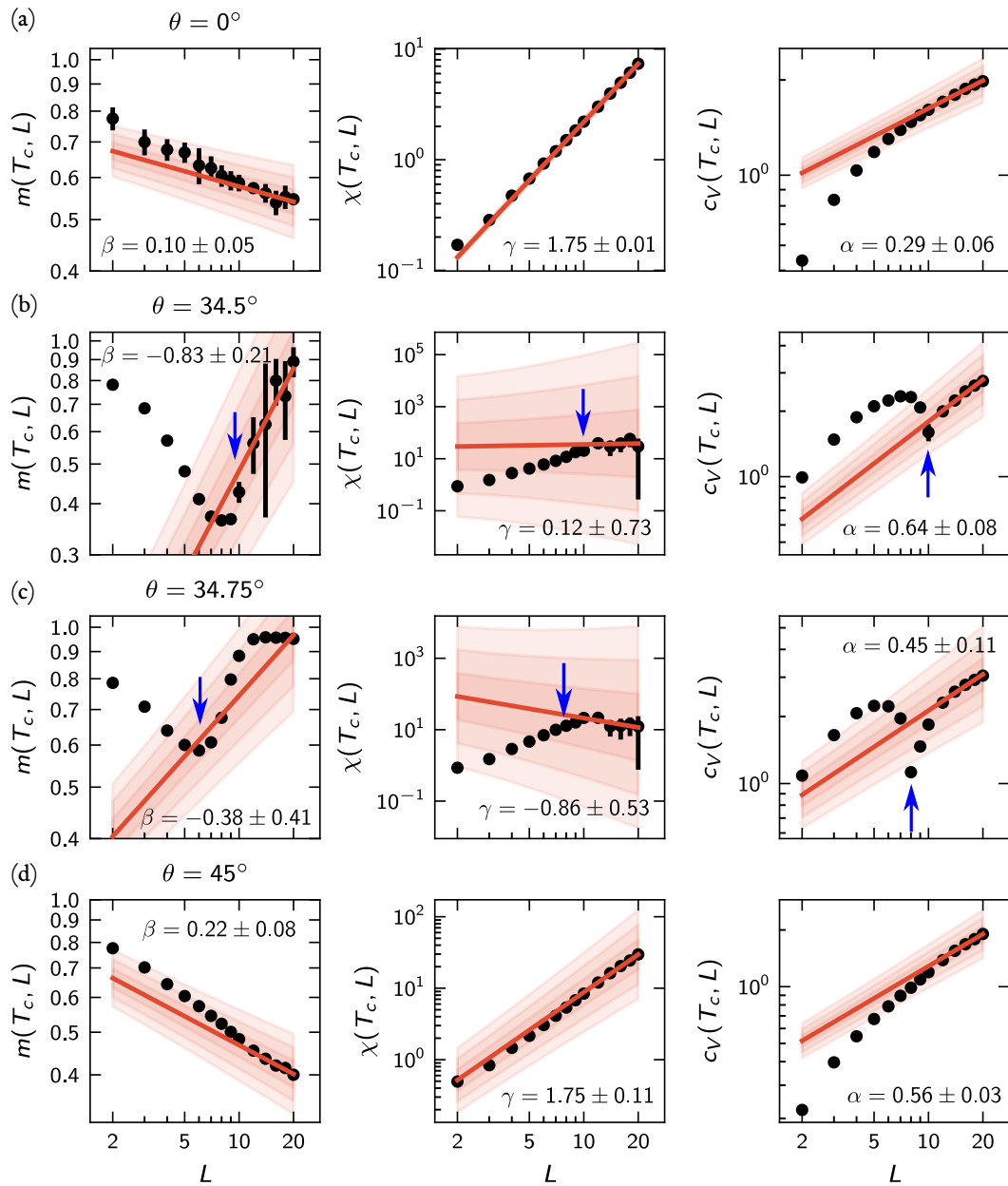
Figure 5.11: Finite size scaling at the critical temperature for rotation angles: (a) $\theta = 0°$, (b) $\theta = 34.5°$, (c) $\theta = 34.75°$, and (d) $\theta = 45°$. From L-R, observables are the staggered magnetisation, the susceptibility, and the heat capacity. To mitigate corrections to scaling, only system sizes above $L = 14$ are used for fitting (roughly, data in the right third of each plot). The 1-, 2-, and 3-σ confidence intervals are shaded around the best-fit. The estimate for the critical exponent is marked on each plot. Not all system sizes share the same ordering near to the critical angles. This leads to cusps in the scaling curves; these are indicated with a blue arrow.
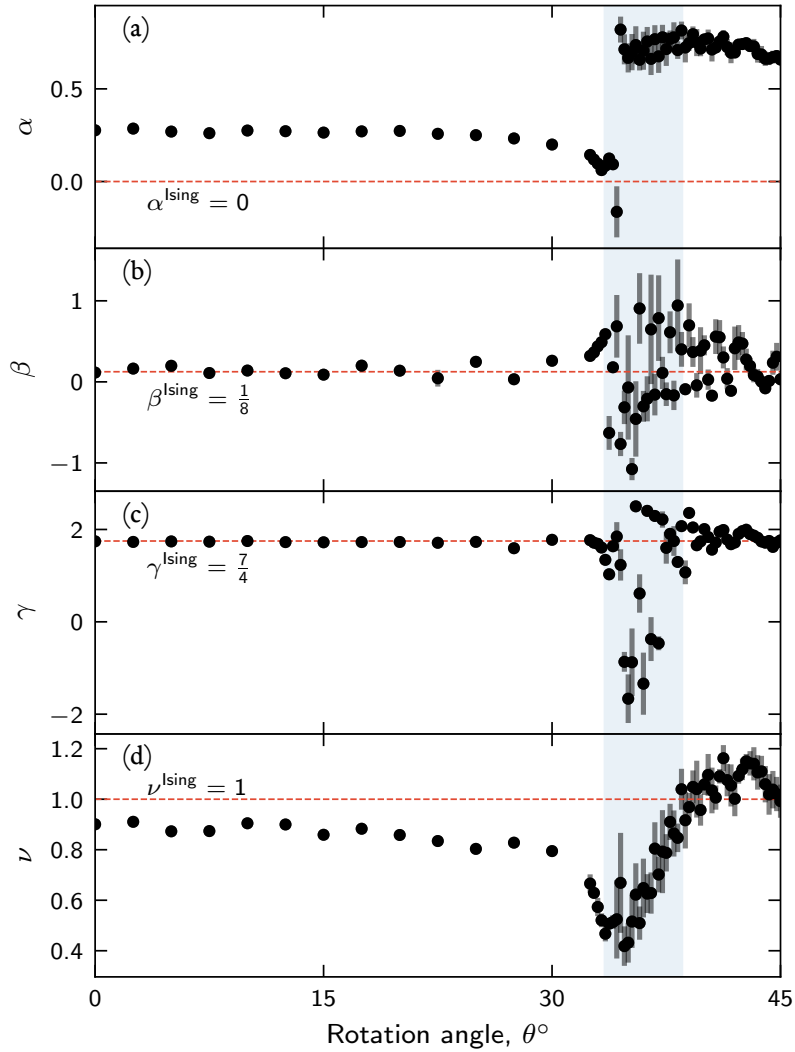
Figure 5.12: Critical exponents as a function of rotation angle. Exponents considered are those associated with (a) the heat capacity, α, (b) the magnetisation, β, (c) the staggered susceptibility, γ, and (d) the correlation length, ν. In each panel, the red line gives the exact value for the 2D Ising model exponent, while the blue band shows the range over which θ_c changes [Fig. 5.8] and for which, consequently, the scaling hypothesis no longer holds. For interest, 10^5 CPU hours (~ 11 years) were required to generate the data for this figure.

5.6 | Pinwheel states

In this section, we focus on the predicted configurations exhibited by the $\theta = 45°$ pinwheel geometry (though our comments apply equally well to any lattice in the ferromagnetic region). In the presence of periodic boundary conditions, both diamond edge and lucky knot edge arrays form single domains, composed of a uniform tiling of T_2 vertices. This is shown in Fig. 5.13(a) and (c), respectively, in terms of the spin configuration [upper panel] and vertex maps [lower panel]. For finite systems (i.e., those without periodic boundary conditions), macro-structures are formed. These are similar to the Landau flux closure patterns found in soft-ferromagnetic media with cubic anisotropy [261, 262] and prove energetically favourable over the uniformly magnetised state once the array is of sufficient size. For both terminations, $L = 3$ is the minimum edge length at which such a closure domain can be supported. Even though these configurations host T_3 and T_4 vertices—which are, in principle, higher in energy than a T_2 vertex at $\theta = 45°$—they minimise stray field and compensate magnetic charge at the boundaries. In analogy with the Bloch point observed in magnetic thin films, T_1 and T_4 vertices act as the core of these closure structures, while the net moments of ferromagnetic T_2 and T_3 vertices circulate around: in effect, a constrained *XY* model. This behaviour is manifestly not observed in 0° square ice where the minimum energy configuration of any finite-size array and, indeed, in the thermodynamic limit is always a chequerboard pattern of alternating T_1 vertices.

Finally, we emphasise the role that aspect ratio and system size have on the emergent configurations that form in finite-size pinwheel arrays. Rectangular arrays—such as those shown in Fig. 5.14—possess an effective uniaxial anisotropy like that found in elongated ferromagnetic nanobars [184]. The vertex maps in Fig. 5.14 are taken from independent thermalisations (i.e., started under different random seeds) of diamond and lucky knot edge arrays with a 1:4 aspect ratio and containing 400 spins. For the diamond edge case in Fig. 5.14(a), an elongated flux closure structure is formed. This houses the ASI-equivalent of 90°- and 180°-Néel domain walls. As with their continuous-film counterparts, the net vertex moment rotates in the plane of the array as an ASI Néel domain wall is traversed. In thin-film systems, the width of a

Néel domain wall is

$$\delta_{\text{Néel}} = \pi \sqrt{\frac{A}{K} + \frac{2A}{\mu_0 M_S^2}}, \tag{5.13}$$

where A and K are the exchange and anisotropy constants, respectively [44]. In the pinwheel lattice, the predicted domain walls are thin, just one vertex wide. For ASI in general, the largest energy scale is set by the coercive field of the individual islands—far larger even than the dipolar coupling between nanomagnets. The best natural comparison for these systems then would be to ferromagnetic materials with high coercivity ($K \rightarrow \infty$) in which domain walls are of the order of the exchange length.

At the same time, a separate thermalisation can achieve a state with similar energy but in which more closure structures are packed [Fig. 5.14(b)]. In general, as the number of spins is increased in the system, it becomes possible to support more closure structures. This is consistent with the behaviour of thin film systems where, for example, increasing the lateral dimensions of the film increases the likelihood of finding multiple closure patterns [263]. As ever, the formation of these mesoscopic domain walls is governed by a competition among competing interactions. In continuous media, the relevant contributions are often the exchange, the anisotropy and the magnetostatic energies. In such cases, the system forms domains so as to lower its total magnetostatic energy at the expense of not all spins remaining collinear (c.f. the discussion of shape anisotropy in Chapter 2, Fig. 2.7). In the pinwheel system, this competition is between the uncompensated charges at the boundaries of the array and the energetic cost of forming high-energy T_3 vertex walls in the bulk. In Fig. 5.14(c) and (d), we show two independent simulations of the lucky knot edge for the 1:4 aspect ratio. These show a zig-zag pattern of domains, and a structure similar to a cross-tie wall. In this case, only 90° vertex domains walls appear to form.

To summarise: increasing the array size or changing the aspect ratio facilitates a greater number of domains. The type of closure structure supported is dependent on the array edge, and analogues of flux closure patterns and cross-tie walls are observed.
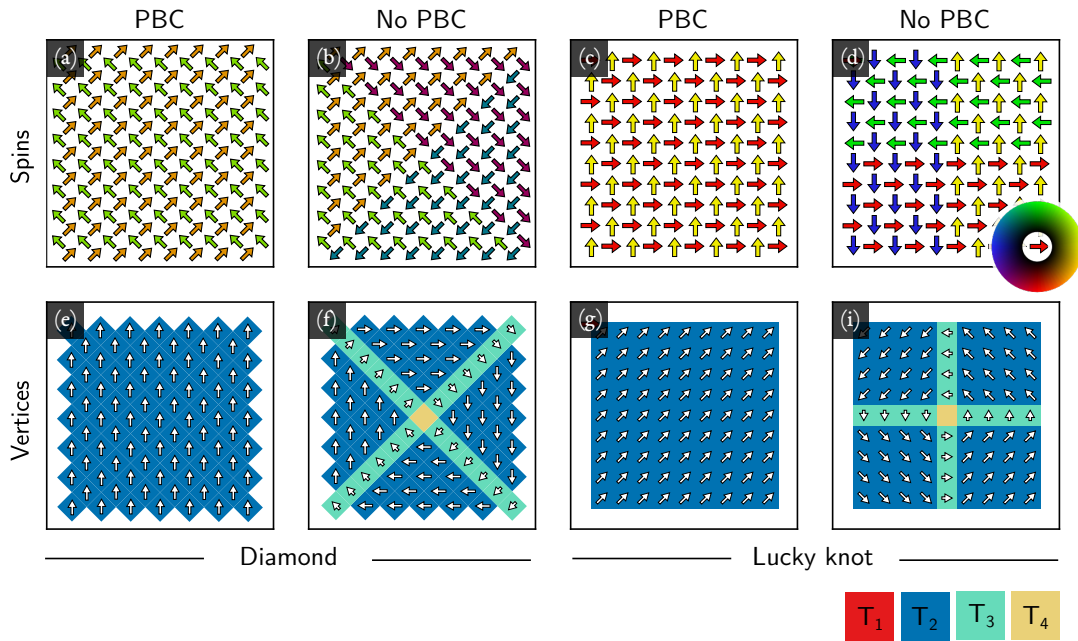
Figure 5.13: Typical spin configurations [upper row] and vertex maps [lower row] for diamond and lucky knot edge pinwheel arrays with and without periodic boundary conditions. (a,c) In the presence of PBC, a uniformly magnetised state is obtained. This is composed of a uniform tiling of one of the four possible T_2 vertices. (b,d) In the case of finite-size arrays, closure structures are obtained. The rôle of the Bloch point is played by a T_4 vertex. These closure structures minimise the stray field. The spins are coloured according to the colour wheel in (d). The vertices are coloured as given in the key. The vertex moment (magnitude and direction) is shown using arrows for FM vertices.
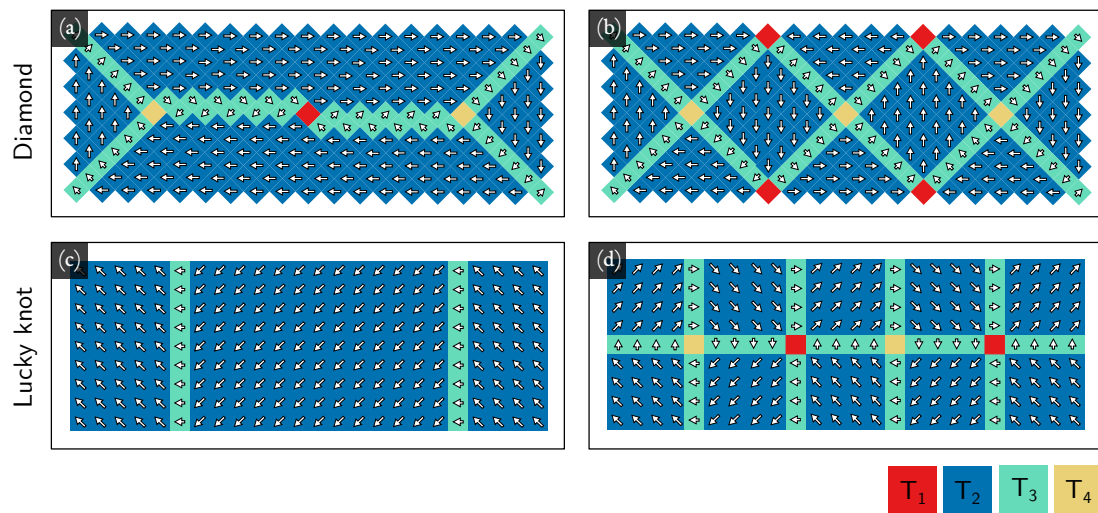
Figure 5.14: Vertex maps of (a,b) diamond edge and (c,d) lucky-knot edge arrays with 1:4 aspect ratio. For the diamond edge array, we observe an elongated flux closure structure (with both 90° and 180° *vertex* domain walls) and an equivalent structure which supports several closure domains. For the lucky knot edge, a zig-zag pattern and a cross-tie wall structure are obtained. Data taken from independent thermalisations of a 400-spin array. The vertices are coloured as given in the key. The vertex moment (magnitude and direction) is shown using arrows for FM vertices.

5.7 | Summary

This chapter has outlined a new continuum of artificial spin ice geometries, which is generated by rotating the islands in the canonical square ice about an angle, θ. The point dipole model was justified before it was used to show that this rotation weakens the nearest-neighbour interactions which dominate the square lattice. We will return to this minimal model in later chapters. As the rotation angle approaches $45°$, a highly degenerate system is created in which all couplings are of similar magnitude. We call the $\theta = 45°$ case *pinwheel* ice. This rotation leads to a transition in spin ordering from antiferromagnetism in the square lattice to ferromagnetism in the pinwheel lattice. This is an unusual form of phase transition, one mediated by the dipolar interaction and driven by a geometrical parameter rather than simply temperature. The transition is second order everywhere except at the critical angles where it appears first-order. Extensive finite-size scaling analysis shows that this class of geometries belongs to the Ising universality class although a definitive classification near to the critical angle proves difficult. Finally, we considered low-energy states of the pinwheel lattice. Here, the ferromagnetic T_2 and T_3 vertices play the role of *meta*-spins. We term this effect *apparent* [1] or *macro*-ferromagnetism [3]. Similar structures to those seen in continuous ferromagnetic media are identified, including flux closure patterns and cross-tie walls. These can be controlled by the array boundary and aspect ratio.

We now turn to confirming this transition with experiment.

6

Ice rules made manifold: thermalisation and defects in 2D artificial spin ice

6.1 | Introduction

This chapter explores the nature of the predicted transition in ordering between square and pinwheel ice experimentally. Using Lorentz transmission electron microscopy (LTEM) on thermally annealed cobalt arrays, we show a preference for ferromagnetism in pinwheel ice, confirming the numerical study presented in Chapter 5. Beyond this, we find that the rotation angle indirectly controls the degree to which arrays are thermalised: some lattices, like square, quickly settle into a steady-state while others, like pinwheel, never reach equilibrium and are only in the early stages of forming ground-state clusters. This finding leads onto a discussion of how artificial spin systems approach equilibrium.

The structure of this chapter is as follows: Sec. 6.2 presents an overview of the experiment, including sample fabrication using focused electron-beam-induced deposition (FEBID), the annealing protocol, and the process by which the magnetisation was extracted from Fresnel

images. Sec. 6.3 discusses the experimental results in terms of vertex populations and correlations, and concludes that there is a transition to a short-ranged ferromagnetic (FM) phase for geometries near to pinwheel ice. As a corollary, an approximate *ice manifold* is recovered. In Sec. 6.4, the correlation length is extracted from the experimental data. We show that quenching inevitably occurs during annealing because the relaxation timescales, controlled indirectly by the island rotation angle, θ, are vastly different. In Sec. 6.5, we show that this change in timescales leads to an apparent change in the nature of the defects supported: from one-dimensional (1D) strings in square ice to two-dimensional (2D) vortex-like structures in pinwheel ice. Using parallel tempering Monte Carlo, we show that the numerical scaling of these quantities agrees with that predicted by the Kibble-Zurek mechanism of defect formation for the 2D Ising universality class.

6.1.1 Attribution

The majority of the work in this chapter can be found in Ref. [2]. This chapter presents an expanded account of the paper but contains a greater emphasis on the experimental technique (including sample deposition, processing of Fresnel contrast in ASI, and a comparison with simulation); measurements of the two-point correlator and correlation length; and a more complete characterisation of the excitations in FM-like arrays. Although these topics may not appear in [2] (or appear only in passing or in the supplementary), they lend additional support to its conclusions.

Y.L. and I optimised the deposition process and performed atomic force microscopy on the samples while the data analysis was done by me. The results are presented in Appendix A. With the assistance of G.W.P., I performed the TEM heating experiments. I wrote the Python scripts which processed the Fresnel images. Monte Carlo simulations were produced by the Julia package, JASI [6], that I developed. I wrote the manuscript; all authors offered feedback. R.L.S. and S.McV. supervised the project.
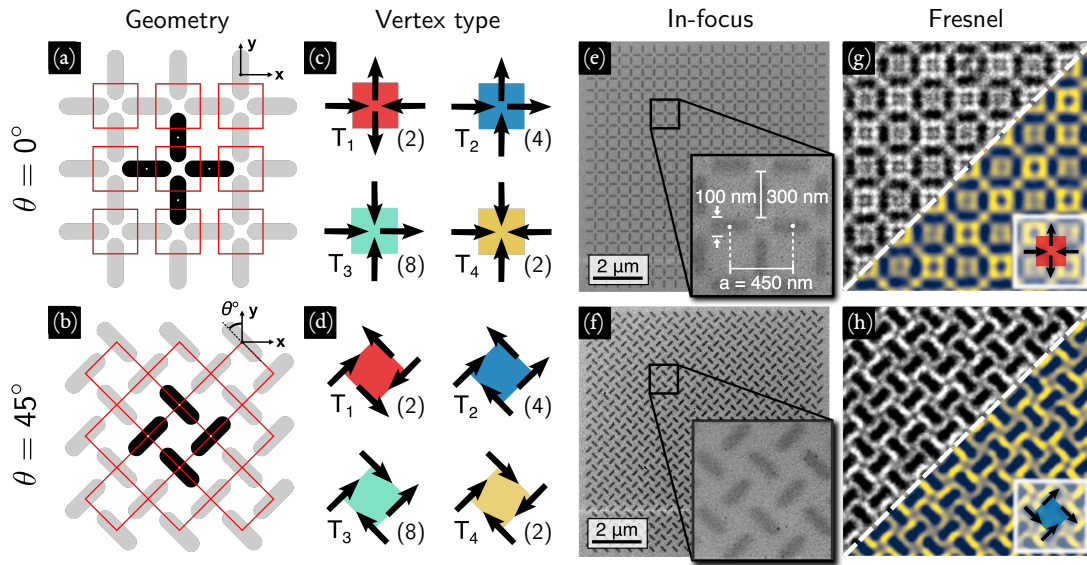
Figure 6.1: The open-edge square geometry in (a) is transformed into the diamond-edge pinwheel lattice on rotation of each island by 45° about its centre. A reminder of the four vertex types for (c) $\theta = 0°$ square and (d) $\theta = 45°$ pinwheel ice. The degeneracy of each type is indicated in brackets. The colour coding for type accords with that used in Chapter 5. (e), (f) In-focus TEM images of FEBID arrays for these two angles; dimensions indicated in the inset to (e) are the same as those in (f) and, indeed, for all fabricated arrays. (g), (h) Fresnel images (raw in greyscale, Fourier-filtered in colour for emphasis) obtained after annealing for square and pinwheel ice. The asymmetry in contrast across the long axis of each island (dark edge compared with light edge) allows for the macrospin direction to be identified. By translating the spin configuration into the vertex picture, the type of ordering supported by an array can be identified. Adapted, with changes, from Ref. [2].

6.2 | Experimental overview

Fig. 6.1 neatly encapsulates the rationale behind this experiment. We are seeking to probe the transition in spin ordering predicted by the Monte Carlo results of Chapter 5. To do this, we fabricate ASI arrays with rotation angles in the range $[0°, 90°]$. As the patterns possess C_4 symmetry, it is sufficient to consider this restricted angular range provided that the individual arrays are large enough. This ensures that any finite-size asymmetries around 45° are negligible (compare the behaviour of the critical angle with system size as given in Chapter 5, Fig. 5.8.) We choose an array sequence starting with an open-edge $\theta = 0°$ square ice array; a reminder is

shown in Fig. 6.1(a). This is transformed into a diamond-edge pinwheel array on rotation of the islands through 45° [Fig. 6.1(b)]. The predicted transition in sublattice ordering is independent of the exact choice of lattice termination although it does affect the exact configurations supported in the FM phase, as we have discussed.

To characterise the ordering present within the arrays, we use the relative populations of types. An example of each type is shown again for square and pinwheel ice in Fig. 6.1(c,d) where the number in brackets indicates the degeneracy. The 'two-in-two-out' vertices, T_1 and T_2, are vertices which satisfy the ice-rule. We treat them as *indicator species* [264]: an excess of T_1 suggests that the array is antiferromagnetic, while an excess of T_2 (which has a net moment) suggests that the array is ferromagnetic. Vertex populations—the number density, n_i, of vertices of type T_i—thus act as a proxy for how close a system is to its ground state. This approach was pioneered by Wang *et al.* in [8] for the numbers of ice-rule vertices formed on AC demagnetisation of square ice arrays, and extended to the notion of effective temperature in [76]. Beyond interacting arrays of nanomagnets, counting vertex types has been applied to analogues of frustrated systems made from colloidal traps [265] and nanostructured superconductors [266]. As we shall see, this two-valued order parameter, (n_1, n_2), is by no means a perfect figure of merit. We emphasise two subtleties.

First, two systems that share the same vertex populations are not necessarily contiguous in phase space. For example, the two equivalent ground states of square ice present the same vertex population—$n_1 = 1$, all other $n_i = 0$—but require a global spin flip to connect them. Moving between these configurations, e.g. through some field protocol, is difficult, well nigh impossible [267]. On the other hand, states that present vastly different vertex populations can be connected by the application of a single field: compare the ease by which the square ice array in Fig. 6.1(a) can be prepared in a T_2- or T_3-polarised state by applying a field along the $(1, 1)$ or $(1, 0)$ directions, respectively.

Second, information is unavoidably lost through the aggregate nature of n_i (as opposed to, say, the full spatially-exact ensemble of vertices or spins). For example, Ref. [35] discusses the propagation of monopolar T_3 vertices on a square lattice. At each step, T_2 or T_3 vertices are created and destroyed in equal amounts such that the global vertex population does not

change even though the spin configuration does. As a result, n_i fails adequately to capture dynamic information.

Nonetheless, we choose populations to characterise the ordering between square and pinwheel ice as they are experimentally accessible quantities, at least by means of LTEM.

6.2.1 Sample fabrication using FEBID

Arrays were deposited using focused electron beam induced deposition of the metal-organic precursor $Co_2(CO)_8$ on a dual column Helios Plasma Focused Ion Beam instrument. A description of this technique is contained in Chapter 4. The arrays were written on ~ 40 nm thick electron transparent Si_3N_4 to allow measurement by TEM. Before Co deposition, carbon was sputtered onto the membranes. Similarly, after Co deposition, a thin carbon FEBID film was applied atop. These steps inhibit oxidation of the samples and charging during subsequent TEM measurement.

Significant time was spent optimising sample preparation in terms of both array and deposition parameters. Samples needed to be thin enough so as to be thermally active within the accessible temperature window from $-150\,°C$ to $250\,°C$, while still being thick enough to present sufficient magnetic contrast for LTEM. To date, most thermal studies of ASI are obtained on samples fabricated using electron beam lithography (for example, according to a wedge process in [180]) though novel techniques (e.g. using two-photon lithography [203]) have recently been proposed. To the best of our knowledge, this is the first demonstration of *in-situ* observation of thermally active FEBID magnetic samples of any type, not just ASI.

Insofar as possible, arrays were fabricated under identical conditions to ensure the intrinsic energy barrier of each island was the same. Resulting differences in behaviour would then reflect the anisotropic features of the dipolar field rather than quenches disorder. The scanning electron microscope beam current was 0.69 nA; the accelerating voltage was 5 kV; and the half screen window size was 20.7 μm (magnification: $10000\times$). The working distance was 4 mm. The deposition time per array was 3 minutes. It was observed that the gas flux of the precursor would tend to decrease over the course of a deposition session (~ 8 hours). In order to account for this, arrays were deposited in a random order during each deposition session.

Arrays were deposited from 0° to 90° in steps of 5°. Several arrays were fabricated for each θ (at least four repetitions; six for those in the range [35°, 45°]; with an extra two for the $\theta = 45°$ pinwheel ice.) Each array covered $(10.8 \,\mu m)^2$, comprising 840 islands (a lattice of at least 20×20 vertices). The lateral dimensions of the islands were 300 nm by 100 nm. The lattice constant, taken as the distance between second-nearest-neighbours, was $a = 450$ nm, as shown in Fig. 6.1(e). Island and array dimensions are similar to those used in other studies [232]. The thickness of the islands over the central portion of each array was measured to be ~ 3 nm using atomic force microscopy. We present the results these measurements in Appendix A. Closer to the edges of the array, islands tended to be thicker (~ 4 nm). This consistent with the effects of gas diffusion [268]. In FEBID, the precursor tends to deplete in the centre of the pattern whereas, at the edges, it is replenished by migration from surrounding, unexposed areas. In line with this observation, magnetic contrast was poorer around the boundary of the array, suggesting lower local cobalt content and a greater deposit of carbon. Our subsequent processing steps account for this.

6.2.2 Fresnel imaging of artificial spin ice

As discussed in Chapter 5, contrast in the Fresnel mode of Lorentz microscopy arises from the deflection of the electron beam by the integrated induction of the sample. This is depicted in Fig. 6.2(a,b) for the two Ising states of a single island. The usual assumptions for an infinite thin film—that both the magnetisation, **M**, and the magnetic induction, **B**, lie in plane and are uniform throughout the thickness, t, of the islands—apply equally well here. In the classical picture, the electrons undergo a deflection through an angle,

$$\beta = \frac{e\lambda}{h} B_y t, \tag{6.1}$$

where λ is the wavelength of the electrons, and h is Planck's constant. This deflection leads to an asymmetry in the image intensity parallel to the long axis of the island. Since we assume $\nabla \cdot \mathbf{M} = 0$, the magnetisation and the induction are effectively the same inside an island (within a factor of μ_0). The macrospin orientation can be assigned by comparing the intensity on either side of the long axis. In Fig. 6.2(c), we show the phase contributions accrued by the electron wavefront on passing through the induction given in panel (b); these are separated
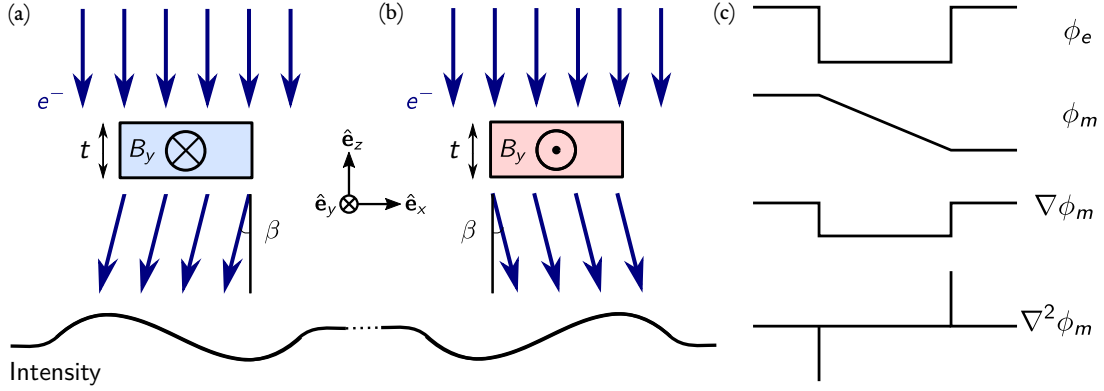
Figure 6.2: Deflection of electrons through an angle, β, by a single-domain magnetic island with magnetisation directed: into the page, as in (a); and out of the page, as in (b). In the inscribed coordinate system, the magnetic induction within the islands is aligned along the $\mp y$-axis, respectively, with magnitude, B_y. (c) Contributions to the phase of the electron wavefront are separated into the electrostatic phase, ϕ_e, and the magnetic phase, ϕ_m. The Fresnel contrast depends on the magnetic phase through $\nabla^2 \phi_m$.

into the electric, ϕ_e, and the magnetic, ϕ_m, contributions (and derivatives thereof). To first order, Fresnel contrast depends on the Laplacian of the magnetostatic phase, $\nabla^2 \phi_m$ (see the discussion in Chapter 4, Sec. 4.3).

In Fig. 6.3, we simulate the magnetisation distribution of a single island, with dimensions matching those used in experiment. All simulations were performed using the GPU-accelerated Mumax3 package [98]. The in- and out-of-plane cell sizes were 2 nm and 3 nm, respectively; the exchange constant was 21.0 pJm^{-1}; and the saturation magnetisation was set to 70% that of bulk Co, consistent with comments we make in Sec. 6.2.3. The chosen cell sizes are below the exchange length, $l_{\mathrm{ex}} \approx 4.46$ nm, in all directions. To speed up convergence, the damping parameter, α, was set to 0.5. In Fig. 6.3(b), the magnetic phase, ϕ_m, is calculated according to the algorithm proposed by Mansuripur [269], and subsequently realised by McVitie *et al.* [270]. This algorithm provides a complete framework to describe the phase change of an electron wavefront impinging on an arbitrary magnetic thin film. We consider a range of typical defocus values, Δf, ranging from 1 mm to 5 mm [Fig. 6.3(c)]. The asymmetry in contrast is easily observed, even if the structure of the island is blurred for large Δf. Line
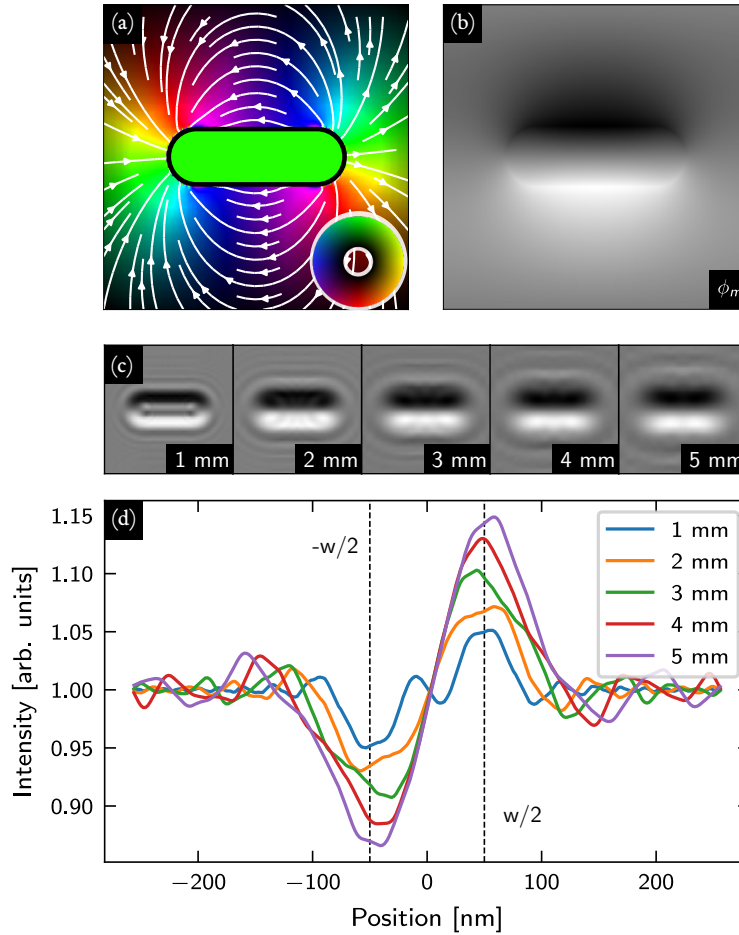
Figure 6.3: (a) Simulated magnetisation, **m**, and stray field, $\mathbf{B}_{\mathrm{demag}}$, for a single island, calculated using Mumax3. The dimensions match those of the experimental islands, with properties consistent with 70% pure Co. The stray field is plotted on a logarithmic scale. The colour wheel inset to (d) represents the orientations and relative magnitude of the vectors. The island is outlined in black for emphasis. (b) Magnetic phase contribution, ϕ_m, arising from the induction in (a) is shown for the case of an incident, uniform electron wavefront. (c) A defocus series, in terms of Δf, for the single island in (a). The asymmetry in contrast is easily observed, especially at large Δf where the shape of the island is blurred. (d) Line traces averaged over the central portion of the islands in (c). The asymmetry (peak-to-trough) increases with increasing defocus. The dashed lines delineate the extent of the island.

traces over the central portion of each island provide a systematic way of categorising the orientation [Fig. 6.3(d)].

Fig. 6.4 extends this discussion to sixty-island ASI arrays for both $\theta = 0°$ square ice and $\theta = 45°$ pinwheel ice. As before, the dimensions and properties match those of the experimental

arrays. Four configurations are considered from left to right: the T_1 ground state of square ice, a T_2-polarised FM state of square ice; T_2-polarised FM state of pinwheel ice; and the predicted *flux closure* ground state of pinwheel ice for a diamond-edge array [c.f. Chapt. 5, Fig. 5.13]. We draw attention to the T_1 ground state of square ice in particular, for which the Fresnel image forms a chequerboard pattern.
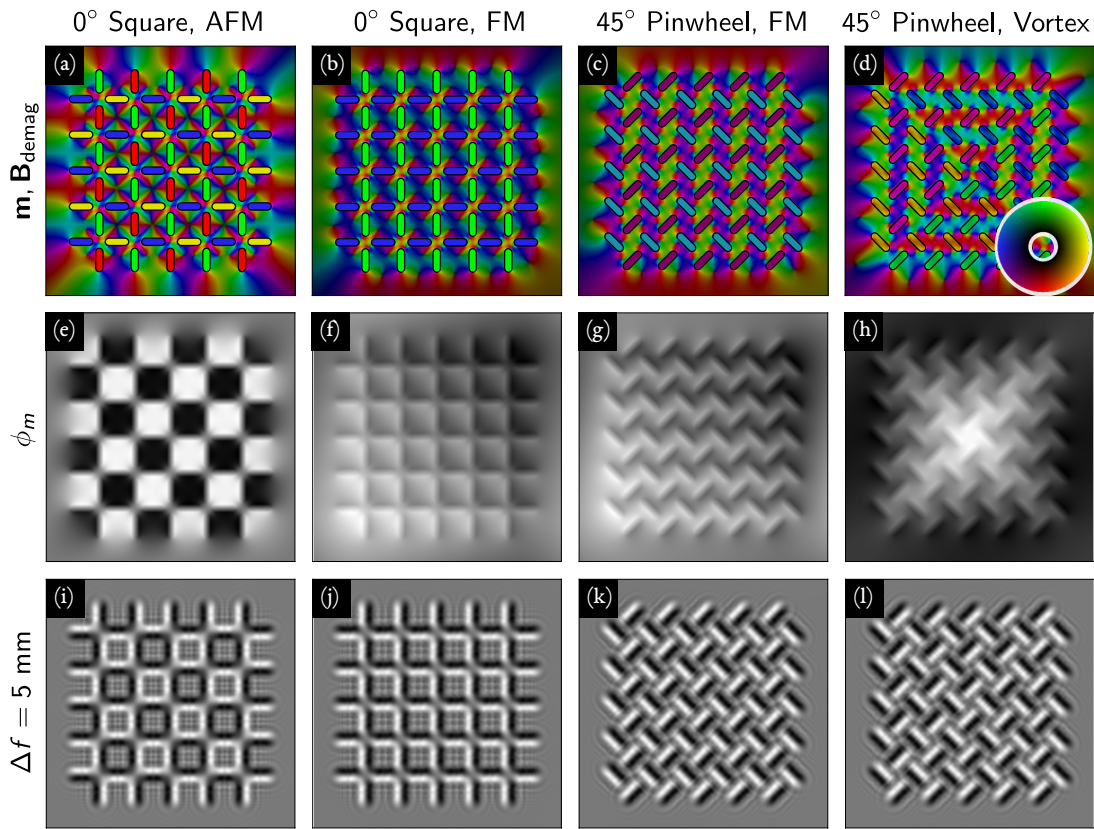
Figure 6.4: Sixty-island arrays in terms of their: magnetisation, **m**, and stray field, $\mathbf{B}_{\text{demag}}$ [top row]; magnetic phase contribution, ϕ_m [middle row]; and Fresnel contrast for a typical defocus of $\Delta f = 5$ mm [bottom row]. The island dimensions and properties match those used in the experiment. The stray field is plotted on a logarithmic scale. The colour wheel inset to (d) represents the orientations and relative magnitude of the vectors. The streamlines, present previously in Fig. 6.3(a), are omitted in the top row for clarity. From L-R, the arrays considered are: a T_1 AFM ground state of 0° square ice; a T_2-polarised FM state of 0° square ice; a T_2-polarised FM state of 45° pinwheel ice; and the predicted closure ground state for 45° diamond-edge pinwheel ice.

6.2.3 Annealing Protocol

The annealing was carried out *in situ* in a JEOL ARM200cF TEM equipped with a cold field emission gun operated at 200 kV. The emission current was 14 pA, and a 70 μm condenser aperture was used. The objective lens was nulled before sample insertion to ensure a field-free environment ($\leq$ 0.1 Oe). This was critical to avoid biasing as the samples were cooled. A Gatan HC3500 sample holder was used to heat the arrays to 250 °C, so that the macrospin associated to each island became superparamagnetic. This temperature was maintained for two hours before the arrays were cooled at a rate of 1.5 °C min^{-1} to approximately -10 °C.

Initially, before heating, the islands appeared frozen as the energy barrier to their reversal was many orders of magnitude greater than the average thermal fluctuations, $k_B T$. Assuming a model of coherent rotation, the energy barrier is

$$
\begin{aligned}
E_\mathrm{b} &= KV \\
&= \frac{1}{2}\mu_0 \Delta \mathrm{D} M_s V,
\end{aligned}
$$
(6.2)

where K is the shape anisotropy constant, thereafter re-expressed in terms of the difference between the components of the demagnetisation tensor[1] along the long and short axis of the island, $\Delta \mathrm{D}$. Far from the critical temperature, the saturation magnetisation is assumed to follow a Bloch-like dependence with temperature through

$$
M_S(T) = M_S(0)\left[1 - \left(\frac{T}{T_\mathrm{Curie}}\right)^{\frac{3}{2}}\right],
$$
(6.3)

where T_Curie is the Curie temperature for the material. By way of comparison, $T_\mathrm{Curie} = 1127$ °C for pure cobalt.

We define the blocking temperature, T_B, as the temperature at which the moment reorientation is on the order of the measurement time, t, i.e.

$$
T_B = \frac{KV}{k_B \ln(t/\tau_0)},
$$
(6.4)

---

[1]The demagnetisation tensor, **D**, relates the magnetisation of a ferromagnetic body to its demagnetisation field, $\mathbf{H} = -\mathbf{D}\,\mathbf{m}$. In general, **D** can be tricky to calculate unless the body of the sample is particularly simple [44]. Its form for ellipsoids is often used to approximate the behaviour of islands in ASI—see, among others, Ref. [271].

where τ_0 is a fundamental attempt rate on the order of 10^{10} seconds [272]. This blocking temperature can be identified with the critical temperature, T_C, described in Chapter 5 though it is not an exact comparison. Below the blocking temperature, the islands are frozen only within the duration of the measurement but there may exist a significant probability that they flip outwith it. By contrast, the critical temperature is independent of measurement and reflects the average spacing between energy levels. Above T_B, islands spins are superparamagnetic and have sufficient energy to overcome the hard-axis energy barrier. Correlations between neighbouring spins emerge as the system is cooled through T_B and the system falls into a low-energy state. We will return to probing the dynamics of an ASI system as the ordering transition is traversed in Chapter 7. Suffice to say here, the efficacy of the annealing protocol depends heavily on a number of experimental conditions, including island thickness and shape, temperature, and duration [273].

Eq. (6.4) provides a way to estimate T_B for our samples. Approximating the islands as ellipsoids, we take $\Delta D = 0.01$ following the method outlined by Osborne [274]. Combined with a measurement time of 1 second, this gives $T_B = 802\,°C$. This is significantly higher than observed in experiment. Across all samples, the onset of flipping occurred at around $110\,°C$ and continued until $250\,°C$, strongly suggesting that the true energy barrier, E_b, is modified by the local field environment. Recently, this effect was quantified for square ice in [275], which demonstrated that E_b is reduced by approximately 35% and the lifetime of certain states by up to seven orders of magnitude when interactions are included. Others have similarly found that eq. (6.4) overestimates T_B by an order of magnitude or more [53, 276]. This is often explained by positing an effective activation volume, $\tilde{V} \ll V$, which seeds the reversal at lower temperatures. Here for example, an activation volume half that of the nominal value would render a realistic T_B. Ferromagnetic resonance simulations provide some support for this. These have shown that the ends of islands are magnetically softer and, as a consequence, less Ising-like than the bulk [277]. In addition, micromagnetic simulations performed as part of this thesis and reported in [4] show that the islands in pinwheel ice reverse through nucleation of domain-wall textures from endstates rather than by coherent rotation of **m**.

Perhaps a more useful measure is to calculate the characteristic energy scale in terms of the dipolar constant, $\mathcal{D} = \mu_0 (M_S V)^2/(4\pi a^3)$, where V is the volume of the island. This

allows us to estimate an approximate size of the fluctuations. Assuming a saturation magnetisation, M_S, equal to 70 % that of bulk Co (consistent with the purity obtained under similar deposition conditions [278, 279]), $\mathcal{D} = 0.033$ eV, corresponding to a temperature of 118 °C—extremely close to the observed onset of flipping. Were the experiment repeated, it would be beneficial to measure the saturation magnetisation explicitly using, say, differential phase contrast techniques combined with thickness profiles of individual islands.

6.2.4   Processing Fresnel images

After cooling, Fresnel images were taken and analysed with the aid of semi-automatic image processing to extract the moment direction for each island. A typical workflow is shown for a square ice array in Fig. 6.5, but the method is applicable to any island rotation angle. The data-processing was performed in Python specifically by the SciPy [280], Hyperspy [281], and fpd [282] libraries. Conventional, in-focus TEM images were taken [Fig. 6.5(a)]; these allowed for the determination of Δf and the electrostatic phase contrast, and the identification of larger carbon deposits which spoil the magnetic contrast. Typical defocus values for the Fresnel images were between 5 mm and 10 mm. Imaging conditions were optimised separately for each array. A Hough transform was used to find the array edges and the image was rotated to align with the coordinate axes as shown in Fig. 6.5(b). The background was corrected using bilinear interpolation, and the islands located using a centre-of-mass algorithm. Building on comments made in Sec. 6.2.1 and taking the thickness profiles in Appendix A, the Fresnel contrast was found to be poorer towards the edges of the array. As a result, moments were only assigned to islands falling within a central, 'best-contrast' region [yellow boundary, Fig. 6.5(c)]. Usually, this encompassed about 70% of the available islands (though varied between 40% and 90%).

Considering only the central portion of each array conferred several advantages. First, it omitted those topological defects that form at the boundaries where the local field environment is different. Previous LTEM studies of square ASI have shown that string-like dislocations of T_2/T_3 vertices form at the lattice edge and can easily extend throughout the bulk [175]. Second, islands at the edges tended to be thicker and would, therefore, possess higher blocking temperatures. Finally, we established in Chapter 5 that the phase diagram of this rotated ASI was sensitive to the number of neighbours in the dipolar sum. Islands at the edges of the

array do not have their full complement of neighbouring pairs, and this necessarily restricts the range of angles for which apparent ferromagnetism is predicted to occur. This procedure thus mitigates finite-size effects and enables us to probe something approaching the bulk behaviour of each tiling pattern.
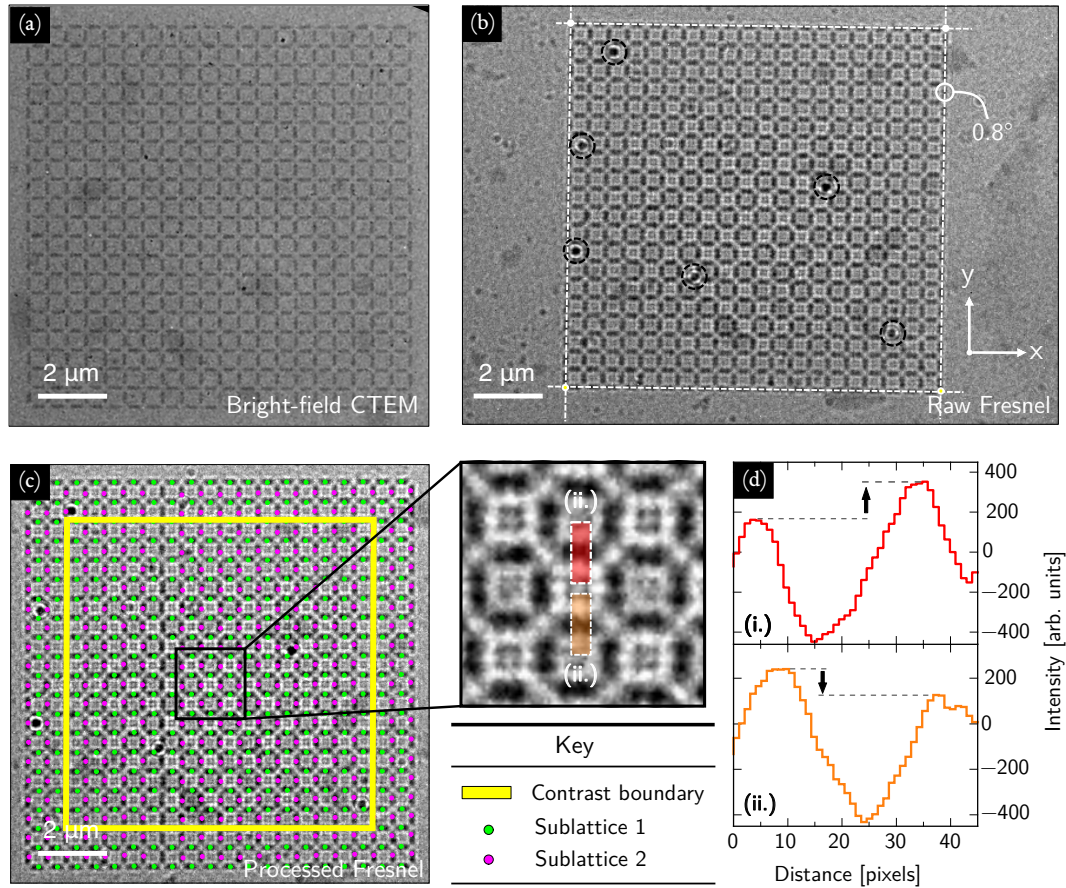
Figure 6.5: Assigning moment orientations to islands based on experimental Fresnel images. (a) Bright-field TEM image of a typical square ice array. The dark splotches are heavier carbon deposits, a by-product of the sputtering prior to deposition. (b) Raw Fresnel image of the corresponding array. A Hough transform is used to identify the lattice boundary, and the image is rotated—here, counterclockwise by 0.8° as indicated—to align with the inscribed coordinate axes. Cross-correlating the Fresnel image with the in-focus TEM image in (a) allows carbon deposits to be identified [marked by black circles]. These can obscure the magnetic contrast from individual islands. (c) The background is corrected using bilinear interpolation and centre-of-mass algorithm locates each island [islands in separate sublattices shown in green and purple]. The 'best-contrast' boundary is marked in yellow. Blow-up to (c): a chequerboard pattern is noticeable in the Fresnel contrast, akin to that predicted in Fig. 6.4(i). (d) Line profiles are averaged over the central portion of each island; two examples, (i.) and (ii.) are shown which exhibit opposite asymmetry in edge intensity, i.e. the spins are antiparallel.

6.3 | **Population and correlation results**

The results of this analysis are contained in Fig. 6.6 where the change in *excess* populations of the four types is shown against rotation angle, θ. Populations are shown with reference to a perfectly uncorrelated sample following Ref. [8]. In a random configuration, the four types appear with frequencies matching their intrinsic multiplicity, that is, in the ratio 1:2:4:1. For 0° square ice (and its translated $\theta = 90°$ sibling), there is a strong excess of T_1 vertices—consistent with the results first obtained by Morgan *et al.* [283]. As the angle of the tiling pattern is increased from 0° to 90° in steps of 5°, the T_1 population decreases and attains its minimum value at 45° before rising to a maximum once more at 90°. From around 39° to 53°, FM T_2 vertices are in *slight* excess above AFM T_1 vertices [shaded region, Figs. 6.6(a,c,d)]. The high energy types, T_3 and T_4, are always suppressed. These results are consistent with those predicted by the Monte Carlo simulations of Chapter 5.

We make three further comments. First, the ferromagnetic signal is weak: the excess T_2 population is only $\sim 10\%$ when averaged over all samples. We return to this idea later when we discuss defect formation in the pinwheel and related geometries as a consequence of incomplete thermalisation. While arrays near to pinwheel are weakly coupled, we emphasise, however, that these results and those we subsequently report are not consistent with paramagnetism. An uncorrelated sample would require, e.g., that the 45° and 50° results be simultaneously off by 3.1σ and 4.5σ. Second, the transition between the two ordering regimes is gradual rather than abrupt. This suggests the intriguing prospect of observing arrays which support mixed phases, i.e. containing both AFM and FM regions. Third, the 45° and 50° results almost satisfy $n_2 = 2n_1$, a necessary—but not sufficient—condition for the ice phase. At these angles, the lattice is effectively an ice manifold for which all two-in-two-out vertices are equally likely. This is not conclusive proof that the ice phase is *itself* supported. This would require an improved annealing protocol and interrogation of the resulting correlations—the existence of pinch points in the magnetic structure would be persuasive. In this sense, usage of the term 'ice manifold' is consistent with that in Ref. [284] where periodic notches are used to render quasi-degenerate a connected square lattice. Other methods of creating an ice manifold have relied on introducing a height offset between sub-lattices [239, 285, 34] or by coupling

XY mesospins to the square tiling [286]. Here, we realise a planar ice manifold simply by modifying the orientations of the nano-magnets.

These observations can be explained in terms of pairwise correlations between neighbouring spins. Three classes of neighbours are depicted in Fig. 6.6(b): first-nearest-neighbours ($1nn$); second-nearest-neighbours which are separated *laterally* i.e. within the same vertex ($2nn$-L); and second-nearest neighbours which are separated in a *transverse* fashion i.e. in adjacent vertices ($2nn$-T). Wang *et al.* [8] assigned correlations, $\mathcal{C}_\alpha$, to these neighbours according to their point dipolar energy: a pair of islands contribute $+1$ (-1) if the two moments are aligned in such a way as to minimise (maximise) E_{dip}. If the dipolar energy of a pair is zero, it is ignored.

These correlations functions are shown in Fig. 6.6(c). In general, those arrays which exhibit majority T_1 populations possess strong $1nn$ correlations. As with the T_1 population itself, $\mathcal{C}_{1nn}$ falls away with rotation angle until $45°$. Strongly-coupled $1nn$ pairs drive the AFM ordered ground state of square ice, whereas the relative strength of the $2nn$ correlation functions for $\vartheta \in \left[39°, 53°\right]$ stabilise T_2 formation. For pinwheel ice and similar geometries in fact, separating the two classes of second-nearest neighbours is a false dichotomy. As such, a combined second-nearest correlation,

$$\mathcal{C}_{2nn} = \mathcal{C}_{2nn\text{-}L} + \mathcal{C}_{2nn\text{-}T},$$ (6.5)

is a more appropriate figure of merit. This parameter is plotted against the first-nearest-neighbour correlation, $\mathcal{C}_{1nn}$, in Fig. 6.6(d). Error bars reflect ± 1 standard deviation when the data are averaged over all samples.

Figure 6.7 displays vertex maps obtained after annealing $0°$, $15°$, $30°$, $35°$, $40°$, and $45°$ tilings. Similar to the mode of presentation in Chapter 5, each vertex is represented by a colour-coded square. Each panel contains at least 15×15 vertices, reflecting the cut made to remove spins close to the edges of the array. The square ice array [Fig. 6.7(a)] displays long-range ordered T_1-domains. Where the two possible T_1 ground states abut, they are separated by string defects formed by chains of T_2 and T_3 vertices. For the pinwheel ice case [Fig. 6.7(f)], the majority of vertices are ferromagnetic but the ordering appears purely short-ranged. A variety of structures is observed, including zig-zag domains, small uniformly magnetised regions
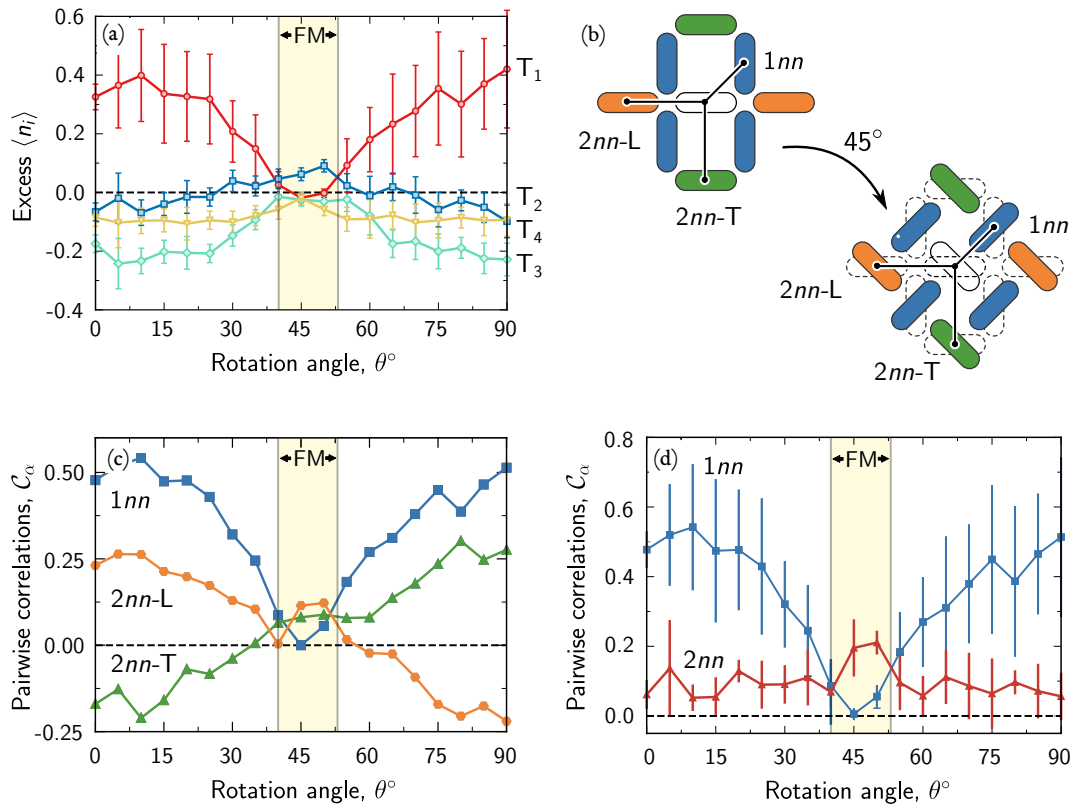
Figure 6.6: A transition in ground state ordering with rotation angle. (a) The change in excess fractional populations of T_1, T_2, T_3 and T_4 vertices with rotation angle, θ. Error bars reflect ± 1 standard deviation when the data is averaged over all samples. (b) The schematic distinguishes between three classes of near neighbours pairs in square and pinwheel ice: $1nn$, $2nn$-L, and $2nn$-T. (c) Correlations, $\mathcal{C}_\alpha$ for these are calculated as described in the text. (d) For pinwheel ice, there is no difference between $2nn$-L and $2nn$-T neighbours and so a combined $2nn$ correlation is plotted. This dominates in the FM phase. For each plot, the dashed, horizontal line refers to the expected statistics for an uncorrelated sample while the shading highlights the angular region for which there are more FM T_2 vertices than AFM T_1 vertices.

and flux closure states [marked (i.), (ii.) and (iii.), respectively]. Comparing these panels, we find a gradual transition from AFM T_1-dominated arrays to a short-range, incoherent T_2/T_3-majority arrays near to $\theta = 45°$.
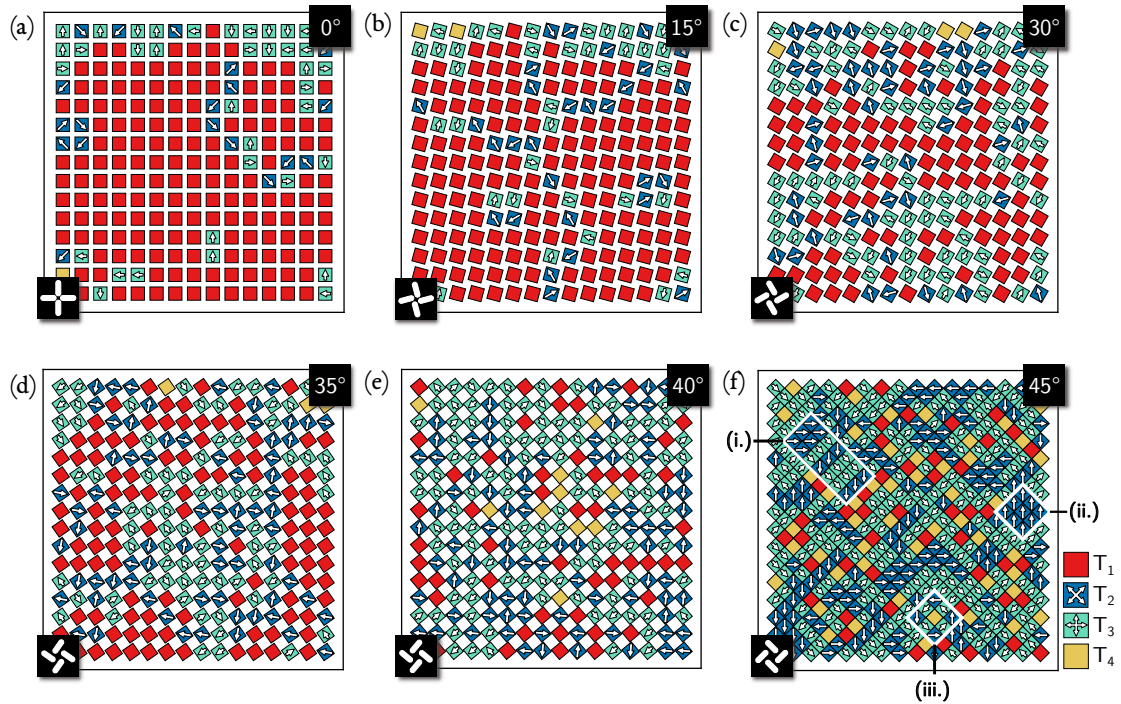
Figure 6.7: Typical annealed configurations in terms of vertex type for 0°, 15°, 30°, 35°, 40°, and 45° tilings (reading left-to-right then top-to-bottom). Each 15×15 configuration is drawn from the central 'best contrast' portion of an experimental array. Each square represents a four-island-vertex in the array as depicted in bottom left hand corner of each panel. The vertex moment (magnitude and direction) is shown using arrows for FM vertices. Over the course of this rotation series, we see a breakdown from large T_1 domains in the square ice, to small FM T_2/T_3 domains in the pinwheel ice. Three such structures are marked in panel (f): (i.) a zig-zag domain; (ii.) a uniformly magnetised domain and (iii.) a small flux-closure structure.

6.4 | Quench behaviour

6.4.1 On estimating the correlation length

In general, the experimental results appear to confirm the predicted change in sublattice ordering. However, neither aggregate populations nor spatially resolved vertex maps show an abrupt transition between antiferromagnetism and ferromagnetism. Rather, the long-range T_1 coverage for geometries near to square ice breaks down gradually to be replaced by FM T_2/T_3 domains with dimensions spanning only a few lattice constants in pinwheel ice. To get deeper insight, we attempt a more sophisticated analysis of the correlations based on the equal time two-point correlation function. This will allow us to extract the typical cluster size as a function of angle.

A vertex encompasses four islands, all mutually within $1a$ [Fig. 6.1(e)]. In this sense, it constitutes the smallest cooperative length scale for which AFM and FM ordering can reasonably be defined. To quantify the decrease in correlation length with angle, we calculate

$$\mathcal{G}(r) = \langle \mathbf{s}_i \cdot \mathbf{s}_j \rangle, \tag{6.6}$$

for the ensemble of island moments. This is the *disconnected* form of the correlation function in which the thermal average, $\langle \mathbf{s}_i \rangle$, is not subtracted. Calculating $\langle \mathbf{s}_i \rangle$ over the limited range of samples with good signal-to-noise proved difficult. Clearly, the functional form of eq. (6.6) decouples the two perpendicular sublattices, and offers no information on their cross-talk. Fig. 6.8(a) presents a spatially resolved form of $\mathcal{G}(r)$ for square and pinwheel ice [(i.) and (ii.), respectively]. Square ice shows a strong AFM signal (roughly speaking, alternating red and blue squares) out to at least $5a$. Correlations in the $45°$ pinwheel tiling decay much faster though all second nearest neighbours (markers closest to the centre of the pattern) show a positive correlation, consistent with ferromagnetism.

Plotting the staggered correlator in Fig. 6.8(b), there exists a sharp fall in the correlations between $0°$ square ice and $45°$ pinwheel ice. The noise floor is taken as 0.05 by inspection of the long-term behaviour of square ice. We can define an integrated correlation length,

$$\xi^{\text{int}} = \int \mathrm{d}r |\mathcal{G}(r)|, \tag{6.7}$$

in analogy with the integrated correlation time of Chapter 3, Sect. 3.6. This gives a correlation length of $\sim 16a$ in square ice but only $\sim 4a$ in pinwheel ice [Fig. 6.8(c)].

6.4.2   Relaxation timescales

We justify this decrease in correlation length with angle by considering the effect of inter-island interactions on the likelihood of flips. This analysis will show that the rotation angle determines the timescale needed to establish equilibrium. In general, arrays approach their ground state by making a number of Ising spin flips. Each flip may or may not be energetically favourable but is driven by some local fluctuation, ΔE, on a scale set by the interactions in the system and, hence, indirectly by ϑ. Instances of these fluctuations allow the spin to overcome the intrinsic energy barrier to switching, E_{b}. For simplicity, we take $E_{\mathrm{b}} \gg \Delta E(\vartheta)$, to be the same for every island and in every geometry. It is common to assume a Néel-Arrhenius law for the switching behaviour [287] such that the rate, Γ, at which a process occurs is

$$\Gamma = \frac{1}{\tau_0} \mathrm{e}^{-\beta(E_b - \Delta E)}. \tag{6.8}$$

In this, we have approximated the effect of the fluctuation through a concomitant reduction in the size of the barrier. That is, E_b is taken as the energy barrier for an isolated island to switch. The energy difference between the initial and final states then acts to adjust slightly this energy barrier. An analogous effect in chemistry, the Bell-Evans-Polanyi principle, relates the activation energy for a process with its enthalpy of reaction. Some studies weight the effect of the fluctuation by a factor of one half, under the assumption of a symmetric transition path [23]. Other works do not, and merely provide an estimate for Γ [271]. Comparing rates in the T_1-excess arrays (typified by the 0° case) to that in the T_2-excess arrays (typified by the 45° case), we obtain the ratio

$$\frac{\Gamma_{0°}}{\Gamma_{45°}} = \frac{\mathrm{e}^{-\beta(E_{\mathrm{b}} - \Delta E(0°))}}{\mathrm{e}^{-\beta(E_{\mathrm{b}} - \Delta E(45°))}} \tag{6.9}$$

$$= \mathrm{e}^{\beta(\Delta E(0°) - \Delta E(45°))}. \tag{6.10}$$

In arriving at eq. (6.9), we have neglected any angular dependence in the prefactor, τ_0. In a fuller treatment, the attempt frequency would be affected by the diminution in interaction strengths with ϑ. For example, studies using harmonic transition state theory have shown
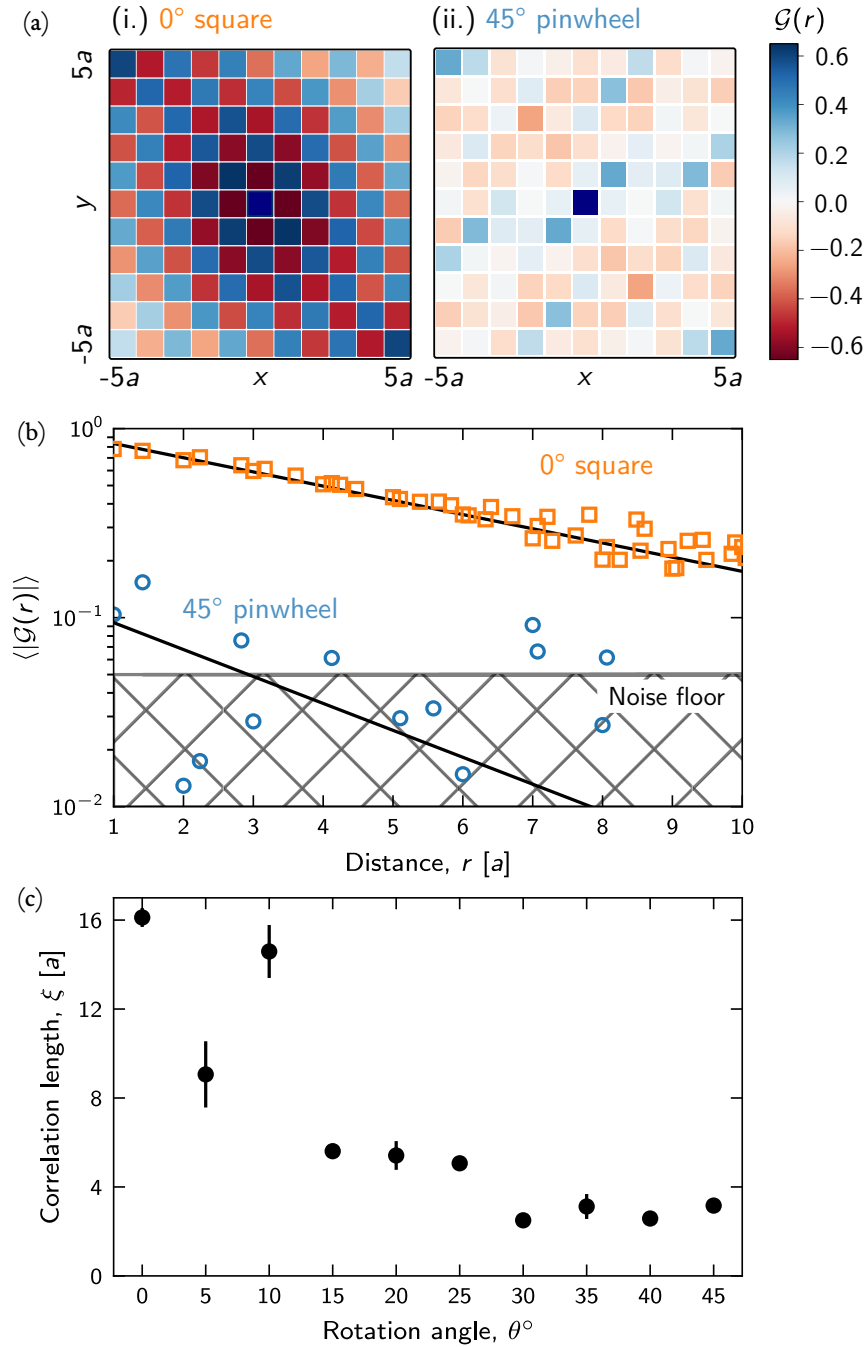
Figure 6.8: Behaviour of the two-point correlation function for square and pinwheel ice. (a) Spatially resolved maps up to $5a$ of $\mathcal{G}(r) = \langle \mathbf{s}_i \cdot \mathbf{s}_j \rangle$ for (i.) $\theta = 0°$ square ice and (ii.) $\theta = 45°$ pinwheel ice. Both maps are plotted with the same colour scale. AFM correlations i.e., alternating red/blue markers, are apparent in square ice. Correlations in pinwheel ice are less pronounced though all markers closest to the origin possess the same positive correlation. (b) The staggered correlators for square and pinwheel ice are plotted on semilogarithmic axes. Correlations in square ice show the expected trend whereas those in pinwheel ice decay almost immediately. (c) The integrated correlation length, ξ^{int}, is shown against angle for $\theta \in [0°, 45°]$.

that symmetry reduction can lead to a signifcant decrease in τ when comparing one and two ring kagome ASI arrays [272]. In fact, when calculating both ΔE and τ in this scheme, the change in the prefactor can have a larger effect on the rate than the reduction in barrier height. This may be relevant for weakly coupled geometries, such as near to pinwheel ice, where different magnetic configurations are almost degenerate, and there exists the likelihood of a return to the initial state after subsequent spin flips. Nonetheless, approximating the islands as point dipoles, the largest interaction strength in square ice (originating from the first-nearest-neighbours, $J_{1nn} = 3\sqrt{2}\,\mathcal{D}$) is six times greater than the largest interaction energy in pinwheel spin ice (originating from the third-nearest-neighbours, $J_{3nn} = \mathcal{D}/\sqrt{2}$). Associating the size of the fluctuation with the largest interaction term, the ratio of the rates at 250 °C should go as $\Gamma_{0°}/\Gamma_{45°} \approx 10$. This estimate suggests that pinwheel ice requires approximately one decade of time more to undergo the same number of spin flips as does square ice.

Fig. 6.9 explores this via Monte Carlo (MC) simulations. In Fig. 6.9(a), we show the percentage of ground state coverage for square and pinwheel ice as a function of the rate at which the systems are cooled from the high-temperature Ising paramagnetic phase. The systems are initialised above their ordering temperatures, and then the temperature is decreased to zero in a variable number of steps; this acts as a proxy for cooling rate. At each temperature point, one MC step is performed and the final vertex population at $T = 0$ is recorded. In the limit of an infinite number of steps, the arrays should explore all phase space and find the true ground state, equivalent to cooling the systems adiabatically. This approach implicitly assumes that our systems are not glassy and do not jam in a metastable minimum. The free energy landscape of a glass tends to have multiple low-energy states separated by activation barriers. In such a case, relaxation times are large and a system can become stuck in a well which is not the ground state. We identify the change in temperature per MC step with a cooling rate, $\mathcal{R}$, an approach compatible with that in Ref. [288]. Pinwheel ice needs to equilibrate for longer to reach a similar coverage of ground state vertices and thus lags behind square ice by approximately one decade of steps.

The weak excess in the numbers of T_2 vertices in the region $[39°, 53°]$ [Fig. 6.6(a)] then reflects the fact that the T_2-preference tilings are quenched to a greater extent than T_1 tilings during the same anneal process. Because of these different relaxation timescales (set indirectly

by the rotation angle), the same annealing protocol will inevitably lead to different amounts of low-energy vertices. By 'quenched', we are not referring to in-built quenched disorder in our arrays, which manifests itself through a spread in the distribution of coercive fields. While it is likely that such disorder makes geometries near to pinwheel harder to thermalise, we refer to the fact that the anneal protocol, which works for square ice, is not necessarily slow enough to drive other tilings to low energies. Fig. 6.9(b) demonstrates this by plotting the excess T_1 and T_2 populations as predicted by MC simulations over the full range of angles for two cases: perfectly annealed infinite systems (dashed-dotted line) and a rapid quench (solid line with markers). These are evaluated at the fast cooling rate marked in Fig. 6.9(a). The perfectly annealed simulations show an abrupt transition between AFM and FM ordering. On the other hand, the quenched simulations—which are purposely not allowed to equilibrate at each temperature step—show excess populations in good agreement with those obtained in the experiment. In particular, there exists only a weak excess in the number of ground state vertices in the region $[39°, 53°]$. The effect of this temperature quench is similar but not identical to that seen in other ASI systems [289], or in Ising and Potts model systems [290], where fast changes in the heat bath temperature lead to a coarsening of domains and a reduction in the correlation length.

At this stage, we emphasise the two separate transitions that these geometries exhibit. Firstly, the ordering within the ground state is controlled by ϑ, i.e. it is a non-thermal transition, controlled instead by a geometrical parameter. In addition, each tiling undergoes a second-order phase transition as the blocking temperature is traversed. In the experiment, a cooling rate of 1.5 °C min^{-1} resulted in a non-uniform degree of ordering for different island rotations. This is a consequence of the fact that relaxation times differ substantially with rotation angle, and so different arrays drop out of equilibrium at different stages during their cooling. This *critical slowing down* arises from the divergence of the relaxation time and correlation length at the phase boundary [103]. Regions of incommensurate symmetries form, separated by topological defects. An example occurs when helium-4 is quenched across the superfluid transition and quantised vortices separate ordered regions [291] Analogously, Zurek proposed that galaxy formation in the early universe was seeded by cosmic strings [292]. The Kibble-Zurek mechanism describes the universal scaling laws underpinning the formation of such

defects with cooling rate. Our experiments allow us to investigate this mechanism for artificial spin ices in a novel way.
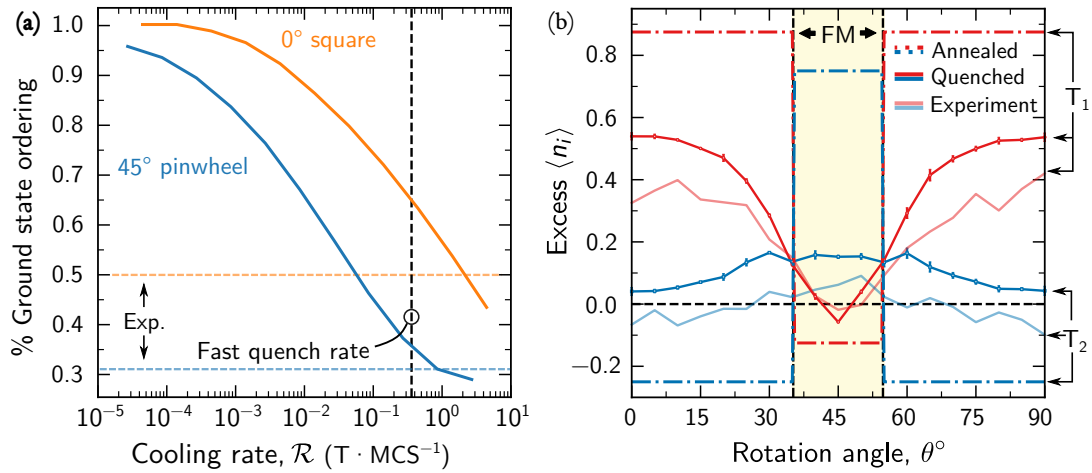
Figure 6.9: Statistics for quenched samples from Monte Carlo simulations. (a) Percentage of ground state vertices as a function of cooling rate from above T_c for 0° and 45° geometries with periodic boundary conditions. The dashed vertical line highlights a fast cooling rate which matches well the populations obtained by our experimental annealing protocol for square and pinwheel ice. In general, the 45° tiling lags the 0° tiling in ground state coverage. (b) Expected vertex populations from MC simulations for both quenched (solid) and perfectly annealed (dashed-dotted) cases across the full angular range, all evaluated at the quench rate marked out in (a). The perfectly annealed samples show abrupt transitions between AFM and FM ordering. In the quenched case, these transitions are smeared out, consistent with the experimental populations of Fig. 6.6 [faded lines]. MC simulations performed for 50×50 vertex arrays with PBC. The angular FM region is consistent with the results presented in Chapter 5.

6.5 | Defect formation and the Kibble Zurek mechanism

Before exploring the Kibble Zurek mechanism in these artificial spin ice geometries, we must first identify what form our defects take in the two phases.

6.5.1   An apparent transition in defect dimensionality

Ordering proceeds in square ASI by the formation of strings—either excited T_2 vertices on a ground state T_1 background [293], or low-energy T_1 vertices on a polarised T_2 lattice [294]. Both these structures are present in our annealed AFM configurations [Fig. 6.7(a)]. For weakly-coupled geometries such as the pinwheel ice, we observe a melting transition mediated by the formation of two-dimensional structures, in particular, vortices. These are composed of nearby vertices, such that the vertex moments circulate around a central core. For angles near to $45°$, the moments in a T_4 vertex are arranged similarly to a vortex, while the moments in a T_1 vertex are akin to an anti-vortex. These are thus short-range equivalents of the closure structures predicted for the array as a whole in Chapter 5.

To quantify the emergence of a vortex regime, we treat the lattice of vertex moments as a discrete vector field, $\mathbf{V}$, and calculate its curl through a finite difference scheme to obtain a measure of the local circulation at each vertex. As the vertex moments are constrained to lie in-plane, only the z-component of $\nabla \times \mathbf{V}$ is non-zero. Wrtiting the vertex moment at the lattice point (i, j) as $\mathbf{V}^{(i,j)} = (V_x^{(i,j)}, V_y^{(i,j)})$, the curl is

$$[\nabla \times \mathbf{V}]_z = \partial_x V_y - \partial_y V_x \tag{6.11}$$

$$\approx \frac{1}{2a}\left(V_y^{(i+1,j)} - V_y^{(i-1,j)} - V_x^{(i,j+1)} + V_x^{(i,j-1)} \right), \tag{6.12}$$

in terms of the components of $\mathbf{V}$ at neighbouring lattice points. For completeness, an equivalent expression for the divergence, $\nabla \cdot \mathbf{V}$, is

$$\nabla \cdot \mathbf{V} = \partial_x V_x + \partial_y V_y \tag{6.13}$$

$$\approx \frac{1}{2a}\left(V_x^{(i+1,j)} - V_x^{(i-1,j)} + V_y^{(i,j+1)} - V_y^{(i,j-1)} \right). \tag{6.14}$$

These quantities are tabulated in Fig. 6.10 for selected configurations of a 3×3 pinwheel lattice. This size was chosen as it is the maximum system size that supports a closure state subject to the experimental correlation length of $4a$ for pinwheel ice. As expected, the pinwheel analogues of vortices and anti-vortices are extrema of the curl and divergence, respectively. The vortex state is the lowest-energy configuration despite incorporating T_4 and T_3 vertices. This is *unlike*

	Vortex	Single domain	Vortex/two-in-two-out hybrids		Anti-vortex
$|\nabla \times \mathbf{V}|$	$2\sqrt{2}$	0	0	0	0
$|\nabla \cdot \mathbf{V}|$	0	0	0	0	$4\sqrt{2}$
$E_{\text{dip}}/\mathcal{D}$	-0.82	-0.66	-0.51	0.22	0.53

Figure 6.10: Sixteen-island pinwheel configurations with direct analogues to structures seen in magnetic thin films. Configurations are arranged L-R in terms of increasing dipolar energy, and classified according to their curl and divergence.
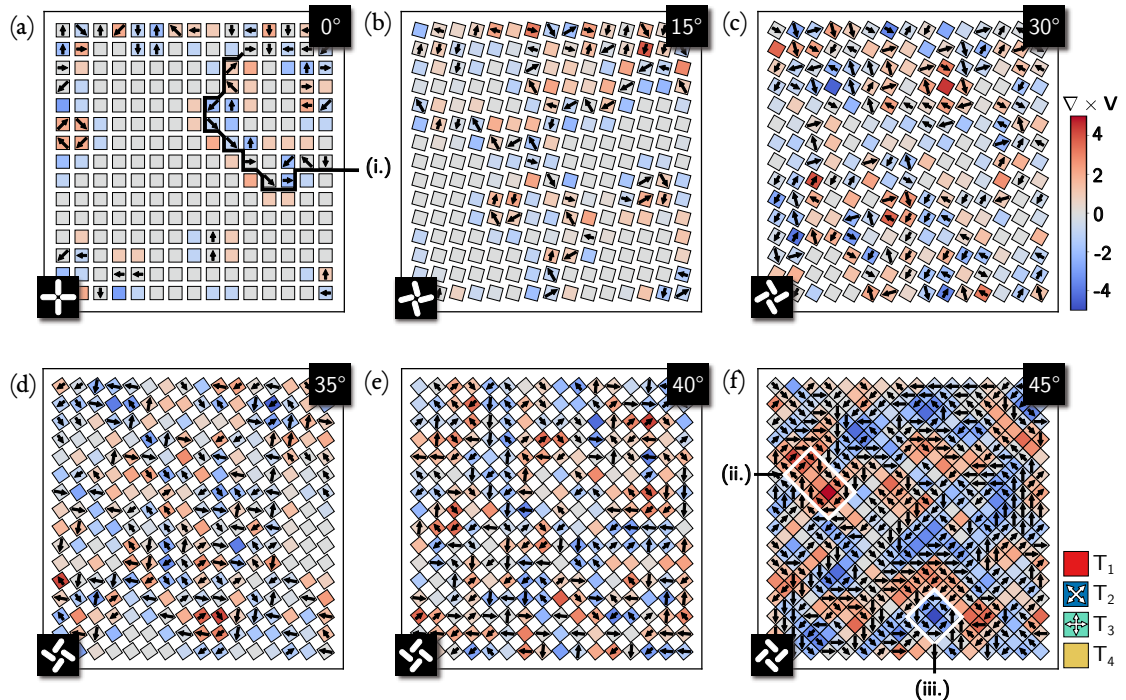
Figure 6.11: Curl maps corresponding to the experimentally obtained vertex configurations in Fig. 6.7. The curl for all tilings is plotted across the same colour scale. Topological defects [(i.) a string in square ice; (ii.), (iii.) vortices, in pinwheel ice] are highlighted.

square ice for which the minimum energy configuration of any array is always a tiling of its ground state vertices, irrespective of system size.

In Fig. 6.11, we display heat maps of $\nabla \times \mathbf{V}$ corresponding to the experimentally-obtained vertex configurations in Fig. 6.7. The curl is plotted on the same scale with the net moment shown atop FM vertices as before. Comparing arrays with different rotation angles (in effect, moving from (a) to (f)), the curl becomes significantly more pronounced and attains a greater magnitude at its peak. Instances of topological defects are highlighted for both square and pinwheel ice; for example, (i.) in Fig. 6.7(a) labels a Dirac string within square ice. In pinwheel ice, the defects are no longer one-dimensional chains but instead two-dimensional; (ii.) and (iii.) in Fig. 6.7(f) mark out instances of vortices with a clockwise and counter-clockwise circulation, respectively. In both examples for pinwheel ice, FM T_2/T_3 vertices surround an inner core of T_1/T_4 vertices. These cooperative structures constitute extrema of $\nabla \times \mathbf{V}$.

Integrating $\nabla \times \mathbf{V}$ over the area of an array then gives a measure of the net circulation. Typical results from our experimental data are shown in Fig. 6.12(a). The solid line is taken from experimental data, and the dashed line refers to the mean statistics expected from MC simulations of quenched finite-size arrays matching those in the experiment. The shaded region highlights ± 1 standard deviation around this mean. It is evident that there is excellent agreement between the experimental data and that taken from MC simulations: both show a clear peak near to $\theta = 45°$ when the system acquires a net circulation through its tendency to form multiple, short-length-scale vortex structures.

This observation is consistent with the idea that the those arrays which have a preference for forming T_2 vertices are dominated by vortices. On its own, however, it is not conclusive proof of a vortex-dominated melting/freezing transition. To show this, we consider MC simulations of the two prototypical angles, $0°$ and $45°$, as a function of temperature in Fig. 6.12(b). Here, we do not quench the systems but quasi-adiabatically increase the temperature from $T = 0$ so as to keep the arrays as close to equilibrium as possible. In both cases, the systems are initialised in their respective ground states. The systems are equilibrated at each temperature point, with a difference between consecutive temperatures of $10^{-5}\,\mathcal{D}/k_b$, which is approximately ~ 4 mK in units appropriate to the dimensions of our islands. For systems with periodic boundary conditions (PBCs), the integrated curl is no longer an appropriate
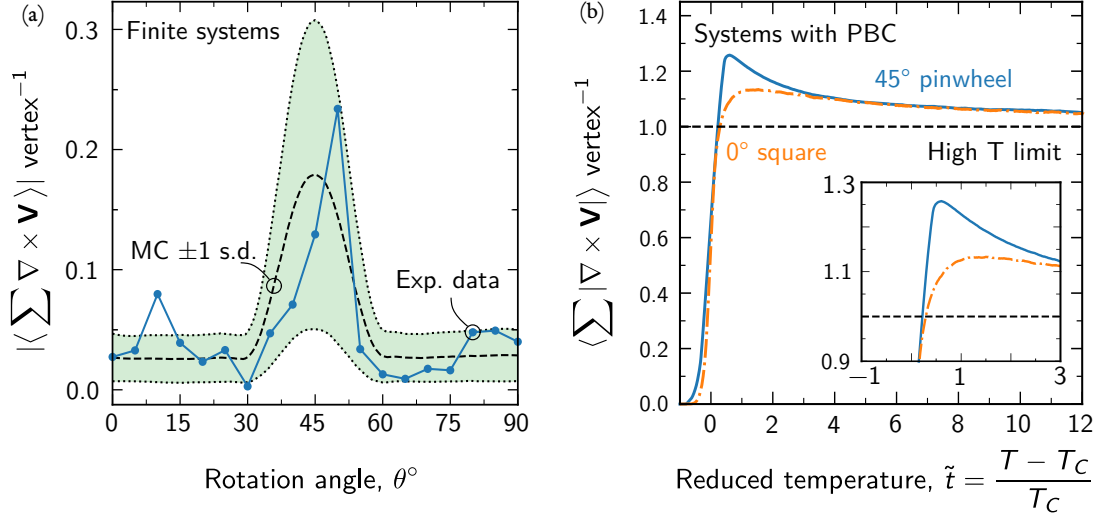
Figure 6.12: Vorticity as a signature of apparent ferromagnetism. (a) For finite systems, we integrate the curl over the area of the array as a measure of the net circulation. The shaded region highlights ± 1 standard deviation around the mean MC statistics (dashed line) for this integrated curl. Both the experimental results (filled markers) and MC statistics for quenched finite-size arrays support the hypothesis that these excitations impart a net circulation in the FM phase. Uncorrelated arrays have an integrated curl of 0 [horizontal, dashed line] due to symmetry. (b) For systems with PBC, we must use the integrated absolute value of the curl. This is shown against temperature. The vortex phase persists even when the arrays are heated quasi-adiabatically. There exists a region around $\tilde{t} = 0$ for which both square and pinwheel ice rapidly produce curl, but this feature is more pronounced in the FM phase.

figure of merit as neither tiling acquires a consistent net circulation in the thermodynamic limit. Instead, we chose the integrated absolute value of the curl. In the paramagnetic limit, this quantity tends to ≈ 1 per vertex.[2] In the low temperature limit, the ground state of square ice (uniform T_1 tiling) and pinwheel ice (uniform T_2 tiling) have $\langle \sum |\nabla \times \mathbf{V}| \rangle = 0$. In Fig. 6.12(b), we plot the evolution of this quantity with temperature. To make a comparison between square and pinwheel ice, we work in reduced units, $\tilde{t} = (T - T_C)/T_C$, in terms of the appropriate critical temperatures, $T_C(\vartheta)$, for each tiling.

---

[2]In fact, it can be shown analytically that the two tilings tend to slightly different limits in the paramagnetic regime:

$$\lim_{T \to \infty} \sum |\nabla \times \mathbf{V}| = \begin{cases} \frac{674 + 223\sqrt{2}}{1024} & \approx 0.966 \text{ vertex}^{-1} \quad \text{for } \vartheta = 0° \\ \frac{15(181 + 248\sqrt{2})}{8192} & \approx 0.974 \text{ vertex}^{-1} \quad \text{for } \vartheta = 45°. \end{cases}$$

Near to the ordering transition at $\tilde{t} = 0$, both systems show curl varying rapidly as a function of temperature. However, this feature is more pronounced and the integrated curl attains a greater magnitude in 45° tiling. As the system melts to a disordered phase, 2D structures—in particular, vortices—proliferate, spoiling the long-range ordering. We emphasise that this vortex-mediated regime persists even when the temperature is changed slowly, as in Fig. 6.12(b). This suggests that these defects play a more general role in establishing magnetic order during melting and freezing. Furthermore, their existence in MC simulations even when PBCs are applied implies that they can nucleate anywhere within arrays and do not simply migrate from edges. Movement of the vortices is observed in MC simulations

6.5.2 Scaling of the defect density in the Kibble Zurek mechanism

The Kibble Zurek mechanism (KZM) is a statement of the expected power law dependence of the defect density with the speed at which the phase transition is traversed. Attributing the mechanism to a system undergoing a phase transition relies on the values of the equilibrium critical exponents, and the scaling behaviour of the correlation length near T_c. For a continuous second order phase transition, the equilibrium correlation length, ξ, and equilibrium correlation time, τ, diverge as

$$\xi = (T - T_C)^{-\nu}; \tag{6.15}$$

$$\tau = (T - T_C)^{-z\nu}, \tag{6.16}$$

where ν is the exponent associated with the correlation length, and z is the dynamic critical exponent. The KZM describes the dynamics of a system as the critical temperature, T_C, is traversed in time. We define a temperature detuning, $\Delta T \equiv T - T_C$, which we assume can be varied linearly so that

$$\Delta T(t) = \mathcal{R}t, \tag{6.17}$$

at time, t, for some rate, $\mathcal{R}$. Here, we use Monte Carlo steps as a proxy for time, meaning $\mathcal{R}$ has units of $T \cdot \mathrm{MCS}^{-1}$. Equating the time to the critical point with the relaxation time yields a timescale,

$$t^* = \mathcal{R}^{\frac{-z\nu}{1+z\nu}}, \tag{6.18}$$

commonly called the *freeze-out* time. Close to the critical point, there exists a region in which the order parameter no longer evolves adiabatically. The average correlation length at this freeze-out time is

$$\xi(t = t^*) = \mathcal{R}^{\frac{-\nu}{1+z\nu}}. \tag{6.19}$$

Previously in Chapter 5, we demonstrated that this class of geometries belongs to the 2D Ising universality class. Assuming then the exponents relevant to that transition ($\nu = 1$, $z \approx 2.1665$ [295]), the expected value for the KZM exponent is ~ 0.315.

6.5.3 Numerical evidence of the Kibble Zurek mechanism in ASI

To complete this discussion, Fig. 6.13 examines the correlation length, ξ, as extracted from the two point correlator, $\mathcal{G}(r) = \langle \mathbf{s}_i \cdot \mathbf{s}_j \rangle$, and the defect density, $\langle \sum |\nabla \times \mathbf{V}| \rangle$, as a function of cooling rate, $\mathcal{R}$, for square and pinwheel ice using MC simulations. We have chosen $\nabla \times \mathbf{V}$ as a measure of the defect density as it appears a natural choice to identify the vortices which form in T_2-excess arrays. It is not necessarily as good a measure in the AFM tilings where another quantity—string length, perhaps—would be more appropriate. Note that in the scheme outlined in eq. (6.11), the curl is based on the sum and difference of the components of neighbouring vertex moments. The vertex moments are themselves simply the sum of the island moments in each vertex. Taking the absolute value introduces products of at most two spin components—exactly the same as in the two-point correlator. We thus expect $\langle \sum |\nabla \times \mathbf{V}| \rangle$ to scale similarly to the correlation length except with the opposite sign to reflect its nature as a density: $\langle \sum |\nabla \times \mathbf{V}| \rangle \sim \xi^{-1}$.

The integrated curl in pinwheel ice exhibits a peak [dotted vertical line, Fig. 6.13(b)]. We relate this feature to the freeze-out behaviour predicted by the KZM. There appears a maximum cooling rate beyond which pinwheel ice cannot respond to changes in temperature. For fast cooling rates, the curl stays close to the high temperature limit, and even vortices appear frozen out.

We perform a least squares fit to the linear portion of each series in Fig. 6.13 and extract the exponents (values ± 1 standard deviation are listed in Table 6.1). All values are close to those predicted for the 2D Ising universality class. Other universality classes would predict different

	Scaling Exponent	
	ξ	$\langle \sum \lvert \nabla \times \mathbf{V} \rvert \rangle$
$\vartheta = 0°$	-0.340 ± 0.005	0.370 ± 0.004
$\vartheta = 45°$	-0.332 ± 0.018	0.314 ± 0.017

Table 6.1: Best fit critical exponents for ξ and $\langle \sum \lvert \nabla \times \mathbf{V} \rvert \rangle$ associated with cooling rate, $\mathcal{R}$. Extracted from the linear portion of each series in Fig. 6.13 for $\theta = 0°$ square and $\theta = 45°$ pinwheel ice. Assuming only the KZM and the equilibrium critical exponents of the 2D Ising model, these quantities are predicted to scale with $\mathcal{R}$ as $\sim \pm 0.315$. Uncertainties refer to ± 1 standard deviation in the least squares fit used.

scaling exponents. For example, it would be natural to draw an analogy between the formation of vortex structures in the pinwheel tiling and those vortices which depin during a Kosterlitz-Thouless transition. However, the exponential behaviour of the correlation length even at the critical point in a Kosterlitz-Thouless transition gives rise to a more complex dependence on $\mathcal{R}$, i.e. one which is not simply some form of power-law. Further, assuming the asymptotic values of the critical exponents [296] in this case (an approach which neglects key aspects of the KZM as applied to the Kosterlitz-Thouless transition [297]) would give an estimate for the scaling exponent of ~ 0.5. We have thus shown numerically that these geometries appear to obey the KZM, consistent with the 2D Ising universality class.
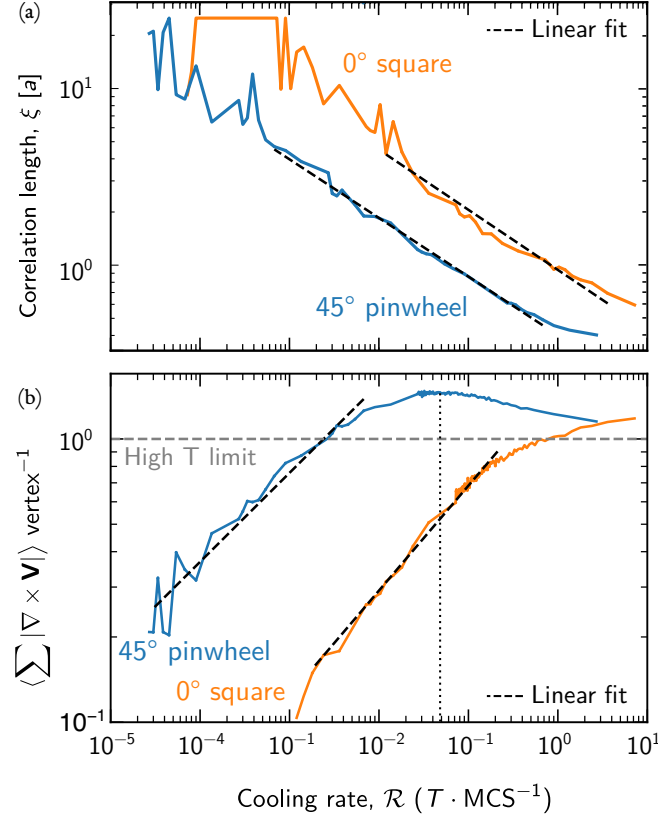
Figure 6.13: Scaling of correlation length and defect density with cooling rate. (a) Correlation length, ξ, in units of the lattice constant, a, as a function of cooling rate for square and pinwheel ice. Taken from parallel tempering Monte Carlo simulations of 50×50 vertex arrays (10000 spins) with PBC. (b) As in (a) but for the appropriate defect density, $\langle \sum |\nabla \times \mathbf{V}| \rangle$. A maximum in the curl density is observed for pinwheel ice at the rate indicated by the dotted line. This corresponds to a rate above which the dynamics of the system remain frozen. The linear portion of each series is used for fitting (points explicitly shown with markers; fits are shown in black dashed lines). Here, cooling rate is measured in units of temperature, T, per Monte Carlo step. Adapted from Ref. [2].

6.6 | Discussion

In this chapter, we have probed experimentally the transition in sublattice ordering between square and pinwheel ice. Using LTEM on thermally annealed Co arrays, we found evidence of a transition from AFM T_1-majority arrays near to square ice to arrays which show a slight preference for FM T_2 ordering near to pinwheel ice. Values of ϑ close to the transition give rise to competition between phases. In fact, thermalising better those arrays may open up the

possibility of probing the ice-rule phase in a highly degenerate manifold. Furthermore, arrays comprising a mixture of tiling patterns—square ice, say, joined to pinwheel ice—would offer the opportunity to study phase coexistence at interfaces and, even, engineer an ASI analogue of exchange bias.

Once more, we stress the relative scarcity of the T_2 populations in the FM phase. In ASI, the largest energy scale is set by the coercive field of the individual islands—far larger than even the dipolar coupling between nanomagnets. In this respect, the best natural comparison for these systems would be to ferromagnetic materials with high coercivity. Like ASI, these materials form small domains under demagnetisation. Because it is energetically favourable for them to form, domain walls are relatively numerous and "thin", much as we observe in pinwheel ice.

For tilings close to the pinwheel geometry, experimental limitations mean we were unable to wait till the system recovered all the way to its true ground state, if indeed it would. This is a direct consequence of the change in relaxation timescales as controlled by the array tiling angle. For comparison, in the work of Gliga *et al.* [180], thermally active pinwheel arrays are allowed to relax over some 20 hours from one T_2 configuration to another—one order of magnitude greater than achievable in our setup. This is almost exactly the increase in cooling time that we predict would be necessary to achieve a more pronounced excess of T_2 vertices.

In concert with this transition in ordering, we observe 2D defect textures in the ferromagnetic phase. The densities of these within the framework of Monte Carlo simulations appear consistent with the Kibble-Zurek mechanism at least in terms of the correlation length and integrated squared curl. However, a systematic investigation of their experimental scaling with cooling rate over several orders of magnitude for each individual array would provide conclusive proof. In doing so, identification of all structures—strings, vortices, and domains—would enable the correct defect density to be calculated for a given tiling pattern.

In conclusion, the work reported in this chapter has allowed us to use artificial spin ice to probe phase transitions and non-equilibrium processes such as defect formation. It has also laid a foundation for further studies; in particular around the possibility of observing competing phases in a two-dimensional artificial spin system.

7

From local to global: Configuring artificial spin ice

7.1 | Introduction

So far we have explored the continuum between the square and pinwheel lattice by studying two related aspects of the underlying physics—critical phenomena and ordering. In this chapter, we change focus and discuss a way in which artificial spin ices can be made *configurable*. We outline a hybrid system based on the classic square lattice in which site-specific exchange bias fields are applied to certain islands. These constrain not just their dynamics but the kinetics of the system as a whole, and provide a pathway connecting local fluctuations to global behaviour.

We study the situation in which the pinning repeats at lengths which are integer multiples of the lattice constant, along one sublattice of the square geometry. In what follows, we show that varying the pinning density controls equilibration processes and yields insight into quenched disorder. Further, the pinning period controls the emergence of different magnetic textures in the ground state, including a striped ferromagnetic phase, and an unconventional

charge-ordered state.

The chapter is structured as follows. In Sec. 7.2, we discuss the set-up of this system, its rationale and sample fabrication. In Sec. 7.3, the Hamiltonian of the system is reviewed. We outline how exchange bias is incorporated, and we use micromagnetic simulations to extract a realistic estimate for the coercive field and energy barriers of our islands. In Sec. 7.4, the effect of the pinning on relaxation timescales is investigated. We provide an estimate for the radius of influence that a pinned spin has on its neighbours, and discuss the difficulties of relating the correlation time obtained from Monte Carlo simulations to a physically meaningful measurement. In Sec. 7.5, a model for field-driven spin dynamics is outlined. From this, we compare configurations from a simulated rotating-field demagnetisation to those obtained experimentally by collaborators. Odd and even pinning periodicities are treated separately. Finally, a simulated thermal annealing [Sec. 7.6] highlights how this hybrid system effectively tunes critical phenomena.

7.1.1 Attribution

Much of this work is currently under review [5]. This work arose as part of a collaboration among the Krishnan group at the University of Washington, and the Universities of Manitoba and Glasgow. VMP undertook sample fabrication and subsequent magnetic force microscopy measurements, along with their processing. I am grateful to VMP and KMK for allowing me to include typical experimental vertex maps in this chapter for comparison. Where they appear, these results are acknowledged explicitly in the caption. I performed the micromagnetic simulations, designed the spin dynamics model, provided the interpretation of the pinning in terms of relaxation timescales and its effect on the ground state order, and investigated the critical behaviour. The manuscript was written by VMP and myself; all other authors provided feedback.

The spin dynamics model was originally developed to examine domain wall processes in pinwheel artificial spin ice, and is discussed in Ref. [3]. Routines to implement a variety of field protocols are contained in the software package, JASI [6], which I developed. This model is by no means unique; many others works in ASI employ a similar approach to simulating field-driven processes. Similarly, extracting the coercive field barrier for islands is an extension of

work reported in Ref. [4]. This work investigated the misalignment between the geometrical and anisotropy axes in pinwheel lattices.

7.2 | A hybrid artificial spin ice

7.2.1 Rationale

Previous studies of ASI have concentrated on understanding the collective behaviour of arrays of identical moments, with an emphasis on different lattice geometries in order to explore anisotropic features of the dipolar field (*inter alia* Refs. [8, 298, 22, 84, 180, 16, 2]). Indeed, we have probed exactly this interplay between the spin and spatial degrees of freedom when we considered an island rotation angle. From an applied standpoint however, there is growing interest in designing ASI systems in which specific microstates can be addressed both with [299] and without [300] the help of an external magnetic field. Beyond interest purely in the physics involved, this reconfigurability is a necessary step for practical applications in information storage [301], magnonic crystals [302, 89], and as the architecture for neural networks [94, 303].

As a concrete example, Gartside *et al.* used a scanning technique they christened "topological defect-driven magnetic writing" to realise the hitherto unobserved ground state of the kagome lattice through controlled domain wall nucleation [40, 41]. In a similar vein, adjusting the shape anisotropy of certain islands (in effect, narrowing their width while leaving their length unchanged) during fabrication has been shown to affect avalanche dynamics [304], increase the probability of reaching chiral states [305], and influence the resulting resonance spectra [306]. However, these effects have been limited to relatively small systems, e.g. one- or two-ring kagome lattices.

In this context, exchange bias provides a route to tuning the properties of large ASI systems by adjusting the coercivity of individual islands. Exchange bias is an interfacial effect that occurs at the boundary between a ferromagnet and an antiferromagnet [307, 308]. Ferromagnets are strongly exchange coupled, but often have little or no intrinsic anisotropy. Antiferromagnets, by contrast, have strong anisotropic interactions which make their spin configurations particularly stable [309]. In a heterostructure, coupling between these two materials produces strong exchange interactions and strong anisotropy. This exchange anisotropy is

uni-directional and so the associated hysteresis loop is not centred on the zero-field value but, rather, shifted off-axis. The effect of this exchange bias is to pin the ferromagnetic layer along a specific direction.

In previous work [310], collaborators at the University of Washington constructed an artificial square ice in which an exchange bias field is applied to all islands within one sublattice. This is illustrated for a single vertex in Fig. 7.1(a). The exchange bias is orientated parallel to the long axis of the horizontal islands. In doing so, it effectively pins the magnetisation for these islands and constrains their reversal dynamics. Over the array as a whole, this rearranges the energies of the sixteen distinct vertices such that a classification into four degenerate types is no longer possible. In effect, the geometric frustration of the square lattice is modified by the addition of a global, non-frustrated exchange field. In varying the lattice constant, Ref. [310] observed a transition between antiferromagnetism and ferromagnetism in the configurations obtained from a field-driven demagnetisation.

In this chapter, we consider a natural extension to this idea. Rather than applying the exchange bias field to every island within a sublattice, we restrict it to certain sites. In particular, we consider different periodicities, p, in units of the lattice constant, a, within a sublattice. Varying the periodicity of the exchange bias adjusts the density of constrained spins: a small p means dense pinning; a high p means less dense pinning. This is shown in Fig. 7.1(b,c) for the case of $p = 2a$ and $p = 4a$ lattices. Pinned spins are coloured black; all other spins are identical. We term this *hybrid* square artificial spin ice, written h_{pa}-ASI, as it is a composite of non-identical islands which have either uniaxial (no pinning, Fe only) and unidirectional anisotropy (exchange-biased, Fe and IrMn bilayer). As in [310], the exchange bias field is orientated along the long axis of pinned islands.

7.2.2 Sample Fabrication

Sample fabrication was performed by VMP at the University of Washington. An exchange-biased epitaxial bilayer, composed of 7 nm Fe and 8 nm IrMn, was deposited on MgO substrates using ion beam sputtering. A 2 nm thick layer of Pt was applied to inhibit later oxidation. Epitaxial—as opposed to a polycrystalline—growth helped ensure a uniform direction for the exchange bias. The direction of the bias was controlled by application of external field
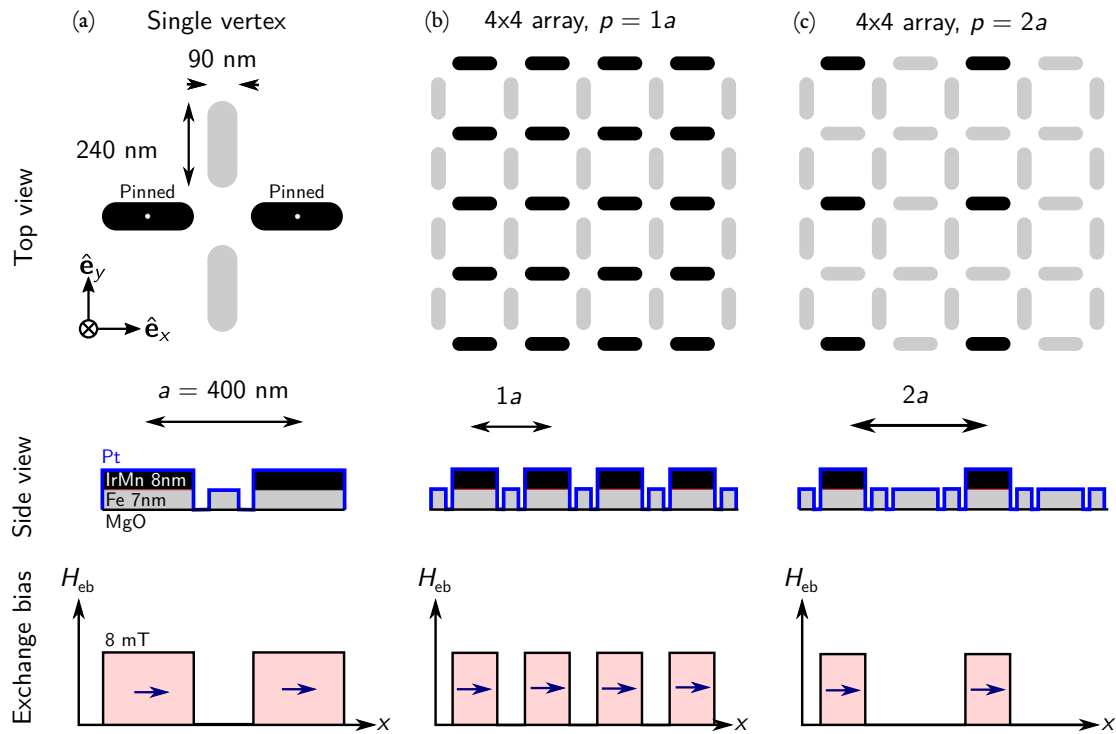
Figure 7.1: A hybrid artificial spin ice with site-specific bias fields. Top row: (a) square vertex in which the two horizontal islands are pinned (solid black). The island dimensions and lattice constant used in this work are marked. We consider different periodicities of the exchange bias pinning, showing examples of (b) $p = 2a$ and (c) $p = 4a$ lattices. Middle row: side view of the corresponding lattices. The arrays are deposited on MgO substrates. Pinned islands are made from an Fe/IrMn bilayer with thicknesses 7 nm and 8 nm, respectively. The IrMn is etched away from unpinned islands, leaving the Fe layer intact. A thin layer of Pt inhibits oxidation. Bottom row: schematic showing the magnitude of the exchange bias as a function of x-position, using the coordinate system indicated in (a). Using MOKE magnetometry, the magnitude of the exchange bias was measured as 8 mT.

during deposition. Subsequent magneto-optical Kerr effect (MOKE) measurements indicated an off-axis shift of the hysteresis loop by 8 mT. A two-step lithographic process was used to fabricate the ASI. First, the sample was patterned into square ice using electron beam lithography. The lateral dimensions of the islands were 240 nm by 90 nm, with a lattice constant, $a = 400$ nm [annotated explicitly in Fig. 7.1(a)]. In the second stage, ion milling removed the IrMn layer from most islands, leaving it intact only on the pinned sites. Less than 1 nm of IrMn was left by this procedure. A full description of this technique is contained in an

accompanying methods paper [311].

7.3 | Modelling the effect of site-specific pinning

For this hybrid ice, we assume that the Hamiltonian separates as

$$\mathcal{H} = \mathcal{H}_{\text{dip}} + \mathcal{H}_{\text{Zeeman}} + \mathcal{H}_{\text{eb}} + \mathcal{H}_{\text{ani}}, \tag{7.1}$$

where the terms on the right-hand-side represent the dipolar interactions between islands, their Zeeman coupling to an external field, the site-specific pinning energy, and their shape anisotropy, respectively.

As justified in Chapter. 5, we assume that our islands are separated sufficiently to be approximated as point dipoles and Ising-like so that their magnetic moment lies in one of two stable orientations. The spin at site i has a magnetic moment $\mathbf{s}_i = M_S V s_i \boldsymbol{\sigma}_i$, with $s_i \in \{-1, +1\}$, an Ising variable which represents the polarity of the spin and $\boldsymbol{\sigma}_i$, a unit vector parallel to its in-plane long axis. In this picture, each nanomagnet sits in the dipolar field of every other, and so the mutual interaction energy of a configuration is

$$\mathcal{H}_{\text{dip}} = \mathcal{D} \sum_{i \neq j} s_i s_j \left[\frac{\boldsymbol{\sigma}_i \cdot \boldsymbol{\sigma}_j}{r_{ij}^3} - \frac{3(\boldsymbol{\sigma}_i \cdot \mathbf{r}_{ij})(\boldsymbol{\sigma}_j \cdot \mathbf{r}_{ij})}{r_{ij}^5} \right]. \tag{7.2}$$

The second term in eq. (7.1) is the Zeeman energy which couples the magnetisation of each island to the external field, $\mathbf{B}_{\text{ext}}$, through

$$\mathcal{H}_{\text{Zeeman}} = - \sum_i \mathbf{s}_i \cdot \mathbf{B}_{\text{ext}}. \tag{7.3}$$

The exchange bias is incorporated in a similar way by positing an additional effective Zeeman contribution at pinned sites

$$\mathcal{H}_{\text{eb}} = - \sum_{i, \text{pinned}} \mathbf{s}_i \cdot \mathbf{B}_{\text{eb}}, \tag{7.4}$$

where $B_{\text{eb}} \approx 60\,\text{mT}$ is the magnitude of the pinning field. We emphasise that this term applies only if site i has been pinned. Since exchange bias is an interfacial effect mediated by atomic-scale interactions, the pinning field does not extend beyond the island to which it is applied.

Finally, each moment is constrained to lie parallel to its in-plane long axis, which appears as a uniaxial anisotropy contribution to the total energy,

$$\mathcal{H}_{\text{ani}} = -\sum_i K_i (\mathbf{s}_i \cdot \boldsymbol{\sigma}_i), \tag{7.5}$$

where $K_i > 0$ is the anisotropy constant of island i, and the sum runs over all islands in the array. This can be equivalently restated as each island has a coercive field barrier, B_c^i, which must be overcome before the moment can reverse. We now turn to estimating this energy barrier for the islands used in experiment.

7.3.1 Estimating energy barriers

We are interested in comparing the results of experimental field-driven protocols with simulation. This requires an estimate of the coercive field required to switch an island. We make the following assumptions: the rotation of the magnetisation is coherent (discussed in Chapt. 6, Sec. 6.2.3); the dimensions are as listed in Sec. 7.2.2, which imply $\Delta\mathrm{D} = 0.025$ [274]; and the saturation magnetisation of iron is $M_S = 1.7 \text{ MAm}^{-1}$ [55]. Then, the energy barrier for an isolated island is

$$E_{\text{b}} = \frac{1}{2}\mu_0 \Delta\mathrm{D} M_s V \approx 43 \text{ eV}, \tag{7.6}$$

The characteristic scale of the dipolar interactions, given by

$$\mathcal{D} = \frac{\mu_0 (M_S V)^2}{4\pi a^3} \approx 0.6 \text{ eV}, \tag{7.7}$$

is significantly weaker.

To obtain a more realistic estimate for E_{b}, we perform micromagnetic simulations using the GPU-accelerated Mumax3 package [98]. The island dimensions and lattice constant match those given in Sec. 7.2.2. The in- and out-of-plane cell sizes were 2 nm and 1 nm, respectively. The exchange constant was 21.0 pJm^{-1}, and the cubic anisotropy of iron was taken as 48 kJm^{-3}, matching the values given in Refs. [55, 310]. The chosen cell sizes are below the exchange length, $l_{\text{ex}} \approx 4.34$ nm, in all directions. The Gilbert damping parameter, α, was set to 0.02.

Fig. 7.2(a) plots the coercive field astroid, $B_c(\alpha)$, as a function of the applied field angle, α, as defined in the inset. The coercive field was determined by the point at which the magnetisation reversed along the in-plane long axis of the island. For a broad range of α near to the direction of the in-plane long axis, the coercive field is between 60 mT and 80 mT—almost exactly the value of the exchange bias used. This suggests that pinned islands have at least double the switching field of their unpinned counterparts. Only when the field is applied near to the hard axis does B_c increase appreciably ($> 140\,\text{mT}$). By way of example, Fig. 7.2(b) shows a hysteresis loop for the horizontal Fe island when the external field is applied at an angle of 45°. The components of the magnetisation parallel (M_x, blue) and perpendicular (M_y, orange) to the in-plane long axis, and that along the direction of the applied field (M_α, green) are shown. At the switching field, 64.6 mT, the magnetisation along the long-axis of the island reverses. This switching field corresponds to an energy, $M_S V B_c = 102\,\text{eV}$, and the transition is abrupt.

In Fig. 7.3, we show the time-resolved evolution of the energy, magnetisation and stray field during this sharp reversal. The applied field is increased by 25 μT from just below to just above the coercive field and quantities are recorded every picosecond. The reversal occurs over the course of one nanosecond. The ends of the islands reverse first, growing in extent before a multi-domain configuration forms at the point of maximum energy. Finally, domains walls are expelled at the edges of the island, aligning its moment with that of the applied field. These steps are illustrated in Fig. 7.3(i)-(iii), respectively. We estimate the barrier height as the difference in energy between that at the peak and at the onset of reversal, which is $E_\text{b} = 52.3$ eV as marked.
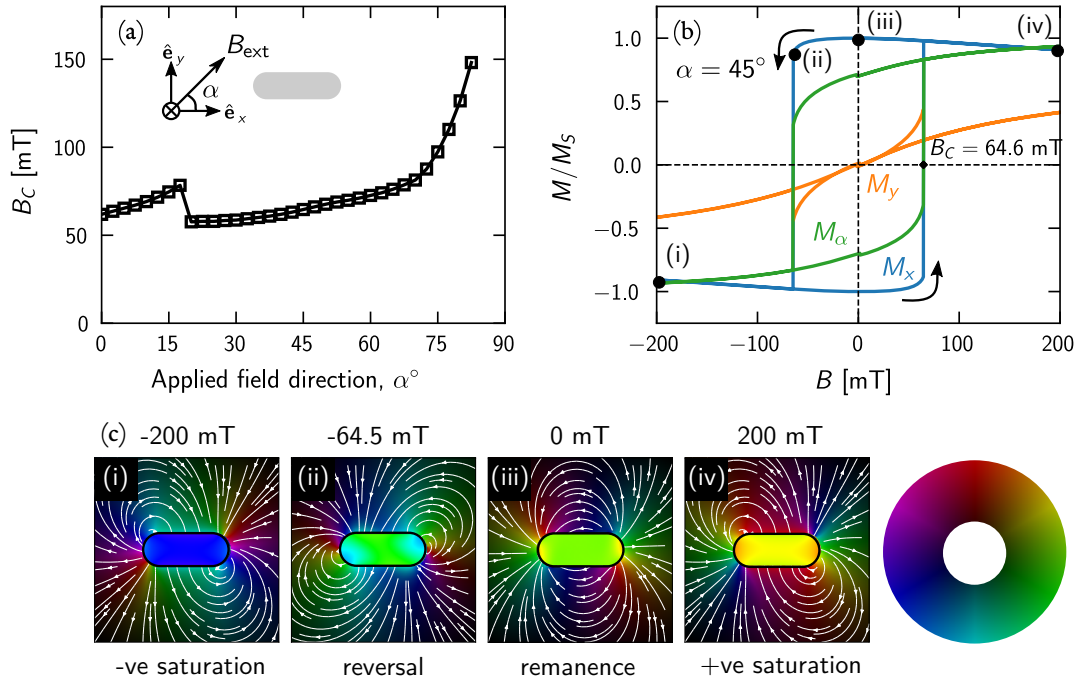
Figure 7.2: Coercive fields and hysteresis loops as a function of applied field angle for an isolated Fe island as taken from micromagnetic simulations. (a) Dependence of the coercive field, B_c, on the applied field angle, α. The inset defines the orientation of the applied field and the simulation grid with respect to the island geometry. For a broad range of applied field angles near to this long axis, the switching field of the island is between 60 mT and 80 mT. (b) Example M-B hysteresis loop when the field is applied at $45°$. The switching field, $B_c = 64.6$ mT, is annotated explicitly. Arrows show the direction of the hysteresis loop. Three components of the magnetisation are drawn: that parallel to the in-plane long axis (M_x, blue); that parallel to the in-plane short axis (M_y, orange); and that in the direction of the applied field (M_α, green). (c) Stray field and magnetisation configurations corresponding to points marked in the hysteresis loop: (i) at negative saturation; (ii) at reversal; (iii) at remanence; and (iv) at positive saturation. The stray field is plotted on a logarithmic scale. The colour wheel represents the orientation and relative magnitudes of the vectors. Dimensions and material parameters match those in experiment.
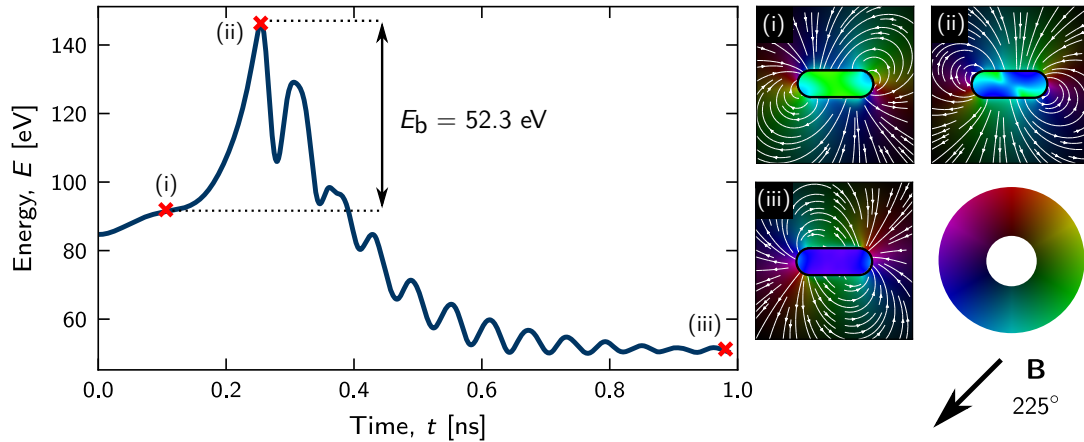
Figure 7.3: Estimating the energy barrier for an isolated island from micromagnetic simulations. (a) Evolution of the sum of the magnetostatic and exchange energies during island reversal. The applied field angle is $\alpha = 225°$ (down-loop of $\alpha = 45°$ hysteresis sequence). At $t = 0$, the field was increased by 25 μT to just above the switching field. The energy, magnetisation and stray field were recorded every picosecond during island reversal. As marked, the energy barrier is approximately 52.3 eV. Three configurations are shown: (i) at the start of the reversal, island with a net moment to the right; (ii) at top of the energy barrier, where an approximate multi-domain state has formed within the island; and (iii) in equilibrium, post-reversal, where the island macrospin points to the left. The stray field is plotted on a logarithmic scale. The colour wheel represents the orientations and relative magnitudes of the vectors.

7.4 | Engineering relaxation timescales

7.4.1 Pinned spins as source of an effective bias field

Now, we consider the effect that introducing a pinned spin has on neighbouring islands in the lattice. We will assume that a pinned spin always aligns with its exchange bias field, $\mathbf{B}_{eb}$ and so it remains constant. The pinned site effectively tilts the local energy landscape by biasing nearby spins through its dipolar field. This assumption—that pinned spins are effectively frozen and do not reverse—is supported by our micromagnetic estimates and confirmed by the experimental results which we will report in Sec. 7.5.

Fig. 7.4 illustrates this biasing effect by showing the net dipolar field from a pinned spin evaluated at the position of its immediate neighbours. The arrows are scaled and orientated
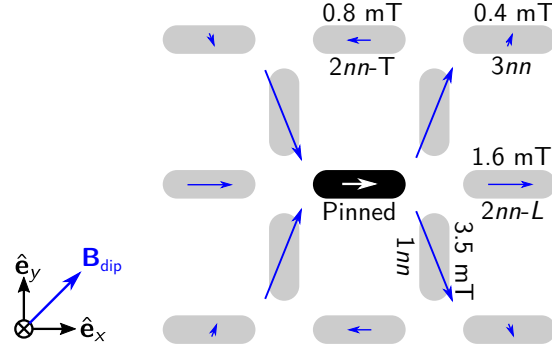
Figure 7.4: A pinned spin (central island, black) acts as a source of an effective bias field on its neighbours through the dipolar interaction. The arrows indicate the magnitude and direction of this dipolar field, $\mathbf{H}_{\mathrm{dip}}$, acting on islands out to $3nn$. Its magnitude is greatest for nearest neighbours, although remains a substantial fraction of the exchange bias field even out to $3nn$.

according to the magnitude and direction of the dipolar field, assuming the nominal island dimensions and parameters. As in previous chapters, we adopt the naming convention of Wang. *et al.* [8] and discriminate amongst first nearest-neighbours ($1nn$), second nearest neighbours located in the same vertex ($2nn$-L), and second nearest neighbours which span adjacent vertices ($2nn$-T). To this, we now also consider third-nearest-neighbours ($3nn$). The dipolar field from the central pinned spin is greatest for the $1nn$ neighbours, and remains a substantial fraction of the exchange bias field even out to $3nn$. However, it is still well below the coercive fields as estimated using micromagnetic simulations.

To quantify the influence of this bias field, we consider its effect on relaxation timescales. Within the framework of a Metropolis-Hastings Monte Carlo, we can define the time displaced autocorrelation of a single spin at site i through

$$\mathcal{C}_i(t) = \int \mathrm{d}t' \Big(s_i(t') s_i(t' + t) - \langle s_i \rangle^2 \Big), \tag{7.8}$$

where $s_i(t)$ is the polarity of spin i at time t. Here, time is measured in units of Monte Carlo steps (MCS). We perform 1000 independent simulations of a 20×20 array (1600 spins) with periodic boundary conditions, in the presence of a single pinned spin at its centre. The simulations are allowed to equilibrate for 10^5 MCS, at which point fluctuations in energy are less than 1%. Then, the dynamical evolution of each spin is recorded for a subsequent 10^5 MCS and compared with statistics drawn from a reference array which contains no pinning.
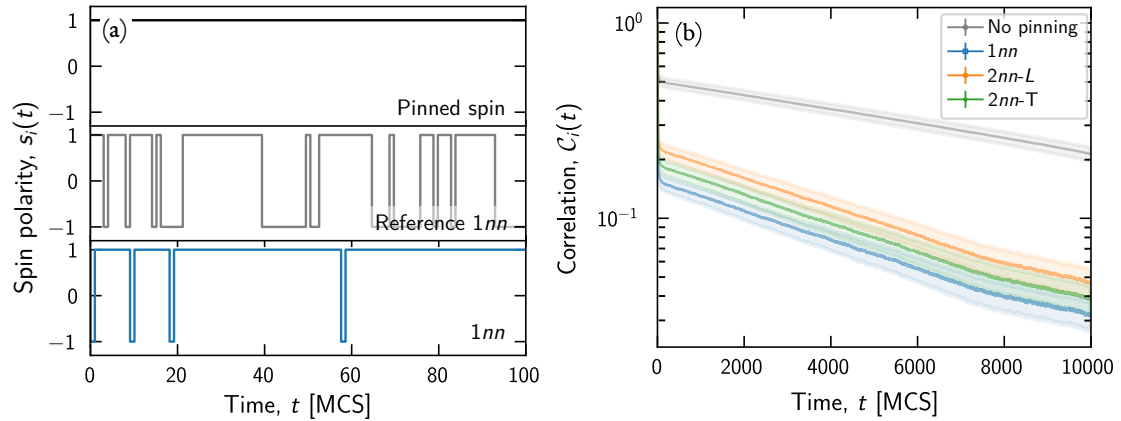
Figure 7.5: Influence of a pinning site on the autocorrelation of neighbouring spins. (a) Example time series for $s_i(t)$ for three cases: a pinned spin [upper panel], a reference spin belonging to an unpinned array [middle panel], and the first nearest neighbour to a pinned spin [bottom panel]. Time is measured in units of Monte Carlo steps (MCS), and the simulation is carried out at the critical temperature of the square lattice, $T_C = 7.2\,\mathcal{D}\,k_B^{-1}$. In our model, the polarity of a pinned spin is not allowed to change i.e., $s_i(t) = +1$ for all t. (b) The autocorrelation, $\mathcal{C}_i(t)$, is evaluated at T_C for the first- and second-nearest-neighbours to a pinned spin. The autocorrelation function of a reference spin in an unpinned array appears in grey. Data are averaged over 1000 independent realisations; the standard error is shown as a shaded region around the mean. The overall effect of pinning is to supress fluctuations of nearby spins.

Representative time series for the polarity are shown in Fig. 7.5(a) for three cases: (i) the pinned spin, which has a fixed polarity for all time, t; (ii) a generic spin taken from the unpinned reference array; and (iii) the first-nearest neighbour to a pinned spin.

Rather than evaluate the autocorrelation directly via eq. (7.8), it is computationally simpler to use (fast) Fourier transforms.[1] After [139], it can be shown that $\mathcal{C}_i(t) = \mathcal{F}^{-1}\{\tilde{\mathcal{C}}_i(\omega)\}$, where $\tilde{\mathcal{C}}_i(\omega)$ is the power spectrum defined through

$$\tilde{\mathcal{C}}_i(\omega) = |\mathcal{F}^{-1}\{s_i(t) - \langle s_i \rangle^2\}|. \tag{7.9}$$

In Fig. 7.5(b), we plot $\mathcal{C}_i(t)$ evaluated at the critical temperature, $7.2\,\mathcal{D}\,k_B^{-1}$, of the square ice lattice for the first- and second-nearest-neighbours adjacent to a pinning site. For comparison,

---

[1]We will write $\mathcal{F}\{f\}(\omega)$ to indicate the Fourier transform of a generic function, $f(t)$.

the behaviour of a reference spin belonging to the unpinned lattice is also drawn. The autocorrelation function for the near-neighbour spins decays faster than for the reference spin, which suggests that fluctuations are reduced as a consequence of introducing pinning.

In general, we expect $C_i(t)$ to drop off exponentially in time with a characteristic timescale, τ, the correlation time [139, 141]. The integrated correlation time is defined through

$$\tau_{\text{int}}^i = \int C_i(t)\,\mathrm{d}t, \tag{7.10}$$

as discussed in Chapter 3. For a given spin, τ_{int} is a measure of the time required for two subsequent measurements to be independent or, equivalently, for the spin to forget its starting state. In h_{pa}-ASI, this timescale depends on the distance, r, between a given spin and the nearest pinning site i.e., $\tau_{\text{int}} = \tau_{\text{int}}(r)$. Fig. 7.6 explores a comparison between the correlation timescales in the singly pinned and unpinned arrays. While the autocorrelation time is known to scale with system size, we are interested in a comparison amongst those spins closest to the central pinned island (i.e., relatively far from the boundaries), and between the behaviour of these spins and their counterparts in an unpinned reference array. This explains our choice of a relatively small lattice in which to simulate this process. We note in passing that that similar behaviour is observed in a 40×40 vertex lattice, though the exact value of τ_{int} differs in accordance with the scaling relation, $\tau_{\text{int}} \sim L^z$, where L is the system size and z is the dynamic critical exponent [139]. Fig. 7.6(a) makes clear that the introduction of single pinned spin does not alter the correlation time of bulk quantities, such as the magnetisation, $\langle m \rangle$. Both the singly pinned array and the reference array agree to within statistical errors, and there is no appreciable movement of the critical temperature. Locally however, correlations are affected. Here, τ_{int} is reduced by up to 60% for spins closest to the pinning site [Fig. 7.6(b)].

Finally, by plotting the variance, $\langle s_i^2 \rangle - \langle s_i \rangle^2$, as a function of temperature and, separately, distance from the pinning site [Fig. 7.7(a,b), respectively], we provide an estimate for the effective radius over which fluctuations are affected. In Fig. 7.7(b), we choose to evaluate fluctuations at the critical temperature as the spatial correlation length is largest here. Working at T_C thus provides an upper bound for the influence exerted by the pinned site. The data for the pinned system approaches the uniform value found for the unpinned array at
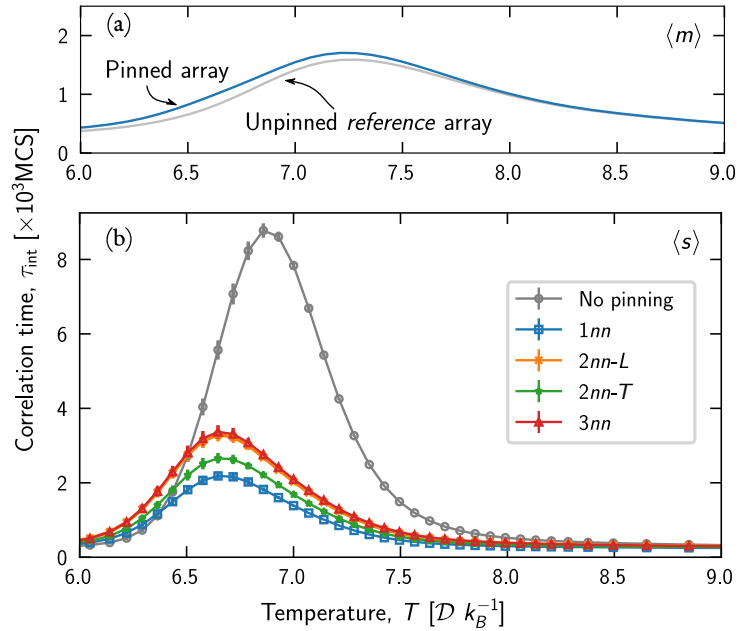
Figure 7.6: Effect of introducing a single pinned spin on the integrated correlation time, τ_{int}. (a) Integrated correlation time of the staggered sublattice magnetisation, $\langle m \rangle$, as a function of temperature for the singly pinned array (blue) and unpinned reference array (grey). The introduction of the single pinned island does not affect this bulk correlation time as the two cases overlap. (b) Individual spin correlation times are affected. The behaviour of four neighbours to a pinning site is considered; a $1nn$ island (blue), a $2nn$-L island (orange), a $2nn$-T island (green), and a $3nn$ island (red) are compared to the correlation time taken from the unpinned array (grey).

$r \sim 6a$, demonstrating that the long-range effects are to all intents and purposes confined within this radius.

At this stage, we can draw an analogy with the effect of impurities in bulk spin ice materials. Revell et al. consider the situation in which extra magnetic Dy ions are substituted for non-magnetic Ti ions in the pyrochlore $Dy_2Ti_2O_7$ [312]. The extra magnetic impurities act as "stuffed" spins which adjust both the density of excitations and the relaxational dynamics of the system.

7.4.2 On obtaining physical measures of the timescales

Our analysis of relaxation has been performed solely within the framework of equilibrium Monte Carlo, where we have quoted results, in particular, in terms of an abstract time unit, the
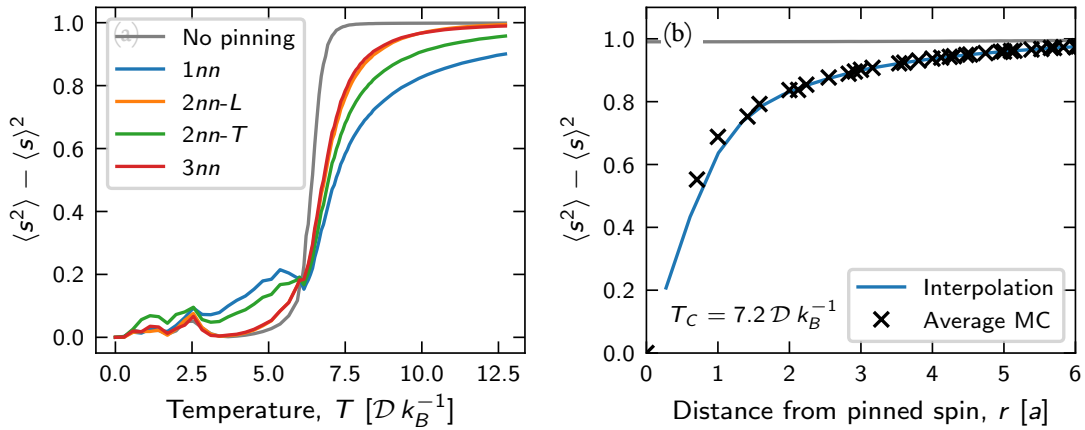
Figure 7.7: Estimating the extent to which a pinned spin affects fluctuations of its neighbours. The variance, $\langle s^2 \rangle - \langle s \rangle^2$, is shown as function of (a) temperature, T, and (b) distance from the central pinning site, r. In both plots, the data drawn from the unpinned reference array appears in grey.

Monte Carlo step. There is not necessarily a general link between the evolution of a simulated system in Monte Carlo time and the evolution of a physical system in real time [254] although a phenomenological rescaling may allow for a comparison in certain situations [313, 314]. The lack of direct correspondence arises because a Markov chain is a stochastic process, whereas a real system is governed by a deterministic equation of motion. Often then, τ_{int} is seen as a purely statistical quantity which indicates how well successive configurations of the Markov chain are decorrelated. In this section, we justify how equilibrium Monte Carlo timescales can be compared with the temporal behaviour of a physical system.

Existing work in spin ice has demonstrated that Monte Carlo timescales match well to experimentally measured relaxation times when they are appropriately weighted by an activation barrier [312, 315]. Separately, Nowak *et al.* have provided an interpretation of Monte Carlo time in terms of the underlying physical processes [316, 317]. This 'time-quantified' method relies on associating Monte Carlo time with the timescale predicted by Langevin dynamics [318], and has been applied to magnetic hyperthermia [319], thermally-assisted switching [320], and magnetoresistance measurements in arrays of dipolar-coupled nanoparticles [321].

In general, the rate, Γ, at which a spin reverses follows a Néel-Arrhenius law,

$$\Gamma = \frac{1}{\tau_0} \exp\left(-\frac{E_{\text{b}}}{k_B T}\right) \exp\left(-\frac{\Delta E}{k_B T}\right), \qquad (7.11)$$

where ΔE is the energy difference between the initial and final states. The quantities τ_0 and E_b are an experimentally determined lifetime and energy barrier, respectively. The pre-factor, τ_0, can vary by several orders of magnitude and depends on the island shape and transition [322, 323, 324]. Our analysis of the integrated correlation time sets τ_0 and the Boltzmann weight of the energy barrier to unity, and probes only the initial and final states through ΔE. In h_{pa}-ASI, the bias field from a pinned spin produces shifts in the energy barriers of neighbouring sites. This suppresses correlation times and fluctuations. We can imagine rescaling our simulated results by an appropriate Boltzmann factor to reflect the activation energy for a given transition. Then, the behaviour of τ_{int} [Fig. 7.6] should carry over to experiment since the evolution in both real and Monte Carlo time does depend on the nature of the free energy landscape i.e., ΔE.

Before closing this section, we note that a kinetic Monte Carlo approach would allow an absolute quantification of the rates in eq. (7.11). This naturally includes a measure of the time for thermal fluctuations without any further need for calibration. Even so, both E_b and τ_0 are often treated as empirical parameters; for example, Farhan *et al.* choose plausible values (E_b = 0.925 eV and τ_0 = 1 Gs) to obtain good agreement with experimental relaxation times in thermally active one- and two-ring kagome lattices [325].

7.5 | Field-driven dynamics

Our samples are too thick to be thermally active and allow for a direct measurement of these relaxation timescales. Indeed, assuming a 1 s measurement time, their blocking temperature is $\approx$ 20000 K—far higher than the Curie or even melting temperature of iron. However, we can compare our prediction that large, long range correlations arise from pinning to the non-equilibrium dynamics that occur during field-driven processes. The physical basis behind this idea is illustrated in Fig. 7.8. Rather than relying on thermal fluctuations alone to overcome the energy barrier to switching [Fig. 7.8(a,b)], the application of an external field can tilt the free energy landscape. When the applied field is of similar magnitude to the coercive field, the islands become susceptible to thermal fluctuations [326] and, therefore, individual macrospins can reverse.

We now consider an alternating field protocol in which a magnetic field is rotated in the plane of the sample and gradually stepped down in magnitude. At the same time, the sense of rotation is periodically inverted. This situation is depicted in Fig. 7.9. During this magneto-agitation, quenched disorder plays a similar role to thermal fluctuations. This disorder reflects an underlying spread in energy barriers caused by variations introduced during fabrication, and opens up extra pathways in phase space between nearly degenerate configurations [267, 22]. In this sense, pinned islands are examples of *structured* quenched disorder i.e., they are sites purposely introduced into the lattice which affect locally the dissipative dynamics. Since they possess a higher coercive field (originating from both the exchange bias and their intrinsic energy barrier), they are expected to freeze at a higher external field.
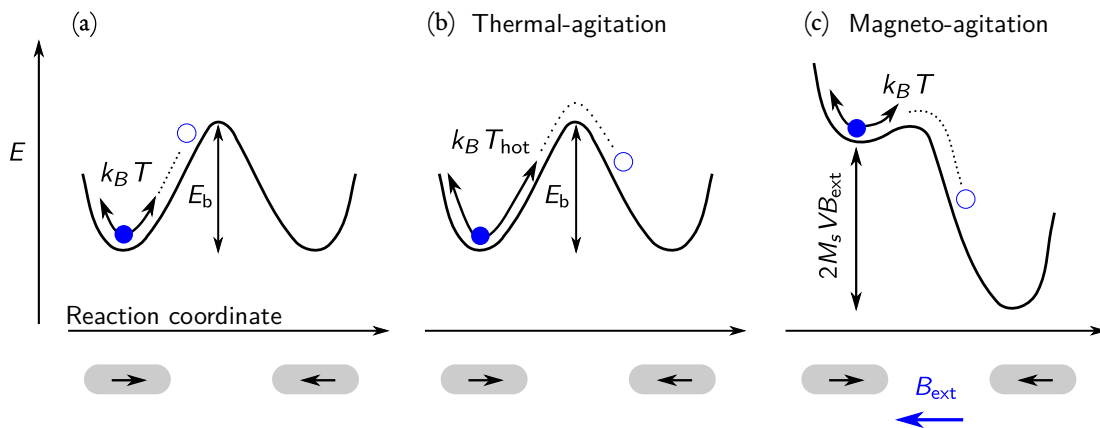
Figure 7.8: Driving artificial spin ice to a low energy state by thermal- and magneto-agitation. (a) The bistable magnetic states of a single island are separated by an energy barrier, $E_b \gg k_B T$. (b) By increasing the temperature to T_{hot}, the larger thermal fluctuations alone may be sufficient to reverse the island (c.f. Chapter 6). (c) The barrier can also be surmounted by tilting the energy landscape with an external field, B_{ext}. This reduces E_b by $M_S V B_{ext}$ as shown. In each panel, the vertical axis labels energy and the horizontal axis is any suitable reaction coordinate (a commonly chosen one is the angle between the macrospin and the in-plane long axis). Compare the schematic in (c) with that presented in Fig. 7.3(a).
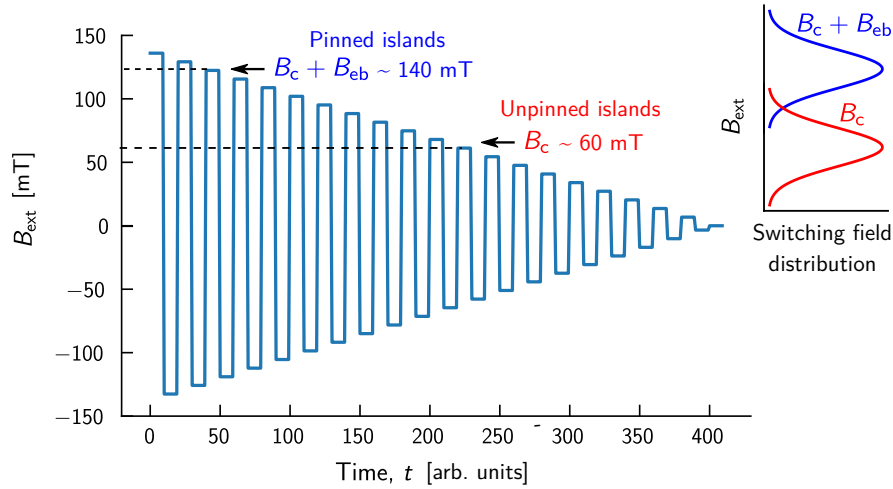
Figure 7.9: Alternating field protocol used to demagnetise h_{pa}-ASI. The field is rotated in plane. After a given number of revolutions, the magnitude is decreased and the sense of rotation inverted. We expect pinned magnets to freeze at higher fields compared with unpinned ones. The coercive fields marked are estimates based on the micromagnetic simulations discussed in Sec. 7.3. In reality, quenched disorder ensures a Gaussian spread in both B_c and B_{eb}, as shown in the inset.

7.5.1 Experimental demagnetisation

VMP performed and analysed the results of the experimental demagnetisation. During the experiment, the samples were rotated at ~ 1000 revolutions per minute between the poles of an electromagnet. They were initially saturated with a ~ 150 mT field. The amplitude of the field was then decreased by $8\ \mu\text{Ts}^{-1}$, and the polarity switched every 2 seconds. This form of protocol has previously been shown to be the most effective at demagnetising ASI samples [327], although it is not clearly understood why the polarity switch of the field should affect the results. Nisoli speculates that peaks in the rate of change of the external field may be essential [64]. Each demagnetisation took 48 hours. Magnetic force microscopy images were obtained using an Asylum Research MFP3D, and processed using Python to extract spin configurations.

7.5.2 Simulated demagnetisation

The most accurate way to model the effect of this field demagnetisation would be to use micromagnetic simulations. This would take impractically long for more than a few islands, though

it does prove useful in obtaining estimates for energy barriers and switching fields (c.f. Sec. 7.3).

We choose a far simpler approach. Dynamics at zero temperature are implemented according to the following condition: a spin, $\mathbf{s}_i$, is flipped if the projection of the total field along its long axis—the sum of the external field and the dipolar fields of other spins—exceeds its coercive field i.e.,

$$(\mathbf{B}_{\mathrm{ext}} + \mathbf{B}_{\mathrm{dip}}^i) \cdot \hat{\boldsymbol{\sigma}}_i > B_c^i. \qquad (7.12)$$

This "threshold-model" is extensively used in the literature and has been shown to agree well with experimental results for athermal ASI subjected to a field protocol [267, 22]. More recent work has implemented a modified Stoner-Wohlfarth criterion [328] in place of relation (7.12), though this produces qualitatively similar behaviour [329]. That this model works so well is somewhat surprising; insight from micromagnetic simulations suggests that the true magnetisation reversal is more complex and often involves the propagation of domain walls within islands.

Note that the switching criterion does not depend on time explicitly. Magnetisation reversal within an island occurs quickly (over the course of one nanosecond, as in Fig. 7.3, and confirmed experimentally by Refs. [330, 331]). This is far faster than the change in field angle or amplitude, and so it is realistic to expect that the system fully responds to each field step before proceeding to the next.

Based on the micromagnetic simulations presented in Sec. 7.3, we know that the energy barrier for an isolated island is at least one order of magnitude above the scale of the dipolar interactions, $\mathcal{D}$. For the rest of this work, we will set $E_{\mathrm{b}} = 30\mathcal{D} \sim 24$ eV, with a Gaussian spread of 10%, equivalent to working in the high disorder regime [267]. This is below the value, 52.3 eV, calculated in Sec. 7.3, though is close to the value used in other studies. The exact value does not matter greatly provided that it is sufficiently above the magnitude of the dipolar interactions. In this regime, changing the value of B_c merely changes the field value at which the arrays as a whole switch.

The field demagnetization protocols are simulated for different pinning periodicities. The system is initialised in a random configuration. At each step, spins are randomly accessed and flipped according to criterion (7.12). After a spin has been flipped, the dipolar fields are

updated and the process is repeated until no more spins can be found. The in-plane field direction is incremented by 1° and the process is repeated. After a set number of in-plane revolutions, the polarity of the field is switched, and its magnitude stepped down by ΔB. In general, two revolutions were sufficient to ensure that the system had reached a steady state near to the coercive field—though this is clearly far less than the number of revolutions used in the experiment. All results presented in this section are averaged over twenty independent realizations of the disorder. Error bars reflect one standard deviation in the statistics. Following the experiment, the reversal percentage of pinned spins was very low ($< 2\%$). To reflect this, in the simulations these spins are assumed to be fixed along the EB direction and no dynamics were permitted. Different array sizes were simulated with different ramp rates, ΔB. An array size of 6400 spins (spanning an area of 40×40 vertices) is chosen as a standard for comparing with experiments. Results were checked up to system sizes of 100×100 vertices and no appreciable difference was seen. This reflects the fact that square ice is dominated by nearest-neighbour dipolar interactions (for example, increasing the system size from $L = 40$ to $L = 100$ changes the dipolar energy density by less than 0.5%). Simulating comparatively small systems thus captures the key physics.

7.5.3   Results

7.5.3.1   Even pinning.   Simulated and experimental vertex statistics for the case of even pinning are presented in Fig. 7.10. Filled (open) markers represent the results the simulated (experimental) protocol. Typical vertex maps from both simulation and experiment are shown in Fig. 7.11. For the first non-trivial even pinning, $p = 2a$, exchange bias is applied at alternate sites in one sublattice [Fig. 7.1(b)]. This breaks the degeneracy of the two usual T_1 ground states, one of which is preferentially selected by the choice of pinning centres. This results in a unique T_1 ground state which can be attained based on a field protocol alone in both simulation and experiment [Fig. 7.11(b,e)]. This is comparable to what can be achieved with a thermal annealing [79]. As the field is reduced, pinned islands freeze first and these bias the local energy landscape in such a way that the formation of a particular T_1 tiling is selected. The pinned spins act as nucleation sites for the ground state configuration and, in particular, when the pinned sites are spaced at even intervals, low energy regions of T_1 vertices are able

to nucleate. These domains are all in-phase, and can grow together coherently. First seen with $p = 4a$ and evident also for wider spacings, T_1 domains of opposite phase begin to appear in regions between the pinning centres. These lead to different topological defects above the antiferromagnetic order, including small T_2 domain walls and T_3 pairs [Fig. 7.11(c,f)] These structures are also observed in thermal annealing experiments [79, 273].

From our analysis of the fluctuations, the influence of a pinned spin extends to about $6a$. Beyond this, we would expect regions more than $6a$ from a pinning site to behave more like unpinned square ice, in which the usual quenched disorder acts as nucleation sites. Clearly, when the T_1 domains around such quenched disorder region are out-of-phase, then domain walls form. For $p > 6a$, the pinning sites are far enough away that their effects become indistinguishable from random quenched disorder and the vertex statistics tend to the $p = 0a$ case. This is confirmed by both experiment and simulation.

7.5.3.2 Odd pinning. Arrays with odd pinning exhibit features distinct from those of the even case. Population statistics and typical vertex maps are shown in Fig. 7.12 and Fig. 7.13, respectively. When $p = 1a$, the islands in one entire sublattice are pinned. Considering just spins in the other, free, sublattice, the $2nn$-L dipolar interaction promotes chains of ferromagnetically ordered islands, while the $2nn$-T interaction ensures that these chains are arranged antiparallel. In this way, pinning results in a system in which the dominant free interaction is that between second nearest neighbours. Thus, the highly constrained h_{1a}-ASI hosts a T_2-dominated array with alternating stripes of uniform magnetisation.

In the case of h_{3a}-ASI, the T_1 ground states which nucleate at adjacent pinning sites are out-of-phase. This leads to the formation of an intricate network of T_2 domain walls along with isolated T_3 pairs; in effect, the pinning elevates the frustration of the square lattice by ensuring that a complete T_1 ground state cannot form. Neither simulated nor experimental field protocols produce a long-ranged ordered state.

As the pinning periodicity is lengthened, the density of topological defects drops as the available area for in-phase T_1 domains expand. For $p \geq 7a$, the vertex populations and maps converge to those of a regular ASI as seen in both experiment and simulation.
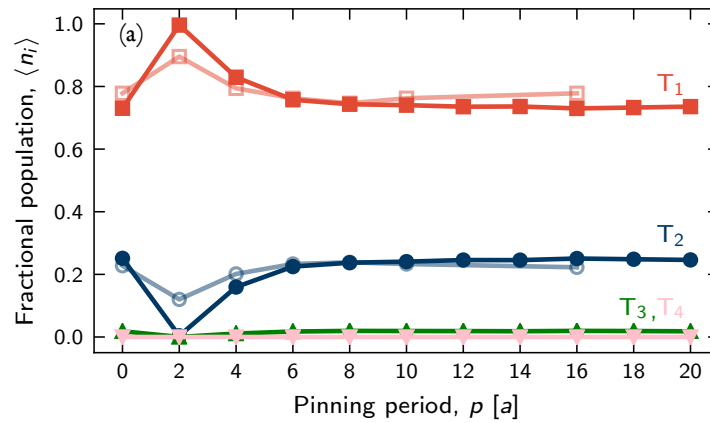
Figure 7.10: Vertex statistics as a function of pinning period, p, for even pinning. Filled and open symbols represent the results of simulation and experiment, respectively. When $p = 2a$, a complete T_1 ground state, i.e, $\langle n_1 \rangle = 1$, is obtained based on field-demagnetisation alone. Above $p = 6a$, the vertex statistics return to those of the unpinned system. Errorbars are less than the marker width. Experimental statistics courtesy of VMP.
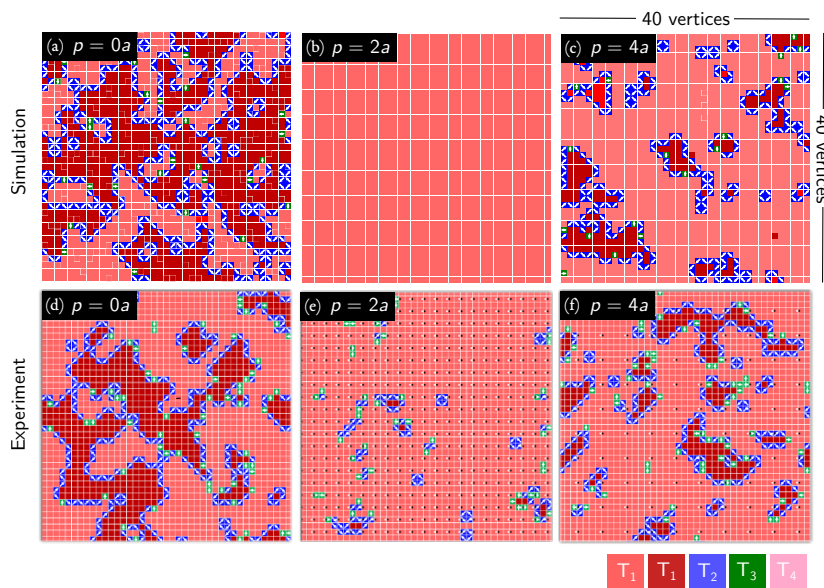
Figure 7.11: Typical vertex maps for the case of even pinning using both simulation and experiment [top and bottom rows, respectively]. For the case of $p = 2a$, an almost complete T_1 ordering is attained based on a field protocol alone. Each square represents a four-island square vertex. Experimental configurations were measured using magnetic force microscopy. Experimental vertex maps courtesy of VMP.
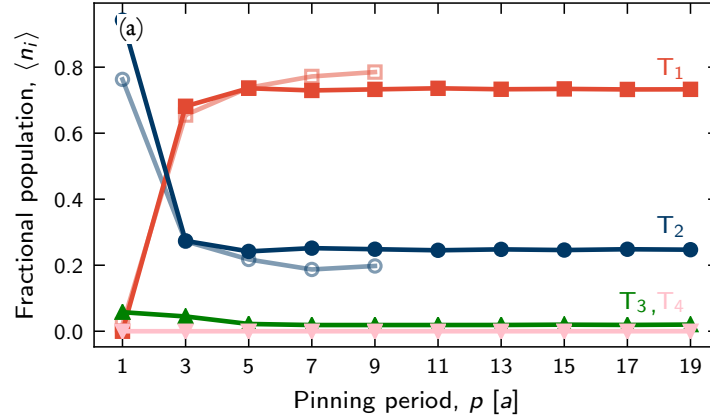
Figure 7.12: Vertex statistics as a function of pinning period, p, for odd pinning. Filled and open symbols represent the results of simulation and experiment respectively. For the highly constrained $p = 1a$ lattice, a transition to T_2 ferromagnetism is obtained in both experiment and simulation. Above $p = 5a$, the vertex statistics return to those of the unpinned system. Errorbars are less than the marker width. Experimental configurations were measured using magnetic force microscopy. Experimental vertex maps courtesy of VMP.
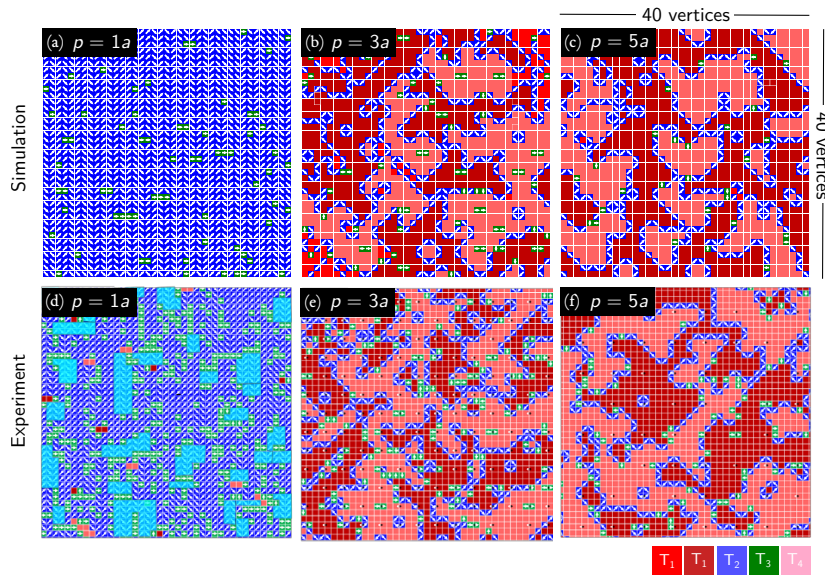
Figure 7.13: Typical vertex maps for the case of odd pinning using both simulation and experiment [top and bottom rows, respectively]. For $p = 1$, there is a transition to striped, ferromagnetic phase. Experimental vertex maps courtesy of VMP.

7.5.3.3 Discussion. Two concluding paragraphs are apposite.

First, excellent agreement has been obtained between the model and the experiment. The slight difference in population statistics observed in Figs. 7.10 and 7.12 are explicable by noting that the field step in simulations is large compared with that of experiment. Generally, a smaller the field step is better as it ensures that the system spends more time near to the coercive field. This is akin to the effect we explored in Chapter 6. In that instance, it was a thermally-driven phenomenon such that waiting longer in the vicinity of the critical point promoted a better anneal. We quantify this effect in Fig. 7.14, where we show how the final vertex populations scale as a function of the field step over two orders of magnitude. The experimental field step is marked. Extrapolating the simulated populations back to the experimental field step gives excellent agreement.
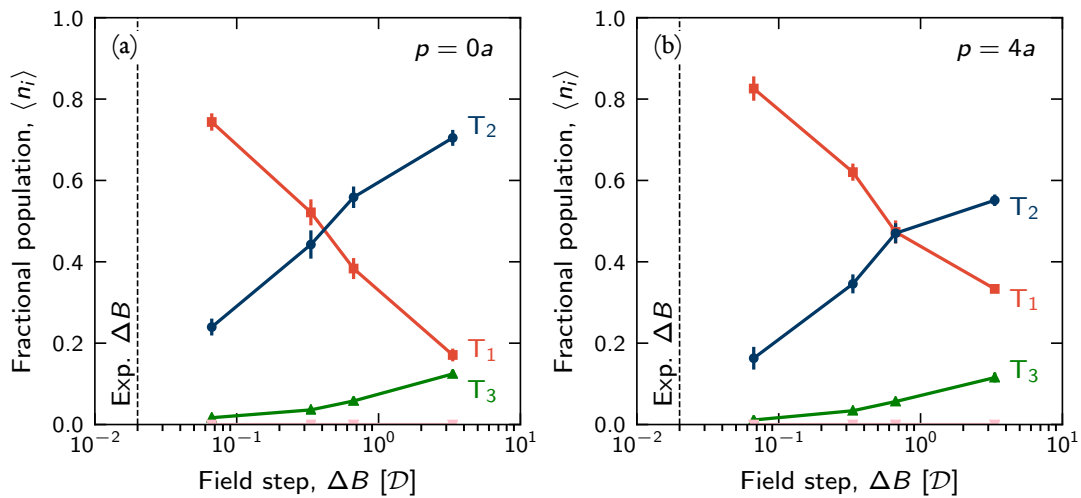
Figure 7.14: Effect of changing the field step, ΔB, on the vertex populations obtained after a field protocol for (a) no pinning, and (b) $p = 4a$. The vertical, dashed line gives the experimental field step, presented in units of the dipolar constant, $\mathcal{D}$. It can be rescaled to a field value according to $\mathcal{D} \rightarrow \mathcal{D}/(M_S V)$.

Second, the consequences of induced correlations are especially clear for the highest pinning densities ($p = 1a$ or $p = 2a$). Varying the pinning periodicity thus allows for engineering vertex populations, and through this, it offers control over the resultant global magnetic texture of an array. As a corrolary, Fig. 7.15 shows the evolution of the four types during the field

protocol (taken from simulation). Changing from $p = 0a$ to $p = 1a$ for example, allows for

population inversion between T_1 and T_2 vertices.
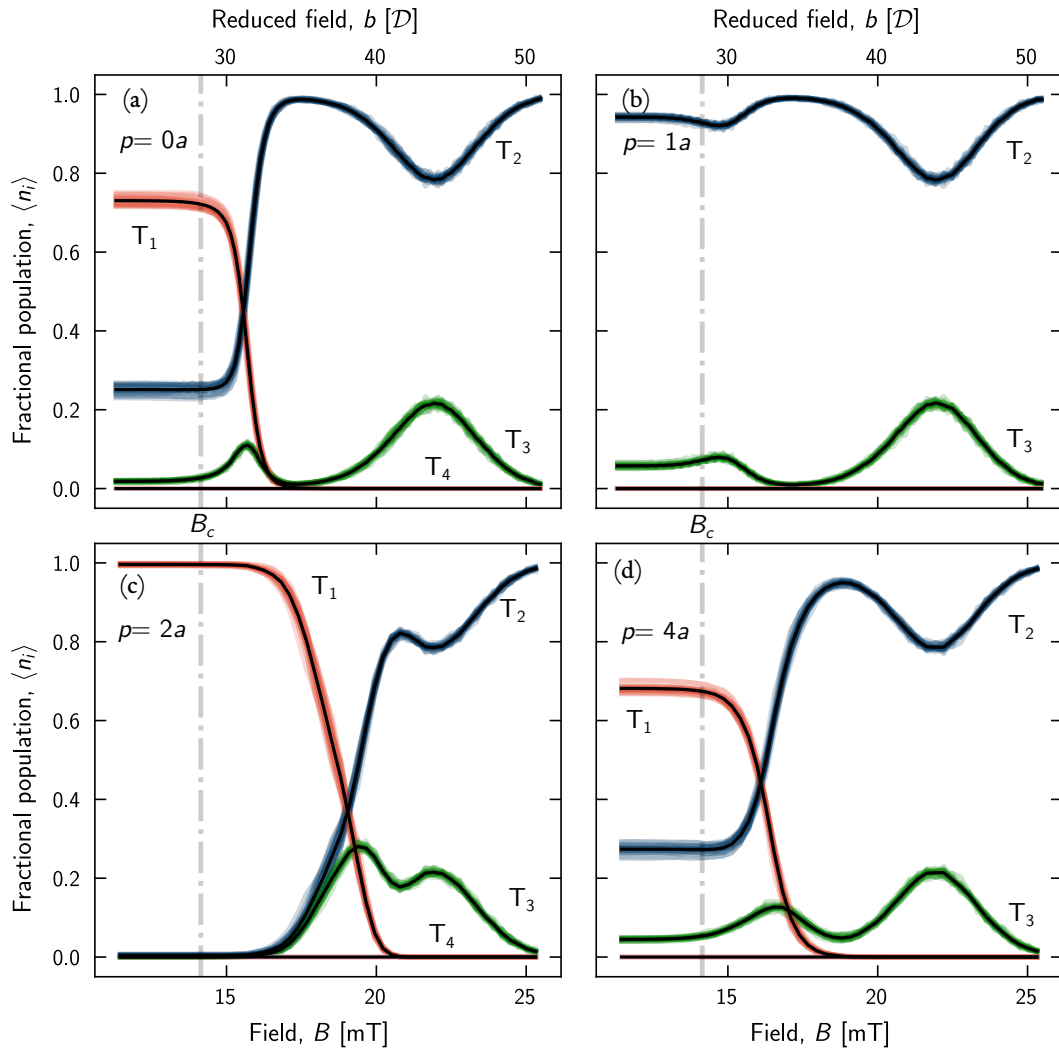
Figure 7.15: Typical vertex populations for (a) no pinning, (b) $p = 1a$, (c) $p = 2a$, (d) $p = 3a$ as a function of reduced field during demagnetisation. Both physical (lower axis) and reduced units (upper axis) are given. The assumed coercive field, $\mathcal{D} = 30$, is indicated by the dashed-dotted line. The system size is $L = 40$ (6400 spins). Populations are shown for twenty independent realisations, with the mean traced in each case by the black line. Oscillations at $b \approx 45\mathcal{D}$ arise from the formation of T_3 domain walls.

7.6 | Thermal processes

As we have seen, field demagnetisation simulations reproduce faithfully the experimental behaviour of the hybrid ice. Neither simulation nor experiment, however, establish definitively the true nature of the long-range ordered ground state in the presence of pinning. To answer this, we use feedback-optimised parallel tempering as described in Chapter 5. Fig. 7.16 displays the heat capacity curves for h_{pa}-ASI. As reminder, the location of the peak marks the transition to the ordered phase. For undoped square ice, i.e., h_{0a}-ASI, this peak occurs at $T_C = 7.2$ $\mathcal{D}\, k_B^{-1}$. Even periodicities of the exchange bias pinning increase the critical temperature while odd pinning periodicities lower it. For the case of p even, this can be explained by noting that the pinning reinforces the ground state order; disrupting it requires larger thermal fluctuations. For the $p = 1a$, a transition from paramagnetic to a zig-zag ferromagnetic phase is observed at a much lower temperature. This is due to the reduced coupling strength as the dominant interaction term is now the second-nearest-coupling. Ground states for the $p = 1a$ and $p = 3a$ systems are shown in Fig. 7.17. A similar logic also holds for p = 3. Here, the regular T1 order is no longer supported, but rather disrupted by the T_3 pairs. Fluctuations are present to lower temperatures. In this way, local pinning allows for control of global critical quantities.

The h_{3a}-ASI exhibits a ground state with two-fold degeneracy comprising a majority T_1 ordering with T_3 pairs at alternating pinning sites. During the transition from the disordered paramagnetic phase to an ordered phase, the system spontaneously adopts one ground state over the other. The T_3 pairs—composed of adjacent vertices with charges, ± 2—are the minimal excitation above the ground state that satisfy the pinning constraint. In this way, the effect of pinning is qualitatively the same as that observed by Fallon *et al.* in the case of ion-irradiated multilayer samples [332]. There, point-like defects that are introduced by a focused ion beam promote the controlled formation of skyrmions. In our system, a large pinning field gives rise to lattice sites which naturally host magnetically charged defects. We have found that this occurs in both field and thermal annealing. Using pinning as a way to seed monopolar vertices within the square ice array enables an interesting avenue for future development [35].
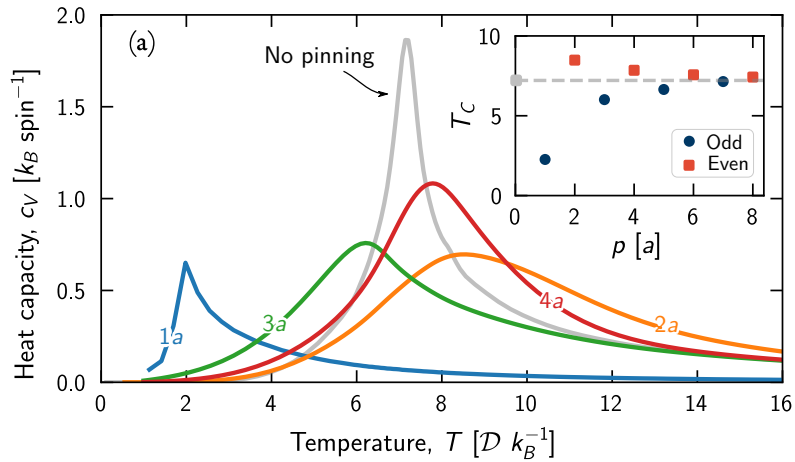
Figure 7.16: Thermal averages for the specific heat capacity, c_v, for different pinning periodicities, p. The unpinned, i.e, $p = 0a$, array is shown by the grey line. The inset shows the movement of the critical temperature with p. Beyond $p = 7a$, there is little movement of the critical temperature at least within the resolution of the simulation. In units appropriate to our arrays, $1\,\mathcal{D}\,k_B^{-1} \approx 8000$ K, with a resolution in temperature of ≈ 150 K. The data are taken from 10 independent simulations of a 50×50 vertex array (10000 spins).
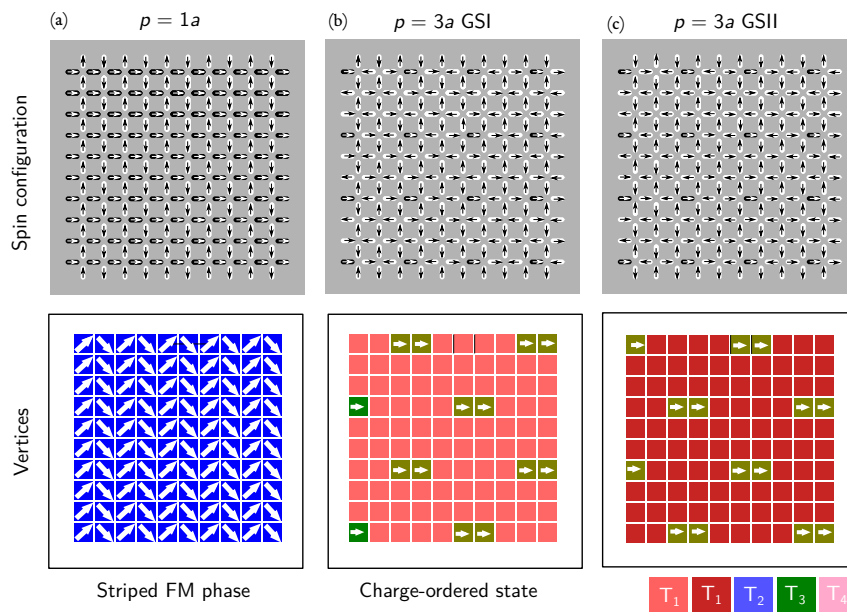
Figure 7.17: Thermal ground state for the $p = 1a$ and $p = 3a$ arrays in terms of their spin configuration [top row] and vertex maps [bottom row]. (a) In the case of the $p = 1a$ system, all spins within one sublattice are fixed. The remaining spins in the other sublattice order antiferromagnetically. This leads to a striped ferromagnetic phase. (b,c) Ground states (GS) of the $p = 3a$ admit charge-ordered monopole/antimonopole pairs at the pinning sites. In this sense, pinning introduces a new frustration into the lattice.

7.7 | Summary

We have explored a hybrid artificial spin ice, composed of islands with both uniaxial and site-specific unidirectional anisotropy. This variant of ASI exhibits different magnetic textures according to a controlled periodicity, p, which allows for a degree of configurability. Exchange-bias is used to apply magnetic fields at local sites of a square ASI. These sites, in turn, narrow the dynamics in phase space and enable control over the ground state configuration. This local pinning offers a route to controlling correlations within arrays, allowing for the engineering of vertex populations. As a corollary, we show that the conventional ground state of square ASI can be achieved based on a field protocol alone for $p = 2a$—in effect, thermal demagnetization without a thermal bath. Monte Carlo results of thermal annealing of this system, show that this hybrid system allows for fine scale tuning of critical phenomena. A variety of magnetic textures is observed: from a zigzag ferromagnetic phase ($p = 1a$) to complete T_1 ordering attainable just through an external field protocol ($p = 2a$) to an unconventional ground state with T_3 excited pairs embedded in the antiferromagnetic T_1 phase ($p = 3a$). The pinning fields then act as *structured* disorder which drive differences in vertex populations. In fact, pinning sites could even be used to seed high energy magnetically-charged vertices within arrays, offering a means to achieve true configurability within a single array. A natural extension to the present work would be to create a thermally active form of this system in which the pinned sites remain frozen while the remaining array is dynamic. Such a structure will offer the opportunity of observing intrinsically interesting phenomena, such as the controlled creation of magnetic monopoles, their dynamics, and phase transitions in the presence of random fields.

8

Conclusions

We shall not cease from exploration

And the end of all our exploring

Will be to arrive where we started

And know the place for the first time.

Four Quartets, Little Gidding, T. S. Eliot

Since the first experimental realisation by Wang *et al.* in 2006 [8], artificial spin ices have proven a fruitful playground in which to explore aspects of low-dimensional magnetism [66]. This thesis is offered entirely in that spirit of adventure. Here, we have played with both the geometry of the underlying lattice and the introduction of structured disorder thereby enabling us to study phase transitions and non-equilibrium phenomena. Superficially, this could be summarised as examining the interesting behaviour that arises when assemblies of tiny magnets are thrown together. However, the tiny magnets in our artificial spin ices were not just scattered randomly on the substrate. Rather, our aim was guided directly by computation into areas which would expand the existing work in this field. Underpinning this thesis lie the twin paradigms that have dominated the study of condensed matter for the past half century:

that *less is more* and that sometimes *more is different*. The first hints at the promise held by nanoscale physics [333], while the second encapsulates the idea that complex, collective behaviour can emerge through combining simple building blocks [334].

8.1 | Results

In Chapter 5, we described the pinwheel ice, which is created by rotating the islands in the canonical square lattice through 45° about their centre. The square and pinwheel geometries thus stand at either end of a continuum, with the rotation angle of the islands acting as a proxy for tuning the interactions. In the square lattice, the dominant interaction is an antiferromagnetic coupling between first-nearest-neighbours, while the relative degeneracy of the pinwheel ice is determined by a weaker ferromagnetic interaction among more distant neighbours. Using equilibrium Monte Carlo simulations, we described an intriguing phase transition: one controlled not by temperature but by the anisotropic nature of the dipolar interaction. This promotes a ferromagnetic-ordered state for geometries close to the pinwheel lattice—an effect termed apparent ferromagnetism [1]. The transition is second order everywhere except at the critical angles where it appears first-order. Finite-size scaling suggests that these geometries belong to the two-dimensional Ising universality class. For pinwheel systems, the array boundary and extent act as an effective anisotropy which determines the domain configurations within arrays.

In Chapter 6, we probed the nature of this predicted transition experimentally using *in-situ* Lorentz transmission electron microscopy on thermally annealed cobalt samples. Consistent with the numerical results of Chapter 5, a preference for ferromagnetic ordering was observed in the pinwheel ice. Near to the transition angles, a planar ice-manifold was recovered. The island rotation angle controls the extent to which the arrays reach equilibrium. This allowed us to study the formation of defects—strings in the square lattice, vortices in the pinwheel—across the two phases. These scale numerically in accordance with the Kibble-Zurek mechanism for defect formation.

In Ref. [132], Sethna provides a framework for classifying phase transitions based on: (i) identifying the broken symmetry; (ii) defining a suitable order parameter; (iii) examining the

excitations; (iv) investigating the topological defects; and (v) interrogating their dynamics. Together, Chapters 5 and 6 provide an almost complete account of the first four of these conditions. In both square and pinwheel ice, as in all disconnected forms of artificial spin ice, the broken symmetry arises from the Ising-like nature of the islands. The vertex populations provide a suitable order parameter for mapping the transition, and topological defects are observed in varying densities across the annealed arrays. Only the last of Sethna's points—a classification of their dynamics—remains.

In Chapter 7, we outlined a hybrid artificial spin ice in which exchange bias is applied to specific sites of the classic square lattice. The effect of the bias is to pin the magnetisation of those islands, which provides a pathway connecting local correlations to global behaviour. By varying the periodicity of pinning, critical phenomena are effectively tuned and different magnetic textures can be engineered. This degree of reconfigurability is a necessary step for device-based applications.

8.2 | What's next?

The results reported in this thesis prepare the ground for many avenues of future research. Here, we briefly discuss a selection, including some that are motivated directly by the work discussed here, and others which, by their very nature, are more speculative.

8.2.1 Short-term

As regards the transition between square and pinwheel ice, what remains to be examined is the thermally active dynamics across both phases. Only a persistent equipment malfunction prevented this work from being included here.[1] Initial data in this area has been taken using samples fabricated using focused electron beam lithography. These show correlated chains of spin flips in both square and pinwheel ice. Further work remains however, including repeating the analysis along the transition angle between ferromagnetism and antiferromagnetism. In any case, this is a task ideally suited to the use of fast pixelated detectors in electron microscopy. These offer frame rates in excess of 100 Hz, and are limited mainly by the available beam

---

[1] A broken heating rod which proved difficult for the manufacturer to repair because it had become obsolete.

current [335, 336]. This is at least three orders of magnitude greater than the temporal resolution of comparable real-space techniques such as x-ray magnetic circular dichroism [34]. Even using soft x-ray photon correlation spectroscopy, which is limited to reciprocal space information, most studies on artficial spin ice appear limited to around 100 ms as a time for image acquisition [337].

Often in this thesis, we have resorted to determining relaxation timescales via an Arrhenius law with a constant energy barrier and prefactor. Forward flux sampling by Desplat *et al.* has shown that assuming a constant attempt frequency is not a sound approach in predicting the retention time of isolated single domain elements [338]. This is because the activation energy for a process can be provided by the heat bath in multiple ways. As to the energy barrier itself, Koraltan *et al.* have found substantial variations for square spin ice, which reflect the multiple pathways for reversal [275]. In tandem therefore, a model for the lifetime of thermally-activated magnetisation processes in artificial spin ice would offer insights into the inter-island interactions.

In a similar vein, the work in this thesis has highlighted the potential for using artificial spin ice to explore the creation and destruction of long-range order in low dimensional systems. Existing work in this area is not conclusive [339]. In fact, it is an open question whether 2D systems melt via an intermediate hexatic phase, as was recently observed in skymionic lattices [340], or whether the transition is purely first order [341, 342]. Examining *in-situ* the behaviour of artificial spin ice as it melts should offer some insight into this topic.

Finally, probing systems exactly on the critical angle between square and pinwheel ice would give the possibility of observing a first order magnetic phase transition in an artificial spin system. Often, these transitions exhibit complex mixed phases which are still not well understood [343].

8.2.2 Long-term

There remain several open questions in the field of artificial spin ice. These span both pure and applied areas.

This thesis has worked exclusively within the two-dimensional Ising universality class, although there exist many other types of phase transitions. Creating novel lattice geometries

to host these—whether Kosterlitz-Thouless [18], Potts [17] or even more esoteric cross-over behaviour [344]—will depend on advances in fabrication using techniques such as focused electron beam induced deposition. As a concrete example, a natural extension to the work in Chapter 7 would involve coupling the islands to a truly random field to create an artificial counterpart of a spin glass. Previous studies in this area have considered tree-like Cayley lattices [345] or positional disorder in the islands [346] but have not yet observed glassy dynamics.

Similarly, the flexibility of artificial spin ice offers the possibility of creating analogues to phenomena observed in bulk crystal. In this vein, inducing frustration at interfaces between tiling patterns, in bilayers, or in three-dimensional extensions of artificial spin ice offers ample scope for investigation. Fig. 8.1 shows examples of these ideas. Combining tiling patterns that support different phases—square ice, say, joined to pinwheel ice—would offer the opportunity to study phase coexistence along edges [347] and perhaps even the possibility of engineering an analogue of exchange bias. Motivated by recent results in graphene [348, 349, 350], we suggest a Moiré superlattice composed of two stacked kagome sheets that are twisted with respect to each other [351]. The effect of this twist on both equilibrium properties and the propagation of magnetically charged vertices merits some investigation, especially in the context of proposed magneto-resistive applications [352, 353]. Branford *et al.* showed previously that single sheets of the kagome ice exhibited an anomalous Hall signal arising from chiral edge modes [354], for which a similar phenomenon has also been noted in bilayer graphene [355]. Any modifications that reduce the energy barrier to the propagation of monopoles, or provide control over reversal branching ratios [356] would prove significant in this respect. Separately, we envisage probing the spectral response of these systems and of three-dimensional artificial spin ice more generally as a vehicle towards designing reconfigurable magnonic crystals. Coupling such systems to a low-damping magnetic spacer layer, such as yitrium iron garnet, may allow spin wave propagation to be directed via the choice of array microstate. Work in these areas is ongoing [89].

Finally, perhaps the most exciting application lies in the realm of nanomagnetic computation and neural networks [66, 38], for which artificial spin ice could act as non-linear reservoir [357]. The initial building blocks of logic gates have been demonstrated [358, 37, 90], although interfacing them with conventional circuity still proves difficult. As of yet, there
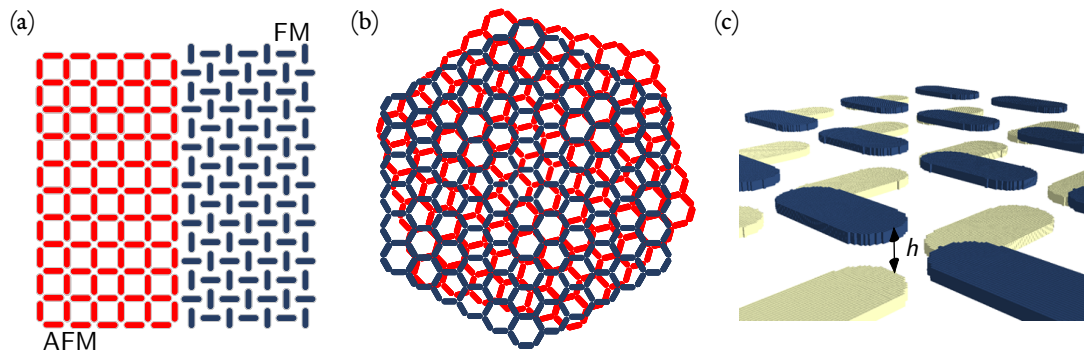
Figure 8.1: New horizons for artificial spin ice. (a) Phase coexistence at an interface between antiferromagnetic square ice and ferromagnetic pinwheel ice [red and blue regions, respectively]. (b) A twisted superlattice, composed of stacked sheets of kagome ice, exhibits a unit cell which changes with mismatch angle. By changing both the mismatch and the interlayer spacing, control over reversal modes may be possible. (c) A spectral analysis of a three-dimensional form of artificial spin ice, in which islands in one sublattice are raised through a height, h, out of the plane with respect to the other, may prove useful for probing monopole deconfinement.

exists no practicable method of adjusting interactions—the weights—on-the-fly in an artificial spin ice array. This necessarily limits their usefulness as elements of a reconfigurable neural network. However, building on an idea expressed in Ref. [39], localised application of temperature to reduce the moment of selected islands may prove one such route to writing microstates directly.

8.3 | Summary

What originally attracted the author to study artificial spin ice was the fact that it remains feasible to combine experiment, theory and modelling. We began this thesis by considering the behaviour of simple, elemental building blocks. We end by returning to where we started, now armed with an enhanced understanding of their emergent behaviour, and with a program for future investigations into artificial spin ice that envisages "no end of all our exploring".

Appendices

A

Atomic force microscopy on FEBID ASI

Samples were fabricated using focused electron beam induced deposition (FEBID) of cobalt (Co) on Si_3N_4 membranes with conditions as reported in the Chapter 6. Atomic force microscopy was performed using a Digital Instruments DimensionTM 3100 Scanning Probe Microscope operated in tapping mode. Measurements were taken by Y. L. and the author. The author processed the data shown here. Fig. A.1 presents thickness profiles of length 5 μm taken across two lines of 7 parallel islands in a typical square ice array. Both profiles suggest that islands closer to the centre of the array are thinner by approximately 1 nm, consistent with the effects of gas diffusion during deposition. Fig. A.2 gives thickness profiles taken across the central portion of six islands (labelled 1-6), each drawn from a pinwheel ice sample. The islands are located in different environments: along the edge of the array (1); at corners (2, 3); within the array but still near to an edge (4); and closer to the centre (5, 6). As with the data in Fig. A.1, islands closer to the central portion of the array are thinner by about 1 nm. The thickness profiles of individual islands are Gasusian-shaped, rather than the sharp-edged, rectangular profiles common to electron beam lithography. In this respect, they are similar to the profiles reported in Ref. [359], except our structures are thinner, by necessit by an order
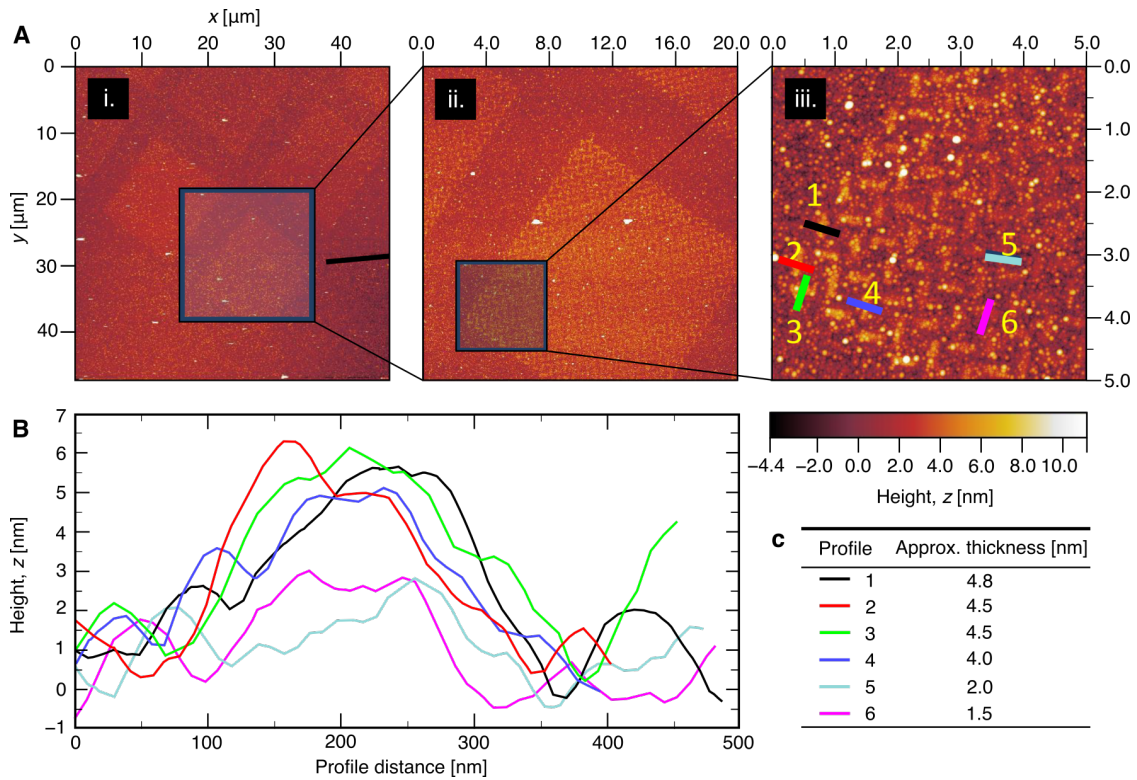
Figure A.1: Thickness profiles of parallel islands in a typical $\theta = 0°$ square spin ice array. (a) Successive scans of a portion of a FEBID square ice array. The approximate locations of islands within a single vertex are shown in panel (ii), right hand bottom corner. Thicker carbon deposits—sputtered onto the membrane prior to Co deposition—create surface roughness. These can dwarf the thickness of the pattern. (b) Line profiles through two sequences of seven parallel islands corresponding to the dashed marks in (a). The thickness decreases from approximately 3 nm to 2 nm closer to the centre of the array. This figure appears in the supplementary to Ref. [2].

of magnitude. Localised carbon deposits can dwarf the thickness of particular islands e.g. the irregular white spots in (ii) of Fig. A.2.
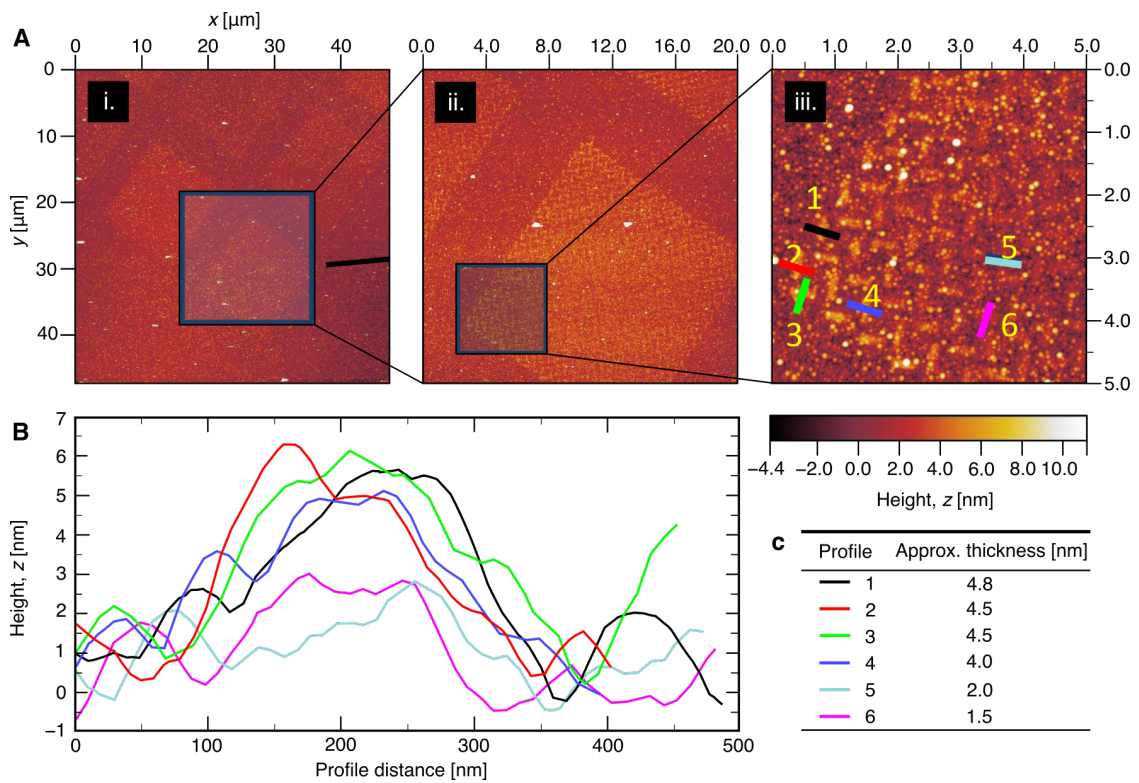
Figure A.2: Thickness profiles of specific islands in a typical $\theta = 45°$ pinwheel spin ice array. (a) Successive scans of a portion of a FEBID pinwheel ice array. Six islands located in a variety of positions are marked in (iii). (b) Thickness profiles of those six islands taken along their width. (c) Table giving the average thickness of the islands over their central portion, neglecting the elongated tails common to FEBID defined structures. This figure appears in the supplementary to Ref. [2].

Bibliography

[1] R. Macêdo, G. M. Macauley, F. S. Nascimento, and R. L. Stamps. "Apparent ferro-magnetism in the pinwheel artificial spin ice". In: *Phys. Rev. B* 98 (1 July 2018), p. 014437. DOI: 10.1103/PhysRevB.98.014437.

[2] G. M. Macauley et al. "Tuning magnetic order with geometry: Thermalization and defects in two-dimensional artificial spin ices". In: *Phys. Rev. B* 101 (14 Apr. 2020), p. 144403. DOI: 10.1103/PhysRevB.101.144403.

[3] Y. Li et al. "Superferromagnetism and Domain-Wall Topologies in Artificial "Pinwheel" Spin Ice". In: *ACS Nano* 13.2 (Feb. 2019), pp. 2213–2222. DOI: 10.1021/acsnano.8b08884.

[4] G. W. Paterson et al. "Heisenberg pseudo-exchange and emergent anisotropies in field-driven pinwheel artificial spin ice". In: *Phys. Rev. B* 100 (17 Nov. 2019), p. 174410. DOI: 10.1103/PhysRevB.100.174410.

[5] V. M. Parakkat, G. M. Macauley, R. L. Stamps, and K. M. Krishnan. "Configurable artificial spin ice with site-specific local magnetic fields". In: (*review,2020*).

[6] G. M. Macauley. *JASI:* a Julia package for Monte Carlo simulations of artificial spin ice. https://github.com/gmacauley/JASI. 2020.

[7] G. M. Macauley. *JIsing:* a Julia package for Monte Carlo simulations of the 1D and 2D Ising Model. https://github.com/gmacauley/JIsing. 2020.

[8] R. F. Wang et al. "Artificial 'spin ice' in a geometrically frustrated lattice of nanoscale ferromagnetic islands". In: *Nature* 439.7074 (2006), pp. 303–306. DOI: 10.1038/nature04447.

[9] Y. Malozovsky and V. Rozenbaum. "Orientational ordering in two-dimensional systems with long-range interaction". In: *Physica A: Statistical Mechanics and its Applications* 175.1 (1991), pp. 127–145.

[10] P. Politi, M. G. Pini, and R. L. Stamps. "Dipolar ground state of planar spins on triangular lattices". In: *Phys. Rev. B* 73 (2 Jan. 2006), p. 020405.

[11] M. J. Harris et al. "Geometrical Frustration in the Ferromagnetic Pyrochlore $Ho_2Ti_2O_7$". In: *Phys. Rev. Lett.* 79 (13 Sept. 1997), pp. 2554–2557. DOI: 10.1103/PhysRevLett.79.2554.

[12] R. P. Cowburn and M. E. Welland. "Room Temperature Magnetic Quantum Cellular Automata". In: *Science* 287.5457 (2000), pp. 1466–1468.

[13] U. B. Arnalds et al. "A new look on the two-dimensional Ising model: thermal artificial spins". In: *New Journal of Physics* 18.2 (Jan. 2016), p. 023008.

[14] V.-D. Nguyen et al. "Competing interactions in artificial spin chains". In: *Phys. Rev. B* 96 (1 July 2017), p. 014402.

[15] C. Nisoli. "Nano-Ising". In: *New Journal of Physics* 18.2 (Feb. 2016), p. 021007.

[16] J. Sklenar et al. "Field-induced phase coexistence in an artificial spin ice". In: *Nature Physics* 15.2 (2019), pp. 191–195. ISSN: 1745-2481.

[17] D. Louis et al. "A tunable magnetic metamaterial based on the dipolar four-state Potts model". In: *Nature Materials* 17.12 (2018), pp. 1076–1080.

[18] R. Streubel et al. "Spatial and Temporal Correlations of XY Macro Spins". In: *Nano Letters* 18.12 (2018), pp. 7428–7434.

[19] D. Schildknecht, L. J. Heyderman, and P. M. Derlet. "Phase diagram of dipolar-coupled XY moments on disordered square lattices". In: *Phys. Rev. B* 98 (6 Aug. 2018), p. 064420.

[20] N. Leo et al. "Collective magnetism in an artificial 2-D XY spin system". In: *Nature Communications* 9.1 (2018), p. 2850. ISSN: 2041-1723.

[21] M. Tanaka et al. "Magnetic interactions in a ferromagnetic honeycomb nanoscale network". In: *Phys. Rev. B* 73 (5 Feb. 2006), p. 052411. DOI: 10.1103/PhysRevB.73.052411.

[22] E. Mengotti et al. "Real-space observation of emergent magnetic monopoles and associated Dirac strings in artificial kagome spin ice". In: *Nature Physics* 7 (Oct. 2010), p. 68.

[23] A. Farhan et al. "Direct Observation of Thermal Relaxation in Artificial Spin Ice". In: *Phys. Rev. Lett.* 111 (5 Aug. 2013), p. 057204. DOI: 10.1103/PhysRevLett.111.057204.

[24] S. A. Daunheimer, O. Petrova, O. Tchernyshyov, and J. Cumings. "Reducing Disorder in Artificial Kagome Ice". In: *Phys. Rev. Lett.* 107 (16 Oct. 2011), p. 167201.

[25] Y. Qi, T. Brintlinger, and J. Cumings. "Direct observation of the ice rule in an artificial kagome spin ice". In: *Phys. Rev. B* 77 (9 Mar. 2008), p. 094418. DOI: 10.1103/PhysRevB.77.094418.

[26] S. D. Pollard, V. Volkov, and Y. Zhu. "Propagation of magnetic charge monopoles and Dirac flux strings in an artificial spin-ice lattice". In: *Phys. Rev. B* 85 (18 May 2012), p. 180402. DOI: 10.1103/PhysRevB.85.180402.

[27] D. M. Burn, M. Chadha, and W. R. Branford. "Angular-dependent magnetization reversal processes in artificial spin ice". In: *Phys. Rev. B* 92 (21 Dec. 2015), p. 214425.

[28] Y. Li et al. "Superferromagnetism and domain-wall topologies in artificial "pinwheel" spin ice". In: *ACS Nano* 13.2 (2019), pp. 2213–2222.

[29] B. L. Le et al. "Effects of exchange bias on magnetotransport in permalloy kagome artificial spin ice". In: *New Journal of Physics* 17.2 (Feb. 2015), p. 023047.

[30] M. B. Jungfleisch et al. "High-Frequency Dynamics Modulated by Collective Magnetization Reversal in Artificial Spin Ice". In: *Phys. Rev. Applied* 8 (6 Dec. 2017), p. 064026.

[31] S. A. Morley et al. "Vogel-Fulcher-Tammann freezing of a thermally fluctuating artificial spin ice probed by X-ray photon correlation spectroscopy". In: *Phys. Rev. B* 95 (10 Mar. 2017), p. 104422.

[32] B. Canals et al. "Fragmentation of magnetism in artificial kagome dipolar spin ice". In: *Nature Communications* 7 (May 2016), p. 11446.

[33] S. Ladak et al. "Direct observation of magnetic monopole defects in an artificial spin-ice system". In: *Nature Physics* 6 (Apr. 2010).

[34] A. Farhan et al. "Emergent magnetic monopole dynamics in macroscopically degenerate artificial spin ice". In: *Science Advances* 5.2 (2019). DOI: 10.1126/sciadv.aav6380. eprint: https://advances.sciencemag.org/content/5/2/eaav6380.full.pdf.

[35] E. Y. Vedmedenko. "Dynamics of Bound Monopoles in Artificial Spin Ice: How to Store Energy in Dirac Strings". In: *Phys. Rev. Lett.* 116 (7 Feb. 2016), p. 077202.

[36] A. Imre et al. "Majority Logic Gate for Magnetic Quantum-Dot Cellular Automata". In: *Science* 311.5758 (2006), pp. 205–208. ISSN: 0036-8075. DOI: 10.1126/science.1120506. eprint: https://science.sciencemag.org/content/311/5758/205.full.pdf.

[37] H. Arava et al. "Computational logic with square rings of nanomagnets". In: *Nanotechnology* 29.26 (May 2018), p. 265205. DOI: 10.1088/1361-6528/aabbc3.

[38] J. Grollier, D. Querlioz, and M. D. Stiles. "Spintronic Nanodevices for Bioinspired Computing". In: *Proceedings of the IEEE* 104.10 (2016), pp. 2024–2039.

[39] M. Pancaldi, N. Leo, and P. Vavassori. "Selective and fast plasmon-assisted photo-heating of nanomagnets". In: *Nanoscale* 11 (16 2019), pp. 7656–7666. DOI: 10.1039/C9NR01628G.

[40] J. C. Gartside, D. M. Burn, L. F. Cohen, and W. R. Branford. "A novel method for the injection and manipulation of magnetic charge states in nanostructures". In: *Scientific Reports* 6.1 (2016), p. 32864. DOI: 10.1038/srep32864.

[41] J. C. Gartside et al. "Realization of ground state in artificial kagome spin ice via topological defect-driven magnetic writing". In: *Nature Nanotechnology* 13.1 (2018), pp. 53–58. DOI: 10.1038/s41565-017-0002-1.

[42] J. D. Jackson. *Classical electrodynamics*. 3rd ed. New York, NY: Wiley, 1999. ISBN: 9780471309321.

[43] P. J. Mohr, D. B. Newell, and B. N. Taylor. "CODATA recommended values of the fundamental physical constants: 2014". In: *Rev. Mod. Phys.* 88 (3 Sept. 2016), p. 035009. DOI: 10.1103/RevModPhys.88.035009.

[44] S. Blundell. *Magnetism in Condensed Matter*. Oxford Master Series in Condensed Matter Physics. Oxford: Oxford Univ. Press, 2001.

[45] J. K. Rowling. *Harry Potter and the Deathly Hallows*. 1st ed. New York, NY : Arthur A. Levine Books, 2007., 2007.

[46] X. Lu et al. "Superconductors, orbital magnets and correlated states in magic-angle bilayer graphene". In: *Nature* 574.7780 (2019), pp. 653–657. DOI: 10.1038/s41586-019-1695-0.

[47] A. Einstein and W. J. de Haas. "Experimenteller Nachweis der Ampèreschen Moleku-larströme". In: *Deutsche Physikalische Gesellschaft* 17 (Jan. 1915), pp. 152–170.

[48] S. J. Barnett. "Magnetization by Rotation". In: *Phys. Rev.* 6 (4 Oct. 1915), pp. 239–270. DOI: 10.1103/PhysRev.6.239.

[49] R. Feynman. *The Feynman Lectures on Physics: Volume 2*. Vol. 2. The Feynman Lectures on Physics. Boston: Addison-Wesley, 1963.

[50] H.-J. Van Leeuwen. "Problèmes de la théorie électronique du magnétisme". In: *J. Phys. Radium* 2.12 (1921), pp. 361–377. DOI: 10.1051/jphysrad:01921002012036100.

[51] "II. The Doctor's Dissertation (Text and Translation)". In: *EARLY WORK (1905–1911)*. Ed. by L. Rosenfeld and J. R. Nielsen. Vol. 1. Niels Bohr Collected Works. Elsevier, 1972, pp. 163–393. DOI: https://doi.org/10.1016/S1876-0503(08)70015-X.

[52] T. Lancaster and S. J. Blundell. *Quantum field theory for the gifted amateur*. Oxford: Oxford University Press, Apr. 2014. DOI: 0199699321.

[53] S. A. Morley et al. "Effect of FePd alloy composition on the dynamics of artificial spin ice". In: *Scientific Reports* 8.1 (2018), p. 4750. DOI: 10.1038/s41598-018-23208-6.

[54] M. S. Andersson et al. "Thermally induced magnetic relaxation in square artificial spin ice". In: *Scientific reports* 6 (Nov. 2016), pp. 37097–37097. DOI: 10.1038/srep37097.

[55] M. Bode et al. "Comment on "Three-Dimensional, Spin-Resolved Structure of Magnetic Vortex and Antivortex States in Patterned Co Films Using Scanning Ion Microscopy with Polarization Analysis"". In: *Phys. Rev. Lett.* 100 (2 Jan. 2008), p. 029703. DOI: 10.1103/PhysRevLett.100.029703.

[56] M. Fˊahnle and C. Illg. "Electron theory of fast and ultrafast dissipative magnetization dynamics". In: *Journal of Physics: Condensed Matter* 23.49 (Nov. 2011), p. 493201. DOI: 10.1088/0953-8984/23/49/493201.

[57] L. Landau and E. Lifshitz. "3 - On the theory of the dispersion of magnetic permeability in ferromagnetic bodiesReprinted from Physikalische Zeitschrift der Sowjetunion 8, Part 2, 153, 1935." In: *Perspectives in Theoretical Physics*. Ed. by L. Pitaevski. Amsterdam: Pergamon, 1992, pp. 51–65. ISBN: 978-0-08-036364-6. DOI: https://doi.org/10.1016/B978-0-08-036364-6.50008-9.

[58] T. L. Gilbert. "Formulations, Foundations and Applications of the Phenomenological Theory of Ferromagnetism". PhD thesis. Chicago: Illinois Institute of Technology, June 1956.

[59] P. A. M. Dirac. "On the theory of quantum mechanics". In: *Proceedings of the Royal Society of London. Series A, Containing Papers of a Mathematical and Physical Character* 112.762 (1926). communicated by Fowler, R. H., pp. 661–677. DOI: 10.1098/rspa.1926.0133. eprint: https://royalsocietypublishing.org/doi/pdf/10.1098/rspa.1926.0133.

[60] W. Heisenberg. "Mehrkörperproblem und Resonanz in der Quantenmechanik". In: *Zeitschrift für Physik* 38.6 (1926), pp. 411–426. DOI: 10.1007/BF01397160.

[61] J. Van Vleck. *The Theory of Electric and Magnetic Susceptibilities*. International Series of Monographs on Physics. reprinted 1985. Oxford: Oxford University Press, 1932.

[62] A. Aharoni. *Introduction to the Theory of Ferromagnetism*. International Series of Monographs on Physics. Clarendon Press, 2000. ISBN: 9780198508090.

[63] R. Siddharthan, B. S. Shastry, and A. P. Ramirez. "Spin ordering and partial ordering in holmium titanate and related systems". In: *Phys. Rev. B* 63 (18 Apr. 2001), p. 184412. DOI: 10.1103/PhysRevB.63.184412.

[64] C. Nisoli, R. Moessner, and P. Schiffer. "Colloquium: Artificial spin ice: Designing and imaging magnetic frustration". In: *Rev. Mod. Phys.* 85 (4 Oct. 2013), pp. 1473–1490. DOI: 10.1103/RevModPhys.85.1473.

[65] L. J. Heyderman and R. L. Stamps. "Artificial ferroic systems: novel functionality from structure, interactions and dynamics". In: *Journal of Physics: Condensed Matter* 25.36 (Aug. 2013), p. 363201.

[66] S. H. Skjærvø, C. H. Marrows, R. L. Stamps, and L. J. Heyderman. "Advances in artificial spin ice". In: *Nature Reviews Physics* 2.1 (2020), pp. 13–28. DOI: 10.1038/s42254-019-0118-3.

[67] P.-M. Binder. "Frustration in Complexity". In: *Science* 320.5874 (2008), pp. 322–323. ISSN: 0036-8075. DOI: 10.1126/science.1156940. eprint: https://science.sciencemag.org/content/320/5874/322.full.pdf.

[68] G. H. Wannier. "Antiferromagnetism. The Triangular Ising Net". In: *Phys. Rev.* 79 (2 July 1950), pp. 357–364. DOI: 10.1103/PhysRev.79.357.

[69] J. D. Bernal and R. H. Fowler. "A Theory of Water and Ionic Solution, with Particular Reference to Hydrogen and Hydroxyl Ions". In: *The Journal of Chemical Physics* 1.8 (1933), pp. 515–548. DOI: 10.1063/1.1749327. eprint: https://doi.org/10.1063/1.1749327.

[70] L. Pauling. "The Structure and Entropy of Ice and of Other Crystals with Some Randomness of Atomic Arrangement". In: *Journal of the American Chemical Society* 57.12 (Dec. 1935), pp. 2680–2684. DOI: 10.1021/ja01315a102.

[71] W. F. Giauque and J. W. Stout. "The Entropy of Water and the Third Law of Thermodynamics. The Heat Capacity of Ice from 15 to 273 °K." In: *Journal of the American Chemical Society* 58.7 (July 1936), pp. 1144–1150. DOI: 10.1021/ja01298a023.

[72] P. W. Anderson. "Ordering and Antiferromagnetism in Ferrites". In: *Phys. Rev.* 102 (4 May 1956), pp. 1008–1013. DOI: 10.1103/PhysRev.102.1008.

[73] A. P. Ramirez et al. "Zero-point entropy in 'spin ice'". In: *Nature* 399.6734 (1999), pp. 333–335. DOI: 10.1038/20619.

[74] C. Castelnovo, R. Moessner, and S. L. Sondhi. "Magnetic monopoles in spin ice". In: *Nature* 451.7174 (2008), pp. 42–45. DOI: 10.1038/nature06433.

[75] P. A. M. Dirac. "Quantised singularities in the electromagnetic field," in: *Proceedings of the Royal Society of London. Series A, Containing Papers of a Mathematical and Physical Character* 133.821 (1931), pp. 60–72. DOI: 10.1098/rspa.1931.0130. eprint: https://royalsocietypublishing.org/doi/pdf/10.1098/rspa.1931.0130.

[76] C. Nisoli et al. "Effective Temperature in an Interacting Vertex System: Theory and Experiment on Artificial Spin Ice". In: *Phys. Rev. Lett.* 105 (4 July 2010), p. 047205. DOI: 10.1103/PhysRevLett.105.047205.

[77] S. Xu and D. J. Dunlop. "Theory of alternating field demagnetization of multidomain grains and implications for the origin of pseudo-single-domain remanence". In: *Journal of Geophysical Research: Solid Earth* 98.B3 (), pp. 4183–4190. DOI: 10.1029/92JB02570.

[78] K. Asencio, M. Acevedo, I. Zuriguel, and D. Maza. "Experimental Study of Ordering of Hard Cubes by Shearing". In: *Phys. Rev. Lett.* 119 (22 Dec. 2017), p. 228002. DOI: 10.1103/PhysRevLett.119.228002.

[79] J. P. Morgan, A. Stein, S. Langridge, and C. H. Marrows. "Thermal ground-state ordering and elementary excitations in artificial magnetic square ice". In: *Nature Physics* 7.1 (2011), pp. 75–79. DOI: 10.1038/nphys1853.

[80] G. Möller and R. Moessner. "Magnetic multipole analysis of kagome and artificial spin-ice dipolar arrays". In: *Phys. Rev. B* 80 (14 Oct. 2009), p. 140409. DOI: 10.1103/PhysRevB.80.140409.

[81] G.-W. Chern, P. Mellado, and O. Tchernyshyov. "Two-Stage Ordering of Spins in Dipolar Spin Ice on the Kagome Lattice". In: *Phys. Rev. Lett.* 106 (20 May 2011), p. 207202. DOI: 10.1103/PhysRevLett.106.207202.

[82] L. Anghinolfi et al. "Thermodynamic phase transitions in a frustrated magnetic metamaterial". In: *Nature Communications* 6.1 (2015), p. 8278. DOI: 10.1038/ncomms9278.

[83] M. J. Morrison, T. R. Nelson, and C. Nisoli. "Unhappy vertices in artificial spin ice: new degeneracies from vertex frustration". In: *New Journal of Physics* 15.4 (Apr. 2013), p. 045009. DOI: 10.1088/1367-2630/15/4/045009.

[84] Y. Lao et al. "Classical topological order in the kinetics of artificial spin ice". In: *Nature Physics* 14.7 (2018), pp. 723–727. DOI: 10.1038/s41567-018-0077-0.

[85] D. Shi et al. "Frustration and thermalization in an artificial magnetic quasicrystal". In: *Nature Physics* 14.3 (2018), pp. 309–314. DOI: 10.1038/s41567-017-0009-4.

[86] V. Brajuskovic, F. Barrows, C. Phatak, and A. K. Petford-Long. "Real-space observation of magnetic excitations and avalanche behavior in artificial quasicrystal lattices". In: *Scientific Reports* 6.1 (2016), p. 34384. DOI: 10.1038/srep34384.

[87] V. Brajuskovic, A. Addi, C. Phatak, and A. K. Petford-Long. "Observation of transient states during magnetization reversal in a quasicrystal artificial spin ice". In: *Phys. Rev. B* 98 (9 Sept. 2018), p. 094424. DOI: 10.1103/PhysRevB.98.094424.

[88] F. Barrows, V. Brajuskovic, A. K. Petford-Long, and C. Phatak. "Emergent magnetic ordering and topological frustration in quasicrystal artificial spin ices". In: *Phys. Rev. B* 99 (9 Mar. 2019), p. 094424. DOI: 10.1103/PhysRevB.99.094424.

[89]   S. Gliga, E. Iacocca, and O. G. Heinonen. "Dynamics of reconfigurable artificial spin ice: Toward magnonic functional materials". In: *APL Materials* 8.4 (2020), p. 040911. DOI: 10.1063/1.5142705. eprint: https://doi.org/10.1063/1.5142705.

[90]   H. Arava et al. "Engineering Relaxation Pathways in Building Blocks of Artificial Spin Ice for Computation". In: *Phys. Rev. Applied* 11 (5 May 2019), p. 054086. DOI: 10.1103/PhysRevApplied.11.054086.

[91]   J. Grollier et al. "Neuromorphic spintronics". In: *Nature Electronics* 3.7 (2020), pp. 360–370. DOI: 10.1038/s41928-019-0360-9.

[92]   M. Romera et al. "Vowel recognition with four coupled spin-torque nano-oscillators". In: *Nature* 563.7730 (2018), pp. 230–234.

[93]   I. Gilbert et al. "Direct visualization of memory effects in artificial spin ice". In: *Phys. Rev. B* 92 (10 Sept. 2015), p. 104417.

[94]   J. H. Jensen, E. Folven, and G. Tufte. "Computation in artificial spin ice". In: *Artificial Life Conference Proceedings* 30 (2018), pp. 15–22. DOI: 10.1162/isal_a_00011. eprint: https://www.mitpressjournals.org/doi/pdf/10.1162/isal_a_00011.

[95]   J. J. Hopfield. "Neural networks and physical systems with emergent collective computational abilities". In: *Proceedings of the National Academy of Sciences* 79.8 (1982), pp. 2554–2558. ISSN: 0027-8424.

[96]   G. M. Wysin, W. A. Moura-Melo, L. A. S. Mól, and A. R. Pereira. "Dynamics and hysteresis in square lattice artificial spin ice". In: *New Journal of Physics* 15.4 (Apr. 2013), p. 045029. DOI: 10.1088/1367-2630/15/4/045029.

[97]   M. J. Donahue and D. G. Porter. *OOMMF User's Guide, Version 1.0*. Interagency Report NISTIR 6376. National Institute of Standards and Technology, Gaithersburg, MD, 1999.

[98]   A. Vansteenkiste et al. "The design and verification of MuMax3". In: *AIP Advances* 4.10 (2014), p. 107133. DOI: 10.1063/1.4899186. eprint: https://doi.org/10.1063/1.4899186.

[99]   W. H. Press, S. A. Teukolsky, W. T. Vetterling, and B. P. Flannery. *Numerical Recipes in C*. Second. Cambridge, USA: Cambridge University Press, 1992.

[100] C. D. Broad. "Sir Arthur Eddington's "The Philosophy of Physical Science"". In: *Philosophy* 15.59 (1940), pp. 301–312. ISSN: 00318191, 1469817X.

[101] C. Finn. *Thermal Physics*. second. Physics and its applications. Taylor & Francis, 1993.

[102] A. Guenault. *Statistical Physics*. Student Physics Series. Springer Netherlands, 2007.

[103] P. M. Chaikin and T. C. Lubensky. *Principles of Condensed Matter Physics*. Cambridge University Press, 1995. DOI: 10.1017/CBO9780511813467.

[104] D. Goodstein. *States of Matter*. Dover Books on Physics. Dover Publications, 1985. ISBN: 9780486649276.

[105] J. W. Gibbs. *Elementary Principles in Statistical Mechanics: Developed with Especial Reference to the Rational Foundation of Thermodynamics*. Cambridge Library Collection - Mathematics. Cambridge University Press, 2010. DOI: 10.1017/CBO9780511686948.

[106]   BIPM. *Le Système international d'unités / The International System of Units ('The SI Brochure')*. Ninth. Bureau international des poids et mesures, 2019. ISBN: 978-92-822-2272-0.

[107]   M. L. Cohen and S. G. Louie. *Fundamentals of Condensed Matter Physics*. Cambridge University Press, 2016. DOI: 10.1017/CBO9781139031783.

[108]   I. S. Jacobs and P. E. Lawrence. "Metamagnetic Phase Transitions and Hysteresis in $FeCl_2$". In: *Phys. Rev.* 164 (2 Dec. 1967), pp. 866–878. DOI: 10.1103/PhysRev.164.866.

[109]   J. E. Jaffe, J. A. Snyder, Z. Lin, and A. C. Hess. "LDA and GGA calculations for high-pressure phase transitions in ZnO and MgO". In: *Phys. Rev. B* 62 (3 July 2000), pp. 1660–1665. DOI: 10.1103/PhysRevB.62.1660.

[110]   P. K. Galenko, I. G. Nizovtseva, K. Reuther, and M. Rettenmayr. "Kinetic transition in the order–disorder transformation at a solid/liquid interface". In: *Philosophical Transactions of the Royal Society A: Mathematical, Physical and Engineering Sciences* 376.2113 (2018), p. 20170207. DOI: 10.1098/rsta.2017.0207. eprint: https://royalsocietypublishing.org/doi/pdf/10.1098/rsta.2017.0207.

[111]   S. Sachdev. *Quantum Phase Transitions*. 2nd ed. Cambridge University Press, 2011. DOI: 10.1017/CBO9780511973765.

[112]   P. W. Anderson. "Plasmons, Gauge Invariance, and Mass". In: *Phys. Rev.* 130 (1 Apr. 1963), pp. 439–442. DOI: 10.1103/PhysRev.130.439.

[113]   P. W. Higgs. "Broken Symmetries and the Masses of Gauge Bosons". In: *Phys. Rev. Lett.* 13 (16 Oct. 1964), pp. 508–509. DOI: 10.1103/PhysRevLett.13.508.

[114]   G. S. Guralnik, C. R. Hagen, and T. W. B. Kibble. "Global Conservation Laws and Massless Particles". In: *Phys. Rev. Lett.* 13 (20 Nov. 1964), pp. 585–587. DOI: 10.1103/PhysRevLett.13.585.

[115]   T. Sauer. "A look back at the Ehrenfest classification". In: *The European Physical Journal Special Topics* 226.4 (2017), pp. 539–549. DOI: 10.1140/epjst/e2016-60344-y.

[116]   K. Amann-Winkel et al. "Colloquium: Water's controversial glass transitions". In: *Rev. Mod. Phys.* 88 (1 Feb. 2016), p. 011002. DOI: 10.1103/RevModPhys.88.011002.

[117]   N. Goldenfeld. *Lectures on phase transitions and the renormalization group*. 1st ed. Addison-Wesley Publishing Company, 1992.

[118]   O. Sendetskyi et al. "Continuous magnetic phase transition in artificial square ice". In: *Phys. Rev. B* 99 (21 June 2019), p. 214430. DOI: 10.1103/PhysRevB.99.214430.

[119]   S. J. Blundell and K. M. Blundell. *Concepts in thermal physics*. 2nd ed. New York, NY: Oxford Univ. Press, 2010. DOI: 10.1093/acprof:oso/9780199562091.001.0001.

[120]   J. P. Sethna, K. A. Dahmen, and C. R. Myers. "Crackling noise". In: *Nature* 410.6825 (2001), pp. 242–250. DOI: 10.1038/35065675.

[121]   P. A. Houle and J. P. Sethna. "Acoustic emission from crumpling paper". In: *Phys. Rev. E* 54 (1 July 1996), pp. 278–283. DOI: `10.1103/PhysRevE.54.278`.

[122]   E. M. Kramer and A. E. Lobkovsky. "Universal power law in the noise from a crumpled elastic sheet". In: *Phys. Rev. E* 53 (2 Feb. 1996), pp. 1465–1469. DOI: `10.1103/PhysRevE.53.1465`.

[123]   J. P. Sethna et al. "Hysteresis and hierarchies: Dynamics of disorder-driven first-order phase transformations". In: *Phys. Rev. Lett.* 70 (21 May 1993), pp. 3347–3350. DOI: `10.1103/PhysRevLett.70.3347`.

[124]   G. Bertotti and I. Mayergoyz. "The Science of Hysteresis". In: ed. by G. Bertotti and I. D. Mayergoyz. Oxford: Academic Press, 2006. ISBN: 978-0-12-480874-4.

[125]   P. Heller and G. B. Benedek. "Nuclear Magnetic Resonance in MnF_2 Near the Critical Point". In: *Phys. Rev. Lett.* 8 (11 June 1962), pp. 428–432. DOI: `10.1103/PhysRevLett.8.428`.

[126]   A. Taroni, S. T. Bramwell, and P. C. W. Holdsworth. "Universal window for two-dimensional critical exponents". In: *Journal of Physics: Condensed Matter* 20.27 (June 2008), p. 275233. DOI: `10.1088/0953-8984/20/27/275233`.

[127]   K. H. Fischer and J. A. Hertz. *Spin Glasses*. Cambridge Studies in Magnetism. Cambridge University Press, 1991. DOI: `10.1017/CBO9780511628771`.

[128]   R. B. Griffiths. "Thermodynamic Functions for Fluids and Ferromagnets near the Critical Point". In: *Phys. Rev.* 158 (1 June 1967), pp. 176–187. DOI: `10.1103/PhysRev.158.176`.

[129]   J. J. Binney, N. J. Dowrick, A. J. Fisher, and M. Newman. *The Theory of Critical Phenomena: An Introduction to the Renormalization Group*. first. Oxford University Press, 1992. ISBN: 0198513933.

[130]   S. G. Brush. "History of the Lenz-Ising Model". In: *Rev. Mod. Phys.* 39 (4 Oct. 1967), pp. 883–893. DOI: `10.1103/RevModPhys.39.883`.

[131]   L. Onsager. "Crystal Statistics. I. A Two-Dimensional Model with an Order-Disorder Transition". In: *Phys. Rev.* 65 (3-4 Feb. 1944), pp. 117–149. DOI: `10.1103/PhysRev.65.117`.

[132]   J. P. Sethna. *Statistical Mechanics: Entropy, Order Parameters and Complexity*. first edition. Oxford: Oxford University Press, 2006.

[133]   E. W. Montroll. "Obituary: Lars Onsager". In: *Physics Today* 30 (1977), p. 77. DOI: `10.1063/1.3037438`.

[134]   S. Zhang et al. "Perpendicular Magnetization and Generic Realization of the Ising Model in Artificial Spin Ice". In: *Phys. Rev. Lett.* 109 (8 Aug. 2012), p. 087201. DOI: `10.1103/PhysRevLett.109.087201`.

[135]   N. Metropolis et al. "Equation of State Calculations by Fast Computing Machines". In: *The Journal of Chemical Physics* 21.6 (1953), pp. 1087–1092. DOI: `10.1063/1.1699114`. eprint: `https://doi.org/10.1063/1.1699114`.

[136]   N. Metropolis and S. Ulam. "The Monte Carlo Method". In: *Journal of the American Statistical Association* 44.247 (1949). PMID: 18139350, pp. 335–341. DOI: 10.1080/01621459.1949.10483310.

[137]   H. G. Katzgraber. *Introduction to Monte Carlo Methods, given as a lecture at the 3rd international summer school in "Modern Computation Science", Oldenburg (Germany).* 2009. eprint: arXiv:0905.1629.

[138]   W. K. Hastings. "Monte Carlo sampling methods using Markov chains and their applications". In: *Biometrika* 57.1 (Apr. 1970), pp. 97–109. ISSN: 0006-3444. DOI: 10.1093/biomet/57.1.97.

[139]   M. N. Ǵ. Barkema. *Monte Carlo Methods in Statistical Physics.* Oxford Uinversity Press, 1999.

[140]   K. Binder and D. Heermann. *Monte Carlo Simulation in Statistical Physics: An Introduction.* 2nd ed. Springer Series in Solid-State Sciences 80. Springer-Verlag, 1992.

[141]   O. Penrose and J. L. Lebowitz. "On the exponential decay of correlation functions". In: *Communications in Mathematical Physics* 39.3 (1974), pp. 165–184. DOI: 10.1007/BF01614239.

[142]   E. Östman et al. "Ising-like behaviour of mesoscopic magnetic chains". In: *Journal of Physics: Condensed Matter* 30.36 (Aug. 2018), p. 365301.

[143]   H. Stopfel et al. "Magnetic order and energy-scale hierarchy in artificial spin-ice structures". In: *Phys. Rev. B* 98 (1 July 2018), p. 014435. DOI: 10.1103/PhysRevB.98.014435.

[144]   P. L. Krapivsky, S. Redner, and E. Ben-Naim. *A Kinetic View of Statistical Physics.* Cambridge University Press, 2010. DOI: 10.1017/CBO9780511780516.

[145]   U. Wolff. "Critical slowing down". In: *Nuclear Physics B - Proceedings Supplements* 17 (1990), pp. 93–102. ISSN: 0920-5632. DOI: https://doi.org/10.1016/0920-5632(90)90224-I.

[146]   C. Djurberg et al. "Dynamics of an Interacting Particle System: Evidence of Critical Slowing Down". In: *Phys. Rev. Lett.* 79 (25 Dec. 1997), pp. 5154–5157. DOI: 10.1103/PhysRevLett.79.5154.

[147]   M. E. Fisher and M. N. Barber. "Scaling Theory for Finite-Size Effects in the Critical Region". In: *Phys. Rev. Lett.* 28 (23 June 1972), pp. 1516–1519. DOI: 10.1103/PhysRevLett.28.1516.

[148]   V. Privman and M. E. Fisher. "Universal critical amplitudes in finite-size scaling". In: *Phys. Rev. B* 30 (1 July 1984), pp. 322–327. DOI: 10.1103/PhysRevB.30.322.

[149]   K. Binder. "Critical Properties from Monte Carlo Coarse Graining and Renormalization". In: *Phys. Rev. Lett.* 47 (9 Aug. 1981), pp. 693–696. DOI: 10.1103/PhysRevLett.47.693.

[150]   R. H. Swendsen and J.-S. Wang. "Replica Monte Carlo Simulation of Spin-Glasses". In: *Phys. Rev. Lett.* 57 (21 Nov. 1986), pp. 2607–2609. DOI: 10.1103/PhysRevLett.57.2607.

[151] P. A. Midgley and J. M. Thomas. "Multi-Dimensional Electron Microscopy". In: *Angewandte Chemie International Edition* 53.33 (2014), pp. 8614–8617. DOI: 10.1002/anie.201400625. eprint: https://onlinelibrary.wiley.com/doi/pdf/10.1002/anie.201400625.

[152] J. M. Thomas, R. K. Leary, A. S. Eggeman, and P. A. Midgley. "The rapidly changing face of electron microscopy". In: *Chemical Physics Letters* 631-632 (2015), pp. 103–113. ISSN: 0009-2614. DOI: https://doi.org/10.1016/j.cplett.2015.04.048.

[153] L. de Broglie. "Recherches sur la théorie des quanta. (French) [Research on quantum theory]". French. Presented at the Sorbonne on 25 November 1924. Doctoral thesis. Paris, France: La Sorbonne, 1925.

[154] J. Thomson. *The Structure of Light*. A transcription of the Fison Memorial Lecture, given at King's College, London, 1925. Cambridge: Cambridge University Press, 1925.

[155] G. P. THOMSON and A. REID. "Diffraction of Cathode Rays by a Thin Film". In: *Nature* 119.3007 (1927), pp. 890–890. DOI: 10.1038/119890a0.

[156] C. J. Davisson. "The Diffraction of Electrons by a Crystal of Nickel". In: *Bell System Technical Journal* 7.1 (1928), pp. 90–105. DOI: 10.1002/j.1538-7305.1928.tb00342.x.

[157] C. J. Davisson and L. H. Germer. "Reflection of Electrons by a Crystal of Nickel". In: *Proceedings of the National Academy of Sciences* 14.4 (1928), pp. 317–322. ISSN: 0027-8424. DOI: 10.1073/pnas.14.4.317. eprint: https://www.pnas.org/content/14/4/317.full.pdf.

[158] E. Ruska. "The Development of the Electron Microscope and of Electron Microscopy (Nobel Lecture)". In: *Angewandte Chemie International Edition in English* 26.7 (1987), pp. 595–605. DOI: 10.1002/anie.198705953.

[159] T. Mulvey, B. Kazan, and P. Hawkes. *The Growth of Electron Microscopy*. ISSN. Elsevier Science, 1996. ISBN: 9780080577623.

[160] E. Hecht. *Optics*. seventh edition. Addison-Wesley, 2002.

[161] Z.-B. Fan et al. "Silicon Nitride Metalenses for Close-to-One Numerical Aperture and Wide-Angle Visible Imaging". In: *Phys. Rev. Applied* 10 (1 July 2018), p. 014005. DOI: 10.1103/PhysRevApplied.10.014005.

[162] M. Kang, Y. Ra'di, D. Farfan, and A. Alù. "Efficient Focusing with Large Numerical Aperture Using a Hybrid Metalens". In: *Phys. Rev. Applied* 13 (4 Apr. 2020), p. 044016. DOI: 10.1103/PhysRevApplied.13.044016.

[163] R. F. Egerton. "Electron energy-loss spectroscopy in the TEM". In: *Reports on Progress in Physics* 72.1 (Dec. 2008), p. 016502. DOI: 10.1088/0034-4885/72/1/016502.

[164] E. Rutherford. "LXXIX. The scattering of α and β particles by matter and the structure of the atom". In: *The London, Edinburgh, and Dublin Philosophical Magazine and Journal of Science* 21.125 (1911), pp. 669–688. DOI: 10.1080/14786440508637080.

[165] L. A. Harris. "Analysis of Materials by Electron-Excited Auger Electrons". In: *Journal of Applied Physics* 39.3 (1968), pp. 1419–1427. DOI: 10.1063/1.1656374. eprint: https://doi.org/10.1063/1.1656374.

[166] A. J. Wilkinson and T. B. Britton. "Strains, planes, and EBSD in materials science". In: *Materials Today* 15.9 (2012), pp. 366–376. ISSN: 1369-7021. DOI: https://doi.org/10.1016/S1369-7021(12)70163-3.

[167] D. E. Newbury and N. W. M. Ritchie. "Is Scanning Electron Microscopy/Energy Dispersive X-ray Spectrometry (SEM/EDS) Quantitative?" In: *Scanning* 35.3 (2013), pp. 141–168. DOI: 10.1002/sca.21041. eprint: https://onlinelibrary.wiley.com/doi/pdf/10.1002/sca.21041.

[168] H. Lichte. "Electron Holography". In: *Handbook of Nanoscopy*. John Wiley & Sons, Ltd, 2012. Chap. 5, pp. 153–220. ISBN: 9783527641864. DOI: 10.1002/9783527641864.ch5. eprint: https://onlinelibrary.wiley.com/doi/pdf/10.1002/9783527641864.ch5.

[169] D. Williams and C. B. Carter. "Transmission Electron Microscopy: a Textbook for Materials Science". In: 2nd Edition. USA: Springer, 2009.

[170] O. Krivanek, T. Lovejoy, and N. Dellby. "Aberration-corrected STEM for atomic-resolution imaging and analysis". In: *Journal of Microscopy* 259.3 (2015), pp. 165–172. DOI: 10.1111/jmi.12254. eprint: https://onlinelibrary.wiley.com/doi/pdf/10.1111/jmi.12254.

[171] O. SCHERZER. "Spharische und chromatische Korrektur von Elektronen-Linsen". In: *Optik* 2 (1947), pp. 114–132.

[172] O. Scherzer. "The Theoretical Resolution Limit of the Electron Microscope". In: *Journal of Applied Physics* 20.1 (1949), pp. 20–29. DOI: 10.1063/1.1698233. eprint: https://doi.org/10.1063/1.1698233.

[173] M. E. Hale, H. W. Fuller, and H. Rubinstein. "Magnetic Domain Observations by Electron Microscopy". In: *Journal of Applied Physics* 30.5 (1959), pp. 789–791. DOI: 10.1063/1.1735233. eprint: https://doi.org/10.1063/1.1735233.

[174] C. Phatak et al. "Nanoscale structure of the magnetic induction at monopole defects in artificial spin-ice lattices". In: *Phys. Rev. B* 83 (17 May 2011), p. 174431. DOI: 10.1103/PhysRevB.83.174431.

[175] J. Drisko, T. Marsh, and J. Cumings. "Topological frustration of artificial spin ice". In: *Nature Communications* 8.1 (2017), p. 14009. DOI: 10.1038/ncomms14009.

[176] Y. Aharonov and D. Bohm. "Significance of Electromagnetic Potentials in the Quantum Theory". In: *Phys. Rev.* 115 (3 Aug. 1959), pp. 485–491. DOI: 10.1103/PhysRev.115.485.

[177] L. Desplat, J.-V. Kim, and R. L. Stamps. "Paths to annihilation of first- and second-order (anti)skyrmions via (anti)meron nucleation on the frustrated square lattice". In: *Phys. Rev. B* 99 (17 May 2019), p. 174409. DOI: 10.1103/PhysRevB.99.174409.

[178] D. Wolf et al. "3D Magnetic Induction Maps of Nanoscale Materials Revealed by Electron Holographic Tomography". In: *Chemistry of Materials* 27.19 (Oct. 2015), pp. 6771–6778. DOI: 10.1021/acs.chemmater.5b02723.

[179] P. Stadelmann. "EMS - a software package for electron diffraction analysis and HREM image simulation in materials science". In: *Ultramicroscopy* 21.2 (1987), pp. 131–145. ISSN: 0304-3991. DOI: https://doi.org/10.1016/0304-3991(87)90080-5.

[180] S. Gliga et al. "Emergent dynamic chirality in a thermally driven artificial spin ratchet". In: *Nature Materials* 16.11 (Nov. 2017), pp. 1106–1111. ISSN: 1476-4660. DOI: 10.1038/nmat5007.

[181] B. Freitag et al. "Sub-nanometer Resolution in Field-free Imaging using a Titan 80-300 with Lorentz lens and Image Cs-Corrector at 300kV Acceleration Voltage". In: *Microscopy and Microanalysis* 15.S2 (2009), pp. 184–185. DOI: 10.1017/S143192760909429X.

[182] S. McVitie et al. "Aberration corrected Lorentz scanning transmission electron microscopy". In: *Ultramicroscopy* 152 (2015), pp. 57–62. ISSN: 0304-3991. DOI: https://doi.org/10.1016/j.ultramic.2015.01.003.

[183] M. De Graef. "Phase contrast microscopy". In: *Introduction to Conventional Transmission Electron Microscopy*. Cambridge University Press, 2003, pp. 585–660. DOI: 10.1017/CBO9780511615092.012.

[184] S. McVitie and J. N. Chapman. "Coherent Lorentz Imaging of Soft, Thin-Film Magnetic Materials". In: *MRS Bulletin* 20.10 (1995), pp. 55–58. DOI: 10.1557/S0883769400045371.

[185] Y. Togawa. "Small-angle electron scattering of magnetic fine structures". In: *Microscopy* 62.suppl$_1$ (June 2013), S75–S86. ISSN: 2050-5698. DOI: 10.1093/jmicro/dft007. eprint: https://academic.oup.com/jmicro/article-pdf/62/suppl_1/S75/5854600/dft007.pdf.

[186] M. R. Teague. "Deterministic phase retrieval: a Green's function solution". In: *J. Opt. Soc. Am.* 73.11 (Nov. 1983), pp. 1434–1441. DOI: 10.1364/JOSA.73.001434.

[187] D. V. Dyck and W. M. J. Coene. "A new procedure for wave function restoration in high resolution electron microscopy". In: 1987.

[188] S. McVitie and M. Cushley. "Quantitative Fresnel Lorentz microscopy and the transport of intensity equation". In: *Ultramicroscopy* 106.4 (2006), pp. 423–431. ISSN: 0304-3991. DOI: https://doi.org/10.1016/j.ultramic.2005.12.001.

[189] N. H. Dekkers and H. De Lang. *Differential phase constrast in a STEM*. 1974.

[190] J. Chapman and G. Morrison. "Quantitative determination of magnetisation distributions in domains and domain walls by scanning transmission electron microscopy". In: *Journal of Magnetism and Magnetic Materials* 35.1 (1983), pp. 254–260. ISSN: 0304-8853. DOI: https://doi.org/10.1016/0304-8853(83)90511-5.

[191] M. Krajnak et al. "Pixelated detectors and improved efficiency for magnetic imaging in STEM differential phase contrast". In: *Ultramicroscopy* 165 (2016), pp. 42–50. ISSN: 0304-3991. DOI: https://doi.org/10.1016/j.ultramic.2016.03.006.

[192] D. Gabor. "A New Microscopic Principle". In: *Nature* 161.4098 (1948), pp. 777–778. DOI: 10.1038/161777a0.

[193] D. Gabor and W. L. Bragg. "Microscopy by reconstructed wave-fronts". In: *Proceedings of the Royal Society of London. Series A. Mathematical and Physical Sciences* 197.1051 (1949), pp. 454–487. DOI: 10.1098/rspa.1949.0075.

[194] D. McGrouther, M. J. Benitez, S. McFadzean, and S. McVitie. "Development of aberration corrected differential phase contrast (DPC) STEM". In: *JEOL News* 49.2 (2014), pp. 2–20014.

[195] R. Plackett et al. "Merlin: a fast versatile readout system for Medipix3". In: *Journal of Instrumentation* 8.01 (Jan. 2013), pp. C01038–C01038. DOI: 10.1088/1748-0221/8/01/c01038.

[196] W. F. van Dorp and C. W. Hagen. "A critical literature review of focused electron beam induced deposition". In: *Journal of Applied Physics* 104.8 (2008), p. 081301. DOI: 10.1063/1.2977587. eprint: https://doi.org/10.1063/1.2977587.

[197] J. M. D. Teresa et al. "Review of magnetic nanostructures grown by focused electron beam induced deposition (FEBID)". In: *Journal of Physics D: Applied Physics* 49.24 (May 2016), p. 243003. DOI: 10.1088/0022-3727/49/24/243003.

[198] M. Huth et al. "Focused electron beam induced deposition: A perspective". In: *Beilstein Journal of Nanotechnology* 3 (2012), pp. 597–619. ISSN: 2190-4286. DOI: 10.3762/bjnano.3.70.

[199] Y. Chen. "Nanofabrication by electron beam lithography and its applications: A review". In: *Microelectronic Engineering* 135 (2015), pp. 57–72. ISSN: 0167-9317. DOI: https://doi.org/10.1016/j.mee.2015.02.042.

[200] F. Cerrina. "X-ray imaging: applications to patterning and lithography". In: *Journal of Physics D: Applied Physics* 33.12 (May 2000), R103–R116. DOI: 10.1088/0022-3727/33/12/201.

[201] K. L. Berkowski, K. N. Plunkett, Q. Yu, and J. S. Moore. "Introduction to Photolithography: Preparation of Microscale Polymer Silhouettes". In: *Journal of Chemical Education* 82.9 (Sept. 2005), p. 1365. DOI: 10.1021/ed082p1365.

[202] C. Donnelly et al. "Element-Specific X-Ray Phase Tomography of 3D Structures at the Nanoscale". In: *Phys. Rev. Lett.* 114 (11 Mar. 2015), p. 115501. DOI: 10.1103/PhysRevLett.114.115501.

[203] A. May et al. "Realisation of a frustrated 3D magnetic nanowire lattice". In: *Communications Physics* 2.1 (2019), p. 13. DOI: 10.1038/s42005-018-0104-6.

[204] Y. Liu et al. "Confined Chemical Fluid Deposition of Ferromagnetic Metalattices". In: *Nano Letters* 18.1 (Jan. 2018), pp. 546–552. DOI: 10.1021/acs.nanolett.7b04633.

[205] J. Shen, K. Muthukumar, H. O. Jeschke, and R. Valenti. "Physisorption of an organometallic platinum complex on silica: ab initio study". In: *New Journal of Physics* 14.7 (July 2012), p. 073040. DOI: 10.1088/1367-2630/14/7/073040.

[206] R. L. Stewart. "Insulating Films Formed Under Electron and Ion Bombardment". In: *Phys. Rev.* 45 (7 Apr. 1934), pp. 488–490. DOI: 10.1103/PhysRev.45.488.

[207] Z. Cai, B. Liu, X. Zou, and H.-M. Cheng. "Chemical Vapor Deposition Growth and Applications of Two-Dimensional Materials and Their Heterostructures". In: *Chemical Reviews* 118.13 (July 2018), pp. 6091–6133. DOI: 10.1021/acs.chemrev.7b00536.

[208] O. Guise, J. Ahner, J. Yates, and J. Levy. "Formation and thermal stability of sub-10-nm carbon templates on Si(100)". In: *Applied Physics Letters* 85.12 (2004), pp. 2352–2354. DOI: 10.1063/1.1794369. eprint: https://doi.org/10.1063/1.1794369.

[209]   P. A. Crozier, J. Tolle, J. Kouvetakis, and C. Ritter. "Synthesis of uniform GaN quantum dot arrays via electron nanolithography of D_2GaN_3". In: *Applied Physics Letters* 84.18 (2004), pp. 3441–3443. DOI: 10.1063/1.1736314. eprint: https://doi.org/10.1063/1.1736314.

[210]   W. F. van Dorp et al. "Approaching the Resolution Limit of Nanometer-Scale Electron Beam-Induced Deposition". In: *Nano Letters* 5.7 (July 2005), pp. 1303–1307. DOI: 10.1021/nl050522i.

[211]   A. Botman, J. J. L. Mulders, and C. W. Hagen. "Creating pure nanostructures from electron-beam-induced deposition using purification techniques: a technology perspective". In: *Nanotechnology* 20.37 (Aug. 2009), p. 372001. DOI: 10.1088/0957-4484/20/37/372001.

[212]   S. J. Randolph, J. D. Fowlkes, and P. D. Rack. "Effects of heat generation during electron-beam-induced deposition of nanostructures". In: *Journal of Applied Physics* 97.12 (2005), p. 124312. DOI: 10.1063/1.1942627. eprint: https://doi.org/10.1063/1.1942627.

[213]   I. Utke, P. Hoffmann, and J. Melngailis. "Gas-assisted focused electron beam and ion beam processing and fabrication". In: *Journal of Vacuum Science & Technology B: Microelectronics and Nanometer Structures Processing, Measurement, and Phenomena* 26.4 (2008), pp. 1197–1276. DOI: 10.1116/1.2955728.

[214]   R. M. Thorman, R. K. T. P., D. H. Fairbrother, and O. Ingolfsson. "The role of low-energy electrons in focused electron beam induced deposition: four case studies of representative precursors". In: *Beilstein Journal of Nanotechnology* 6 (2015), pp. 1904–1926. ISSN: 2190-4286. DOI: 10.3762/bjnano.6.194.

[215]   M. F. Mirbach, A. Saus, A.-M. Krings, and M. J. Mirbach. "Thermal, photochemical and alcohol catalyzed formation of $Co_4(CO)_{12}$ from $Co_2(CO)_8$. Kinetics and mechanism". In: *Journal of Organometallic Chemistry* 205.2 (1981), pp. 229–237. ISSN: 0022-328X. DOI: https://doi.org/10.1016/S0022-328X(00)81480-1.

[216]   J. Mulders. "Practical precursor aspects for electron beam induced deposition". In: *Nanofabrication* 1 (2014). DOI: https://doi.org/10.2478/nanofab-2014-0007.

[217]   A. Fernandez-Pacheco, J. M. D. Teresa, R. Cordoba, and M. R. Ibarra. "Magnetotransport properties of high-quality cobalt nanowires grown by focused-electron-beam-induced deposition". In: *Journal of Physics D: Applied Physics* 42.5 (Feb. 2009), p. 055005. DOI: 10.1088/0022-3727/42/5/055005.

[218]   L. Serrano-Ramon et al. "Ultrasmall Functional Ferromagnetic Nanostructures Grown by Focused Electron-Beam-Induced Deposition". In: *ACS Nano* 5.10 (Oct. 2011), pp. 7781–7787. DOI: 10.1021/nn201517r.

[219]   J. D. Fowlkes and P. D. Rack. "Fundamental Electron-Precursor-Solid Interactions Derived from Time-Dependent Electron-Beam-Induced Deposition Simulations and Experiments". In: *ACS Nano* 4.3 (Mar. 2010), pp. 1619–1629. DOI: 10.1021/nn901363a.

[220] R. Winkler et al. "Toward Ultraflat Surface Morphologies During Focused Electron Beam Induced Nanosynthesis: Disruption Origins and Compensation". In: *ACS Applied Materials and Interfaces* 7.5 (Feb. 2015), pp. 3289–3297. DOI: 10.1021/am508052k.

[221] L. Keller et al. "Direct-write of free-form building blocks for artificial magnetic 3D lattices". In: *Scientific Reports* 8.1 (2018), p. 6160. DOI: 10.1038/s41598-018-24431-x.

[222] F. Porrati et al. "Direct writing of CoFe alloy nanostructures by focused electron beam induced deposition from a heteronuclear precursor". In: *Nanotechnology* 26.47 (Nov. 2015), p. 475701. DOI: 10.1088/0957-4484/26/47/475701.

[223] M. Pohlit et al. "Magnetic stray-field studies of a single Cobalt nanoelement as a component of the building blocks of artificial square spin ice". In: *Journal of Magnetism and Magnetic Materials* 400 (2016). Proceedings of the 20th International Conference on Magnetism (Barcelona) 5-10 July 2015, pp. 206–212. ISSN: 0304-8853. DOI: https://doi.org/10.1016/j.jmmm.2015.08.072.

[224] M. Pohlit et al. "First order reversal curves (FORC) analysis of individual magnetic nanostructures using micro-Hall magnetometry". In: *Review of Scientific Instruments* 87.11 (2016), p. 113907. DOI: 10.1063/1.4967940. eprint: https://aip.scitation.org/doi/pdf/10.1063/1.4967940.

[225] M. Pohlit et al. "Experimental and theoretical investigation of the magnetization dynamics of an artificial square spin ice cluster". In: *Journal of Applied Physics* 120.14 (2016), p. 142103. DOI: 10.1063/1.4961705. eprint: https://doi.org/10.1063/1.4961705.

[226] D. Sanz-Hernandez et al. "Fabrication, Detection, and Operation of a Three-Dimensional Nanomagnetic Conduit". In: *ACS Nano* 11.11 (Nov. 2017), pp. 11066–11073. DOI: 10.1021/acsnano.7b05105.

[227] D. Sanz-Hernandez et al. "Artificial Double-Helix for Geometrical Control of Magnetic Chirality". In: *ACS Nano* (July 2020). DOI: 10.1021/acsnano.0c00720.

[228] H. G. Katzgraber, S. Trebst, D. A. Huse, and M. Troyer. "Feedback-optimized parallel tempering Monte Carlo". In: *Journal of Statistical Mechanics: Theory and Experiment* 2006.03 (Mar. 2006), P03018–P03018. DOI: 10.1088/1742-5468/2006/03/p03018.

[229] I. Rozada, M. Aramon, J. Machta, and H. G. Katzgraber. "Effects of setting temperatures in the parallel tempering Monte Carlo algorithm". In: *Phys. Rev. E* 100 (4 Oct. 2019), p. 043311. DOI: 10.1103/PhysRevE.100.043311.

[230] D. P. Landau and K. Binder. "Phase diagrams and critical behavior of Ising square lattices with nearest-, next-nearest-, and third-nearest-neighbor couplings". In: *Phys. Rev. B* 31 (9 May 1985), pp. 5946–5953. DOI: 10.1103/PhysRevB.31.5946.

[231] M. Wyss et al. "Stray-Field Imaging of a Chiral Artificial Spin Ice during Magnetization Reversal". In: *ACS Nano* 13.12 (Dec. 2019), pp. 13910–13916. ISSN: 1936-0851. DOI: 10.1021/acsnano.9b05428.

[232] M. Massouras, D. Lacour, M. Hehn, and F. Montaigne. "Probing the antiferromagnetic-paramagnetic transition in artificial spin ice by tuning interactions". In: *Phys. Rev. B* 101 (17 May 2020), p. 174421. DOI: 10.1103/PhysRevB.101.174421.

[233] Z. Budrikis, P. Politi, and R. L. Stamps. "Vertex Dynamics in Finite Two-Dimensional Square Spin Ices". In: *Phys. Rev. Lett.* 105 (1 June 2010), p. 017201. DOI: 10.1103/PhysRevLett.105.017201.

[234] L. P. Kadanoff. "Scaling laws for ising models near T_c". In: *Physics Physique Fizika* 2 (6 June 1966), pp. 263–272. DOI: 10.1103/PhysicsPhysiqueFizika.2.263.

[235] A. Remhof et al. "Magnetostatic interactions on a square lattice". In: *Phys. Rev. B* 77 (13 Apr. 2008), p. 134409. DOI: 10.1103/PhysRevB.77.134409.

[236] X. Ke et al. "Energy Minimization and ac Demagnetization in a Nanomagnet Array". In: *Phys. Rev. Lett.* 101 (3 July 2008), p. 037205. DOI: 10.1103/PhysRevLett.101.037205.

[237] E. Mengotti et al. "Building blocks of an artificial kagome spin ice: Photoemission electron microscopy of arrays of ferromagnetic islands". In: *Phys. Rev. B* 78 (14 Oct. 2008), p. 144402. DOI: 10.1103/PhysRevB.78.144402.

[238] N. Rougemaille et al. "Artificial Kagome Arrays of Nanomagnets: A Frozen Dipolar Spin Ice". In: *Phys. Rev. Lett.* 106 (5 Feb. 2011), p. 057209. DOI: 10.1103/PhysRevLett.106.057209.

[239] G. Möller and R. Moessner. "Artificial Square Ice and Related Dipolar Nanoarrays". In: *Phys. Rev. Lett.* 96 (23 June 2006), p. 237202. DOI: 10.1103/PhysRevLett.96.237202.

[240] A. Farhan et al. "Nanoscale control of competing interactions and geometrical frustration in a dipolar trident lattice". In: *Nature Communications* 8.1 (2017), p. 995. DOI: 10.1038/s41467-017-01238-4.

[241] M. D. P. Martinez and R. C. Buceta. "Energetic analysis of disorder effects in an artificial spin ice with dipolar interactions". In: *Journal of Physics: Condensed Matter* 32.28 (Apr. 2020), p. 285801. DOI: 10.1088/1361-648x/ab7e58.

[242] H. G. Katzgraber, M. Palassini, and A. P. Young. "Monte Carlo simulations of spin glasses at low temperatures". In: *Phys. Rev. B* 63 (18 Apr. 2001), p. 184422. DOI: 10.1103/PhysRevB.63.184422.

[243] A. Kone and D. A. Kofke. "Selection of temperature intervals for parallel-tempering simulations". In: *The Journal of Chemical Physics* 122.20 (2005), p. 206101. DOI: 10.1063/1.1917749. eprint: https://doi.org/10.1063/1.1917749.

[244] D. A. Kofke. "On the acceptance probability of replica-exchange Monte Carlo trials". In: *The Journal of Chemical Physics* 117.15 (2002), pp. 6911–6914. DOI: 10.1063/1.1507776. eprint: https://doi.org/10.1063/1.1507776.

[245] N. Rathore, M. Chopra, and J. J. de Pablo. "Optimal allocation of replicas in parallel tempering simulations". In: *The Journal of Chemical Physics* 122.2 (2005), p. 024111. DOI: 10.1063/1.1831273. eprint: https://doi.org/10.1063/1.1831273.

[246]   C. Predescu, M. Predescu, and C. V. Ciobanu. "The incomplete beta function law for parallel tempering sampling of classical canonical systems". In: *The Journal of Chemical Physics* 120.9 (2004), pp. 4119–4128. DOI: 10.1063/1.1644093. eprint: https://doi.org/10.1063/1.1644093.

[247]   C. Predescu, M. Predescu, and C. V. Ciobanu. "On the Efficiency of Exchange in Parallel Tempering Monte Carlo Simulations". In: *The Journal of Physical Chemistry B* 109.9 (Mar. 2005), pp. 4189–4196. DOI: 10.1021/jp045073+.

[248]   O. G. Mouritsen and S. J. K. Jensen. "Static properties of spin systems with truncated secular dipolar coupling". In: *Phys. Rev. B* 18 (1 July 1978), pp. 465–479. DOI: 10.1103/PhysRevB.18.465.

[249]   V. J.P. and W. S. G. *A guide to Monte Carlo for statistical mechanics. In: Statistical Mechanics Part A: Equilibrium Techniques.* Ed. by B. Berne. Vol. 5. Plenum Press, 1977, pp. 137–168.

[250]   D. J. Adams and I. R. McDonald. "Thermodynamic and dielectric properties of polar lattices". In: *Molecular Physics* 32.4 (1976), pp. 931–947. DOI: 10.1080/00268977600102351. eprint: https://doi.org/10.1080/00268977600102351.

[251]   R. Kretschmer and K. Binder. "Ordering and phase transitions in ising systems with competing short range and dipolar interactions". In: *Zeitschrift für Physik B Condensed Matter* 34.4 (1979), pp. 375–392. DOI: 10.1007/BF01325203.

[252]   P. P. Ewald. "Die Berechnung optischer und elektrostatischer Gitterpotentiale". In: *Annalen der Physik* 369.3 (1921), pp. 253–287. DOI: 10.1002/andp.19213690304.

[253]   M. Born and K. Huang. *Dynamical Theory of Crystal Lattices.* International series of monographs on physics. Oxford University Press, 1988. ISBN: 9780198503699.

[254]   D. Landau and K. Binder. *A Guide to Monte Carlo Simulations in Statistical Physics.* fourth. USA: Cambridge University Press, 2015. ISBN: 0521842387.

[255]   "IEEE Standard for Floating-Point Arithmetic". In: *IEEE Std 754-2008* (2008), pp. 1–70.

[256]   R. C. Silva et al. "Thermodynamics of elementary excitations in artificial magnetic square ice". In: *New Journal of Physics* 14.1 (Jan. 2012), p. 015008. DOI: 10.1088/1367-2630/14/1/015008.

[257]   Y.-C. Lin, Y. Tang, J. Lou, and A. W. Sandvik. "Correlated valence-bond states". In: *Phys. Rev. B* 86 (14 Oct. 2012), p. 144405. DOI: 10.1103/PhysRevB.86.144405.

[258]   Y. Wu and J. Machta. "Numerical study of the three-dimensional random-field Ising model at zero and positive temperature". In: *Phys. Rev. B* 74 (6 Aug. 2006), p. 064418. DOI: 10.1103/PhysRevB.74.064418.

[259]   G.-W. Chern and O. Tchernyshyov. "Magnetic charge and ordering in kagome spin ice". In: *Philosophical Transactions of the Royal Society A: Mathematical, Physical and Engineering Sciences* 370.1981 (2012), pp. 5718–5737. DOI: 10.1098/rsta.2011.0388. eprint: https://royalsocietypublishing.org/doi/pdf/10.1098/rsta.2011.0388.

[260] Y. .-.-L. Xie, Z. .-.-Z. Du, Z. .-.-B. Yan, and J. .-.-M. Liu. "Magnetic-charge ordering and phase transitions in monopole-conserved square spin ice". In: *Scientific Reports* 5.1 (2015), p. 15875. DOI: `10.1038/srep15875`.

[261] C. Kittel. "Theory of the Structure of Ferromagnetic Domains in Films and Small Particles". In: *Phys. Rev.* 70 (11-12 Dec. 1946), pp. 965–971. DOI: `10.1103/PhysRev.70.965`.

[262] L. D. Landau. "On the theory of the dispersion of magnetic permeabilities in ferromagnetic bodies". In: *Collected Papers of L.D. Landau*. Ed. by D. T. Haar. Pergamon, 1965, pp. 101–114. ISBN: 978-0-08-010586-4. DOI: `https://doi.org/10.1016/B978-0-08-010586-4.50023-7`.

[263] S. Cherifi et al. "Virgin domain structures in mesoscopic Co patterns: Comparison between simulation and experiment". In: *Journal of Applied Physics* 98.4 (2005), p. 043901. DOI: `10.1063/1.2007872`. eprint: `https://doi.org/10.1063/1.2007872`.

[264] V. Heywood. "Global biodiversity assessment /". In: (1995). "R.T. Watson, Chair"., x, 1140 p. :

[265] A. Libál, C. Reichhardt, and C. J. O. Reichhardt. "Realizing Colloidal Artificial Ice on Arrays of Optical Traps". In: *Phys. Rev. Lett.* 97 (22 Nov. 2006), p. 228302. DOI: `10.1103/PhysRevLett.97.228302`.

[266] A. Libál, C. J. O. Reichhardt, and C. Reichhardt. "Creating Artificial Ice States Using Vortices in Nanostructured Superconductors". In: *Phys. Rev. Lett.* 102 (23 June 2009), p. 237004. DOI: `10.1103/PhysRevLett.102.237004`.

[267] Z. Budrikis, P. Politi, and R. L. Stamps. "Diversity Enabling Equilibration: Disorder and the Ground State in Artificial Spin Ice". In: *Phys. Rev. Lett.* 107 (21 Nov. 2011), p. 217204. DOI: `10.1103/PhysRevLett.107.217204`.

[268] W. Ding et al. In: *Journal of Applied Physics* 98.1 (2005), p. 014905.

[269] M. Mansuripur. "Computation of electron-diffraction patterns in Lorentz electron microscopy of thin magnetic films (abstract)". In: *Journal of Applied Physics* 69.8 (1991), pp. 5890–5890. DOI: `10.1063/1.347859`. eprint: `https://doi.org/10.1063/1.347859`.

[270] S. McVitie and G. S. White. "Imaging Amperian currents by Lorentz microscopy". In: *Journal of Physics D: Applied Physics* 37.2 (Dec. 2003), pp. 280–288. DOI: `10.1088/0022-3727/37/2/018`.

[271] S. A. Morley et al. "Thermally and field-driven mobility of emergent magnetic charges in square artificial spin ice". In: *Scientific Reports* 9.1 (2019), p. 15989. DOI: `10.1038/s41598-019-52460-7`.

[272] S. Y. Liashko, H. Jónsson, and V. M. Uzdin. "The effect of temperature and external field on transitions in elements of kagome spin ice". In: *New Journal of Physics* 19.11 (Nov. 2017), p. 113008. DOI: `10.1088/1367-2630/aa8b96`.

[273] X. Zhang et al. "Understanding thermal annealing of artificial spin ice". In: *APL Materials* 7.11 (2019), p. 111112. DOI: `10.1063/1.5126713`. eprint: `https://doi.org/10.1063/1.5126713`.

[274] J. A. Osborn. "Demagnetizing Factors of the General Ellipsoid". In: *Phys. Rev.* 67 (11-12 June 1945), pp. 351–357. DOI: 10.1103/PhysRev.67.351.

[275] S. Koraltan et al. *Dependence of energy barrier reduction on collective excitations in square artificial spin ice: A comprehensive comparison of simulation techniques.* 2020. eprint: arXiv:2006.03828.

[276] S. A. Morley et al. "Vogel-Fulcher-Tammann freezing of a thermally fluctuating artificial spin ice probed by x-ray photon correlation spectroscopy". In: *Phys. Rev. B* 95 (10 Mar. 2017), p. 104422. DOI: 10.1103/PhysRevB.95.104422.

[277] S. Gliga et al. "Broken vertex symmetry and finite zero-point entropy in the artificial square ice ground state". In: *Phys. Rev. B* 92 (6 Aug. 2015), p. 060413. DOI: 10.1103/PhysRevB.92.060413.

[278] R. Córdoba, J. Sesé, J. D. Teresa, and M. Ibarra. "High-purity Cobalt nanostructures grown by focused-electron-beam-induced deposition at low current". In: *Microelectronic Engineering* 87.5 (2010). The 35th International Conference on Micro- and Nano-Engineering (MNE), pp. 1550–1553.

[279] L. M. Belova et al. "Rapid electron beam assisted patterning of pure cobalt at elevated temperatures via seeded growth". In: *Nanotechnology* 22.14 (Mar. 2011), p. 145305.

[280] P. Virtanen et al. "SciPy 1.0: Fundamental Algorithms for Scientific Computing in Python". In: *Nature Methods* 17 (2020), pp. 261–272. DOI: https://doi.org/10.1038/s41592-019-0686-2.

[281] F. de la Peña et al. *hyperspy: HyperSpy 0.8.5.* June 2016. DOI: 10.5281/zenodo.54004.

[282] *FPD: Fast pixelated detector data storage, analysis and visualisation.* https://gitlab.com/fpdpy/fpd. Accessed January 2020.

[283] J. P. Morgan, A. Stein, S. Langridge, and C. H. Marrows. "Thermal ground-state ordering and elementary excitations in artificial magnetic square ice". In: *Nature Physics* 7 (Nov. 2010).

[284] Y. Perrin, B. Canals, and N. Rougemaille. "Quasidegenerate ice manifold in a purely two-dimensional square array of nanomagnets". In: *Phys. Rev. B* 99 (22 June 2019), p. 224434.

[285] Y. Perrin, B. Canals, and N. Rougemaille. "Extensive degeneracy, Coulomb phase and magnetic monopoles in artificial square ice". In: *Nature* 540 (Nov. 2016), p. 410.

[286] E. Östman et al. "Interaction modifiers in artificial spin ices". In: *Nature Physics* 14.4 (2018), pp. 375–379.

[287] C. Nisoli. "On thermalization of magnetic nano-arrays at fabrication". In: *New Journal of Physics* 14.3 (Mar. 2012), p. 035017.

[288] C.-W. Liu, A. Polkovnikov, and A. W. Sandvik. "Dynamic scaling at classical phase transitions approached through nonequilibrium quenching". In: *Phys. Rev. B* 89 (5 Feb. 2014), p. 054307.

[289] P. E. Lammert, V. H. Crespi, and C. Nisoli. "Gibbsianizing nonequilibrium dynamics of artificial spin ice and other spin systems". In: *New Journal of Physics* 14.4 (Apr. 2012), p. 045009.

[290] A. Petri and M. J. De Oliveira. "Temperature of non-equilibrium lattice systems". In: *International Journal of Modern Physics C* 17.12 (2006), pp. 1703–1715.

[291] P. C. Hendry et al. "Generation of defects in superfluid ^{4}He as an analogue of the formation of cosmic strings". In: *Nature* 368.6469 (1994), pp. 315–317.

[292] W. H. Zurek. "Cosmic strings in laboratory superfluids and the topological remnants of other phase transitions". In: *Acta Phys. Polon.* B24 (1993), pp. 1301–1311.

[293] L. A. S. Mol et al. "Magnetic monopole and string excitations in a two-dimensional spin ice". In: *J. Appl. Phys.* 106 (2009), p. 063913.

[294] V. Kapaklis et al. "Melting artificial spin ice". In: *New Journal of Physics* 14.3 (2012), p. 035009.

[295] M. P. Nightingale and H. W. J. Blöte. "Dynamic Exponent of the two-dimensional Ising Model and Monte Carlo Computation of the Subdominant Eigenvalue of the Stochastic Matrix". In: *Phys. Rev. Lett.* 76 (24 June 1996), pp. 4548–4551.

[296] H. Luo et al. "Short-time dynamic behaviour of critical XY systems". In: *Physics Letters A* 250.4 (1998), pp. 383–388.

[297] J. Dziarmaga and W. H. Zurek. "Quench in the 1-D Bose-Hubbard model: Topological defects and excitations from the Kosterlitz-Thouless phase transition dynamics". In: *Scientific Reports* 4 (Aug. 2014).

[298] I. Gilbert et al. "Emergent reduced dimensionality by vertex frustration in artificial spin ice". In: *Nature Physics* 12.2 (2016), pp. 162–165. DOI: 10.1038/nphys3520.

[299] Y.-L. Wang et al. "Rewritable artificial magnetic charge ice". In: *Science* 352.6288 (2016), pp. 962–966. ISSN: 0036-8075. DOI: 10.1126/science.aad8037. eprint: https://science.sciencemag.org/content/352/6288/962.full.pdf.

[300] J. Lehmann et al. "Poling of an artificial magneto-toroidal crystal". In: *Nature Nanotechnology* 14.2 (2019), pp. 141–144. DOI: 10.1038/s41565-018-0321-x.

[301] Z. Budrikis, P. Politi, and R. L. Stamps. "A network model for field and quenched disorder effects in artificial spin ice". In: *New Journal of Physics* 14.4 (Apr. 2012), p. 045008. DOI: 10.1088/1367-2630/14/4/045008.

[302] D. Grundler. "Reconfigurable magnonics heats up". In: *Nature Physics* 11.6 (2015), pp. 438–441. DOI: 10.1038/nphys3349.

[303] P. Zhou et al. *Reservoir Computing with Planar Nanomagnet Arrays.* 2020. eprint: arXiv:2003.10948.

[304] R. V. H́ugli et al. "Artificial kagome spin ice: dimensional reduction, avalanche control and emergent magnetic monopoles". In: *Philosophical Transactions of the Royal Society A: Mathematical, Physical and Engineering Sciences* 370.1981 (2012), pp. 5767–5782. DOI: 10.1098/rsta.2011.0538. eprint: https://royalsocietypublishing.org/doi/pdf/10.1098/rsta.2011.0538.

[305] R. V. Chopdekar et al. "Controlling vortex chirality in hexagonal building blocks of artificial spin ice". In: *New Journal of Physics* 15.12 (Dec. 2013), p. 125033. DOI: 10.1088/1367-2630/15/12/125033.

[306] T. Dion et al. "Tunable magnetization dynamics in artificial spin ice via shape anisotropy modification". In: *Physical Review B* 100 (2019). DOI: 10.1103/PhysRevB.100.054433.

[307] W. H. Meiklejohn and C. P. Bean. "New Magnetic Anisotropy". In: *Phys. Rev.* 102 (5 June 1956), pp. 1413–1414. DOI: 10.1103/PhysRev.102.1413.

[308] W. H. Meiklejohn and C. P. Bean. "New Magnetic Anisotropy". In: *Phys. Rev.* 105 (3 Feb. 1957), pp. 904–913. DOI: 10.1103/PhysRev.105.904.

[309] R. L. Stamps. "Mechanisms for exchange bias". In: *Journal of Physics D: Applied Physics* 33.23 (Nov. 2000), R247–R268. DOI: 10.1088/0022-3727/33/23/201.

[310] V. M. Parakkat, K. Xie, and K. M. Krishnan. "Tunable ground state in heterostructured artificial spin ice with exchange bias". In: *Phys. Rev. B* 99 (5 Feb. 2019), p. 054429. DOI: 10.1103/PhysRevB.99.054429.

[311] V. M. Parakkat and K. M. Krishnan. "Fabrication of hybrid artificial spin ice arrays with periodic site-specific local magnetic fields". In: *Journal of Micromechanics and Microengineering* 30.9 (June 2020), p. 095002. DOI: 10.1088/1361-6439/ab948e.

[312] H. M. Revell et al. "Evidence of impurity and boundary effects on magnetic monopole dynamics in spin ice". In: *Nature Physics* 9.1 (2013), pp. 34–37. DOI: 10.1038/nphys2466.

[313] K. A. Fichthorn and W. H. Weinberg. "Theoretical foundations of dynamical Monte Carlo simulations". In: *The Journal of Chemical Physics* 95.2 (1991), pp. 1090–1096. DOI: 10.1063/1.461138. eprint: https://doi.org/10.1063/1.461138.

[314] K. M. Bal and E. C. Neyts. "On the time scale associated with Monte Carlo simulations". In: *The Journal of Chemical Physics* 141.20 (2014), p. 204104. DOI: 10.1063/1.4902136. eprint: https://doi.org/10.1063/1.4902136.

[315] L. D. C. Jaubert and P. C. W. Holdsworth. "Signature of magnetic monopole and Dirac string dynamics in spin ice". In: *Nature Physics* 5.4 (2009), pp. 258–261. DOI: 10.1038/nphys1227.

[316] U. Nowak, R. W. Chantrell, and E. C. Kennedy. "Monte Carlo Simulation with Time Step Quantification in Terms of Langevin Dynamics". In: *Phys. Rev. Lett.* 84 (1 Jan. 2000), pp. 163–166. DOI: 10.1103/PhysRevLett.84.163.

[317] O. Chubykalo et al. "Monte Carlo technique with a quantified time step: Application to the motion of magnetic moments". In: *Phys. Rev. B* 67 (6 Feb. 2003), p. 064422. DOI: 10.1103/PhysRevB.67.064422.

[318] X. Z. Cheng, M. B. A. Jalil, H. K. Lee, and Y. Okabe. "Mapping the Monte Carlo Scheme to Langevin Dynamics: A Fokker-Planck Approach". In: *Phys. Rev. Lett.* 96 (6 Feb. 2006), p. 067208. DOI: 10.1103/PhysRevLett.96.067208.

[319] S. Ruta, R. Chantrell, and O. Hovorka. "Unified model of hyperthermia via hysteresis heating in systems of interacting magnetic nanoparticles". In: *Scientific Reports* 5.1 (2015), p. 9090. DOI: 10.1038/srep09090.

[320] D. A. Garanin. "Uniform and nonuniform thermal switching of magnetic particles". In: *Phys. Rev. B* 98 (14 Oct. 2018), p. 144425. DOI: `10.1103/PhysRevB.98.144425`.

[321] A. Bupathy, V. Banerjee, and J. Carrey. "Maximal tunnel magnetoresistance in magnetic nanoparticle arrays with perpendicular anisotropy". In: *Phys. Rev. B* 100 (6 Aug. 2019), p. 064420. DOI: `10.1103/PhysRevB.100.064420`.

[322] H.-B. Braun. "Thermally Activated Magnetization Reversal in Elongated Ferromagnetic Particles". In: *Phys. Rev. Lett.* 71 (21 Nov. 1993), pp. 3557–3560. DOI: `10.1103/PhysRevLett.71.3557`.

[323] S. Krause et al. "Magnetization Reversal of Nanoscale Islands: How Size and Shape Affect the Arrhenius Prefactor". In: *Phys. Rev. Lett.* 103 (12 Sept. 2009), p. 127202. DOI: `10.1103/PhysRevLett.103.127202`.

[324] W. Wernsdorfer et al. "Experimental Evidence of the Néel-Brown Model of Magnetization Reversal". In: *Phys. Rev. Lett.* 78 (9 Mar. 1997), pp. 1791–1794. DOI: `10.1103/PhysRevLett.78.1791`.

[325] A. Farhan et al. "Exploring hyper-cubic energy landscapes in thermally active finite artificial spin-ice systems". In: *Nature Physics* 9.6 (2013), pp. 375–382. DOI: `10.1038/nphys2613`.

[326] K. Zeissler et al. "Low temperature and high field regimes of connected kagome artificial spin ice: the role of domain wall topology". In: *Scientific Reports* 6.1 (2016), p. 30218. DOI: `10.1038/srep30218`.

[327] X. Ke et al. "Energy Minimization and ac Demagnetization in a Nanomagnet Array". In: *Phys. Rev. Lett.* 101 (3 July 2008), p. 037205. DOI: `10.1103/PhysRevLett.101.037205`.

[328] J. H. Jensen et al. *flatspin: A Large-Scale Artificial Spin Ice Simulator*. 2020. eprint: `arXiv:2002.11401`.

[329] Z. Budrikis. "Athermal dynamics of artificial spin ice: disorder, edge and field protocol effects". English. PhD thesis. 2012.

[330] X. F. Han et al. "Magnetic Instability Regions in Patterned Structures: Influence of Element Shape on Magnetization Reversal Dynamics". In: *Phys. Rev. Lett.* 98 (14 Apr. 2007), p. 147202. DOI: `10.1103/PhysRevLett.98.147202`.

[331] D. Chumakov et al. "Nanosecond time-scale switching of permalloy thin film elements studied by wide-field time-resolved Kerr microscopy". In: *Phys. Rev. B* 71 (1 Jan. 2005), p. 014410. DOI: `10.1103/PhysRevB.71.014410`.

[332] K. Fallon et al. "Controlled Individual Skyrmion Nucleation at Artificial Defects Formed by Ion Irradiation". In: *Small* 16.13 (2020), p. 1907450. DOI: `10.1002/smll.201907450`. eprint: `https://onlinelibrary.wiley.com/doi/pdf/10.1002/smll.201907450`.

[333] R. P. Feynman. "There's Plenty of Room at the Bottom". In: *Feynman and Computation: Exploring the Limits of Computers*. USA: Perseus Books, 1999, pp. 63–76. ISBN: 0738200573.

[334] P. W. Anderson. "More Is Different". In: *Science* 177.4047 (1972), pp. 393–396. ISSN: 0036-8075.

[335] R. Beacham et al. "Medipix2/Timepix detector for time resolved Transmission Electron Microscopy". In: *Journal of Instrumentation* 6.12 (Dec. 2011), pp. C12052–C12052. DOI: 10.1088/1748-0221/6/12/c12052.

[336] G. W. Paterson et al. "Sub-100 nanosecond temporally resolved imaging with the Medipix3 direct electron detector". In: *Ultramicroscopy* 210 (2020), p. 112917. ISSN: 0304-3991. DOI: https://doi.org/10.1016/j.ultramic.2019.112917.

[337] X. M. Chen et al. "Spontaneous Magnetic Superdomain Wall Fluctuations in an Artificial Antiferromagnet". In: *Phys. Rev. Lett.* 123 (19 Nov. 2019), p. 197202. DOI: 10.1103/PhysRevLett.123.197202.

[338] L. Desplat and J. .-.-V. Kim. *Entropy-reduced retention times in magnetic memory elements: A case of the Meyer-Neldel Compensation Rule.* 2020. eprint: arXiv:2007.02152.

[339] K. J. Strandburg. "Two-dimensional melting". In: *Rev. Mod. Phys.* 60 (1 Jan. 1988), pp. 161–207. DOI: 10.1103/RevModPhys.60.161.

[340] P. Huang et al. "Melting of a skyrmion lattice to a skyrmion liquid via a hexatic phase". In: *Nature Nanotechnology* (2020). DOI: 10.1038/s41565-020-0716-3.

[341] T. V. Ramakrishnan. "Density-Wave Theory of First-Order Freezing in Two Dimensions". In: *Phys. Rev. Lett.* 48 (8 Feb. 1982), pp. 541–545. DOI: 10.1103/PhysRevLett.48.541.

[342] H. Kleinert. "Disclinations and first order transitions in 2D melting". In: *Physics Letters A* 95.7 (1983), pp. 381–384. ISSN: 0375-9601. DOI: https://doi.org/10.1016/0375-9601(83)90413-9.

[343] D. Sander et al. "The 2017 Magnetism Roadmap". In: *Journal of Physics D: Applied Physics* 50.36 (Aug. 2017), p. 363001. DOI: 10.1088/1361-6463/aa81a1.

[344] P. C. W. Holdsworth, M. J. P. Gingras, B. Bergersen, and E. P. Chan. "Random bonds and random fields in two-dimensional orientational glasses". In: *Journal of Physics: Condensed Matter* 3.35 (Sept. 1991), pp. 6679–6694. DOI: 10.1088/0953-8984/3/35/001.

[345] M. Saccone et al. "Elevated effective dimension in tree-like nanomagnetic Cayley structures". In: *Nanoscale* 12 (1 2020), pp. 189–194. DOI: 10.1039/C9NR07510K.

[346] M. Saccone et al. "Towards artificial Ising spin glasses: Thermal ordering in randomized arrays of Ising-type nanomagnets". In: *Phys. Rev. B* 99 (22 June 2019), p. 224403. DOI: 10.1103/PhysRevB.99.224403.

[347] L. Miao et al. "Two-dimensional magnetic monopole gas in an oxide heterostructure". In: *Nature Communications* 11.1 (2020), p. 1341. DOI: 10.1038/s41467-020-15213-z.

[348] Y. Choi et al. "Electronic correlations in twisted bilayer graphene near the magic angle". In: *Nature Physics* 15.11 (2019), pp. 1174–1180. DOI: 10.1038/s41567-019-0606-5.

[349] H. Polshyn et al. "Large linear-in-temperature resistivity in twisted bilayer graphene". In: *Nature Physics* 15.10 (2019), pp. 1011–1016. DOI: 10.1038/s41567-019-0596-3.

[350] C. Shen et al. "Correlated states in twisted double bilayer graphene". In: *Nature Physics* 16.5 (2020), pp. 520–525. DOI: 10.1038/s41567-020-0825-9.

[351] Personal communication among G. M. Macauley, R. Popy and R. L. Stamps. 2020.

[352] B. L. Le et al. "Understanding magnetotransport signatures in networks of connected permalloy nanowires". In: *Phys. Rev. B* 95 (6 Feb. 2017), p. 060405. DOI: 10.1103/PhysRevB.95.060405.

[353] G.-W. Chern. "Magnetotransport in Artificial Kagome Spin Ice". In: *Phys. Rev. Applied* 8 (6 Dec. 2017), p. 064006. DOI: 10.1103/PhysRevApplied.8.064006.

[354] W. R. Branford et al. "Emerging Chirality in Artificial Spin Ice". In: *Science* 335.6076 (2012), pp. 1597–1600. ISSN: 0036-8075. DOI: 10.1126/science.1211379. eprint: https://science.sciencemag.org/content/335/6076/1597.full.pdf.

[355] A. L. Sharpe et al. "Emergent ferromagnetism near three-quarters filling in twisted bilayer graphene". In: *Science* 365.6453 (2019), pp. 605–608. ISSN: 0036-8075. DOI: 10.1126/science.aaw3780. eprint: https://science.sciencemag.org/content/365/6453/605.full.pdf.

[356] S. Ladak et al. "Disorder-independent control of magnetic monopole defect population in artificial spin-ice honeycombs". In: *New Journal of Physics* 14.4 (Apr. 2012), p. 045010. DOI: 10.1088/1367-2630/14/4/045010.

[357] J. H. Jensen and G. Tufte. "Reservoir Computing in Artificial Spin Ice". In: *Artificial Life Conference Proceedings* 32 (2020), pp. 376–383. DOI: 10.1162/isal_a_00268. eprint: https://www.mitpressjournals.org/doi/pdf/10.1162/isal_a_00268.

[358] S. Bhanja et al. "Non-Boolean computing with nanomagnets for computer vision applications". In: *Nature Nanotechnology* 11.2 (2016), pp. 177–183. DOI: 10.1038/nnano.2015.245.

[359] A. Fernández-Pacheco et al. "Magnetization reversal in individual cobalt micro- and nanowires grown by focused-electron-beam-induced-deposition". In: *Nanotechnology* 20.47 (Oct. 2009), p. 475704. DOI: 10.1088/0957-4484/20/47/475704.